Characterisation and modelling of natural fracture networks: geometry, geomechanics and fluid flow

Qinghua Lei

Department of Earth Science and Engineering

Imperial College London

A thesis submitted for the degree of

Doctor of Philosophy

London 2016

for my parents:

Shiyu Lei and Yuping Zhang

Declaration of originality

I hereby declare that all work presented in this thesis is my own work, and all else is appropriately referenced.

Declaration of copyright

Acknowledgements

I still remember the exciting moment of about four years ago when I received and accepted the offer for doing a PhD at Imperial College London. It has proven to be a right decision. During this adventurous journey, I couldn't accomplish all the challenges without the support and help from many generous individuals.

Preface

The publications written by the author during the PhD studies are listed as below, corresponding to different chapters of this thesis.

Chapter 2

- Lei Q, Wang X. 2016. Tectonic interpretation of the connectivity of a multiscale fracture system in limestone. Geophysical Research Letters, 43, 1551-1558.

Chapter 3

- Lei Q, Latham J-P, Tsang C-F. The use of discrete fracture networks for modelling coupled geomechanical and hydrological behaviour of fractured rocks. International Journal of Rock Mechanics and Mining Sciences (to be submitted).

Chapter 4

- Lei Q, Latham J-P, Xiang J. Implementation of a joint constitutive model in finite-discrete element analysis of the geomechanical behaviour of fractured rocks. Rock Mechanics and Rock Engineering (in revision).

Chapter 5

- Lei Q, Latham J-P, Xiang J, Guo L. 2013. A geomechanical comparison between a naturally fractured rock mass and its DFN equivalent based on FEMDEM simulation. 3rd ISRM SinoRock Symposium, 18-20 June, Shanghai, China.

- Lei Q, Latham J-P, Xiang J, Tsang C-F, Lang P, Guo L. 2014. Effects of geomechanical changes on the validity of DFN representation of a realistic 2D fractured rock. International Journal of Rock Mechanics and Mining Sciences, 70: 507-523.

Chapter 6

- Lei Q, Latham J-P, Xiang J, Lang P. 2014. Representation of large scale network geometry with realistic apertures determined by mesoscale geomechanical modelling of a natural fracture system. 48th US Rock Mechanics/Geomechanics Symposium, 1-4 June, Minneapolis, USA (this paper was awarded *2015 Rock Mechanics Research Award* by American Rock Mechanics Association).

- Lei Q, Latham J-P, Tsang C-F, Xiang J, Lang P. 2015. A new approach to upscaling fracture network models while preserving geostatistical and geomechanical characteristics. Journal of Geophysical Research: Solid Earth, 120: 4784-4807.

Chapter 7

○ Lei Q, Latham J-P, Xiang J, Lang P. 2014. Coupled FEMDEM-DFN model for characterising the stress-dependent permeability of an anisotropic fracture system. 1st International Conference on Discrete Fracture Network Engineering, 19-24 October, Vancouver, Canada.

- Lei Q, Latham J-P, Xiang J, Tsang C-F. 2015. Polyaxial stress-induced variable aperture model for persistent 3D fracture networks. Geomechanics for Energy and the Environment, 1: 34-47.

Chapter 8

○ Lei Q, Wang X, Xiang J, Latham J-P. 2016. Influence of stress on the permeability of a three-dimensional fractured sedimentary layer. 50th US Rock Mechanics/Geomechanics Symposium, 26-29 June, Houston, USA.

Chapter 9

- Lei Q, Latham J-P. Progressive rock mass failure around a tunnel excavation in a geological formation with discontinuities: A numerical study. International Journal of Rock Mechanics and Mining Sciences (under review).

Abstract

Natural fractures are ubiquitous in crustal rocks and often dominate the bulk properties of geological formations. The development of numerical tools to model the geometry, geomechanics and fluid flow behaviour of natural fracture networks is a challenging issue which is relevant to many rock engineering applications. The thesis first presents a study of the statistics and tectonism of a multiscale fracture system in limestone, from which the complexity of natural fractures is illustrated with respect to hierarchical topologies and underlying mechanisms. To simulate the geomechanical behaviour of rock masses embedded with natural fractures, the finite-discrete element method (FEMDEM) is integrated with a joint constitutive model (JCM) to solve the solid mechanics problems of such intricate discontinuity systems explicitly represented by discrete fracture network (DFN) models. This computational formulation can calculate the stress/strain fields of the rock matrix, capture the mechanical interactions of discrete rock blocks, characterise the non-linear deformation of rough fractures and mimic the propagation of new cracks driven by stress concentrations. The developed simulation tool is used to derive the aperture distribution of various fracture networks under different geomechanical conditions, based on which the stress-dependent fluid flow is further analysed. A novel upscaling approach to fracture network models is developed to evaluate the scaling of the equivalent permeability of fractured rocks under in-situ stresses. The combined JCM-FEMDEM model is further applied to simulate the progressive rock mass failure around an underground excavation in a crystalline rock with pre-existing discontinuities. The scope of this thesis covers the scenarios of both two-dimensional (2D) and three-dimensional (3D) fracture networks with pre-existing natural fractures and stress-induced new cracks. The research findings demonstrate the importance of integrating explicit DFN representations and conducting geomechanical computations for more meaningful assessments of the hydromechanical behaviour of naturally fractured rocks.

Contents

List of tables

List of figures

1 Introduction

1.1 Fractures in rock

Natural fractures such as joints and faults are ubiquitous in crustal rocks. These naturally occurring discontinuities often comprise complex networks and create highly disordered geological conditions. The appearance of natural fractures and fracture networks raises a fundamental question of the underlying mechanisms that drive such complicated evolutionary and collective phenomena.

Fractures nucleate from flaws, such as voids and grain boundaries, where the local stress concentrates and exceeds the strength of the rock [Kranz, 1983; Anders et al., 2014]. The concept of fracture initiation from microcracking is supported by field observations [Pollard and Aydin, 1988; Crider and Peacock, 2004], physical experiments [Lockner et al., 1991; Moore and Lockner, 1995] and numerical simulations [Horii and Nemat-Nasser, 1985; Tang and Hudson, 2010]. The propagation of a fracture may be governed by three different strain rate regimes: (i) the subcritical regime that depends on multiple factors including the local stress, rock type, fluid pressure, temperature and stress corrosion agent [Atkinson, 1984], (ii) the quasi-static regime in which the tectonic strain rate exceeds the velocity limit of damaging species and the crack growth is governed by the strain energy dissipation (or fracture toughness) [Segall, 1984a], and (iii) the dynamic regime where fractures can propagate rapidly at a speed comparable to that of sound [Irwin, 1968].

Fractures can be classified into three main types based on their kinematic characteristics: opening-mode joints, shear-mode faults and mixed-mode hybrid fractures [Price and Cosgrove, 1990]. Joints and faults form under different stress, strain and displacement conditions [Pollard and Segall, 1987] that result in their distinct geometrical, textural and mechanical characteristics [Pollard and Aydin, 1988]. The propagation of a joint is controlled by the local tensile stress at the crack tip and is associated with an opening displacement normal to the fracture walls [Segall and Pollard, 1983a]. An oblique dilational displacement may occur in the mixed mode fracturing scenario with the concurrence of tensile and nonzero shear resolved stresses [Ramsey and Chester, 2004], which is however regarded as a variation of the opening mode due to the absence

of frictional sliding [Schultz, 2000]. Faults commonly develop by the shearing, interaction and linkage of pre-existing structures, such as dilatant crack arrays that formed earlier under mode I failure [Segall and Pollard, 1983b; Cox and Scholz, 1988; Petit and Barquins, 1988; Willemse et al., 1997; Healy et al. 2006; Crider, 2015]. This fault growth mechanism explains various field observations, such as the scatter in the relation between maximum shear displacement and fracture trace length [Cartwright et al., 1995], the consistency of mineral fillings in earlier formed joints and later developed faults [Segall and Pollard, 1983b], and the appearance of conjugate sets of en échelon tension gashes [Kidan and Cosgrove, 1996]. A debate exists about whether faults propagate into intact rocks in their own planes [Reches and Lockner, 1994] or not [Segall and Pollard, 1983b; Horii and Nemat-Nasser, 1985]. It was argued that the propagation of a fault may not be restricted to be in-plane from a microscopic constitutive view, but the composite shear failure in the macroscopic scale advances in its own plane by intensifying microcracking damage at its front [Healy et al. 2006]. An exceptional case to this fault growth mechanism is the faults in some types of porous sandstones that evolve from deformation bands, which nucleate with initial shearing and accommodate the shear strain in the narrow localised zones [Antonellini et al., 1994].

Continued strain under an enhanced remote displacement loading (i.e. progressive deformation) or a sequence of tectonic episodes can further promote the interactions of multiple fractures, such as linking or overlapping of subparallel fractures [Cruikshank et al., 1991], wing crack growth and fracture coalescence [Rispoli et al., 1981], intersecting and cross-cutting of angled fracture sets [Renshaw, 1996], inhibition of nucleation in stress shadows [Ackermann and Schlische, 1997; Bai et al., 2000], and termination, reorientation or arrest under stress perturbations [Segall, 1984b; Rawnsley et al., 1992]. Such mechanically-controlled interaction processes produce complex fracture networks with self-organised (i.e. non-random) population statistics, e.g. density, lengths, spacing, intersections, orientations, locations, and displacements [Olson, 1993; Renshaw and Pollard, 1994; Renshaw, 1997; Bonnet et al., 2001; de Joussineau and Aydin, 2007], which have important consequences on rock engineering applications.

1.2 Engineering problems

Fractures, along which rupture has caused cohesion loss and mechanical weakness in the

rock, often dominate the strength [Hoek, 1983] and deformation properties [Kachanov, 1992] of geological formations. Interconnected fractures can serve as conduits or barriers for fluid and chemical migration in subsurface space [Caine et al., 1996; Berkowitz, 2002]. The understanding, characterisation and computational modelling of the important effects of fractures on the hydromechanical properties (e.g. strength, deformability, permeability and anisotropy) of highly disordered geological formations is a challenging issue [Zimmerman and Main, 2004] and is relevant to a variety of engineering applications including the extraction of hydrocarbons, the production of geothermal energy, the remediation of contaminated groundwater, and the geological disposal of radioactive waste [Rutqvist and Stephansson, 2003]. Several key issues in hydromechanical modelling of fractured rocks are summarised as follows.

The first fundamental problem is the geometrical characterisation and representation of complex three-dimensional (3D) discontinuity systems based on limited and potentially biased field measurements, e.g. one-dimensional (1D) borehole imaging or two-dimensional (2D) outcrop mapping [Dershowitz and Einstein, 1988]. Fracture statistics are usually derived from lower-dimensional observations with respect to density, trace lengths, orientation, spacing, and frequency [Priest, 1993], based on which 2D or 3D synthetic discrete fracture networks (DFNs) can be created stochastically [Long et al., 1985; Long and Billaux, 1987] and predications can be achieved by conducting Monte Carlo simulations [Adler and Thovert, 1999; Adler et al., 2012]. However, the degree of realism and uncertainties of the simplified artificial DFNs in representing natural fracture networks that were formed by intricate mechanical and geological processes as discussed by Einstein and Baecher [1983] remains an unresolved debate in the geoscience community.

The second fundamental problem is associated with simulating the discontinuous behaviour of rock media, which includes interaction of multiple discrete bodies [Jing, 2003], fracturing and fragmentation of intact rocks [Hoek and Martin, 2014], opening, shearing and dilation of rough fractures [Bandis et al., 1983; Barton 2013], fluid flow through the fractured and porous space [Berkowitz, 2002], and coupled hydromechanical or multi-physical processes [Tsang 1999; Rutqvist and Stephansson, 2003]. The quest for a means of quantifying the influence of in-situ stresses on the permeability of fractured reservoirs has been driven largely by the motivation

from petroleum engineering [Zoback, 2007]. The understanding of contaminant migration through tectonically strained fractured formations is also important for the groundwater industry [Bear et al., 1993]. The assessment and control of damage evolution in fractured rocks caused by human activities such as excavations is crucial for radioactive waste management [Tsang et al., 2005].

One more critical issue is the upscaling of small-scale modelling results for large-scale predictions and applications. Effective medium theory has been developed to deduce the bulk properties of fractured rocks [Long et al. 1982; Kachanov, 1992; Adler and Thovert, 1999] on a homogenisation scale. However, the fractal and scaling nature of natural fracture patterns implies that the geological system may not have any representative elementary volume beyond which the system properties can be homogenised [Bonnet et al. 2001]. Thus, a more rigorous upscaling approach based on small-scale simulation results to predict multiscale, multiphysical properties of fractured rocks is important for engineering applications.

1.3 Thesis overview

The aims of this study include characterisation of the geometrical complexity of natural fracture networks, development of a computational model to simulate the geomechanical behaviour of naturally fractured rocks, investigation of stress effects on fluid flow in fracture networks, and application of the numerical tools to solve relevant engineering problems. The chapters of the thesis are designed to propose answers to the following scientific and engineering questions:

➢ *How complex are natural fracture networks at different scales? What are the principles behind the observed statistics of fracture systems?*

Chapter 2 presents a statistical study of a multiscale natural fracture system and provides a tectonic interpretation for its connectivity evolution.

➢ *How have natural fracture networks been modelled and for what purposes in the community?*

Chapter 3 presents a review of various fracture network models and the studies that apply them to simulate the geomechanical behaviour of fractured rocks as well as the consequences for fluid flow.

➢ *How can geomechanical models be improved to more realistically simulate natural fractures?*

Chapter 4 presents a finite-discrete element model integrated with a joint constitutive model for a better characterisation of the complex mechanical behaviour of natural fracture networks.

➢ *What new understandings can be gained from having stress introduced into fracture network models? How would the stress affect the fluid flow in fracture networks?*

Chapter 5 presents a study of the stress-dependent deformation and permeability of 2D natural and synthetic fracture networks at a small scale (~1 m).

➢ *How could the small-scale modelling results be used to estimate large-scale properties?*

Chapter 6 presents a novel approach to upscaling 2D fracture network models to larger domains (~100 m) while preserving geostatistical and geomechanical characteristics.

➢ *How would stress-induced fracture kinematics (i.e. fracture opening, shearing and dilatancy) affect fluid flow in 3D fracture networks with simplified geometries?*

Chapter 7 presents a study of the hydromechanical behaviour of a 3D persistent fracture network based on a 3D finite-discrete element formulation combined with a 3D stress-induced variable aperture model.

➢ *How would stress affect fluid flow in more complex 3D fracture networks where new crack propagation can occur?*

Chapter 8 presents a study of the stress-dependent deformation and permeability of a 3D sedimentary layer embedded with realistic joint sets based on a 3D finite-discrete element formulation combined with a joint constitutive model and a crack propagation model.

➢ *Can the developed fracture network models be used to solve some other engineering problems?*

Chapter 9 presents a vivid example of modelling the progressive rock mass failure around an underground excavation in a fractured crystalline formation.

2 Geometrical properties of a natural fracture system linked to an underlying tectonic mechanism

2.1 Introduction

Fractures form under certain mechanically self-organised dynamics, where breakage and fragmentation can occur at all scales [Allegre et al., 1982]. The interaction of fracture growth processes creates a hierarchical geometry that may exhibit long-range correlations from macroscale frameworks to microscale fabrics [Barton, 1995; Bonnet et al., 2001]. An unresolved debate remains whether natural fractures produced by such critical processes are well-connected or poorly-connected [Berkowitz et al., 2002]. The geometrical scaling of a fracture population provides clues for a better understanding of the geology and physics behind the statistics. The power law model having no characteristic length scale can be a useful tool to interpret the scaling phenomena of natural fracture systems, which often do not exhibit a representative elementary volume [Davy, 1993; Pickering et al., 1995; Odling et al., 1999; Marrett et al., 1999; Bour et al., 2002; Davy et al., 2010; Lei et al., 2015a]. This chapter first describes the geological setting of a multiscale fracture system in limestone and further analyses its geometrical scaling properties. Based on the knowledge of regional tectonics and a calculation of the percolation parameter of progressively formed fracture networks during multiple tectonic stages, an underlying tectonic mechanism for the connectivity evolution of the natural fracture system will be proposed.

2.2 Geological setting and fracture dataset

The geological formation studied is located in the Languedoc region of SE France and constitutes a major subsurface aquifer (i.e. the Lez aquifer) for the Montpellier area. The aquifer, with a total thickness of ~300 m, is comprised of Early Cretaceous marly limestones (upper unit) and Late Jurassic massive limestones (lower unit). The extensive documentation of the tectonic history of this area and the accessibility to multiscale fracture data make such a geological site well suited for the research objective.
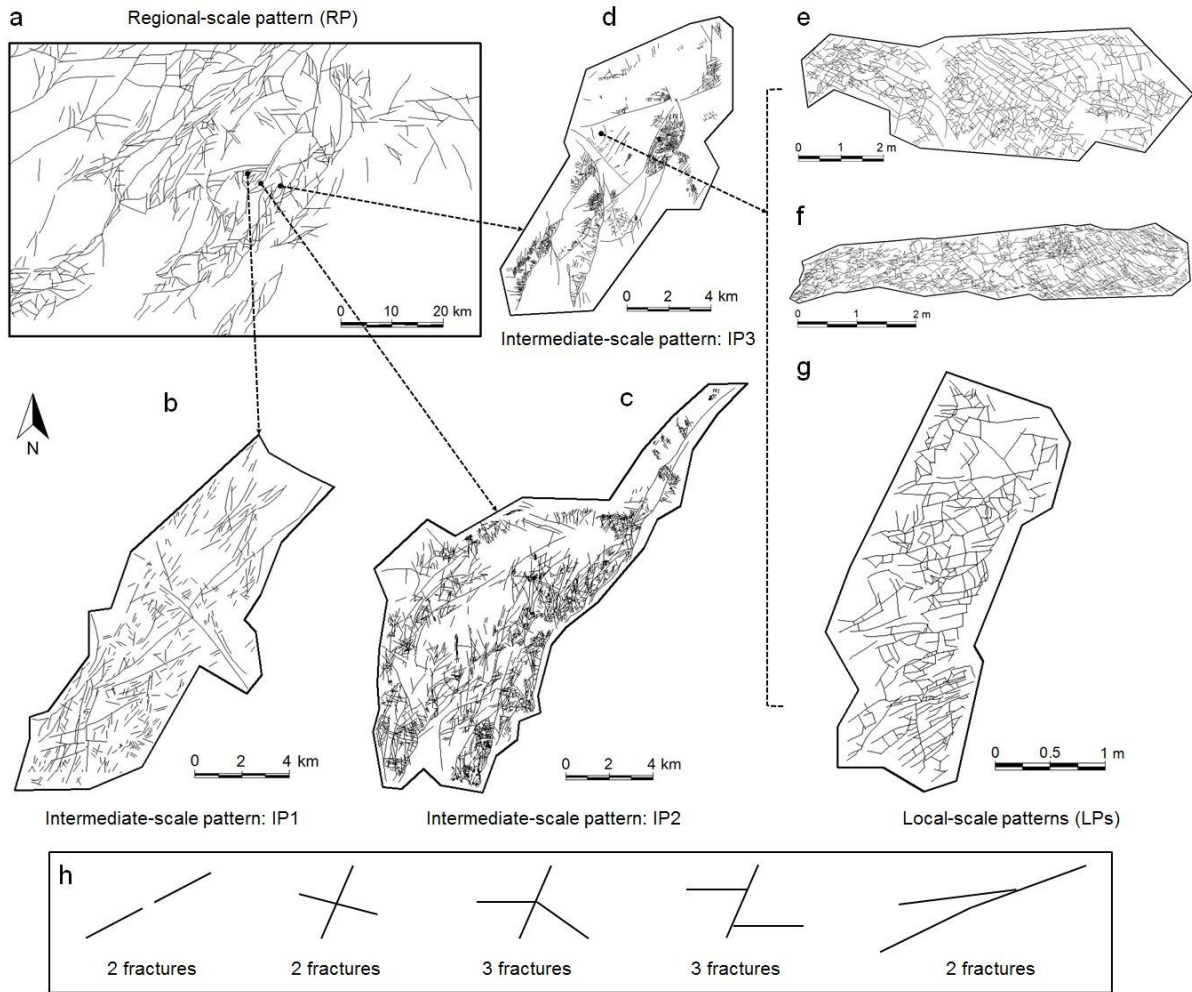
Fig. 2.1 A compilation of multiscale fracture patterns from the Languedoc region in SE France. (a) A regional-scale lineament pattern generated from the regional structural map, (b)-(d) intermediate-scale fracture patterns obtained from aerial photographs and (e)-(g) local-scale outcrop patterns derived from geological exposures. (h) A schematic of the criteria used to distinguish individual fractures from digital maps/images.

The sedimentary basin of SE France contains Mesozoic-Eocene sediments which are characterised by both extensional and compressional tectonic styles [Séranne et al., 1995]. A study of the geological evolution of the Languedoc region indicates that this area has been affected by three key tectonic events. The first is the continental stretching related to the Tethyian rifting which occurred in the Jurassic (Event I). This event generated the prevailing normal faults which strike NE-SW across the region [Benedicto et al., 1999]. During the Late Cretaceous to Eocene, the stress regime in the area changed from NW-SE extension to N-S compression as a result of the Pyrenean Orogeny. The extensional structures were reactivated as

strike-slip faults during this episode (i.e. Event II-A), which may also have created a strike-slip fault set striking NNW and conjugate to the reactivated Jurassic faults, and an opening-mode joint set aligned along the N-S direction [Petit and Mattaeur, 1995]. This plate contraction further gave rise to thrusting (Event II-B) and generated thrust faults striking approximately E-W. The crustal extension during the Oligocene (Event III) is related to the opening of the Gulf of Lion and contributed mainly to the rejuvenation of the regional Jurassic normal faults and the creation of a few new minor normal faults [Benedicto et al., 1999]. The Lez aquifer experienced intensive rifting, faulting and folding during the geological history and consequently a multiscale system of faults and joints has developed as a result of the superposition of multiple fracture sets each linked to a separate tectonic event.

The characterisation of the 3D structure of the fracture system is impeded by the difficulty of direct measurements, so 2D patterns exposed at the Earth's surface are used. A regional-scale (~100 km) fault pattern (Fig. 2.1a), denoted as RP, was generated from the geological map made by Bureau de Recherches Géologiques et Minières (BRGM) [2011] at a scale of 1:250,000. Three intermediate-scale (~10 km) fracture patterns containing both faults and joint corridors, denoted as IP1-3 (Fig. 2.1b-d), were digitised from assembled aerial photographs taken by Institut National de l'Information Géographique et Forestière (IGN) [1954] at a scale of 1:25,000 (resolution may vary slightly due to the uneven terrain). Eleven local-scale (1-10 m) joint patterns, denoted as LPs (three of them are presented in Fig. 2.1e-g), were drawn based on outcrop mapping. Each outcrop map was constructed from a number of images taken at a fixed height of 1.5 m and rectified for perspective distortions before assembly. Fractures were manually traced from the digital maps/photographs and individualised according to the spatial continuity and directional consistency of digitised traces (Fig. 2.1h). The determination of the connectedness of fracture traces may be affected by the resolution limit of the original maps/photographs. Some discontinuous segments may be identified as a single fracture, leading to an overestimation of the occurrence of larger structures [Davy, 1993]. The fracture patterns may suffer from incomplete sampling producing a bias due to lack of exposure caused by the vegetation covers and erosion effects. This can result in an exaggeration of clustering properties, an underestimation of small-scale populations, and superficial segmentations of large structures.

Furthermore, smaller patterns that sample limited local spots of larger domains may underestimate the geological heterogeneity. More details of the multiscale fracture dataset are provided in Appendix A.

2.3 Scaling properties of the multiscale fracture system

Fractal concepts provide a way to identify and quantify the repetition phenomenon of natural fracture systems over a wide range of scales [Mandelbrot, 1982]. The spatial scaling feature can be characterised by the fractal dimension D, which accounts for the manner whereby fractals cluster and spread in the Euclidean space. The standard or modified box-counting method has been widely used to measure the fractal dimension of complex fracture systems [Chilès, 1988; Odling, 1992; Walsh and Watterson, 1993; Barton, 1995; Berkowitz and Hadad, 1997; Roy et al., 2007]. However, the box-counting method has intrinsic biases due to the presence of cross-over regimes between dimensions of 1 (i.e. dimension of fracture lines) and 2 (i.e. dimension of the embedding medium) [Odling, 1992; Berkowitz and Hadad, 1997]. As a result, it is difficult to discriminate between natural fracture patterns and purely random networks, for which the two-point correlation function method can give more appropriate results [Bonnet et al., 2001]. The two-point correlation function describes the spatial correlation of fracture barycentres [Bour and Davy, 1999] as given by

$$C_2(r) = \frac{1}{N^2} N_d(r) \sim r^{D_c} \tag{2.1}$$

where N is the total number of fracture barycentres, and N_d is the number of pairs of barycentres whose distance is smaller than r [Hentschel and Procaccia, 1983]. Barycentres are calculated using the observed traces including those intersecting the boundaries, since the two-point correlation method is valid irrespective of the type of points (barycentre, fracture tips, or any random point on the fracture trace) that are used to represent fracture locations [Bour et al., 2002]. For a fractal population, $C_2(r)$ is expected to scale with r following a power law relation with the exponent D_c defined as the correlation dimension. The D_c value varies for different patterns: 1.68 for RP, 1.66 for IP1, 1.48 for IP2, 1.20 for IP3, and 1.60 ± 0.11 for LPs (Appendix A gives the detailed calculation of D_c and associated logarithmic slopes for each pattern). The low D_c values of IP2 and IP3 may be induced by the effects of incomplete sampling, while the

variability in LPs is probably related to local stress variations and lithological heterogeneity. Thus, 1.65 might be a realistic value for the underlying fractal dimension and the fitting trend is shown in Fig. 2.2a.

A power law is often used to interpret the length distribution of natural fracture traces and its exponent quantifies the manner that frequency decreases with fractures sizes [Odling, 1997; Bonnet et al., 2001; Neuman, 2008]. The density distribution of fracture lengths (i.e. trace lengths) can be modelled by a power law [Bour et al., 2002; Davy et al., 2013] as given by

$$n(l,L) = \alpha L^D l^{-a} \qquad \text{for } l \in [l_{min}, l_{max}] \qquad (2.2)$$

where $n(l, L)dl$ gives the number of fractures with sizes l belonging to the interval $[l, l + dl]$ ($dl \ll l$) in an elementary volume of characteristic size L, a is the power law length exponent, D is the fractal dimension, and α is the density term. The extent of the power law scaling is bounded by an upper limit l_{max} that is probably related to the thickness of the brittle upper crust and a lower limit l_{min} that is constrained by a physical length scale (e.g. grain size) or the resolution of measurement [Ouillon et al., 1999; Berkowitz et al., 2000]. The exponents a and D quantify different scaling of the fracture network: the length distribution (related to a), and the fracture density (related to D). The density term α is related to the total number of fractures in the system and varies as a function of fracture orientations [Davy et al., 2010]. The power law length exponent a can be derived from the density distribution plot of fracture lengths [Pickering et al., 1995]. The fracture length data may suffer from the truncation effect due to limited resolution and the censoring effect due to incomplete sampling [Pickering et al., 1995; Bonnet et al., 2001]. The truncation effect is eliminated by using a lower cut-off of $5\% \times L$ for each map when fitting the power law curve [Odling et al., 1999]. The censoring bias of the regional map is corrected by removing traces that intersect the window sampling boundaries [Bour et al., 2002] with the artificial density perturbation amended using an effective system size estimated as the square root of the coverage area of the remaining fractures. The a value varies for different patterns: 2.61 for RP, 2.41 for IP1, 2.62 for IP2, 2.53 for IP3, and 2.73 ± 0.38 for LPs. The variation may be influenced by the artefact when tracing individual fractures and determining their persistence, and the bias from incomplete mapping. The large standard deviation in LPs may also be related to the heterogeneity of stress and lithology, to which small-scale fracturing would be more

sensitive. Fig. 2.2b gives the length distribution of all fracture networks normalised by their fractal area, i.e. L^D, and the overall trend may be fitted by a power law with $a = 2.65$ and $\alpha = 3.0$.
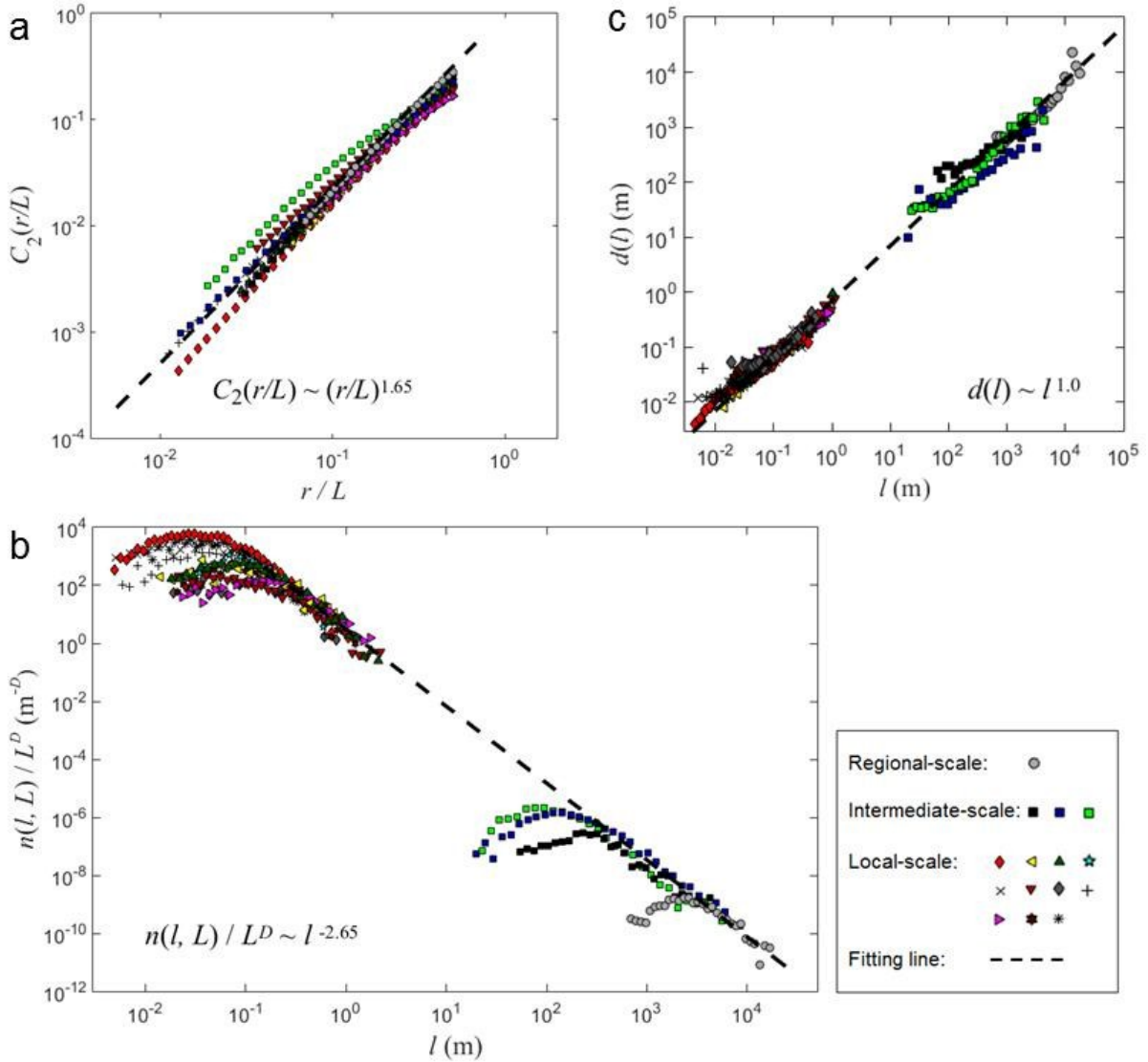
Fig. 2.2 (a) Calculation of the normalised two-point correlation functions $C_2(r/L)$ as a function of r/L. The dashed line represents a power law fitting line with the fractal dimension $D = 1.65$. (b) The normalised density distribution of fracture lengths of the multiscale fracture patterns; the dashed line represents a power law fitting line with an exponent $a = 2.65$ and a density term $\alpha = 3.0$. (c) Scaling of the distance $d(l)$ between the barycentre of a fracture and that of its nearest neighbour having a length larger than l; the dashed line represents a power law fitting line with an exponent $x = 1.0$.

Fractures having a broad-bandwidth power law size distribution are not randomly placed in the geological media, but organised by mechanical interactions that occur during their growth

process [Darcel et al., 2003a; Davy et al., 2010, 2013]. The relationship between the fractal dimension and length exponent observed for the dataset studied here, i.e. $a \approx D+1$, indicates that the multiscale fracture system may be self-similar [Bour et al., 2002]. For a self-similar fracture network, the number of fractures $N(l)$ that have lengths comparable to the domain size L (i.e. $xL < l < x'L$ given x and x' are close to 1) can be derived as:

$$N(xL < l \leq x'L) = \int_{xL}^{x'L} n(l, L)\mathrm{d}l = \alpha L^{D-a+1} \frac{x^{-a+1} - x'^{-a+1}}{a-1} \qquad (2.3)$$

It can be seen that, if $a = D+1$, N is independent of L (i.e. the number of "large" fractures is constant at all scales), which is the signature and necessity of self-similar structures [Darcel et al., 2003a]. A self-similar fracture pattern can emerge under a statistically-valid hierarchical rule that a large fracture inhibits smaller ones from crossing it but not the converse [Davy et al., 2010]. The average distance $d(l)$ between the centroid of a fracture and that of the nearest larger neighbour is theoretically correlated with the fracture length l by $d(l) \propto l^x$ [Bour and Davy, 1999], where $x = (a-1)/D$ and is equal to 1.0 for a self-similar scenario. The distance data of the multiscale patterns tend to fit a power law with $x = 1.0$ (Fig. 2.2c), suggesting that the distance of a fracture to its nearest larger one is linearly correlated with its size, and that the sets of faults and joints were well developed and had reached quite a dense state controlled by their mechanical interaction [Davy et al., 2010]. In addition, the fracture patterns on different scales also exhibit quite similar values for the ratio of $d(l)/l$, implying that fracture interaction may be governed by a similar mechanism over different scales (this may seem surprising given that faulting is a different brittle process to jointing).

It is complicated to accurately compute the connectivity of a 2D natural fracture network involving a fractal organisation and a power law length distribution [Darcel et al., 2003a]. The complex boundaries of the sampled patterns also create difficulties for a direct connectivity measurement by checking the presence of connected pathways from one boundary to its opposite. In this study, a simple equation postulated by Berkowitz et al. [2000] is employed to calculate the percolation parameter p as a connectivity metric of fracture networks, as given by:

$$p(l, L) = \int_{l_{min}}^{L} \frac{n(l, L)l^D}{L^D} \mathrm{d}l + \int_{L}^{l_{max}} n(l, L)\mathrm{d}l \qquad (2.4)$$

Here l_{min} is defined as the fracture length over which all fractures are considered to have been correctly sampled, corresponding to the onset of power law length scaling for each network (given in Appendix A). The connectivity of a fracture network is made up of two parts, as can be seen in Eq. (2.4): the first part describes the contribution made by fractures smaller than the system size L and the second represents the contribution from fractures larger than L [Bour and Davy, 1997]. Mathematically, the connectivity of a self-similar fractal population is scale invariant [Darcel et al., 2003a], and the networks are connected at all scales if p is larger than the percolation threshold p_c. Here p_c is defined as the onset above which a fracture network is, on average, connected from one side of the domain to the other. The range of p_c was determined to be between 5.6 and 6.0 derived using 2D random fracture network realisations [Bour and Davy, 1997]. Uncertainties may exist for this p_c value when it is applied to natural fracture patterns involving distinguishable orientation sets [Robinson, 1983, 1984] and fractal density distributions [Darcel et al., 2003a]. Furthermore, evaluations relying on this p_c for 2D networks usually underestimate the connectivity of actual 3D systems [Bour and Davy, 1998]. A correcting factor of $2/\pi$ was suggested to derive a p_c for 3D geometries [Lang et al., 2014], which yields $p_c \approx 3.6\text{-}3.8$. In the study area, the p value of the fracture patterns at different scales varies significantly: 7.18 for RP, 5.30 for IP1, 14.69 for IP2, 6.90 for IP3 and 6.81 ± 2.17 for LPs. The computed p should be less than the real value because fractures smaller than l_{min} that can contribute to connectivity are not included in the calculation. It can be noted that some patterns seem to be only slightly above the threshold, whereas others have a much higher value. The variation of p may be caused by the diversity of a and D for different samples. The inconsistency in the ratio of L/l_{min} can also have a significant impact on the observed connectivity of a self-similar network [Berkowitz et al., 2000]. However, these factors may still not sufficiently explain the high contrast in the calculated p values, i.e. 4.6 to 14.69 (Table A.1 in Appendix A).

2.4 Are natural fractures well- or poorly-connected?

The connectivity of fracture networks is thought to be a good indicator of the bulk properties (e.g. permeability, elastic modulus) of geological formations [Davy et al., 2010]. The proximity of the connectivity state of natural fracture networks to the percolation threshold remains an unresolved debate. It was argued earlier that natural fracture systems are close to the percolation

threshold [Renshaw, 1997], because the driving force (tectonic stress or hydraulic pressure) is abruptly released once the system is connected, and a diminished mechanical strength and an enhanced hydraulic conductivity is likely to occur [Chelidze, 1982; Madden, 1983; Gueguen et al., 1991; Renshaw, 1996; Zhang and Sanderson, 1998]. However, extensive field observations suggest that crustal fractures can be well-connected and significantly above the threshold [Barton, 1995].

An understanding of the process by which the natural fracture networks evolve might offer an explanation for this. Fracture networks in rock develop over geological time by the superposition of successive fracture sets each linked to a different stress regime and set of crustal conditions. Thus, there is a strong possibility that early fracture sets may become partially or totally cemented as the network evolves and fluids move through it. These sealed or partially sealed early fracture sets may act as barriers to fluid flow and the integrity of the rock has been to some extent recovered [Holland and Urai, 2010]. Although the network geometrically remains almost the same, its "effective" connectivity has been reduced well below the percolation threshold. As a result, subsequent stress fields could continue to propagate new fractures until the critical state is reestablished. However, if the "apparent" connectivity of trace patterns is measured without taking into account their internal sealing conditions, it is likely to derive a percolation state significantly above the threshold. In addition, the intrinsic anisotropy of the fracture network may also permit tectonic energy to accumulate in other directions which have a higher mechanical strength/stiffness and can accommodate more new cracks.

Table 2.1 Percolation parameters of the progressively formed fracture patterns at the end of each different formation stage.

Pattern	Stage 1 (Event I)	Stage 2 (Event II-A)	Stage 3 (Event II-B & III)
RP	3.87	5.05	7.18
IP1	3.06	4.30	5.30
IP2	8.16	12.62	14.69
IP3	3.62	5.69	6.90
LPs	--	4.38 ± 1.54	6.81 ± 2.17

To test this concept, the percolation parameter of the progressively developed fracture

networks at the end of each different formation stage is calculated (Table 2.1). This is achieved simply by re-analysing networks from field data with the appropriate later-staged fractures removed based on the relation between orientation and tectonic events. The three key tectonic events (see section 2.2) governed large-scale faulting and jointing, and produced the regional-scale and intermediate-scale fracture patterns. These networks are the results of the superimposition of multiple fracture sets each of which is associated with distinct orientation and linked to a separate tectonic event. The relative ages of the successively generated fracture sets can therefore be determined according to the sequence of the tectonic events [Park et al., 2010]. Fig. 2.3 presents a schematic illustration of the kinematic evolution of the studied fracture system during the tectonic history. At the small-scale, e.g. the fracture networks observed in outcrop, the fracture systems are bounded by larger faults and often form close to the ground surface. These larger fractures are likely to severely disturb and rotate the local stress field, and the orientation of the resulting small-scale fractures is, therefore, unlikely to reflect that of the regional stress field. The chronological sequence of the local-scale joints was determined based on the abutting relation of the two major sets. Generally, the first set exhibits a connectivity state close to the percolation threshold (see Table 2.1), consistent with the postulation of energy relief at the connecting moment observed in both laboratory experiments [Chelidze, 1982] and numerical simulations [Madden, 1983; Renshaw 1996; Zhang and Sanderson, 1998]. However, because of the possibility of early fractures becoming cemented as has been observed in the Languedoc area [Petit and Mattauer, 1995; Petit et al., 1999], a fracture network which at the time of its formation was at the percolation threshold may subsequently have an "effective" connectivity considerably lower than p_c. Thus, in response to later tectonic events, further cracking may occur within the network until the system once again becomes connected. The incremental rate of p caused by late-stage fracturing seems to gradually decrease due to the presence of early-stage fractures. This is because percolation can be reached more easily by reactivating and/or coalescing existing fractures rather than by generating new ones. The exceptionally high p in the pattern of IP2 may be attributed to its location very close to one of the regional-scale faults, in the vicinity of which concentrated fracturing paced by active calcite precipitation may occur, i.e. more intensive "crack-seal" cycles may be involved [Petit and Mattauer, 1995; Petit et al., 1999].

Note that the calculation and analysis of the observed connectivity seeks to achieve a first-order approximation of the percolation state that may have existed during the multi-stage fracture network evolution. The simplified kinematic analysis may not fully capture the complex faulting process that can involve linkage of early-formed fractures in later episodes (i.e. the sizes of large faults may be slightly different from their original ones).
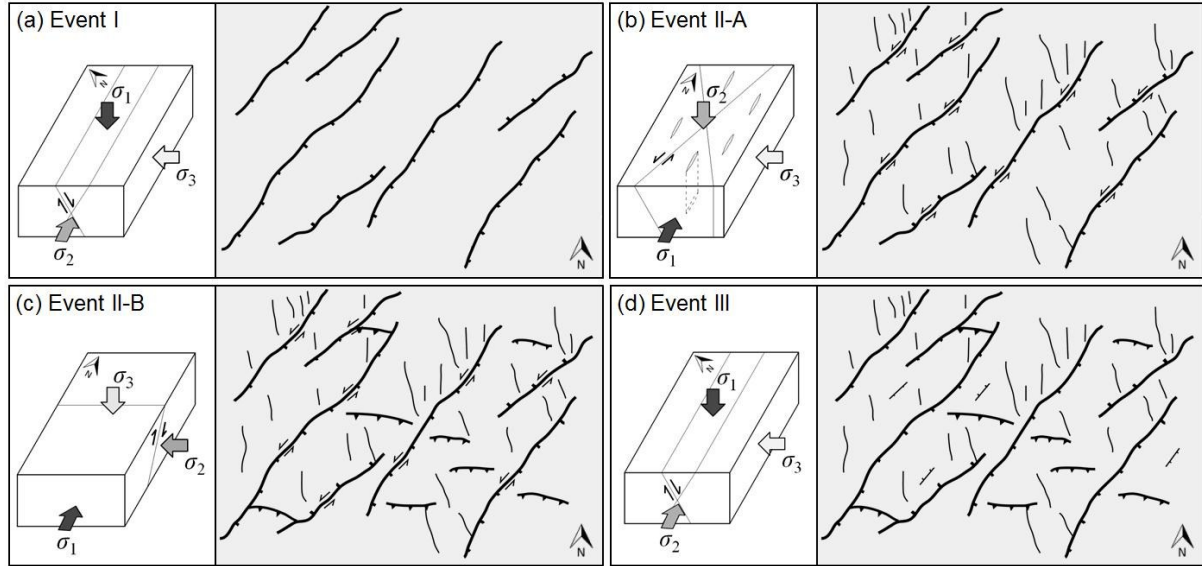
Fig. 2.3 Tectonic events that have affected the geological formations in the Languedoc region, SE France. Note: σ_1, σ_2 and σ_3 denote the maximum, intermediate and minimum tectonic stresses, respectively.

2.5 Discussion

The evolution of the percolation parameter implies that a large amount of energy may have been released during the early-stage fracturing (as revealed by the high p at the end of the first formation stage of each pattern), after which tectonic or hydraulic forces could not be elevated to such high levels because they would be dissipated by the shearing and coalescence of the existing large structures [Petit and Mattauer, 1995; Park et al., 2010]. A likely universal scaling behaviour may exist in a multiscale fracture system [Odling et al., 1999; Marrett et al., 1999; Bour et al., 2002; Du Bernard et al., 2002; Bertrand et al., 2015], whereas inconsistent scaling exponents separated by characteristic lengths can also occur [Ouillon et al., 1996; Hunsdale and Sanderson, 1998; de Joussineau and Aydin, 2007; Putz-Perrier and Sanderson, 2008; Davy et al., 2010]. A break in scaling may be caused by the different growth mechanisms of jointing and faulting [Pollard and Segall, 1987; de Joussineau and Aydin, 2007], the influence of lithological

layering [Ouillon et al., 1996; Hunsdale and Sanderson, 1998; Odling et al., 1999; Putz-Perrier and Sanderson, 2008], and the nature of driving forces (i.e. boundary or body forces) associated with distinct spatial organisation of strains [Bonnet et al., 2001; Davy et al., 2010]. Such effects may have also contributed to the great variability in the scaling exponents of the fracture network studied in this chapter. However, a power law may fit the overall trend of the study system due to a possibility that multiscale fracturing processes in this region were governed by the same set of tectonic factors. The quite low D values (i.e. 1.41-1.74) of the joint patterns in this study, seemingly contradictory to the general understanding that joints tend to be more space filling (i.e. homogeneously distributed), might be induced by the possibility that they have multifractal features and therefore the correlation dimension can be significantly smaller than 2.0 [Bonnet et al., 2001]. Actually, the measured D values here are in the typical range of 1.4-2.0 for joint systems according to the compilation by Bonnet et al. [2001]. Whether mode I fractures are clustered or homogeneously spaced may be related to the stress conditions under which they were formed [Gillespie et al., 2001].

In this chapter, an interpretation is proposed for the connectivity variation of a multiscale fracture system based on its polyphase tectonic history and a crack-seal mechanism. The results revealed a link between the geometrical statistics of fracture networks and the underlying tectonic processes. Note that the assessment using Eq. (2.4) may be associated with uncertainties due to the potential scale-dependence of the percolation parameter at the connectivity threshold, as pointed out by Darcel et al. [2003a]. Furthermore, the findings of this research are based on a specific fracture system which seems to have a self-similar property with $a \approx D+1$. Different connectivity scaling phenomena can occur in other scenarios [Darcel et al., 2003a]. For $a < D+1$, the connectivity is controlled by fractures having a length larger than or of the order of the system size and increases with scale. For $a > D+1$, the connectivity is ruled by fractures much smaller than the system size and thus decreases with scale. To investigate the behaviour of 3D fracture systems, the fractal dimension and power law length exponent in 3D can be extrapolated from the 2D parameters based on the stereological relationships given in Darcel et al. [2003b]. The percolation parameter and percolation threshold of 3D fracture networks with broadly distributed sizes may be estimated using the formulation proposed by de Dreuzy et al. [2000].

2.6 Concluding remarks

To sum up, the spatial and length distributions as well as their cross-relation (i.e. fracture distances) of a multiscale fracture system in limestone has been investigated. Contradicting the prediction that scale-invariant connectivity is associated with idealised self-similar systems, the percolation state of trace patterns mapped at different scales and localities of the study area varies significantly, from well- to poorly-connected. A tectonic interpretation based on a polyphase fracture network evolution history has been proposed to explain this discrepancy. The formation of fracture networks is linked to a succession of tectonic episodes and multiple geological processes. The presented data suggest that the driving force for fracture propagation may be dissipated at the end of each tectonic event when the system becomes connected. However, further fracturing may still be accommodated when later driving forces are applied especially if the "effective" connectivity of the system has been reduced well below the threshold due to the cementation of some of the fractures within the network. In addition, the connectivity anisotropy may also permit additional cracking in directions which have a poorer percolation state. As a result, the "apparent" connectivity measured for fracture networks regardless of their internal sealing conditions can be highly variable depending on the intensity of crack-seal cycles and also indicate a state considerably exceeding the percolation threshold.

This study illustrated the complexity of the geometrical and topological characteristics of natural fracture networks that involves scaling, hierarchy, clustering, anisotropy and connectivity. To characterise and simulate such self-organised geological structures, numerous fracture network models have been proposed and developed during the past few decades, and further applied to solve various engineering problems related to naturally fractured rocks. The next chapter will present a review of the approaches, principles, achievements and outstanding issues in fracture network modelling of the geomechanical behaviour of fractured rocks and the consequences for fluid flow.

3 The use of discrete fracture networks for modelling geomechanical behaviour of fractured rocks and its impacts on fluid flow

3.1 Introduction

Fractured rock is a naturally occurring solid material embedded with various discontinuities, such as faults, joints and veins. Such geological structures often dominate the geomechanical and hydromechanical behaviour of subsurface media [Zimmerman and Main, 2004]. Understanding of the nontrivial effect of fractures is a challenging issue which is relevant to many engineering applications such as underground construction, geothermal energy, petroleum recovery, groundwater management and nuclear waste disposal [Rutqvist and Stephansson, 2003]. The importance of the presence of natural fractures, which can result in heterogeneous stress fields [Pollard and Segall, 1987] and channelised fluid flow pathways [Tsang and Neretnieks, 1998] in highly disordered geological formations, has promoted the development of robust fracture network models for numerical simulation of fractured rocks [Herbert, 1996].

The purpose of this review is to present a summary of various approaches that explicitly mimic natural fracture geometries, and different numerical frameworks that integrate discrete fracture representations for modelling the geomechanical behaviour of fractured rocks as well as further analysis of the consequences on fluid flow. Section 3.2 reviews the methods of representing natural fracture geometries by geological mapping, stochastic generation or geomechanical simulation. Section 3.3 provides a brief overview of continuum and discontinuum models that integrate fracture information for geomechanical modelling of fractured rocks. Section 3.4 summarises numerical studies of geomechanical effects on fluid flow in fractured rocks. A discussion is presented on the pros and cons of the different numerical models as well as some outstanding issues, and finally, concluding remarks are made.

3.2 Geometrical modelling of fracture networks

A "discrete fracture network" (DFN) refers to a computational model of fracture patterns that explicitly represents the geometrical properties of each individual fracture (e.g. orientation,

size, position, shape and aperture), and the topological relationships between individual fractures and fracture sets. Unlike the conventional definition of DFNs that corresponds to stochastic fracture networks, the term DFN here represents a much broader concept of any explicit fracture network model. A DFN can be generated from geological mapping, stochastic realisation or geomechanical simulation. Fracture analogues from physical experiments are not included here as their main purpose is to explore the underlying mechanisms rather than building numerical models.

3.2.1 Geologically-mapped fracture networks

Fracture patterns can be mapped from the exposure of rock outcrops or man-made excavations (e.g. borehole, quarry, tunnel and roadcut). These geologically-mapped fracture networks were widely used to understand the process of fracture formation [Segall and Pollard, 1983a; Pollard, and Segall, 1987], interpret the history of tectonic stresses [Engelder and Geiser, 1980; Olson and Pollard, 1989; Petit and Mattauer, 1995], and derive the statistics and scaling of fracture populations [La Pointe, 1988; Bour et al., 2002]. However, digitised outcrop analogues (Fig. 3.1) can also be used to build DFNs for numerical simulations. For example, a series of discrete fracture patterns were mapped from limestone outcrops at the south margin of the Bristol Channel Basin, UK [Belayneh and Cosgrove, 2004]. The traced DFNs were used to study the connectivity [Masihi and King, 2008], multiphase flow [Belayneh et al., 2006, 2009; Geiger and Matthäi, 2014], solute transport [Geiger et al., 2010] and hydromechanical behaviour [Latham et al., 2013; Figueiredo et al., 2015] of natural fracture systems. Similar outcrop-based DFNs have also been constructed by many other researchers for modelling natural fracture systems [Zhang and Sanderson, 1995, 1996, 1998; Zhang et al., 1996; Brown and Bruhn, 1998; Sanderson and Zhang, 1999; Griffith et al., 2009]. Fracture apertures may be determined from a detailed field mapping [Jourde et al., 2002; Leckenby et al., 2005] and further calibrated by comparing flow simulation results with in-situ measurements [Taylor et al., 1999]. However, apertures were more commonly assumed to be constant or to follow an a priori statistical distribution (sometimes correlated with trace lengths).

Advantages of such an outcrop-based DFN model include preservation of natural fracture features (e.g. curvature and segmentation) and unbiased characterisation of complex topologies

(e.g. intersection, truncation, arrest, spacing, clustering and hierarchy). However, it is often constrained to 2D analysis (of more applicability to research study) and may not be applicable for general 3D problems involving obliquely dipping fractures. The recent technology of LIDAR survey may be able to capture the 3D structural variations in near surface and help build a realistic 3D DFN model [Wilson et al., 2011; Jacquemyn et al., 2015], but it is difficult to use such a technique to measure deeply buried geological complexities. Extrapolation from borehole imaging can provide an estimation of 3D fracture distributions but confidence can only be guaranteed for the areas close to boreholes [Wu and Pollard, 2002]. Seismic data can be used to build 3D maps of large-scale geological structures [Kattenhorn and Pollard, 2001], for which, however, the limited resolution often obscures detailed features such as the segmentation of faults and impedes the detection of small cracks widely spreading in subsurface rocks.
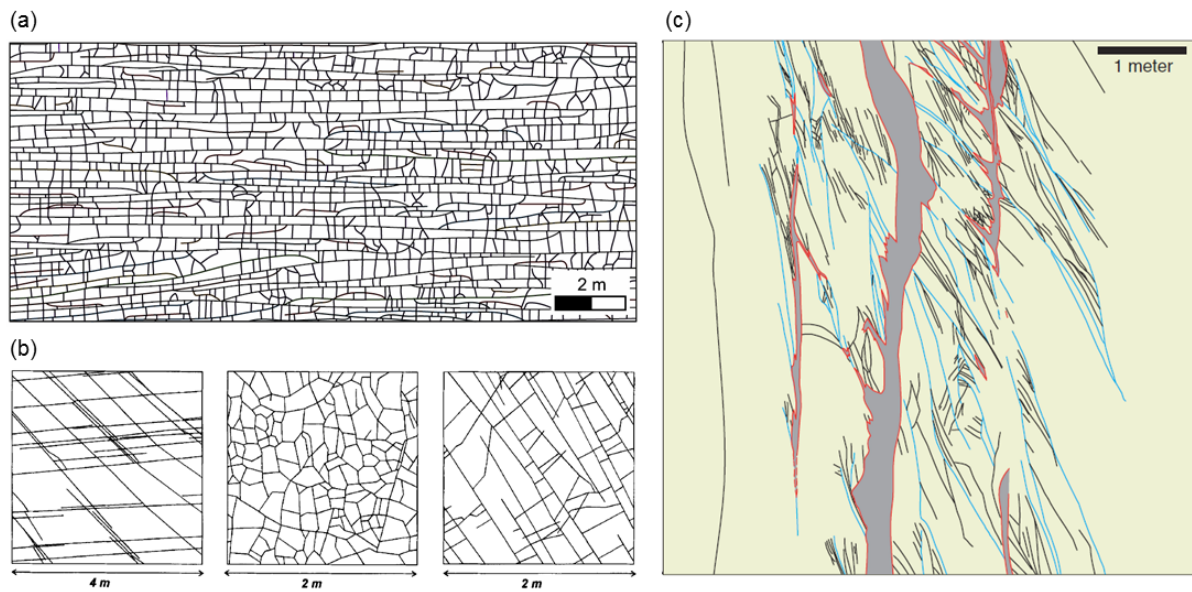
Fig. 3.1 Geologically-mapped DFN patterns based on (a) a limestone outcrop at the south margin of the Bristol Channel Basin, UK [Belayneh and Cosgrove, 2004], (b) sandstone exposures in the Dounreay area, Scotland [Zhang and Sanderson, 1996], and (c) fault zone structures in the Valley of Fire State Park of southern Nevada, USA [Jourde et al., 2002].

3.2.2 Stochastically-generated fracture networks

Due to the difficulty of performing a complete measurement of 3D natural fracture systems, stochastic approaches using statistics from limited sampling have been developed and widely

used [Dershowitz and Einstein, 1988]. The stochastic DFN method emerged in the 1980s with the aims to study the percolation of finite-sized fracture populations [Robinson, 1983, 1984; Balberg and Binenbaum, 1983] and fluid flow in complex fracture networks [Long et al., 1982, 1985; Andersson et al., 1984; Andersson and Dverstorp, 1987; Long and Billaux, 1987].

The general stochastic DFN approach assumes fractures to be straight lines (in 2D) or planar discs/polygons (in 3D), and treats the other geometrical properties (e.g. position, size, orientation, aperture) as independent random variables obeying certain probability distributions derived from field measurements (e.g. scanline/window sampling of outcrop traces and borehole imaging) [Baecher, 1983]. The orientation data can be processed using a rosette or stereogram so that fractures can be grouped into different sets with their orientations characterised by e.g. a uniform, normal or Fisher distribution [Einstein and Baecher, 1983]. Fracture sizes may exhibit a negative exponential, lognormal, gamma or power law distribution [Davy, 1993; Bonnet et al., 2001]. Fracture density can be characterised by fracture spacing, the total number/length of fractures per unit area (in 2D) or total number/surface area of fractures per unit volume (in 3D). Fracture spacing may follow a negative exponential, lognormal or normal distribution depending on the degree of fracture saturations in the network [Rives et al., 1992]. Fracture apertures usually obey a lognormal [Snow, 1970] or power law distribution [Barton and Zoback, 1992; Hooker et al., 2009], and may be related to fracture sizes by a power law [Bonnet et al., 2001] with a linear [Pollard and Segall, 1987] or sublinear [Olson, 2003] scaling relationship. The 1D/2D measurement data may be biased under the truncation and censoring effects and requires to be amended to determine the underlying statistical distributions [Laslett, 1982; Pickering et al., 1995]. 3D parameters can be extrapolated from the 1D/2D data based on stereological analysis [Berkowitz and Adler, 1998]. In the stochastic simulation, fractures are assumed randomly located (represented by their barycentres), while the geometrical attributes can be sampled from the corresponding probability density functions [Dershowitz and Einstein, 1988]. Such a random fracture network modelling approach, termed the Poisson DFN model (Fig. 3.2), has been implemented within the commercial software FracMan [Golder Associate Inc., 2011] and also adopted by many research codes to study the connectivity, deformability, permeability and transport properties of fracture networks in the past three decades [Hestir and Long, 1990;

Zimmerman and Bodvarsson, 1996; Bour and Davy, 1997, 1998; Renshaw, 1999; de Dreuzy et al., 2001a, 2001b, 2002; Min and Jing, 2003; Min et al., 2004a, 2004b; Sanderson and Zhang, 2004; Baghbanan and Jing, 2008; Leung and Zimmerman, 2012; Rutqvist et al., 2013; Zhao et al., 2013; Zhang and Lei, 2013, 2014; Lang et al., 2014] (only a few among many others).
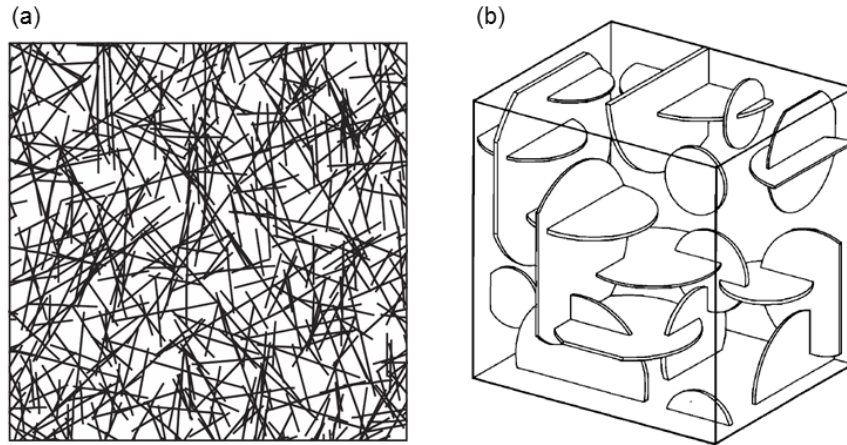
Fig. 3.2 The Poisson DFN models: (a) a 2D random fracture pattern conditioned by field data from the Sellafield site, Cumbria, UK [Min and Jing, 2003], and (b) a 3D random fracture network with three orthogonal sets of disc-shaped fractures [Long et al., 1985].

However, the Poisson DFN model tends to have large uncertainties due to its assumption of a homogeneous spatial distribution, simplification of fracture shape using linear/planar geometries, and negligence of the correlations between different geometrical properties as well as disregard of the diverse topological relations (e.g. "T" type intersections). Several researchers have examined the Poisson DFN model by comparing it with an original natural fracture network with respect to geometrical, hydraulic and mechanical properties and significant discrepancies were observed [Odling and Webman, 1991; Odling, 1992; Berkowitz and Hadad, 1997; Belayneh et al., 2009]. Several improvements on the Poisson DFN model have been developed and include considerations of: (1) the inhomogeneity of fracture spatial distribution based on a geostatistically-derived density field [Long and Billaux, 1987] or a cluster point process (e.g. the parent-daughter method) [Billaux et al., 1989; Xu and Dowd, 2010], (2) the correlation between fracture attributes (i.e. length, orientation and position) based on an elastic energy criterion [Masihi and King, 2007; Shekhar and Jr, 2011], (3) the unbroken areas inside individual fracture planes based on a Poisson line tessellation and zone marking process [Dershowitz and Einstein,

1988; Meyer and Einstein, 2002] (3) the topological complexity based on a characterisation of fracture intersection types [Manzocchi, 2002], and (4) the mechanical interaction between neighbouring fractures based on a stress shadow zone model [Rives et al., 1992; Josnin et al., 2002; Jourde et al., 2007]. It has to be mentioned that an alternative to the Poisson DFN model may use the spacing distribution to locate fractures in the stochastic generation [Lu and Latham, 1999], which is however considered more suitable for highly persistent fracture systems.
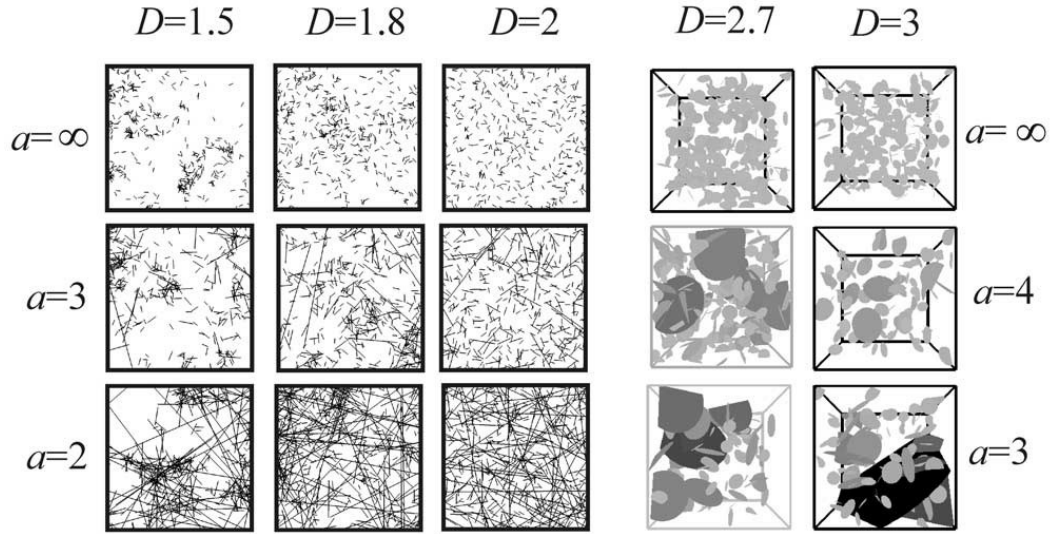
Fig. 3.3 2D and 3D fractal fracture networks generated with different values of the fractal dimension D and the power law length exponent a [Darcel et al., 2003b].

A more systematic characterisation of the hierarchy, clustering and scaling of natural fracture systems may involve the methods of fractal geometry and power law models [Bonnet et al., 2001]. Extensive field observations suggest that fracturing occurs at all scales in the crust and creates a hierarchical structure that can exhibit long-range correlations from macroscale frameworks to microscale fabrics [Allegre et al., 1982; Barton, 1995]. The spatial organisation of natural fracture networks can be characterised by the fractal dimension D, which quantifies the manner whereby fractals cluster and spread in the Euclidean space and can be measured using the box-counting method [Chilès, 1988; La Pointe, 1988; Ehlen, 2000] or the two-point correlation function [Hentschel and Procaccia, 1983; Bour and Davy, 1999]. The density and length distribution of a fracture population can be then described by a statistical model given by [Bour et al., 2002; Davy et al., 2010]: $n(l, L) = \gamma L^D l^{-a}$, for $l \in [l_{\min}, l_{\max}]$ (i.e. Eq. (2.2)), where $n(l, L)dl$ gives the number of fractures with sizes belonging to the interval $[l, l + dl]$ ($dl << l$) in

an elementary volume of characteristic size L, a is the power law length exponent, α is the density term, and l_{min} and l_{max} are the smallest and largest fracture sizes. The exponent a, which defines the respective proportion of large and small fractures, can be derived from the cumulative distribution or density distribution of fracture lengths [Davy, 1993; Pickering et al., 1995]. In theory, D is restricted to the range [1, 2] for 2D and [2, 3] for 3D, and a is restricted to [1, ∞] for 2D and [2, ∞] for 3D. However, extensive measurements based on 2D trace maps reveal that generally D varies between [1.5, 2] and a falls between [1.3, 3.5] [Bonnet et al., 2001]. The D and a measured from 1D/2D samples can be extrapolated to derive 3D parameters based on stereological relationships [Darcel et al., 2003b]. The density term α is related to the total number of fractures in the system and varies as a function of fracture orientations [Davy et al., 2010]. The extent of the power law relation is bounded by an upper limit l_{max} that is probably related to the thickness of the crust and a lower limit l_{min} that is constrained by a physical length scale (e.g. grain size) or the resolution of measurement [Bonnet et al., 2001]. For numerical simulations, the model size L usually meets $l_{min} << L << l_{max}$ [Darcel et al., 2003a]. A fractal spatial distribution of fracture barycentres can be modelled through a multiplicative cascade process governed by a prescribed D value, while fracture lengths can be sampled from a power law distribution with an exponent a [Darcel et al., 2003a]. Fracture orientations can be assigned isotropically or based on statistical distributions. Fractal fracture networks can then be generated by synthesising the different geometrical attributes modelled by independent random variables (Fig. 3.3). A D value of 2 (in 2D) and 3 (in 3D) represents a homogeneous spatial distribution, i.e. "space filling". As D decreases, the fracture pattern becomes more clustered associated with more empty areas. A small a value corresponds to a system dominated by large fractures, while $a \rightarrow \infty$ relates to a pattern with all fractures having an equal size (i.e. l_{min}). The D and a values as well as their relationship may control the connectivity, permeability and strength of fractured rocks [Darcel et al., 2003a; de Dreuzy et al., 2004; Davy et al., 2006; Harthong et al., 2012]. More interestingly, when $a = D+1$, the fracture network is self-similar and the connectivity properties are scale invariant [Darcel et al., 2003a]. A self-similar fracture pattern statistically exhibits a hierarchical characteristic whereby a large fracture inhibits the propagation of smaller ones in its vicinity, but not the converse [Bour et al., 2002; Davy et al., 2010]. Implementation of

such a hierarchical rule together with subcritical fracture growth laws leads to a new DFN model that can simulate the sequential stages of fracture network formation associated with nucleation, propagation and arrest processes (Fig. 3.4a) [Davy et al., 2013].

The assumption of a linear/planar fracture shape in the Poisson model and fractal DFN model may be simplistic, since field observations show that natural fracture geometries can be curved and irregular [Pollard and Aydin, 1988]. The random walk technique proposed by Horgan et al. [2000] for simulating polygonal crack patterns in soil (Fig. 3.4b) may be applied to model the curvature of fractures in rock. The invasion percolation method that has been used to model channel networks [Ronayne and Gorelick, 2006] may provide a way to simulate some highly branched and tortuous fracture systems.
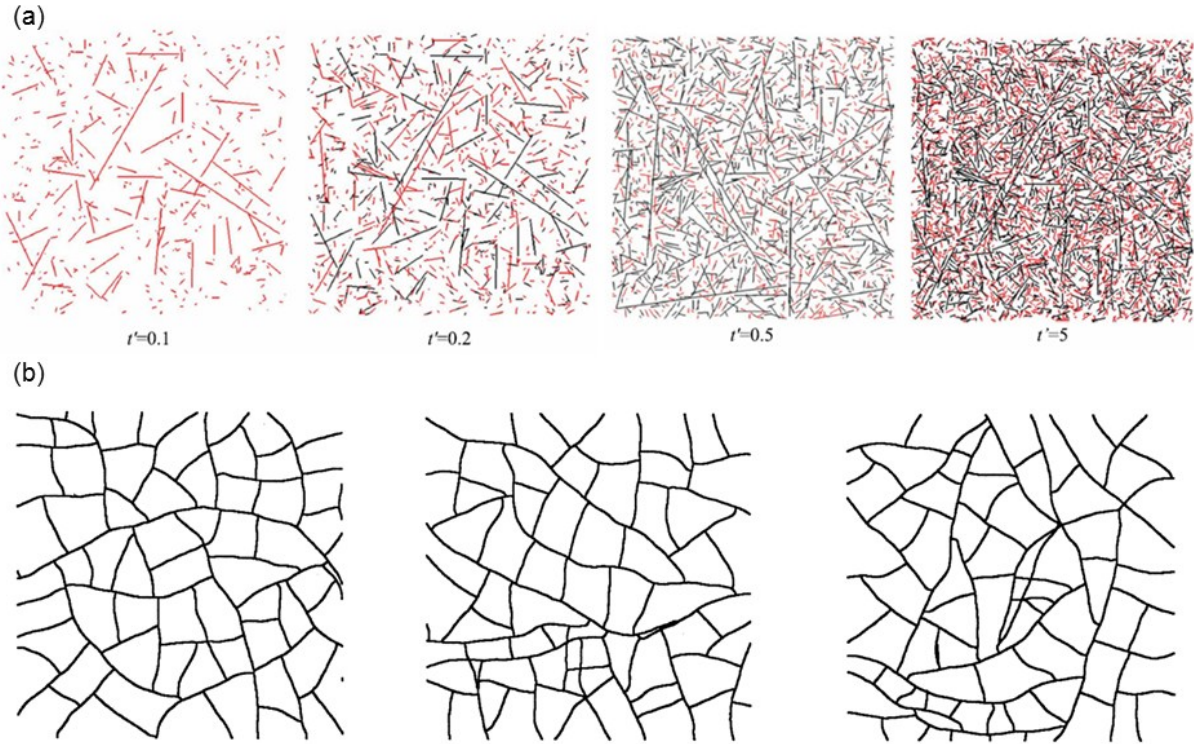
Fig. 3.4 Some new stochastic DFN models: (a) trace map views of a 3D sequential DFN model that simulates the nucleation, growth and arrest processes of natural fractures [Davy et al., 2013], and (b) a 2D stochastic DFN model that simulates the curvature and arrest of cracks in soil [Horgan and Young, 2000].

The stochastic DFN method, in essence, treats problems in a probabilistic framework and regards the real physical system as one possibility among simulated realisations sharing the same statistics. Hence, a sufficient number of realisations based on a Monte Carlo process are

necessary to predict a bounded range. In practice, a balance exists between the benefits of collecting detailed information to create more realistic DFNs and the increased cost of field measurements. The uncertainty can be reduced by constraining the random process with deterministic data, e.g. forcing the 3D DFN generator to reproduce a 2D trace pattern such as one exposed on tunnel walls [Andersson and Dverstorp, 1987]. Calibration and validation of stochastic DFN models are important for solving real problems and can be conducted based on the in-situ data from field mapping and/or hydraulic tests [Dverstorp and Andersson, 1989; Cacas et al., 1990a, 1990b; Kulatilake et al., 1993; Sarda et al., 2002; Follin et al., 2014]. The random nature of the stochastic DFN method may be regarded as an advantageous aspect, since uncertainty is unavoidable when analysing complex geological systems, for which single-valued predictions from deterministic methods may be more risky [Herbert, 1996]. However, it is still very important to continue improving the realism and accuracy of stochastic DFN models, since the predicted range from unrealistic DFNs can be systematically biased from the truth. Developments are needed towards a more thorough characterisation of the underlying statistics (e.g. multifractals for which a single scaling exponent is not sufficient [Berkowitz and Hadad, 1997]), and a more precise and efficient generator to create DFNs respecting more details of real fracture systems, such as the diversity of individual fracture shapes and morphology [Pollard and Aydin, 1988], the topological complexity in fracture populations [Sanderson and Nixon, 2015] and the correlation between geometrical properties [Bour and Davy, 1999; Darcel et al., 2003c; Neuman et al., 2008]. The important difference between 2D and 3D fracture networks with respect to connectivity and permeability [Long et al., 1985; Bour and Davy, 1998; Lang et al., 2014] renders another advantage of the stochastic method—its intrinsic capability to generate 3D networks.

3.2.3 Geomechanically-grown fracture networks

Extensive studies have been conducted to interpret the geological history and the formation mechanism behind field observations (e.g. patterns, statistics and minerals) of natural fracture systems [Engelder and Geiser, 1980; Segall and Pollard, 1983a; Pollard and Aydin, 1988; Olson and Pollard, 1989; Petit and Mattauer, 1995]. The increased knowledge of fracture mechanics [Pollard and Segall, 1987] promoted the development of geomechanically-based DFN models

that incorporate the physics of fracture growth and simulate fracture network evolution as a geometrical response to stress and deformation. By applying a geologically-inferred palaeo-stress/strain condition, natural fracture patterns may be reproduced by such a DFN simulator that progressively solves the perturbation of stress fields and captures the nucleation, propagation and coalescence of discrete fractures. Different numerical methods have been proposed and the one based on linear elastic fracture mechanics (LEFM) is frequently adopted.

In the LEFM model, fracture patterns can be simulated by four main steps in an iterative fashion [Renshaw and Pollard, 1994; Paluszny and Matthäi, 2009]: (1) generation of initial flaws to mimic the process that natural fractures initiate from microcracks, (2) calculation of the perturbed stress field in the rock caused by the presence and evolution of fractures under an imposed boundary condition, (3) derivation of the stress intensity factor (K_I) at the tip of each fracture, and (4) propagation of fractures which satisfy a growth criterion, e.g. a subcritical law $K_O \leq K_I \leq K_{IC}$, where K_O is the stress corrosion limit and K_I is the material toughness [Atkinson, 1984]. The stress field and stress intensity factor can be calculated based on analytical solutions [Renshaw and Pollard, 1994] or (most commonly) numerical methods such as the boundary element method (BEM) [Olson, 1993] and finite element method (FEM) [Paluszny and Matthäi, 2009; Paluszny and Zimmerman, 2011]. The propagation length in each growth iteration can be derived according to a power law relation with the energy release rate G (related to K_I) through the velocity exponent κ (or subcritical index n) [Atkinson, 1984], while the propagation angle may be computed if the curvature and coalescence effects are considered especially when the tectonic stress field is quite isotropic [Olson and Pollard, 1989].

The development of fracture networks is a sophisticated feedback-loop process, in which the complexity of growth dynamics is directly related to the complexity of the developing structures. Specifically, the propagation of a fracture is influenced by the mechanical interaction with others, and the propagated fracture geometries can conversely generate stress perturbations into the system. The mechanical interaction of fractures was found strongly dependent on the velocity exponent κ: an increased κ tends to promote a localised fracture pattern [Olson, 1993, 2004, 2007; Renshaw and Pollard, 1994; Renshaw, 1996]. The fracture pattern evolution is also affected by the attributes of the initial flaws (e.g. density [Renshaw and Pollard, 1994; Renshaw, 1996] and

orientation [Olson and Pollard, 1991]) and the 3D layer confinement effect [Olson, 2004, 2007]. Such a fracture mechanics model has been developed to mimic the evolution of a 2D single set of straight fractures (Fig. 3.5a) [Olson, 1993, 2004; Renshaw and Pollard, 1994], 2D orthogonal sets of straight fractures [Renshaw, 1996], 2D curved fracture patterns (Fig. 3.5b) [Olson and Pollard, 1989, 1991; Olson et al., 2007; Olson, 2007; Paluszny and Matthäi, 2009], and 3D curved fracture geometries (Fig. 3.5c) [Paluszny and Zimmerman, 2013]. The generated DFN pattern can be further used to evaluate the connectivity [Renshaw, 1996, 1999], permeability [Paluszny and Matthäi, 2010] and solute transport properties [Nick et al., 2011] of natural fracture systems.
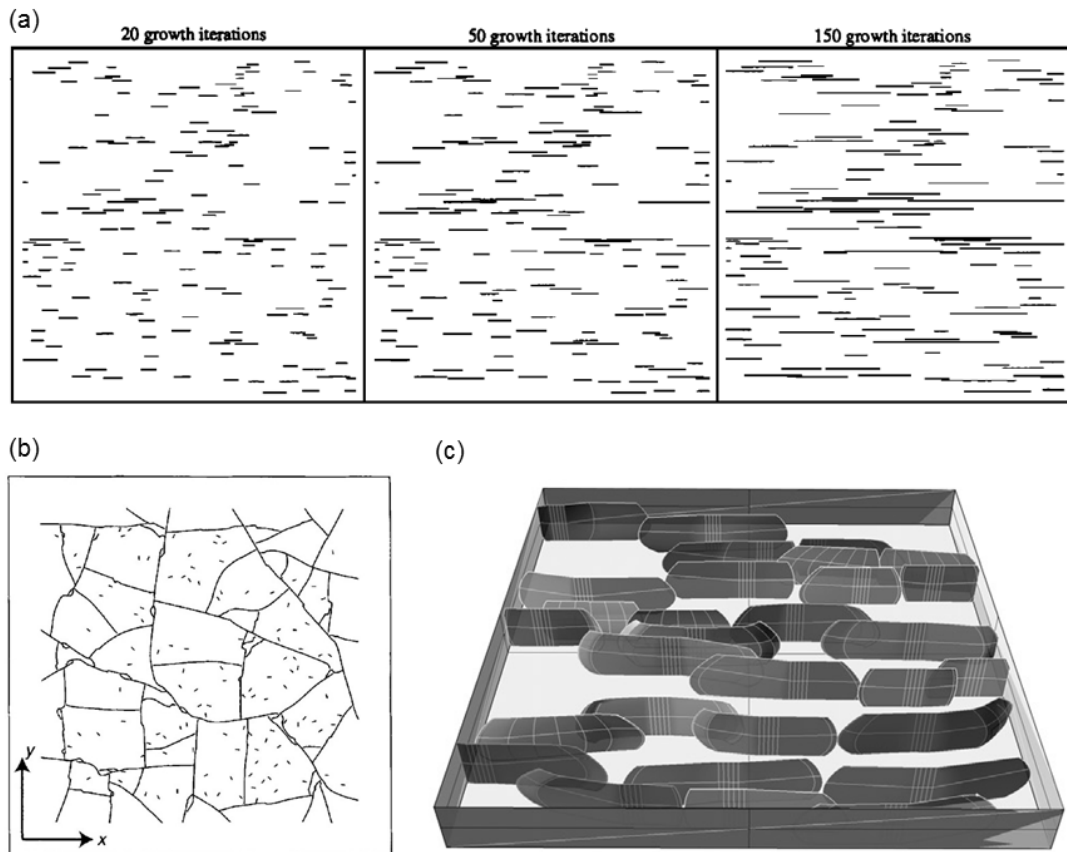
Fig. 3.5 Geomechanically-grown DFN patterns based on linear elastic fracture mechanics: (a) evolution of a 2D fracture set [Renshaw and Pollard, 1994], (b) development of a 2D polygonal fracture pattern [Olson et al., 2007] and (c) growth of 3D layer-restricted fractures [Paluszny and Zimmerman, 2013].

Apart from the LEFM approach, fracture patterns have also been simulated using other numerical methods. Cowie et al. [1993, 1995] developed a lattice-based rupture model to

simulate the anti-plane shear deformation of a tectonic plate and the spatiotemporal evolution of a multifractal fault system. Tang et al. [2006] used a damage mechanics FEM model to simulate the evolution of parallel, laddering or polygonal fracture patterns formed under different boundary conditions, i.e. uniaxial, anisotropic and isotropic tectonic stretch, respectively. Spence and Finch [2014] employed the discrete element method (DEM) to simulate the fracture pattern development in a sedimentary sequence embedded with stratified nodular chert rhythmites. Asahina et al. [2014] coupled the finite volume multiphase flow simulator (i.e. TOUGH2) and a lattice-based elasticity and fracture model (i.e. Rigid-Body-Spring Network) to simulate the desiccation cracking in a mining waste material under a hydromechanically coupled process.

The geomechanically-grown DFN model, as a process-oriented approach, has the advantage of linking the geometry and topology of fracture networks with the conditions and physics of their formation. Another merit is the automatic correlation between the geometrical attributes (e.g. length, orientation, aperture and shear displacement) of individual fractures linked by the governing physics. To solve practical problems, such a DFN generator can be constrained by the measurement of rock properties (e.g. the subcritical index measured from core samples) and the information of geological conditions (e.g. stress, strain, pore pressure and diagenesis) to achieve rational predictions [Olson et al., 2001]. However, difficulty and uncertainty still exist in creating fracture patterns consistent with the real systems for which coupled tectonic, hydrological, thermal and chemical processes may be involved.

3.3 Geomechanical modelling of fractured rocks

The numerical methods for geomechanical modelling of fractured rocks can be categorised as continuum and discontinuum approaches with the classification based on their treatment of displacement compatibility [Jing, 2003]. The preference for a continuum or discontinuum modelling scheme depends on the scale of the problem and the complexity of the fracture system [Jing and Hudson, 2002]. The continuum approach has the advantage of its greater efficiency to handle large-scale problems with the effects of fractures implicitly incorporated, whereas the discontinuum method can explicitly model irregular fracture networks and include complex constitutive laws of rock materials and fractures, and capture the fracturing and fragmentation processes. In this section, commonly used models for simulating the geomechanical behaviour of

fractured rocks will be reviewed: continuum, block-type discontinuum, particle-based discontinuum and hybrid finite-discrete element approaches. It is worth mentioning that the classification here is not intended to be absolute, since the boundary between the continuum and discontinuum methods has become very vague. Some advanced continuum techniques have included contact algorithms and fracture mechanics to consider discontinuities, while many discontinuum models are able to deal with continuous deformations.

3.3.1 Continuum models

The conventional continuum approach treats a rock domain as a continuous body that can be solved by the finite element method (FEM) or finite difference method (FDM). It may be applicable for a fractured rock with only a few or a large number of fractures [Jing, 2003]. If the system consists of only a few discontinuities associated with only a small amount of displacement/rotation, the discrete fractures can be modelled by special "interface elements" (or "joint elements") that are forced to have fixed connectivity with the solid elements [Goodman et al., 1968]. However, such a treatment is difficult to handle the dynamics and large displacement problems of natural fracture systems. When the density of DFN fractures is very high, the rock mass may be divided into a finite number of grid blocks assigned with equivalent properties derived from homogenisation techniques (Fig. 3.6a). The equivalent properties, such as bulk modulus and strength parameters, are usually calculated using empirical formulations that consider the degradation effect caused by pre-existing fractures [Hoek and Brown, 1997; Sitharam et al., 2001] or analytical solutions based on the crack tensor theory [Oda, 1983, 1984]. The crack tensor theory can calculate volume averaged parameters accounting for all fractures in a population with respect to their geometrical properties (e.g. length, orientation and aperture) and was extended to consider coupling between stress and fluid flow [Oda, 1986; Brown and Bruhn, 1998]. Such a crack tensor method has been integrated into the FEM [Oda et al., 1993; Kobayashi et al., 2001] and FDM [Rutqvist et al., 2013] solvers to model the geomechanical and hydromechanical behaviour of fractured rocks. The simulation results may be sensitive to the grid block discretisation especially when a block significantly smaller the representative elementary volume (REV) is adopted [Rutqvist et al., 2013]. The homogenisation-based continuum model may not adequately consider the connectivity effect of very long fractures that

penetrate numerous grid blocks and the results can be even worse if apertures are very heterogeneous and positively correlated with fracture lengths. Thus, it may not be applicable for a fractal fracture system with high variability in density distribution (i.e. a small fractal dimension D) and/or a large proportion of long fractures having a size comparable to the problem domain (i.e. a small power law length exponent a). Furthermore, the crack tensor method cannot consider the interaction between fractures and blocks as well as the resulting localised deformation and damage in the rock. The two conventional continuum schemes may be combined to explicitly model large discontinuities (e.g. dominant faults) using interface elements and then to characterise each isolated block as continuum bodies with bulk properties dependent on the distribution of small fractures.
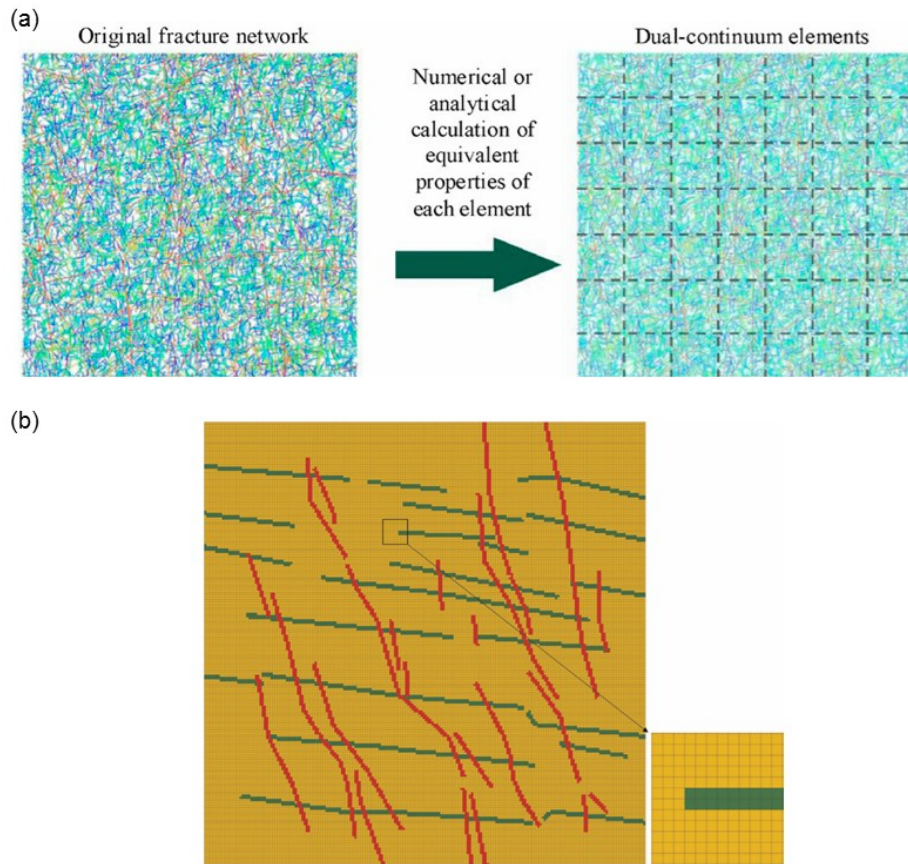
Fig. 3.6 (a) A continuum modelling scheme: a fracture network is divided into a finite number of grid blocks with equivalent properties determined analytically or numerically [Rutqvist et al., 2013], and (b) an extended continuum modelling scheme: the domain is discretised by a regular finite difference grid and fractures are represented by softening and weakening the grid elements intersected by fracture traces [Figueiredo et al., 2015].

51

To more explicitly capture the effects of discrete fractures, an extended continuum model has been developed by assuming fractures to have certain numerical width (for connectivity preservation) and representing them as arrays of grid elements with softening and weakening properties in a very fine finite difference mesh (Fig. 3.6b) [Rutqvist et al., 2009; Figueiredo et al., 2015]. It treats fracture and matrix as a composite elasto-plastic solid system, in which the failure of intact rocks or stress-displacement behaviour of fractures can be modelled by a Mohr-Coulomb criterion with tension cut-off. Similar "weak material" representation of fractures has also been implemented in the rock failure process analysis (RFPA) code (a damage mechanics FEM model) [Tham et al., 2004] and the cellular automation model [Pan et al., 2009]. Such a composite continuum model with explicit DFN representations may be more suitable for simulating cemented fractures (i.e. mineral filled veins), whereas the physical rationale is not intuitive if it is applied to unfilled discontinuities with clean wall surfaces.

3.3.2 Block-type discontinuum models

The block-type discontinuum models include the distinct element method (DEM) with an explicit solution scheme and the discontinuous deformation analysis (DDA) method with an implicit solution form. In this discontinuum modelling framework, the fractured rock is represented as an assemblage of blocks (i.e. discrete elements) bounded by a number of intersecting discontinuities. The geometry of the interlocking block structures can be identified first by e.g. employing the techniques of combinatorial topology [Jing, 2000]. In the subsequent mechanical computations, these blocks can be treated as rigid bodies or deformable subdomains (further discretised by finite difference/volume grids) with their interactions continually tracked by spatial detections during their deformation and motion processes.

(i)   Distinct element method (DEM)

The DEM method was originated by Cundall [1971; 1988] and gradually evolved to the commercial codes UDEC and 3DEC for solving 2D and 3D problems [Itasca, 2013a, 2013b]. Its basic computational procedure can be summarised as four steps [Jing and Stephansson, 2007]: (1) the contact relations of multiple blocks are identified/updated through a space detection, (2) the contact forces between discrete bodies are computed based on their relative positions, (3) the acceleration induced by force imbalance for each discrete element is calculated using Newton's

second law, and (4) the velocity and displacement are further derived by time integration with new positions determined. An explicit time marching scheme is applied to solve the problem iteratively until the block interaction process to be simulated has been completed. The mechanical interaction between blocks is captured by a compliant contact model that accommodates virtual "interpenetrations" governed by assumed finite stiffnesses to derive normal and tangential contact forces. The empirical joint constitutive laws derived from laboratory experiments [Bandis et al., 1983; Barton et al., 1985] can be implemented into the interaction calculation in an incremental form to simulate joint normal and shearing behaviour [Saeb and Amadei, 1990, 1992; Jing et al., 1994; Souley et al., 1995]. A viscous damping parameter may be introduced to reduce dynamic effects for modelling quasi-static conditions [Hart et al., 1988].
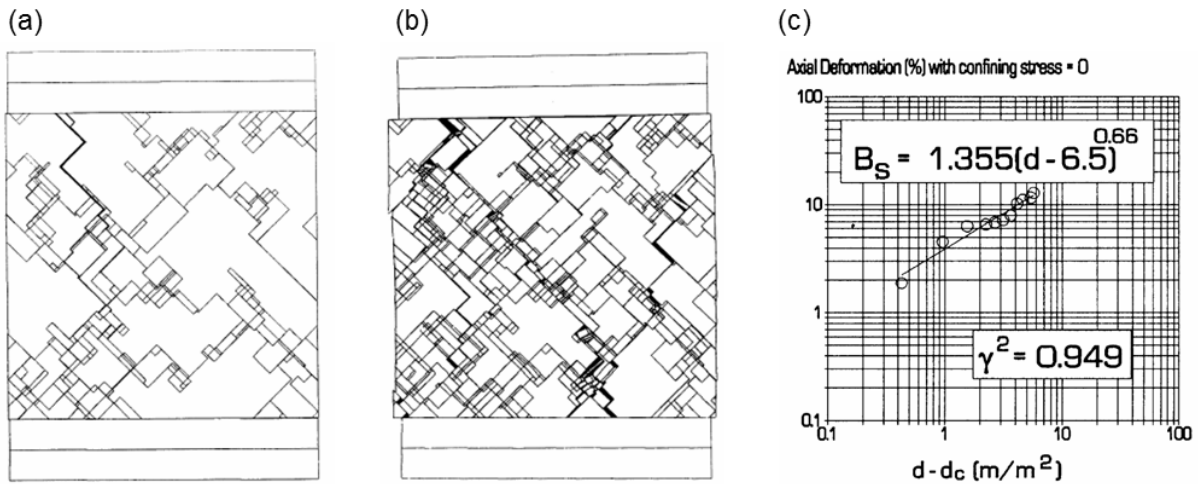
Fig. 3.7 Deformation of fractured rocks with (a) a relatively low fracture density of 5.25 m/m^2 and (b) a high fracture density of 7.77 m/m^2 under a uniaxial compression loading. (c) The deformability B_s of the fractured rock exhibits a power law scaling behaviour when the fracture density d exceeds the mechanical percolation threshold of 6.5 m/m^2, which is higher than the geometrical threshold of 4.0-5.5 m/m^2 of the study networks [Zhang and Sanderson, 1998].

The DEM approach is able to capture the stress-strain characteristics of intact rocks, the opening/shearing of pre-existing fractures and interaction between multiple blocks and fractures. Combined with DFN models, it has been widely applied to study the mechanical behaviour of fractured rocks. Zhang and Sanderson [1998] studied the critical behaviour of fractured rock

deformation and observed an abrupt increase in the deformability associated with a power law scaling when the fracture density exceeds the mechanical percolation threshold (slightly higher than the geometrical threshold) (Fig. 3.7). Min and Jing [2003] examined the scale dependency of the equivalent elastic properties of a fractured rock based on multiple DFN realisations conditioned by the same fracture statistics (Fig. 3.8). In their study, a technique to derive the fourth-order elastic compliance tensor has also been developed for equivalent continuum representations. Min and Jing [2004] further found the equivalent mechanical properties (i.e. elastic modulus and Poisson's ratio) of fractured rocks may also be stress dependent. With the increase of stress magnitudes, the equivalent elastic modulus significantly increases, while the Poisson's ratio generally decreases but can be well above 0.5 (i.e. the upper limit for isotropic materials). Noorian-Bidgoli et al. [2013] extended this DEM-DFN mechanical modelling approach to a more systematic framework to derive the strength and deformability of fractured rocks under different loading conditions, which is further applied to study the anisotropy [Noorian-Bidgoli and Jing, 2014] and randomness [Noorian-Bidgoli and Jing, 2015a] of the strength/deformability of stochastic DFNs. Recently, Le Goc et al. [2014] integrated 3D DFNs into the 3DEC simulator and investigated the effects of fracture density, sizes and orientations on the magnitude and scaling of the equivalent elastic modulus of fractured rocks. In addition, a considerable number of similar DEM-DFN models have been developed where the main motive is to study the effect of stresses on fluid flow. Such models were applied to explicitly capture the fracture opening, closing, shearing and dilational characteristics in complex fracture networks under in-situ stresses, after which the fluid flow implications were investigated [Zhang et al., 1996; Zhang and Sanderson, 1996, 1998, 2004; Min et al., 2004b; Tsang et al., 2007; Baghbanan and Jing, 2008; Zhao et al., 2010, 2011] (more discussion is given section 3.4). Furthermore, some models that incorporate the pore fluid pressure show that the pore pressure level can also significantly influence the mechanical and hydraulic properties of fractured rocks [Sanderson and Zhang, 1999; Noorian-Bidgoli and Jing, 2015b].

The classic DEM formulation cannot simulate the propagation of new fractures in intact rocks driven by stress concentrations, although plastic yielding can capture some aspects of the rock mass failure process [Shen and Barton, 1997]. Such a shortcoming was recently addressed

by introducing a Voronoi polygonal discretisation in matrix blocks that allows fracturing along the internal "grain" boundaries governed by tensile and shear failure criteria [Damjanaca et al., 2007; Kazerani and Zhao, 2010; Kazerani et al., 2012]. The DFN representation can also be integrated into the Voronoi DEM model using a dual-scale tessellation, in which the primary grid represents natural fractures and the secondary discretisation mimics microscopic structures [Ghazvinian et al., 2014].
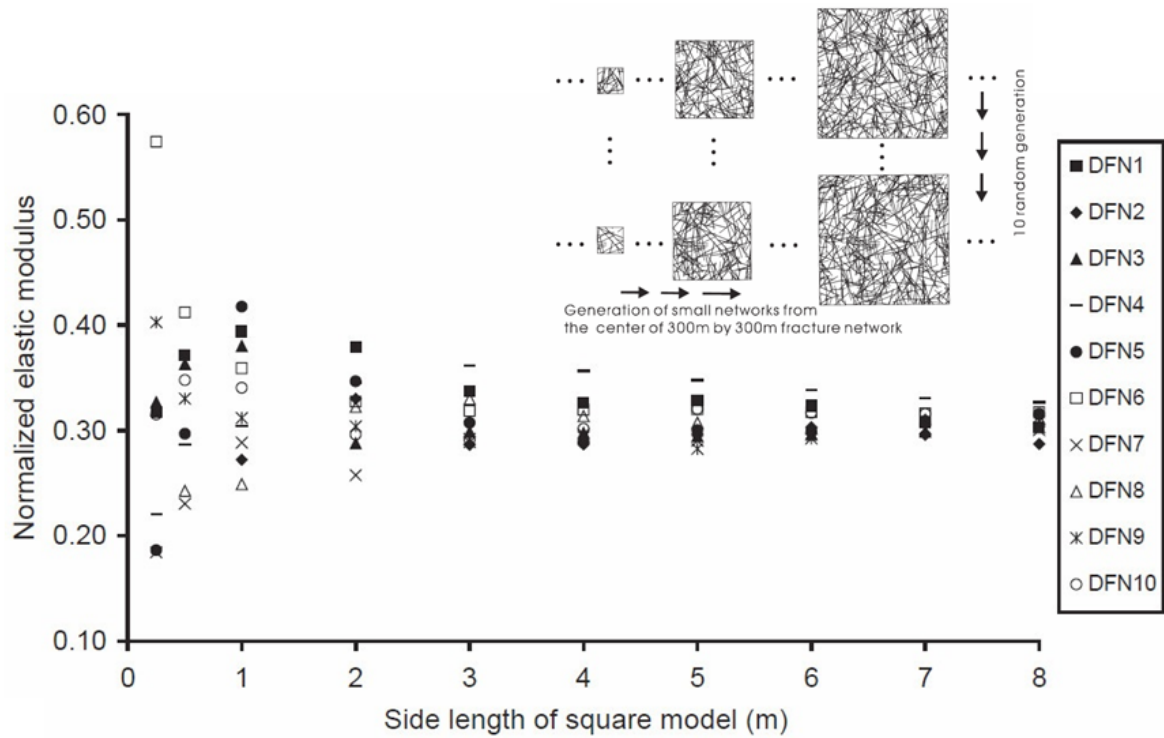
Fig. 3.8 Variation of the elastic modulus of fractured rocks with the increase of the model size. The ratio of shear stiffness to normal stiffness of fractures is assumed to be 0.2. Results are computed using the block-type DEM simulator (UDEC) based on multiple DFN realisations [Min and Jing, 2003].

(ii) Discontinuous deformation analysis (DDA)

The DDA method was first proposed by Shi and Goodman [1985, 1989, 1992] to compute the deformation and motion of a multi-block system. The discretisation of DDA models is quite similar to the one for the DEM, i.e. the medium is dissected into blocks by intersecting discontinuities. However, a fundamental difference between the two methods lies in their computational frameworks. The DEM treats kinematics of each block separately based on an explicit time-marching scheme, while the DDA calculates the displacement field based on a

minimisation of the total potential energy of the whole blocky system and an implicit solution to the established system of equations through a matrix inversion. Thus, the DDA method has an important advantage of fast convergence with unconditional numerical stability compared to the DEM method that requires a time step smaller than a critical threshold [Jing, 2003]. Important extensions of the original DDA method include the finite element discretisation of rock matrix [Jing, 1998], the sub-block technique (similar to the Voronoi DEM) for simulating fracturing processes [Lin et al., 1996], the formulation for modelling coupled solid deformation and fluid flow [Kim et al., 1999; Jing et al., 2001], and the development of 3D models [Jiang and Yeung, 2004]. The mechanical behaviour of fractured rocks has also been investigated based on DDA-DFN simulations, with emphasis on studying the stability of underground excavations and slope engineering (Fig. 3.9) [Wu et al., 2004; Hatzor et al., 2004; Bakun-Mazor et al., 2009]. Recently, Tang et al. [2015] combined the RFPA (a damage mechanics FEM model) with the DDA method to capture crack propagations and block kinematics of a rock slope system.
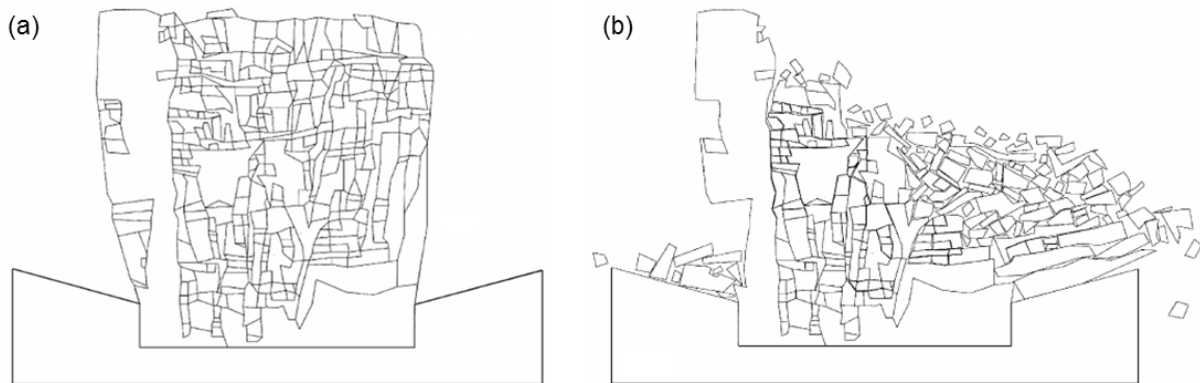
Fig. 3.9 (a) A fractured rock with a geologically-mapped DFN pattern, and (b) its dynamic collapsing process modelled by the DDA method [Hatzor et al., 2004].

3.3.3 Particle-based discontinuum models

The particle-based discontinuum model was originally introduced by Cundall and Strack [1979] to simulate granular materials such as soils/sands and gradually evolved to a commercial code, i.e. particle flow code (PFC) [Itasca, 2014]. Similar to the block-type DEM method, PFC calculates the inertial forces, velocities and displacements of interacting particles by solving Newton's second law through an explicit time-marching scheme. The discrete particles are assumed to be rigid with a circular (in 2D) or spherical (in 3D) shape, and can have variable

sizes which are usually much larger than the physical grain scale. To extend PFC to model rock materials, Potyondy and Cundall [2004] developed a bonded-particle model (BPM), in which intact rocks are represented as assemblages of cemented rigid particles and the macroscopic fracturing is simulated as the breakage of numerous microscopic cohesive bonds. The interaction between particles can be characterised by two types of bond models in PFC, i.e. the contact bond model and the parallel bond model. A contact bond serves as a linear elastic spring with normal and shear stiffness, and transmits forces via the contact point between two particles. A parallel bond with certain normal and shear strength joins two particles to resist against separation under tension, shear and rotation. The parallel bond model is more suitable for simulating rock materials as it can capture the tensile and shear failure as well as the resulting stiffness reduction. To overcome the original deficiency of PFC in reproducing a realistic rock strength ratio (i.e. the ratio of uniaxial compressive strength to tensile strength) and macroscopic friction angle, a hierarchical bonding structure can be built based on a cluster logic [Potyondy and Cundall, 2004] or a clump logic [Cho et al., 2007]. The cluster approach mimics the interlocking effect of irregular grains by defining a higher value of intra-cluster bond strength (i.e. the strength between particles in the same cluster) than that of the strength between cluster boundaries. The clump approach forces the particles of the same clump to displace and rotate as a rigid body (i.e. infinite intra-cluster bond strength).

The BPM representation using particles with idealised circular/spherical shapes can introduce unphysical asperities on discontinuity surfaces, resulting in an additional resistance to frictional sliding. To suppress such an artificial roughness effect, a smooth-joint contact model (SJM) was proposed to simulate fracture wall behaviour based on the geometry and morphology of discontinuities and independent of the arrangement of local contact particles [Mas Ivars et al., 2011]. The smooth contact is assigned to all particle pairs lying on the fracture interface but belonging to opposite matrix blocks, so that they can overlap and pass through each other (Fig. 3.10a). The contact forces are calculated based on the relative displacements and the smooth-joint stiffness in the normal and tangential directions of the local surface. The SJM was found to be able to capture the shear strength and dilational behaviour of natural fractures associated with significant scale effects [Lambert and Coll, 2014; Bahaaddini et al., 2014]. By

simulating intact rocks using the BPM and discrete fractures using the SJM, a synthetic rock mass (SRM) modelling approach (Fig. 3.10b) has been developed to characterise the mechanical properties of fractured rocks including peak strength, damage, fragmentation, brittleness, anisotropy and scale effects [Mas Ivars et al., 2011]. Compared to the Hoek-Brown empirical approach for presumed isotropic rock masses, the SRM method that integrates explicit DFN representations has an advantage to derive the orientation-specific strength of naturally fractured rocks and consider the influence of fracture length distribution and connectivity [Poulsen et al., 2015]. The SRM model has been applied to reproduce the failure behaviour of veined core samples under uniaxial compression tests [Vallejos et al., 2016], estimate the mechanical REV of a jointed rock mass near an underground facility [Esmaieli et al., 2010] and evaluate the stability of wedges around a vertical excavation in a hard rock [Hadjigeorgiou et al., 2009].

Fig. 3.10 Integration of (a) a smooth-joint contact model in PFC to achieve (b) synthetic rock mass (SRM) modelling of fractured rocks with stochastic DFN geometries [Mas Ivars et al., 2011].

An open source particle-based modelling platform named YADE (Kozicki and Donzé, 2008a, 2008b) has recently been developed as an alternative to the commercial code PFC. YADE represents intact rocks using glued discs/spheres and models the fracturing process based on the rupture of inter-particle bonds with the contact bond algorithms following a similar logic to PFC. To reproduce the high ratio of compressive to tensile strengths and the non-linear failure envelope of brittle rocks, the concept of "interaction range" was introduced by Scholtès and Donzé [2013]. They mimic the microstructural complexity by assembling constitutive particles in neighbouring zones (not only the particles in direct contact). A joint contact logic equivalent to the SJM has also been implemented in YADE to avoid the particle interlocking effects between sliding fracture surfaces [Scholtès et al., 2011]. By integrating 3D fractal DFNs into the YADE BPM model associated with the smooth joint contact treatment (Fig. 3.11), Harthong et al. [2012] studied the influence of fracture network properties (i.e. fractal dimension D, power law length exponent a and fracture intensity P_{32}) on the mechanical behaviour of fractured rocks. The strength and elastic modulus of rock masses decrease if P_{32} increases (i.e. more fractures) or a decreases (i.e. higher proportion of larger fractures), while the spatial heterogeneity and scaling of the mechanical properties are affected by D. Such a combined BPM-DFN model has also been applied to analyse the stability of fractured rock slopes, which is controlled by the strengths of both pre-existing fractures and intact rocks [Scholtès and Donzé, 2012; Bonilla-Sierra et al., 2015].
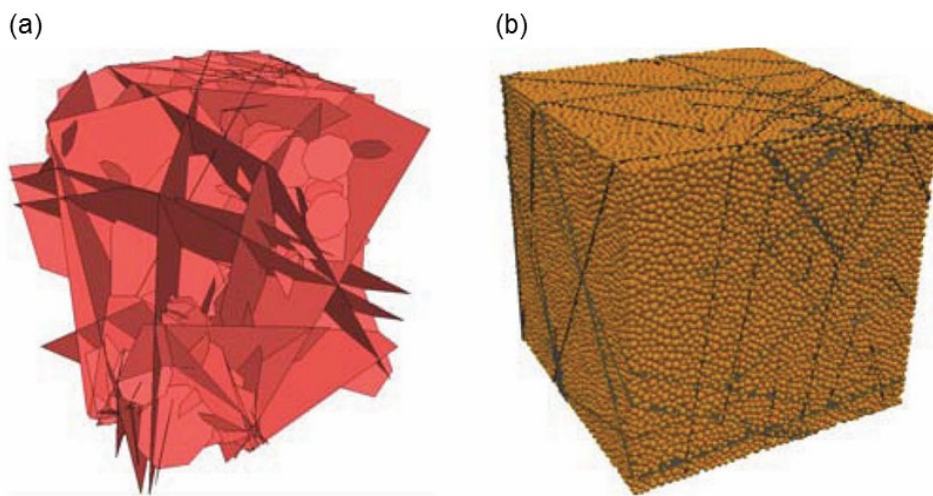
Fig. 3.11 Integration of (a) a fractal DFN into (b) the YADE bonded-particle model (BPM) for mechanical modelling of fractured rocks [Harthong et al., 2012].

3.3.4 Hybrid finite-discrete element models

The hybrid finite-discrete element method (FEMDEM or FDEM) combines the finite element analysis of stress/deformation evolution with the discrete element solutions of transient dynamics, contact detection and interaction. In such a discontinuum modelling scheme, the internal stress field of each discrete matrix block is calculated by the FEM solver, while the translation, rotation and interaction of multiple rock blocks are traced by the DEM algorithms. Pre-existing fractures in rocks are treated as the internal boundaries of rock volumes. The FEMDEM approach also provides a natural solution route to modelling the transitional behaviour of brittle/quasi-brittle materials from continuum to discontinuum (i.e. fracturing processes) by integrating fracture mechanics principles into the formulation. This section will review the two most commonly used FEMDEM models, i.e. the commercial software ELFEN [Rockfield, 2004] and an open source platform Y-code [Munjiza, 2004], which have been broadly used to simulate the mechanical processes in geological media containing pre-existing discontinuities.

(i) ELFEN

The ELFEN code models the degradation of an initial continuous domain into discrete bodies by inserting cracks into a finite element mesh. A nodal fracture scheme was introduced by constructing a non-local failure map for the whole system [Owen and Feng, 2001]. The feasibility of local failure is determined based on the evolution of nodal damage indicators. The fracturing direction (if failure occurs) is calculated based on the weighted average of the maximum failure strain directions of all surrounding elements. A new discrete fracture is then inserted along the failure plane with the local mesh topology updated through either the "intra-element" or "inter-element" insertion algorithm with adaptive mesh refinement applied if necessary [Klerck et al., 2004]. ELFEN provides various material constitutive models including the elastic, elasto-plastic and visco-plastic laws, and many brittle/quasi-brittle failure models including the rotating crack model, the Rankine material model, and the compressive fracture model (i.e. Mohr-Coulomb failure criterion coupled with a tensile crack model) [Owen et al., 2004; Klerck et al., 2004]. The explicit DFN fracture geometries generated from e.g. FracMan can be imported into the ELFEN platform by embedding fracture entities into rock solids and

representing each fracture as opposed free surfaces [Pine et al., 2006, 2007]. To mesh such complex systems, special geometrical treatments may be involved to avoid ill-posed elements caused by subparallel fractures intersecting at a very small acute angle or a fracture tip terminating at the vicinity of another fracture [Rockfield, 2011]. Both pre-existing and newly propagated fractures are assigned with contact properties, e.g. fracture stiffness and friction coefficient, to simulate solid interactions through discontinuity surfaces [Pine et al., 2007]. The degradation of natural fractures during shearing can also be modelled by introducing roughness profiles [Karami and Stead, 2008].
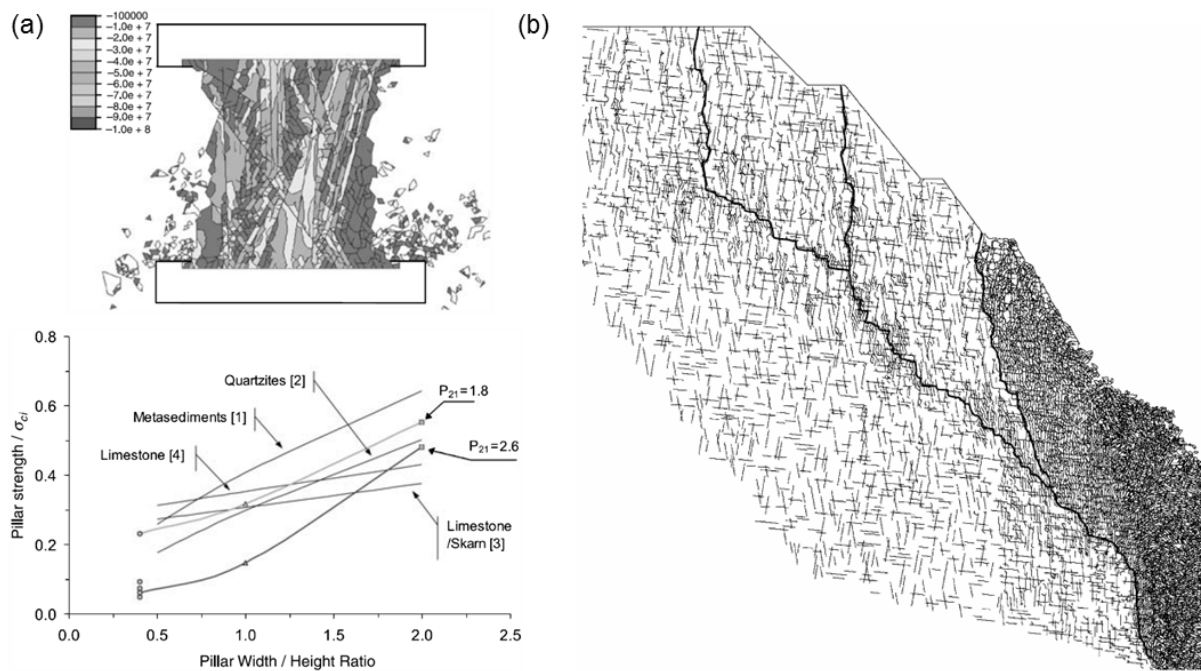
Fig. 3.12 Integration of DFN geometries into the FEMDEM model of ELFEN for modelling strength of (a) a prefractured pillar [Pine et al., 2006] (note: σ_{ci} is the uniaxial compressive strength of intact rocks, P_{21} denotes the fracture intensity, i.e. total length of fractures per unit area) and (b) an open pit slope [Vyazmensky et al., 2010b].

The combined FEMDEM-DFN model has been applied to tackle the geomechanical problems for various engineering applications [Elmo et al., 2013]. The presence of natural fractures may dominate the strength of slender pillars but have a reduced influence for wider pillars (Fig. 3.12a) [Pine et al., 2006]. The orientation and length distribution of DFN fractures also affect the failure mode of the pillar structures, which can exhibit splitting with lateral

kinematic releases or shearing of critically inclined pre-existing fractures linked by new cracks through intact rock bridges [Elmo and Stead, 2010]. This synthetic numerical model has also been used to investigate the progressive failure of rock slopes (Fig. 3.12b) [Vyazmensky et al., 2010a], which in reality is usually triggered by both the reactivation of natural fractures and the propagation of new cracks [Eberhardt et al., 2004]. The FEMDEM model is well suited to mimic the staged failure processes of rock slopes including initiation, transportation/comminution and deposition, which involve yielding and fracturing of intact materials, shearing of fracture surfaces and translational/rotational instabilities [Stead et al., 2006]. The rock mass fabrics and rock bridge properties can have important influences on the stability of large-scale open pit slopes [Vyazmensky et al., 2010a]. The caving-induced rock mass deformations and associated surface subsidence may be controlled by the orientation of joint sets and the location/inclination of major faults [Vyazmensky et al., 2010b]. All these engineering applications highlighted the advantage of the FEMDEM-DFN technique with explicit characterisations of the reactivation/interaction of pre-existing fractures and initiation/propagation of new cracks.

(ii) Y-code

During the 1990s, many algorithmic solutions for 2D and 3D FEMDEM simulation were developed by Munjiza et al. [1995, 1999] and Munjiza and Andrews [1998, 2000]. Extensive developments and applications of the FEMDEM method have been conducted after the release of the open source Y-code [Munjiza 2004], and different versions have emerged including the code developed collaboratively by Queen Mary University and Los Alamos National Laboratory [Munjiza et al., 2011, 2015; Rougier et al., 2014], the Y-Geo program by Toronto University [Mahabadi et al., 2010, 2012; Lisjak and Grasselli, 2014], and the VGeST (recently renamed "Solidity") platform by Imperial College London [Xiang, 2009a, 2009b; Munjiza et al., 2010; Latham et al., 2013]. The FEMDEM model of Y-code accommodates the finite strain elasticity coupled with a smeared crack model and is able to capture the complex behaviour of fractured rocks involving deformation, rotation, interaction, fracturing and fragmentation.

In the Y-code, the fractured rock is represented by a discontinuous discretisation of the model domain using three-noded triangular (in 2D) or four-noded tetrahedral (in 3D) finite elements and four-noded (in 2D) or six-noded (in 3D) joint elements embedded at the interfaces

of finite elements. An important difference with the ELFEN code is that the joint elements are inserted for all edges (in 2D) or surfaces (in 3D) of finite elements. The deformation of the bulk material is captured by the linear-elastic constant-strain finite elements with the impenetrability enforced by a penalty function and the continuity constrained by a constitutive relation [Munjiza et al., 1999], while the interaction of matrix bodies through discontinuity interfaces is simulated by the penetration calculation [Munjiza et al., 2000]. The joint elements are created and embedded between triangular/tetrahedral element pairs before the numerical simulation, and no further remeshing process is performed during later computations. Pre-existing fractures can be represented by a series of joint elements which are initially overlapped (but opposite sides are separately defined) free surfaces [Latham et al., 2013]. The brittle failure of intact materials is governed by both fracture energy parameters (for mode I and mode II failure) and strength properties (e.g. tensile strength, internal friction angle and cohesion) [Lisjak and Grasselli, 2014]. A numerical calibration can be conducted to achieve consistency between the input material strength parameters and simulated macroscopic response [Tatone and Grasselli, 2015]. Code development for modelling 3D crack propagation has also been achieved by different research groups [Rougier et al., 2014; Mahabadi et al., 2014a; Guo et al., 2015, 2016].
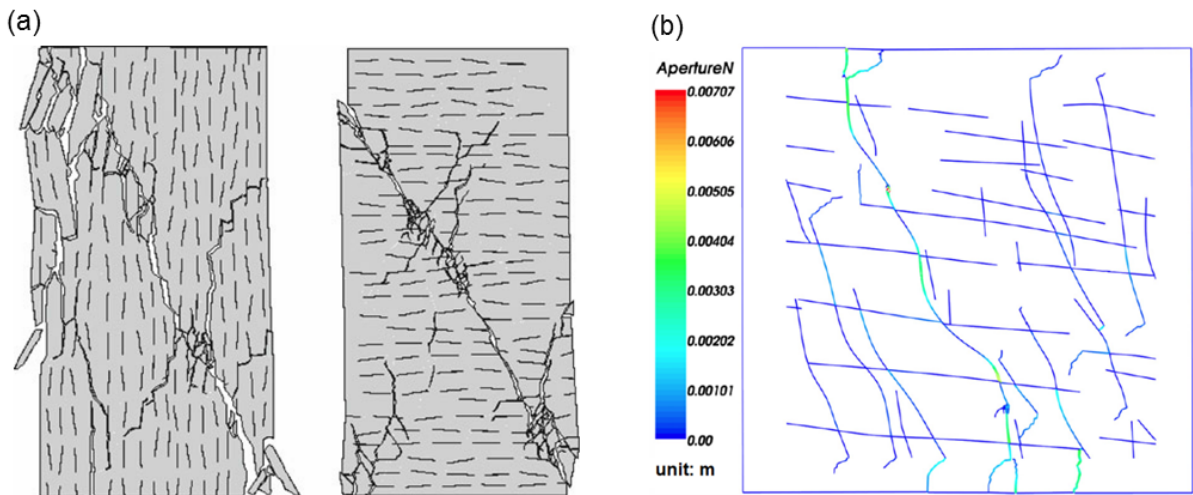
Fig. 3.13 FEMDEM-DFN modelling results. (a) Failure of anistropic argillaceous rock samples under uniaxial compression test [Lisjak et al., 2014c]. (b) Variation of fracture apertures in a geologically-mapped DFN network that accommodates further new crack propagations in response to a biaxial stress condition [Latham et al., 2013].

The advantage of the FEMDEM model for simulating the degradation of continuum into discrete pieces promoted the application to tackle various engineering problems, such as rock blasting [Munjiza et al., 2000], fracture development around excavations in isotropic/anisotropic intact rocks [Lisjak et al. 2014a, 2014b, 2015a, 2015b] and mountain slope failure [Barla et al., 2011]. It has also been used to model the mechanical behaviour of fractured rocks embedded with pre-existing fractures. Lisjak et al. [2014c] integrated DFN crack arrays into the FEMDEM model to imitate the anisotropy of an argillaceous rock. Latham et al. [2013] applied the FEMDEM technique to model a geologically-mapped DFN system under various stress conditions, and captured realistic geomechanical phenomena such as deformation and rotation of matrix blocks, opening, shearing, and dilation of pre-existing fractures as well as new crack propagation. However, the original FEMDEM model is only equipped with the conventional Coulomb friction law [Munjiza, 2004; Munjiza et al., 2011; Xiang et al., 2010b], which requires further code development to account for the complex constitutive behaviour of natural fractures associated with roughness characteristics and size effects.

3.4 Impacts of geomechanical behaviour on fluid flow

The presence of fractures can generate stress perturbations in the rock, such as rotation of stress fields, stress shadows around discontinuities and stress concentration at fracture tips [Pollard and Segall, 1987]. The resulting heterogeneous stress distribution may lead to variable local normal/shear stresses loaded on different fractures having distinct sizes and orientations, and produce various fracture responses such as opening, closing, sliding, dilatancy and propagation. Since the conductivity of fractures is critically dependent on the third power of fracture apertures [Witherspoon et al., 1980], the geomechanical conditions can considerably affect the hydraulic properties of fractured rocks including fluid pathways, bulk permeability and mass transport [Tsang et al., 2007]. Numerical models that integrate explicit DFNs and non-linear rock/fracture constitutive laws provide powerful (and so far irreplaceable) tools to investigate the geomechanical effects on fluid flow in complex fracture networks [Jing et al., 2013].

3.4.1 Fluid pathways

Fracture networks usually serve as the major pathways for fluid migration in subsurface rocks, especially if the matrix is almost impermeable compared to the fractures [Berkowitz, 2002]. The partitioning of fluid flow within a fracture population relies on the spatial connectivity of fracture geometries and the transmissivity of individual fractures, both of which can be affected by the geomechanical conditions.
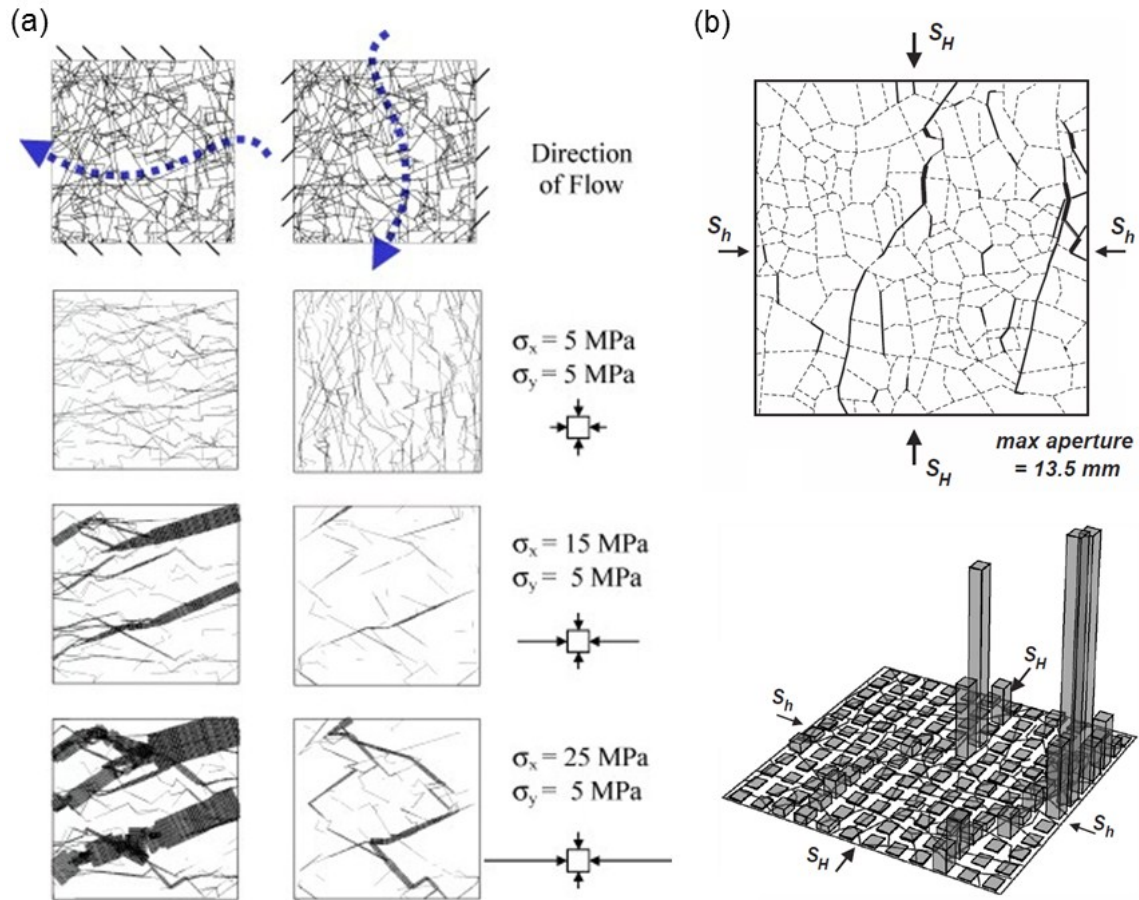
Fig. 3.14 Fluid pathways in fracture networks under in-situ stresses. (a) With the increase of the boundary stress ratio, fluid flow becomes more concentrated in only part of the fractures in the network due to the shear dilation effect [Min et al., 2004b]. (b) The vertical fluid flow through a jointed layer exhibits a highly localised pattern when the fractured rock is deformed under a critical stress state [Sanderson and Zhang, 1999].

Zhang et al. [1996] used the UDEC DEM code to study the deformation of a fractured rock based on a geologically-mapped DFN pattern and found the closure of fractures under applied in-situ stresses can re-organise the fluid pathways. They also found the closed joints of one set

can hinder fluids from passing through not only themselves but open fractures of another set due to the net effect. Zhang and Sanderson [1996] applied the same technique to different types of outcrop DFN patterns with/without systematic fracture sets. The fluid flow in systematic fracture networks tend to be dominated by the primary joint set if it is relatively open, while for non-systematic networks containing fairly randomly oriented small fractures, the flow channels tend to align the direction of the maximum principal stress. Min et al. [2004b] incorporated the fracture shear dilation behaviour in the DEM modelling of a stochastic DFN with a power law distribution of fracture lengths and a uniform distribution of initial (i.e. zero stress) apertures. They observed that, under high differential stresses, a small portion of fractures which have critical/near-critical orientations, good connectivity and long lengths would dilate and form large flow channels (Fig. 3.14a). The "critical orientations" here correspond to a range of fracture orientations that would allow discontinuities with no cohesive strength to slide under the given in-situ differential stress condition. The localised features would be augmented if the initial apertures are broadly distributed (e.g. following a lognormal distribution) and correlated with fracture lengths [Baghbanan and Jing, 2008]. Latham et al. [2013] employed the FEMDEM method integrated with a smeared crack model to study the geomechanical response and fluid flow in an outcrop-based DFN. They found that bent natural fractures under high differential stresses may exhibit evident dilational jogs and can be linked by newly propagated cracks to form major fluid pathways. Similar localised flow channels created by the connection of pre-existing fractures have also been observed by Figueiredo et al. [2015] using a FDM simulator. Sanderson and Zhang [1999, 2004] calculated the fluid flow in the third dimension of sedimentary rocks using an analytical pipe formula based on the deformed 2D fracture networks. They found vertical flow becomes extremely localised when the pore fluid pressure exceeds a critical level and very large aperture channels emerge (Fig. 3.14b). The flow distribution also exhibits significant multifractality when the loading condition approaches the critical state.

3.4.2 Permeability

There are two different notions of rock mass permeability, i.e. equivalent permeability and effective permeability. The equivalent permeability is defined as a constant tensor in Darcy's law to represent flow in a heterogeneous medium, while the effective permeability is an intrinsic

material property based on the existence of an REV at a large homogenisation scale [Renard and de Marsily, 1997]. Permeability here mainly refers to the equivalent permeability of a fractured rock at a specific study scale.

The permeability tensor was observed to be highly dependent on both the geometrical attributes of fracture networks (e.g. density, lengths and orientations) and the in-situ stress conditions (e.g. direction, magnitude and ratio of the principal stresses) [Zhang et al., 1996]. When the differential stress ratio is relatively low, the permeability decreases with the increase of burial depth (or mean stress) of the fractured rock due to the closure of most fractures [Zhang and Sanderson, 1996; Min et al., 2004b]. The non-linear relationship between normal stress and fracture closure results in a phenomenon that the permeability is more sensitive at shallower depths (i.e. smaller mean stresses) and approaches a minimum value when most fractures are closed to their residual apertures under high mean stresses (Fig. 3.15a) [Min et al., 2004b]. The permeability anisotropy of a fracture network with non-systematic fractures is more dependent on the ratio and direction of applied principal stresses than that of a network with systematic fracture sets which is more controlled by the fracture set orientations [Zhang and Sanderson, 1996]. With the increase of differential stresses, the permeability exhibits a decrease and then an abrupt increase separated by a critical stress ratio that begins to cause continued shear dilations along some preferentially oriented fractures (Fig. 3.15b) [Min et al., 2004b]. A similar variation of permeability occurs when the pore fluid pressure is elevated [Figueiredo et al., 2015]. Simultaneously, the permeability anisotropy is also enlarged by the increased stress ratio [Min et al., 2004b]. If initial apertures are correlated with fracture lengths, the permeability of fractured rocks is dominated by larger fractures with wider apertures. This model tends to exhibit a permeability value much higher than the constant initial aperture model (Fig. 3.15c&d) [Baghbanan and Jing, 2008]. The permeability tensor may be destroyed but then reestablished with the increase of differential stresses [Baghbanan and Jing, 2008]. In addition to the shear dilation of fractures, the increase of network connectivity caused by brittle failure and crack propagation under geomechanical loading can also significantly raise the permeability of fractured rocks [Renshaw, 1996; Paluszny and Matthäi, 2009; Latham et al., 2013; Figueiredo et al., 2015]. More interestingly, the emergence of dilational jogs/bends in response to high

differential stresses may lead to even more increase of permeability in the third dimension [Sanderson and Zhang, 1999, 2004]. It has to be mentioned that an increased fracture density may not always lead to an increased permeability under some tectonic conditions (e.g. an extensional regime), because fractures may be closed due to mechanical interactions when they are too densely spaced [Bai and Pollard, 2001].
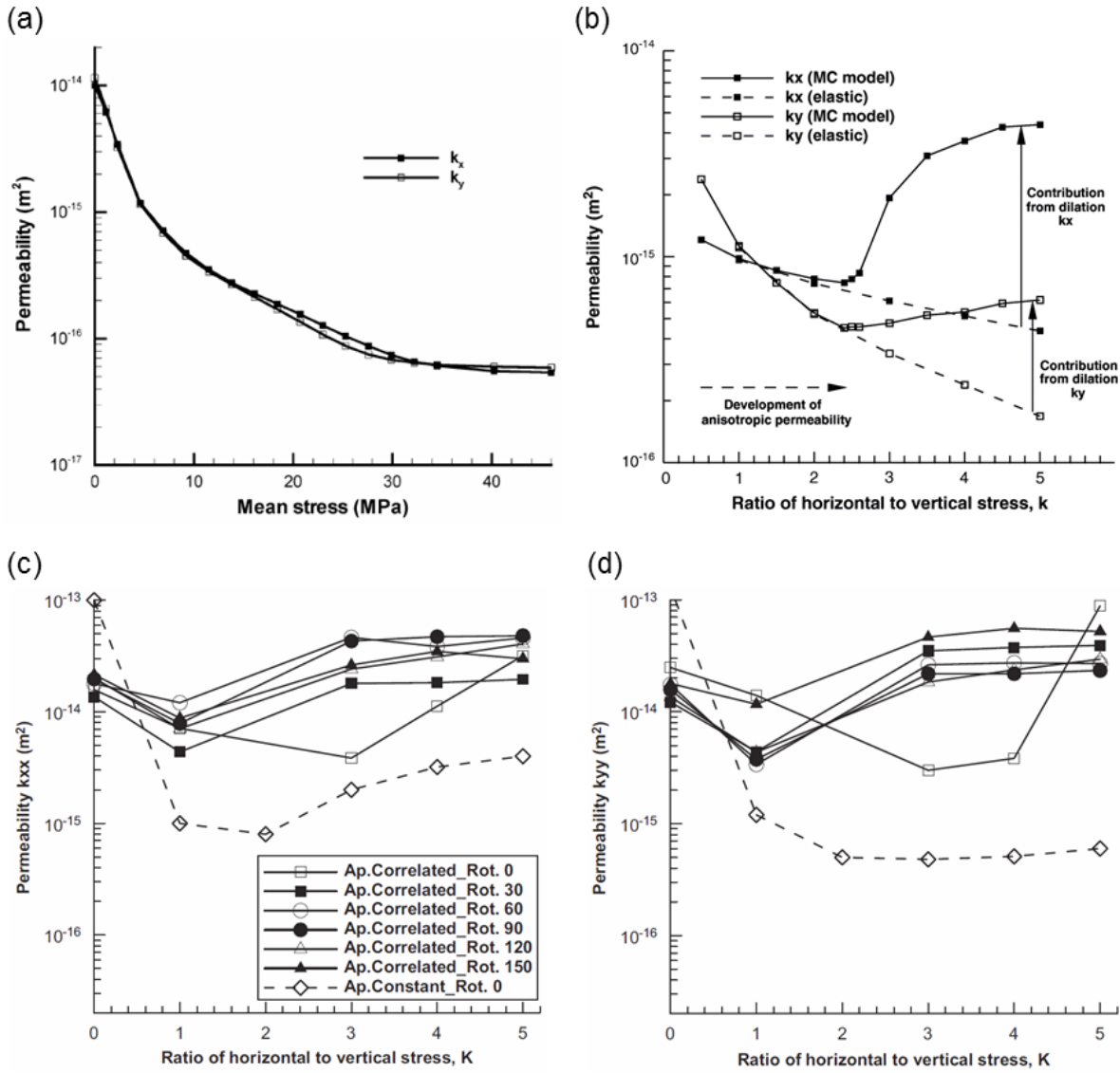
Fig. 3.15 Variation of permeability of fractured rocks in response to the change of stress conditions. (a) Permeability change versus stress change with a fixed principal stress ratio of 1.3 [Min et al., 2004b]. (b) Permeability change with the increase of stress ratio for a DFN with a constant initial aperture [Min et al., 2004b]. (c) and (d) Permeability change with the increase of stress ratio for a DFN with a lognormally distributed and length correlated apertures under rotated stress fields [Baghbanan and Jing, 2008].

3.4.3 Transport

Mass transport in fractured rocks is governed by various mechanisms including advection, dispersion, matrix diffusion, interface sorption and chemical reaction [Bear et al., 1993; Berkowitz, 2002]. The heterogeneous fluid velocity fields in geological media consisting of distributed fractures and porous rocks can result in complex transport phenomena in the system. Computational models employing solute components or tracked particles have been developed to simulate migration processes in fractured rocks [Moreno et al., 1988; Tsang and Neretnieks, 1998]. Recently, numerical studies have also been conducted to investigate the effects of the stress/deformation on the transport properties of fracture networks, as summarised below.

Zhao et al. [2010] coupled the UDEC DEM code and a random walk particle tracking code PTFR and investigated the stress effects on the hydrodynamic dispersion of contaminant solutes in a stochastic DFN system. They found that compressive stresses can close fracture apertures and attenuate the dispersivity, but an increased differential stress ratio could greatly intensify the spreading phenomenon if it exceeds certain threshold for triggering shear dilations. Zhao et al. [2011] extended this modelling technique to incorporate the effects of matrix diffusion and sorption, and conducted a systematic study of the solute transport under various stress conditions. Their results showed that the stress can significantly affect the solute residence time in the fracture network (Fig. 3.16a). When the stress ratio is increased but not very high (<3), the breakthrough curve shifts to the right direction (i.e. the average residence time increases) compared to the initial no stress condition, due to the closure of fractures under relatively isotropic stresses. However, as the stress ratio exceeds 3, fluid velocity is raised drastically in some dominant channels formed by dilated fractures due to shearing, and thus the residence time decreases with the breakthrough curve shifting backward. They also observed that the breakthrough curve for interacting tracers (i.e. with matrix diffusion) exhibits longer tails than that for non-interacting tracers (i.e. without matrix diffusion) due to the meandering of a small amount of particles passing through tortuous fluid pathways. Such long tail phenomena were more significant when the pressure gradient is small, for which the matrix diffusion tends to play a dominant role in solute transport (Fig. 3.16b). Rutqvist et al. [2013] used an extended multiple interacting continua model combined with the crack tensor approach to simulate the

advection-dominated transport (under high hydraulic gradients) and diffusion-retarded transport (under low hydraulic gradients). In addition to the stress-dependent transport behaviour, they also observed a delayed breakthrough in low pressure gradient scenarios due to the residence of solutes in the porous rock matrix. Wang et al. [2014] further applied this multicontinuum method to demonstrate the contribution of inactive fractures (i.e. isolated cracks or dead ends of fractures) for stagnating solutes by providing additional surface areas for diffusive transfer into/out of matrix pores. Zhao et al. [2013] compared the stress-flow models of five different research groups, which showed consistency in predicting the stress-dependency of mass transport in a fractured rock. Apart from the stress-induced aperture change that can affect the transport behaviour, Nick et al. [2011] found that the propagation of fractures under tectonic loading can also vary the breakthrough properties due to the increased fracture density and network connectivity.
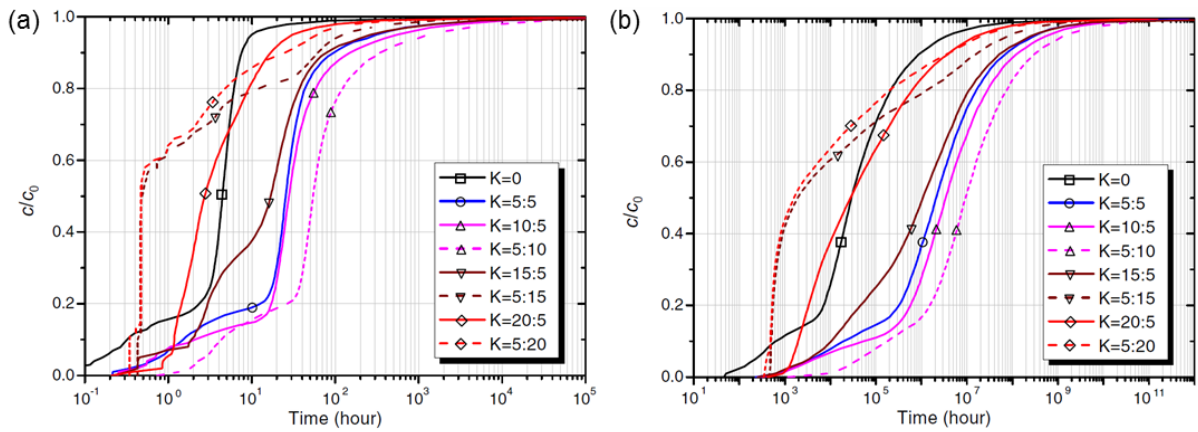
Fig. 3.16 Breakthrough curves for interacting tracers (i.e. with matrix diffusion) in a 2D DFN network stressed by various ratios of horizontal to vertical stresses (i.e. *K*) under a horizontal hydraulic pressure gradient of (a) 1×10^4 Pa/m, and (b) 10 Pa/m [Zhao et al., 2011] (note: c_0 is the initial concentration along upstream boundary, c is the concentration observed at the downstream boundary, $K = 0$ denotes a zero stress condition, and the two figures have different time scales).

3.5 Discussion

Modelling the geomechanical evolution and resulting hydraulic characteristics of fractured rocks is a challenging issue. Previous studies have demonstrated the importance of integrating natural fractures to better characterise the rock mass properties under tectonic stresses or

engineering perturbations (more detailed reviews can be found in Elmo et al. [2013] and Jing et al. [2013]). However, the simulation results rely highly on the accuracy of the constructed fracture networks as well as the implemented constitutive laws for natural fractures [Jing, 2003]. The three types of DFN models exhibit distinct strengths but may all suffer from some limitations, as listed in Table 3.1. The geologically-mapped DFN method can preserve many realistic features of fractures but is hard to characterise deep rocks and 3D structures. The stochastic DFN approach has the merits of simplicity and efficiency as well as applicability for 3D problems. However, its strong geological hypotheses of fracture geometries and topologies that tend to ignore some important underlying mechanical and tectonic constraints may result in large uncertainties. The geomechanical DFN models, which may capture some mechanical characteristics of natural fractures, are sensitive to the assumed/measured rock properties and inferred palaeostress fields. If they are to be improved to become the preferred useable model, they may need to couple with hydraulic, thermal and chemical mechanisms to reproduce actual geological systems. To generate better fracture networks, a future research direction that is attracting much effort is the development of hybrid DFN models that assimilate the advantages of different approaches. Some of the current DFN models have already exhibited such features. For example, Kattenhorn and Pollard [2001] used mechanical simulation to correct the 3D fault structures interpreted from seismic survey data. In the sequential stochastic DFN model by Davy et al. [2013], fractures develop following the subcritical growth law and their interactions are governed by an arrest mechanism.

The geomechanical modelling of fractured rocks can be achieved by continuum or discontinuum approaches, which have important differences in conceptualising geological media and treating displacement compatibility [Jing, 2003]. A detailed comparison of continuum and discontinuum models is presented in Table 3.1. The continuum modelling scheme mainly reflects the material deformation of a geological system from a more overarching view and attempts to bypass the geometrical complexity by using specific constitutive laws and equivalent material properties derived from homogenisation techniques. However, it cannot adequately consider the effects of stress variations, fracture interactions, block displacements and rotations. More importantly, the applicability of a homogenisation process is based on the assumption of an REV,

which may not exist for natural fracture systems usually having no characteristic length scale [Bonnet et al., 2001]. On the other hand, the discontinuum scheme treats the system as an assemblage of interacting individual components and permits the integration of complex constitutive laws for rock materials and fracture interfaces. A discontinuum model can be established at a specific scale of investigation without presuming the existence of an REV. However, some of the input parameters (e.g. bonding strength, joint stiffness) may need to be determined by indirect numerical calibrations rather than from physical measurements. Furthermore, the computational time for solving discontinuous problems can be considerably larger than that for continuum models. To take advantage of the two modelling technologies for tackling practical issues, a discontinuum model can be used to derive the REV size (if it exists) as the onset to treat a geological system as a continuum.

The stress-dependent hydraulic properties of fractured rocks as observed in numerical simulations demonstrate the importance of using explicit DFN representations and incorporating geomechanical modelling for characterising fluid flow in natural fracture systems. The results show consistency with field measurements, e.g. commonly only a small portion of fractures are conductive [Tsang and Neretnieks, 1998; Follin et al., 2014], permeability is less sensitive in deep rocks [Rutqvist and Stephansson, 2003], and critically stressed faults tend to have much higher hydraulic conductivity [Barton et al., 1995; Zoback, 2007]. The results of stress-dependent permeability and solute transport behaviour of fractured rocks have important implications for the groundwater industry [Bear et al., 1993], reservoir engineering [Zoback, 2007] and nuclear waste management [Tsang et al., 2005, 2015]. More effort will be needed in the future for various aspects, such as developing more advanced coupling schemes, modelling geomechanical effects on multiphase slow (i.e. Darcy) or inertia-dominated flow and importantly, extension to 3D work. Another critical issue is to develop appropriate upscaling approaches to fracture network models to evaluate large-scale behaviour, which may require preservation of geostatistical and geomechanical characteristics. Some techniques have been proposed to construct heterogeneous continuum models using upscaled stress-dependent permeability tensors for local grid blocks [Zhang and Sanderson, 1999; Blum et al., 2005, 2009].

3.6 Concluding remarks

To sum up, this chapter began by presenting an overview of various discrete fracture network (DFN) models for simulating the geometry and topology of natural discontinuity systems. Different continuum and discontinuum models that integrate DFN geometries to simulate the geomechanical behaviour of fractured rocks were then surveyed. Numerical results of the fracture-dependent mechanical response and stress-dependent hydraulic characteristics of fractured rocks suggest that it is important to use explicit DFN representations and conduct geomechanical computations to better characterise the bulk behaviour (e.g. strength, deformation, permeability and mass transport) of highly disordered geological systems containing naturally occurring discontinuities.

Several outstanding issues were identified by undertaking this review, according to which the main objectives of this PhD research are designed. To model the complex geomechanical behaviour of natural fractures associated with intrinsic asperities, a joint constitutive model is implemented into the "in-house" solid mechanics code, i.e. 2D/3D FEMDEM Y-code (Chapter 4). To examine the uncertainty of stochastic DFNs, the geomechanical responses of a 2D natural fracture network and its Poisson DFN equivalents are simulated and compared, with their stress-dependent permeability further evaluated (Chapter 5). To estimate the hydromechanical properties of larger scale fractured rocks, an upscaling approach is developed to extrapolate the geometry and apertures of a small-scale 2D fracture network to larger domains (Chapter 6). To explore the stress effects on fluid flow in 3D systems, a 3D FEMDEM model that integrates a stress-induced aperture model is developed to simulate an idealised 3D persistent fracture network (Chapter 7), while an extended 3D code that can also mimic new crack propagations is employed to model a 3D sedimentary layer embedded with realistic joint sets (Chapter 8). The importance of using explicit DFN representations in geomechanical modelling of fractured rocks is further demonstrated in a numerical study of the damage evolution around an underground excavation (Chapter 9).

Table 3.1 Comparison of different numerical models for geometrical and geomechanical modelling of natural fracture networks.

Numerical models	Key inputs	Strengths	Limitations
Geometrical modelling			
Geological DFNs	Analogue mapping, borehole imaging, aerial photographs, LIDAR scan or seismic survey	• Deterministic characterisation of a fracture system • Preservation of geological realisms	• Limited feasibility for deep rocks • Difficulty in building 3D structures • Constraints from measurement scale and resolution
Stochastic DFNs	Statistical data of fracture lengths, orientations, locations, shapes and their correlations	○ Simplicity and convenience ○ Efficient generation ○ Applicability for both 2D and 3D ○ Applicability for various scales	○ Uncertainties in statistical parameters ○ Oversimplification of fracture geometries and topologies ○ Requirement of multiple realisations
Geomechanical DFNs	Palaeostress conditions, rock and fracture mechanical properties	▪ Linking geometry with physical mechanisms ▪ Correlation between different fracture attributes	▪ Uncertainties in input properties and tectonic conditions ▪ Large computational time ▪ Negligence of hydraulic, thermal and chemical processes
Geomechanical modelling			
Continuum models	Equivalent material properties	• Simplicity of geometries • Efficient calculation • Suitability for large-scale industrial applications	• No consideration of fracture interaction, block displacement/interlocking/rotation • Complexity in deriving equivalent material parameters and constitutive laws • Valid only if an REV exists
Block-type & particle-based discrete models	Material properties for both fractures and rocks, damping coefficient, bonding strengths	○ Explicit integration of DFNs ○ Simple particle/grain bonding logic ○ Integrated constitutive laws for rocks/fractures ○ Capturing the interaction of multiple fractures	○ Limited data on joint stiffness parameters ○ Calibration of input particle bonding properties ○ No fracture mechanics principle ○ Large computational time
Hybrid FEMDEM models	Material properties for both fractures and rocks, fracture energy release rate, damping coefficient	▪ Explicit integration of DFNs ▪ Fracture propagation is based on both the strength criterion and fracture mechanics principles ▪ Integrated constitutive laws for rocks/fractures ▪ Capturing the interaction of multiple fractures	▪ Calibration of fracture energy release rates ▪ Large computational time

4 The finite-discrete element method combined with a joint constitutive model

4.1 Introduction

During the 1990s, many algorithmic solutions for discontinuum problems in both 2D and 3D, which later became known as the combined finite-discrete element method (FEMDEM), were developed by Munjiza et al. [1995, 1999] and Munjiza and Andrews [1998, 2000]. Extensive development and application of the FEMDEM method has been conducted during the past few decades, as has been reviewed in Chapter 3. The FEMDEM method has proven its capability in capturing large strain deformation, multibody interaction, fracture and fragmentation [Munjiza, 2004; Munjiza et al., 2011]. However, to model rock fractures associated with intrinsic surface asperities, an extension of the FEMDEM formulation may be important in order to consider complex fracture behaviour with respect to shear strength, normal opening/closure and shear dilatancy as well as important size effects.

To describe the behaviour of individual fractures associated with surface roughness, empirical joint constitutive laws have been developed based on experimental studies. Goodman [1976] proposed a hyperbolic relation to characterise the non-linear closure of fractures under normal compression and studied the effect of mismatch between opposite sides of rough joint walls. Barton and Choubey [1977] introduced an empirical system based on three main index parameters, i.e. joint roughness coefficient (JRC), joint wall compressive strength (JCS) and residual friction angle, to predict the shear strength of natural fractures. These parameters can be measured based on a visualisation comparison chart or from laboratory tilt tests or shear box experiments. Bandis et al. [1983] summarised a series of empirical equations to interpret the deformation characteristics of rock joints in normal loading and direct shear experiments. The effects of size on shear strength and deformation characteristics of individual fractures were also investigated based on laboratory experiments of natural fracture replicas that were cast at different sizes [Bandis, 1980; Bandis et al., 1981; Barton, 1981]. Fractures having the same roughness characteristics but different sizes may exhibit distinctly different mechanical

responses. A longer sample tends to exhibit lower stiffness and less dilation than a shorter one with the same JRC value [Barton and Bandis, 1980; Barton, 2013]. The empirical joint constitutive law was recently improved to capture the stress-dependency of peak shear displacement [Asadollahi and Tonon, 2010].

The objective of this study is to develop a methodology to incorporate such an empirical joint constitutive model (JCM) into the FEMDEM framework for modelling the geomechanical behaviour of fractured rocks with both pre-existing and propagating fractures. The effect of fracture closure and dilatancy under in-situ or engineering-induced stress changes is highly crucial for fluid flow. Therefore, both the implicitly captured microscale roughness effect by the JCM and the explicitly resolved fracture network topology by the FEMDEM must be included to give realistic fracture behaviour.

4.2 Finite-discrete element method (FEMDEM)

4.2.1 Mesh discretisation

The combined fracture-matrix solid system of a 2D fractured rock (Fig. 4.1a) is represented by a discontinuous discretisation of the model domain using three-noded triangular finite elements and four-noded joint elements embedded between edges of triangular elements (Fig. 4.1b). There are two types of joint elements: cohesive (i.e. unbroken) joint elements and fracture (i.e. broken) joint elements. The deformation of the bulk material is captured by the linear-elastic constant-strain triangular finite elements with the impenetrability enforced by a penalty function and the continuity constrained by a constitutive relation for cohesive joint elements [Munjiza et al., 1999], while the interaction of matrix bodies through discontinuity interfaces is simulated by the penetration calculation [Munjiza et al., 2000] along fracture joint elements. Construction of cohesive joint elements is achieved by a detachment algorithm based on the original continuous configuration between triangular elements in the matrix domain, whereas formation of fracture joint elements is realised based on the initial configuration of overlapping edges of the opposite triangular elements along pre-existing fractures. The joint elements (either broken or unbroken) are created and embedded between the edges of triangular element pairs before the numerical simulation, and no further remeshing process is performed during later computations. Propagation of new fractures is modelled by the transition of cohesive joint elements to fracture

joint elements in an unstructured grid system.
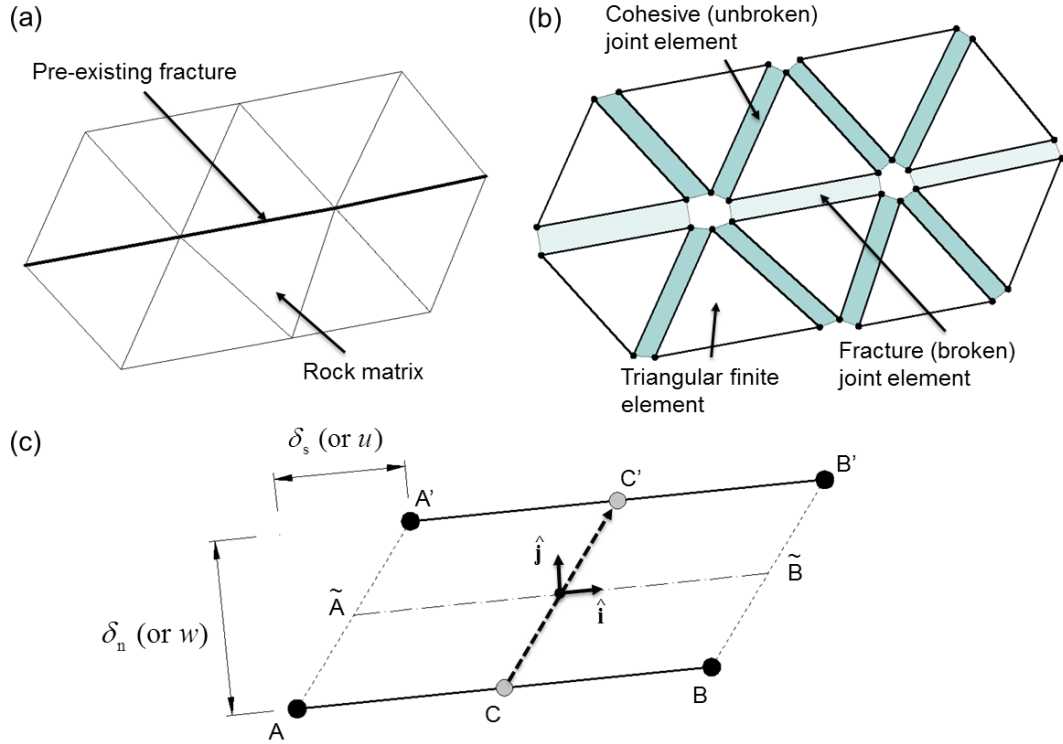
Fig. 4.1 Representation of (a) a 2D fracture-matrix solid system using a mesh consisting of (b) three-noded triangular elements and four-noded cohesive/fracture joint elements embedded between edges of triangular elements. (c) Displacements of a joint element (either unbroken or broken) characterised by the geometrical configuration of its nodal system.

The two opposite edges of a joint element (either unbroken or broken) are assumed initially overlapped, so that the displacements of a joint element during the modelling process can be calculated based on its current nodal coordinates. As shown in Fig. 4.1c, deformation of the joint element AB-A'B' is calculated by a vector of coordinate difference between the mid-points (i.e. C and C') of the opposite edges, given by

$$\hat{\mathbf{v}}_{CC'} = \frac{1}{2}\left(\mathbf{x}_{A'} - \mathbf{x}_A\right) + \frac{1}{2}\left(\mathbf{x}_{B'} - \mathbf{x}_B\right) \tag{4.1}$$

where $\mathbf{x}_A$, $\mathbf{x}_{A'}$, $\mathbf{x}_B$, $\mathbf{x}_{B'}$ are 2×1 arrays of the corresponding nodal coordinates. The median line of the joint element can be represented by a vector as

$$\hat{\mathbf{v}}_{\widetilde{A}\widetilde{B}} = \frac{1}{2}\left(\mathbf{x}_{B'} + \mathbf{x}_B\right) - \frac{1}{2}\left(\mathbf{x}_{A'} + \mathbf{x}_A\right) \tag{4.2}$$

based on which a local orthogonal coordinate system can be established with mutually unit base vectors defined by

$$\begin{cases} \hat{\mathbf{i}} = \dfrac{\widehat{\mathbf{v}}_{\widetilde{A}\widetilde{B}}}{\left\|\widehat{\mathbf{v}}_{\widetilde{A}\widetilde{B}}\right\|} \\ \hat{\mathbf{i}} \cdot \hat{\mathbf{j}} = 0 \end{cases} \tag{4.3}$$

Thus, the normal displacement δ_n and shear displacement δ_s of unbroken joint elements can be calculated as

$$\begin{cases} \delta_n = \hat{\mathbf{v}}_{CC'} \cdot \hat{\mathbf{j}} \\ \delta_s = \hat{\mathbf{v}}_{CC'} \cdot \hat{\mathbf{i}} \end{cases} \tag{4.4a}$$

For a broken joint element, its opening displacement w and shear displacement u can be similarly calculated as

$$\begin{cases} w = \hat{\mathbf{v}}_{CC'} \cdot \hat{\mathbf{j}} \\ u = \hat{\mathbf{v}}_{CC'} \cdot \hat{\mathbf{i}} \end{cases} \tag{4.4b}$$

4.2.2 Governing equation

The motions of elements are controlled by the forces acting on elemental nodes and the governing equation is given by [Munjiza, 2004]:

$$\mathbf{M}\ddot{\mathbf{x}} + \mathbf{f}_{int} = \mathbf{f}_{ext} \tag{4.5}$$

where $\mathbf{M}$ is the lumped nodal mass matrix, $\mathbf{x}$ is the vector of nodal displacements, $\mathbf{f}_{int}$ are the internal nodal forces induced by the deformation of triangular elements (section 4.2.3), $\mathbf{f}_{ext}$ are the external nodal forces including external loads $\mathbf{f}_l$ contributed by boundary conditions and body forces, cohesive bonding forces $\mathbf{f}_b$ caused by the deformation of cohesive joint elements (section 4.2.4), and contact forces $\mathbf{f}_c$ generated by the contact interaction via broken joint elements (section 4.2.5). The equations of motion of the FEMDEM system are solved by an explicit time integration scheme based on the forward Euler method.

4.2.3 Continuum stress and deformation

The stress field of constant-strain triangular elements is solved by the finite strain formulation that treats deformations involving rotations and strains [Munjiza et al., 1995]. Assume a triangular element moves from an initial position $\mathbf{x}_i$ to the current position $\mathbf{x}_c$ in the 2D Euclidean space. The deformation gradient $\mathbf{F}$ is given by:

$$\mathbf{F} = \frac{\partial \mathbf{x}_c}{\partial \mathbf{x}_i} \tag{4.6}$$

and the velocity gradient **L** is given by:

$$\mathbf{L} = \frac{\partial \dot{\mathbf{x}}_c}{\partial \mathbf{x}_i} \tag{4.7}$$

The left Cauchy-Green strain tensor **B** is calculated by:

$$\mathbf{B} = \mathbf{F}\mathbf{F}^{\mathrm{T}} \tag{4.8}$$

and the rate of deformation tensor **D** is obtained by:

$$\mathbf{D} = \frac{1}{2}\left(\mathbf{L} + \mathbf{L}^{\mathrm{T}}\right) \tag{4.9}$$

The Green-St. Venant strain tensor **E** is derived as:

$$\mathbf{E} = \frac{1}{2}\left(\mathbf{B} - \mathbf{I}\right) \tag{4.10}$$

The second-order Cauchy stress tensor **T** for general viscoelastic materials is calculated based on the neo-Hookean constitutive law as given by:

$$\mathbf{T} = 2G\mathbf{E} + \lambda\,\mathrm{tr}(\mathbf{E})\mathbf{I} + \eta\mathbf{D} \tag{4.11}$$

where G and λ are Lamé constants, η is the viscous damping coefficient, **I** is the identity matrix, tr(**E**) is the trace of **E**. Viscous damping is numerically included to consider energy dissipation caused by non-linear material behaviour or to simulate quasi-static processes using dynamic relaxation [Lisjak and Grasselli, 2014]. The internal nodal forces $\mathbf{f}_{int}$ exerted on the edge of a triangular element are given by:

$$\mathbf{f}_{int} = \mathbf{T} \cdot \mathbf{n} \tag{4.12}$$

where **n** is the normal vector of the edge of a triangular element.

4.2.4 Cohesive zone model

The elasto-plastic fracturing behaviour of geological rock materials is modelled by a cohesive zone approach that can capture the non-linear stress-strain characteristics of the plastic zone formed ahead of crack tips [Munjiza, 1999]. Fig. 4.2a shows the transition from the elastic zone to the fracture (broken) zone via the plastic zone, in which a decreasing normal bonding stress occurs due to strain softening, for a mode I fracture tip. The numerical implementation of the cohesive zone model in the FEMDEM system is further illustrated in Fig. 4.2b. The sign

convention for geomechanics is used in the following discussion, i.e. compressive stress is positive and tensile stress is negative.
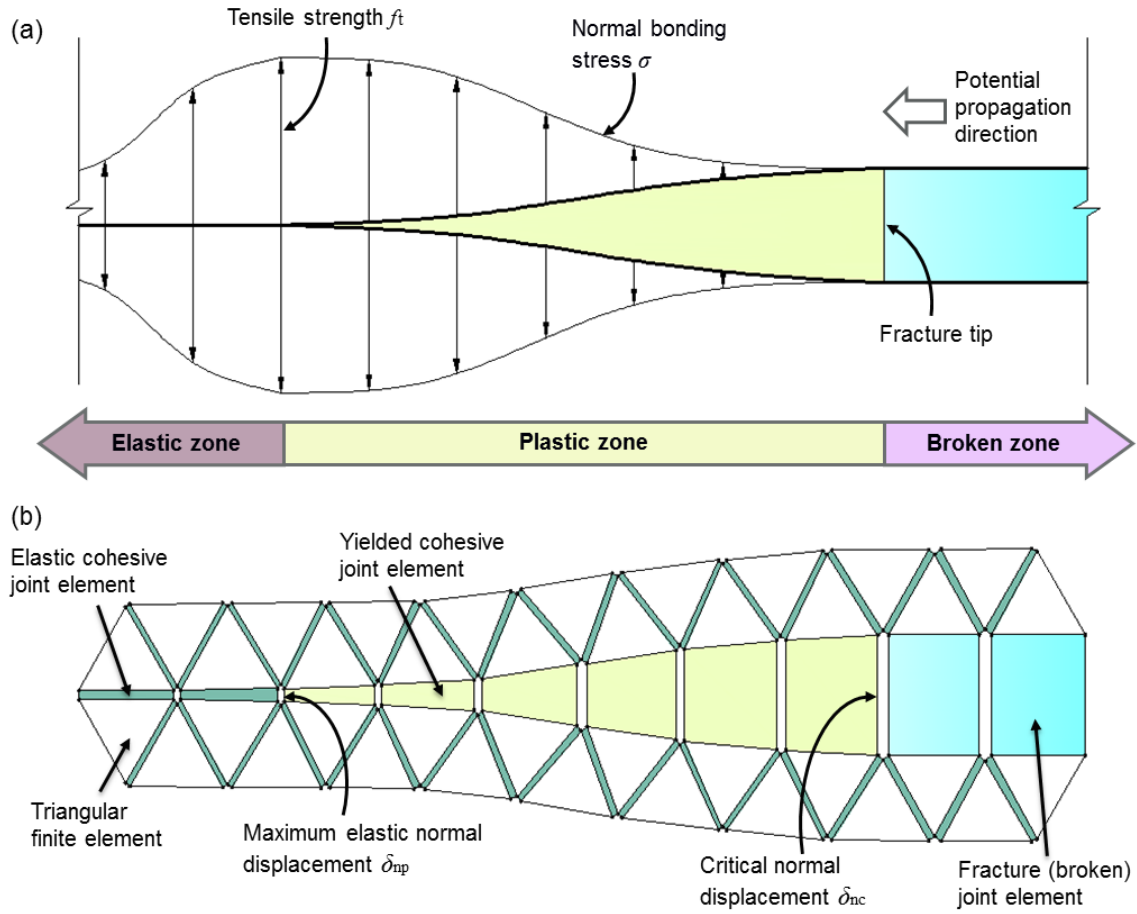
Fig. 4.2 Cohesive zone model: (a) schematic illustration of the transition from the elastic zone to the fracture (broken) zone via the plastic zone around the tip of a mode I fracture, and (b) numerical implementation in the FEMDEM system using three-noded triangular finite elements, four-noded cohesive (unbroken: intact or yielded) joint elements, and four-noded fracture (broken) joint elements (based on a figure by Lisjak et al. [2014a]).

The normal and tangential bonding stresses, σ and τ, for different strain regimes can be calculated as functions of normal displacement δ_n and shear displacement δ_s as given by:

$$\begin{cases} \sigma = -H_n(\delta_n) \cdot f_t \\ \tau = H_s(\delta_s) \cdot (f_s - f_r) + f_r \end{cases} \tag{4.13}$$

where f_t is the intrinsic tensile strength, f_s is the shear strength characterised by the internal cohesion c and the internal friction angle ϕ_i following the Mohr-Coulomb failure criterion with tension cut-off as given by:

$$f_s = c + \sigma \tan\phi_i, \quad \text{with } \sigma \geq f_t \qquad (4.14)$$

f_r is the residual frictional resistance related to the residual friction angle ϕ_r of broken surfaces as given by:

$$f_r = \begin{cases} \sigma \tan\phi_r, & \text{if } \sigma > 0 \\ 0, & \text{if } \sigma \leq 0 \end{cases} \qquad (4.15)$$

The coefficient function H_n for normal bonding stress is given by:

$$H_n = \begin{cases} \left[2\dfrac{\delta_n}{\delta_{np}} - \left(\dfrac{\delta_n}{\delta_{np}}\right)^2 \right], & \text{if } 0 \leq \delta_n \leq \delta_{np} \\ z, & \text{if } \delta_{np} < \delta_n \leq \delta_{nc} \\ 2\dfrac{\delta_n}{\delta_{np}}, & \text{if } \delta_n \leq 0 \end{cases} \qquad (4.16)$$

where δ_{np} is the maximum elastic normal displacement corresponding to the tensile strength f_t, δ_{nc} is the critical normal displacement related to the mode I energy release rate G_I (Fig. 4.3a), and z is a heuristic softening function from curve fitting of experimental data of concrete in tension (Evans and Marthe, 1968) as given by:

$$z = \left[1 - \frac{A+B-1}{A+B} \exp\left(W \frac{A+BC}{(A+B)(1-A-B)} \right) \right] \left[A(1-W) + B(1-W)^C \right] \qquad (4.17)$$

where A, B, C are empirical constants and equal to 0.63, 1.8 and 6.0, respectively, and W is a dimensionless damage factor determined by:

$$W = \begin{cases} 0, & \text{if } \delta_n \leq \delta_{np} \text{ and } \delta_s \leq \delta_{sp} \\ \dfrac{\delta_n - \delta_{np}}{\delta_{nc} - \delta_{np}}, & \text{if } \delta_{np} < \delta_n < \delta_{nc} \text{ and } \delta_s \leq \delta_{sp} \\ \dfrac{\delta_s - \delta_{sp}}{\delta_{sc} - \delta_{sp}}, & \text{if } \delta_{sp} < \delta_s < \delta_{sc} \text{ and } \delta_{ns} \leq \delta_{np} \\ \sqrt{\left(\dfrac{\delta_n - \delta_{np}}{\delta_{nc} - \delta_{np}}\right)^2 + \left(\dfrac{\delta_s - \delta_{sp}}{\delta_{sc} - \delta_{sp}}\right)^2}, & \text{if } \delta_{np} < \delta_n < \delta_{nc} \text{ and } \delta_{sp} < \delta_s < \delta_{sc} \\ 1, & \text{if } \delta_n \geq \delta_{nc} \text{ and } \delta_s \geq \delta_{sc} \end{cases} \qquad (4.18)$$

where δ_{sp} is the maximum elastic shear displacement corresponding to the shear strength f_s, δ_{sc} is the critical shear displacement related to the mode II energy release rate G_{II} (Fig. 4.3b). The five

parts of the piecewise-defined function of damage factor correspond to (i) the elastic regime, (ii) the plastic regime bounded by the mode I failure curve, (iii) the plastic regime bounded by the mode II failure curve, (iv) the plastic regime bounded by the mixed mode I-II failure curve, and (v) the broken regime (Fig. 4.3c). The coefficient function H_s for tangential bonding stress can be obtained by replacing $\delta_n, \delta_{np}, \delta_{nc}$ with $\delta_s, \delta_{sp}, \delta_{sc}$ in Eq. (4.18).
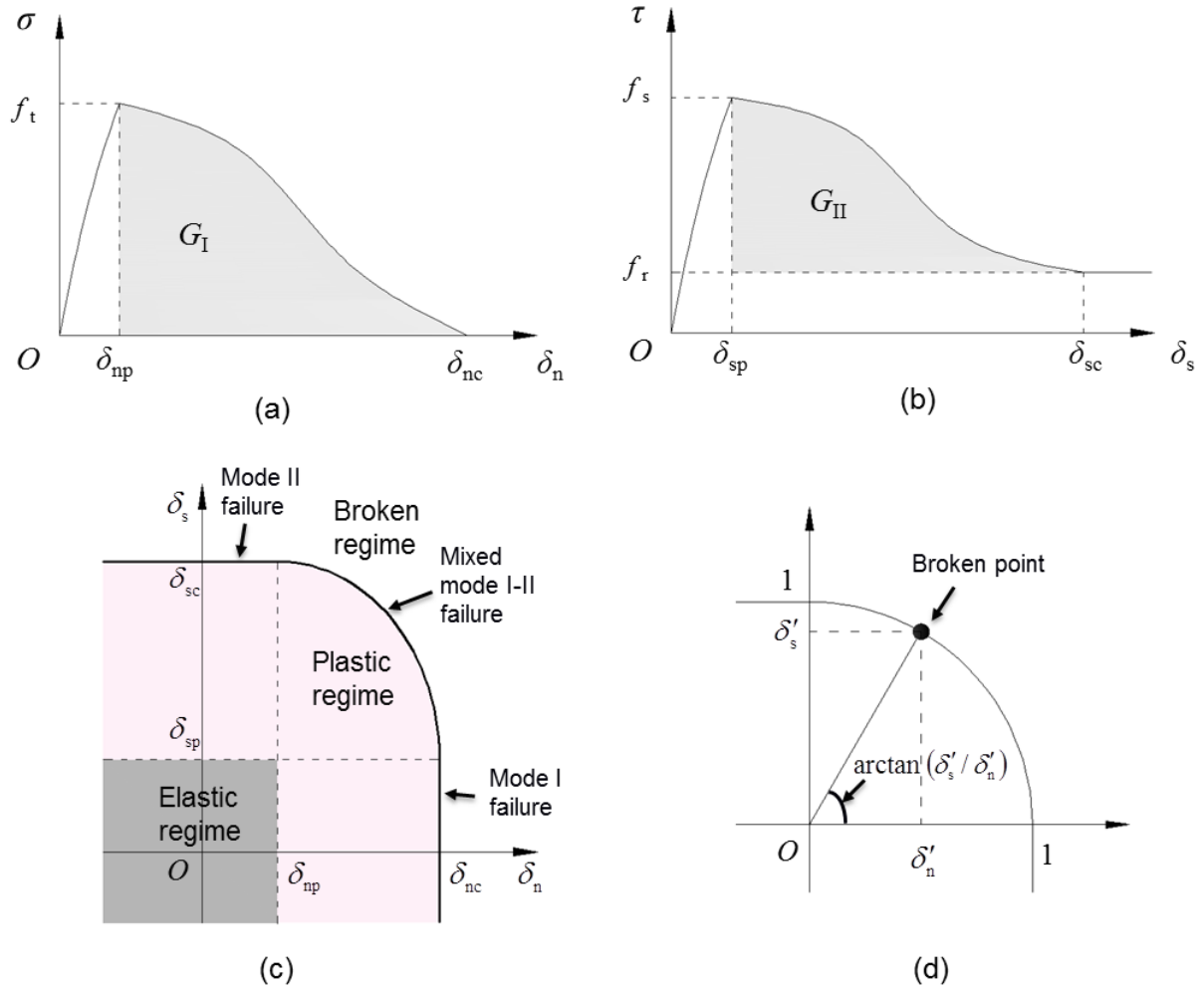
Fig. 4.3 Constitutive relations of the cohesive zone model for (a) mode I and (b) mode II failure. Failure mode analysis: (c) illustration of displacement regimes (elastic, plastic or broken) for cohesive joint elements based on their normal and shear displacements, and (d) determination of failure mode based on normalised displacements (based on a figure by Tatone and Grasselli [2015]).

Fracture propagation in brittle materials, e.g. rock, can be mode I, mode II, or mixed mode I-II failure [Shen and Stephansson, 1993; Lisjak et al., 2014a]. In FEMDEM, the failure mode of a cohesive joint element can be determined by the broken point through which the joint element

exceeds the failure envelope in a normalised coordinate system (Fig. 4.3d), in which the normalised displacement values are given by:

$$\begin{cases} \delta_n' = \dfrac{\delta_n - \delta_{np}}{\delta_{nc} - \delta_{np}} \\ \delta_s' = \dfrac{\delta_s - \delta_{sp}}{\delta_{sc} - \delta_{sp}} \end{cases} \qquad (4.19)$$

The failure mode indicator m $(1 \leq m \leq 2)$ is calculated as

$$m = \begin{cases} 1, & \delta_s' \leq 0 \\ 1 + \dfrac{\arctan(\delta_s'/\delta_n')}{\pi/2}, & \delta_s' > 0 \text{ and } \delta_n' > 0 \\ 2, & \delta_n' \leq 0 \end{cases} \qquad (4.20)$$

4.2.5 Contact force

Contact force between two triangular elements (one is named the contactor and another the target) interacting with each other through fracture joint elements is computed based on the penalty function method [Munjiza et al., 2000] by integration over the boundary of penetration:

$$\mathbf{f}_c = \int_{\Gamma_c} \mathbf{n}(\varphi_c - \varphi_t) d\Gamma_c \qquad (4.21)$$

where $\mathbf{n}$ is the outward unit normal to the penetration boundary Γ_c, while φ_c and φ_t are potential functions for the contactor and target solids, respectively. In the numerical implementation, the total contact force between two discrete solids is calculated as the summation of contact force between a set of couples of interacting finite elements. Interaction between two finite elements is further reduced into interactions between the contactor and the edges of target element. The normal contact force $\mathbf{f}_n$ and tangential friction force $\mathbf{f}_t$ exerted by a contactor onto a target edge are given by [Munjiza, 2004; Munjiza et al., 2011]:

$$\mathbf{f}_n = -\mathbf{n} \int_0^{L_p} p\varphi(l) dl \qquad (4.22)$$

$$\mathbf{f}_t = \mu \|\mathbf{f}_n\| \frac{\mathbf{v}_r}{\|\mathbf{v}_r\|} \qquad (4.23)$$

where L_p is the penetration length, φ is the potential function along the target edge, $\mathbf{v}_r$ is the relative velocity (at the Gauss point) between the contactor and the target edge, p is the penalty term, and μ is the friction coefficient.

4.3 Joint constitutive model (JCM)

4.3.1 Joint normal deformation

Based on laboratory experiments, rock joints were found to exhibit non-linear deformation response under compressive normal stress [Goodman, 1976]. An empirical hyperbolic model was proposed by Bandis et al. [1983] to represent this non-linear relation:

$$\sigma_n = \frac{k_{n0} v_n}{1 - v_n / v_m} \tag{4.24}$$

or

$$v_n = \frac{\sigma_n v_m}{k_{n0} v_m + \sigma_n} \tag{4.25}$$

where v_n is the current closure (mm) under the normal stress σ_n (MPa), k_{n0} is the initial normal stiffness (MPa/mm), and v_m is the maximum allowable closure (mm). Values of k_{n0} and v_m are given by [Bandis et al., 1983]:

$$k_{n0} = -7.15 + 1.75 \, \text{JRC} + 0.02 \times \frac{\text{JCS}}{b_0} \tag{4.26}$$

$$v_m = -0.1032 - 0.0074 \, \text{JRC} + 1.1350 \times \left(\frac{\text{JCS}}{b_0} \right)^{-0.2510} \tag{4.27}$$

where b_0 is the initial aperture (mm), JRC is the joint roughness coefficient, and JCS is the joint compressive strength (MPa). Coefficients derived from experimental measurements of numerous joint samples of five different rock types under a third loading cycle are adopted since in-situ fractures are considered more likely to behave in a manner similar to the third or fourth cycle [Barton et al., 1985]. These empirical equations and coefficients can statistically interpret the observed behaviour of the experiment samples under the specific testing conditions [Bandis et al., 1983]. However, attention is needed if they are applied to actual engineering and geological problems [Baghbanan and Jing, 2008]. Both JRC and JCS are scale-dependent parameters [Bandis et al., 1981; Barton, 1981] and their values for field scale, i.e. JRC_n and JCS_n, can be estimated using [Barton et al., 1985]:

$$\text{JRC}_n = \text{JRC}_0 \left(\frac{L_n}{L_0} \right)^{-0.02 \text{JRC}_0} \tag{4.28}$$

$$JCS_n = JCS_0\left(\frac{L_n}{L_0}\right)^{-0.03\,JRC_0} \tag{4.29}$$

where L_n is the effective joint length (i.e. size of a block edge between fracture intersections) defined by the spacing of cross-joints, JRC_0 and JCS_0 are measured based on the laboratory sample with length L_0. For the laboratory sample, the initial aperture b_0 may be estimated using an empirical relation [Bandis et al., 1983] as given by:

$$b_0 = \frac{JRC_0}{5}(0.2\frac{\sigma_c}{JCS_0} - 0.1) = \frac{JRC_0}{50} \tag{4.30}$$

where σ_c is the uniaxial compressive strength (MPa), and JCS_0 (MPa) can be set equal to σ_c, assuming the effect of weathering can be ignored.

Under a varying normal stress condition, the joint normal stiffness k_{nn} is given by [Saeb and Amadei, 1992]:

$$k_{nn} = \frac{\partial \sigma_n}{\partial v_n} = \frac{(\sigma_n + k_{n0}v_m)^2}{k_{n0}v_m^2} \tag{4.31}$$

4.3.2 Joint shear deformation

Peak shear strength τ_p of fractures under different normal stress levels can be calculated by the following empirical law of friction [Barton and Choubey, 1977]:

$$\tau_p = \sigma_n \tan\left[JRC_n \log_{10}\left(\frac{JCS_n}{\sigma_n}\right) + \phi_r\right] \tag{4.32}$$

where σ_n is the normal compressive stress (MPa) and ϕ_r is the residual friction angle. The shear stress-displacement curve of rock joints in direct shear experiments shows two major phases, i.e. pre-peak and post-peak stages. Such relation can be empirically characterised by replacing JRC_n in Eq. (4.32) with the mobilised value JRC_{mob}:

$$\tau = \sigma_n \tan\left[JRC_{mob} \log_{10}\left(\frac{JCS_n}{\sigma_n}\right) + \phi_r\right] \tag{4.33}$$

where τ is the current shear stress, JRC_{mob} can be calculated using the dimensionless model [Barton et al., 1985] as shown in Table 4.1, in which u is the current shear displacement, and u_p is the peak shear displacement (i.e. the shear displacement that corresponds to the peak shear stress). The scale-dependency of peak shear displacement u_p can be characterised by [Barton et

al., 1985]:

$$u_{\mathrm{p}} = \frac{L_{\mathrm{n}}}{500}\left(\frac{\mathrm{JRC}_{\mathrm{n}}}{L_{\mathrm{n}}}\right)^{0.33} \tag{4.34}$$

which was modified by Asadollahi and Tonon [2010] to further consider its stress-dependency as given by

$$u_{\mathrm{p}} = 0.0077 L_{\mathrm{n}}^{0.45}\left(\frac{\sigma_{\mathrm{n}}}{\mathrm{JCS}_{\mathrm{n}}}\right)^{0.34} \cos\left[\mathrm{JRC}_{\mathrm{n}} \log_{10}\left(\frac{\mathrm{JCS}_{\mathrm{n}}}{\sigma_{\mathrm{n}}}\right)\right] \tag{4.35}$$

For post-peak stage, $\mathrm{JRC}_{\mathrm{mob}}$ can also be estimated using a power-base empirical relation given by [Asadollahi and Tonon, 2010]:

$$\mathrm{JRC}_{\mathrm{mob}} = \mathrm{JRC}_{\mathrm{n}}\left(\frac{u_{\mathrm{p}}}{u}\right)^{0.381} \tag{4.36}$$

Table 4.1 Dimensionless model for shear stress-shear displacement [Barton et al., 1985].

u/u_{p}	0	0.3	0.6	1.0	2.0	4.0	10.0	25.0	100.0
$\mathrm{JRC}_{\mathrm{mob}}/\mathrm{JRC}_{\mathrm{n}}$	$-\phi_{\mathrm{r}}/i$	0	0.75	1.0	0.85	0.70	0.50	0.40	0.0

Note: $i = \mathrm{JRC}_{\mathrm{n}}\log(\mathrm{JCS}_{\mathrm{n}}/\sigma_{\mathrm{n}})$. Clearly, the $\mathrm{JRC}_{\mathrm{mob}}$ at $u = u_{\mathrm{p}}$ corresponds to the JRC value measured in the field, but will diminish under very large shearing.

The joint shear stiffness k_{tt} can be derived as the slope of the shear stress-shear displacement curve:

$$k_{\mathrm{tt}} = \frac{\partial \tau}{\partial u} \tag{4.37}$$

4.3.3 Joint shear dilatancy:

During the shearing process under a normal stress, fractures contract first due to the compressibility of asperities and then dilate with roughness damaged and destroyed. Dilational displacement can be related to the shear displacement based on an incremental formulation given by [Olsson and Barton, 2001]:

$$\mathrm{d}v_{\mathrm{s}} = -\tan d_{\mathrm{mob}}\mathrm{d}u \tag{4.38}$$

where $\mathrm{d}v_{\mathrm{s}}$ is the increment of normal displacement caused by shear dilation, $\mathrm{d}u$ is the increment of shear displacement, and d_{mob} is the mobilised tangential dilation angle.

A quadratic equation was proposed to describe the pre-peak dilational displacement with the

tangential dilation angle given by [Asadollahi and Tonon, 2010]:

$$d_{\text{mob}} = \arctan\left(\frac{v_{\text{p}}}{u_{\text{p}}} \left[4\left(\frac{u}{u_{\text{p}}}\right) - 1 \right] \right) \tag{4.39}$$

where v_{p} is the normal dilational displacement corresponding to the peak shear displacement u_{p} and can be calculated from [Barton and Choubey, 1977]:

$$\frac{v_{\text{p}}}{u_{\text{p}}} = \tan\left(\frac{1}{3M} \text{JRC}_{\text{n}} \log_{10}\left(\frac{\text{JCS}_{\text{n}}}{\sigma_{\text{n}}} \right) \right) \tag{4.40}$$

where M is a damage coefficient that is determined by [Barton and Choubey, 1977]:

$$M = \frac{\text{JRC}_{\text{n}}}{12 \log_{10}\left(\dfrac{\text{JCS}_{\text{n}}}{\sigma_{\text{n}}} \right)} + 0.70 \tag{4.41}$$

For the post-peak phase, surface asperities of fracture walls begin to be damaged as shearing continues and the variation of the tangential dilation angle can be captured by [Olsson and Barton, 2001]:

$$d_{\text{mob}} = \frac{1}{M} \text{JRC}_{\text{mob}} \log_{10}\left(\frac{\text{JCS}_{\text{n}}}{\sigma_{\text{n}}} \right) \tag{4.42}$$

4.3.4 Coupled joint normal and shear behaviour

Fractures in crustal environment may experience complicated loading paths, e.g. shearing under a variable normal stress [Saeb and Amadei, 1992]. By combining Eq. (4.31) and Eq. (4.38), the coupled behaviour of normal and shear deformation can be modelled by an incremental formulation given as:

$$dv = dv_{\text{n}} + dv_{\text{s}} = \frac{k_{\text{n0}} v_m^2}{(\sigma_{\text{n}} + k_{\text{n0}} v_m)^2} d\sigma_{\text{n}} - \tan d_{\text{mob}} du \tag{4.43a}$$

or after rearrangement:

$$d\sigma_{\text{n}} = \frac{(\sigma_{\text{n}} + k_{\text{n0}} v_m)^2}{k_{\text{n0}} v_m^2} dv + \frac{(\sigma_{\text{n}} + k_{\text{n0}} v_m)^2}{k_{\text{n0}} v_m^2} \tan d_{\text{mob}} du \tag{4.43b}$$

It can also be written in a more compact form as:

$$d\sigma_{\text{n}} = k_{\text{nn}} dv + k_{\text{nt}} du \tag{4.44}$$

where k_{nn} and k_{nt} are the corresponding normal stiffness coefficients. A similar equation can be

expressed for the relation between the increments of shear stress and displacement components:

$$\mathrm{d}\tau = k_{\mathrm{tn}}\,\mathrm{d}v + k_{\mathrm{tt}}\,\mathrm{d}u \tag{4.45}$$

where the stiffness coefficient k_{tn} is commonly assumed to be zero (i.e. the normal displacement of a joint is assumed not to generate additional shear stresses) [Jing and Stephansson, 2007] and k_{tt} is derived using Eq. (4.37). A differential formulation for the rock joint deformability can be further expressed by a non-symmetric material tangent stiffness matrix as follows:

$$\begin{bmatrix} \mathrm{d}\sigma_{\mathrm{n}} \\ \mathrm{d}\tau \end{bmatrix} = \begin{bmatrix} k_{\mathrm{nn}} & k_{\mathrm{nt}} \\ k_{\mathrm{tn}} & k_{\mathrm{tt}} \end{bmatrix} \begin{bmatrix} \mathrm{d}v \\ \mathrm{d}u \end{bmatrix} \tag{4.46}$$

4.4 Combined JCM-FEMDEM formulation

4.4.1 Characterisation of fracture systems based on a binary-tree search

Due to the scale-dependency of fracture parameters such as JRC, JCS and peak shear displacement, it is important to characterise the distribution of effective fracture lengths precisely (i.e. size of a block edge between fracture intersections) in the numerical modelling of a disordered, interconnected fracture system. One critical numerical difficulty related to effective fracture lengths is to distinguish the sophisticated topological relations of what is very often a complex system containing numerous joint elements, in which some pre-existing fracture joint elements may connect with each other to form a continuous fracture wall (i.e. block edge) and would act together as an equivalent individual fracture with two facing walls.

A generic algorithm has been developed in this research for the topological diagnosis of general fracture networks involving bends, intersections, termination and impersistence. Connectivity analysis is first implemented to recognise neighbours of each joint element based on the initial geometrical coordinates, in which a joint element connecting the model boundary or a fracture intersection is considered having no neighbour on that side with a '-1' value assigned numerically, as shown by the schematic example in Fig. 4.4a. Binary-tree structures are constructed with the tree-nodes representing joint elements (Fig. 4.4b). When scanning through the binary-tree system, previously visited tree-nodes or unreal neighbour tree-nodes are labelled to be dead (empty nodes in Fig. 4.4b) and will not grow in further loops. Block edges are identified as the connected chains of live tree-nodes (solid nodes in Fig. 4.4b). Thus, the effect of

fracture length on the fracture wall properties (i.e. JRC and JCS) can be modelled by relating the constitutive parameters of each local joint element to the roughness effect for a fracture length of the corresponding block edge.

(a)

(b)
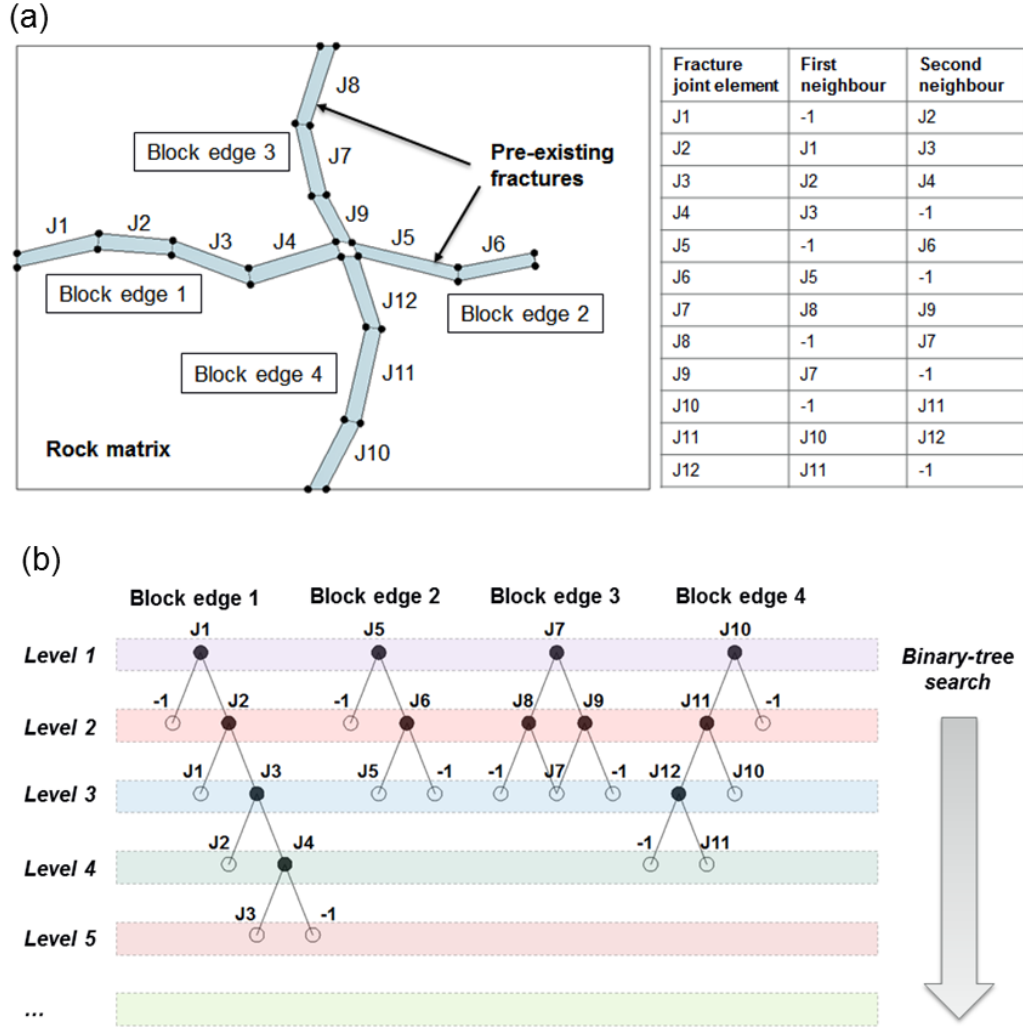
Fig. 4.4 Characterisation of a pre-existing fracture system, in which four block edges from two intersecting fractures are discretised into a number of fracture (i.e. broken) joint elements, based on (a) connectivity analysis and (b) binary-tree search.

4.4.2 Fracture apertures

The mechanical aperture b_m is derived by combing effects of mesoscopic opening (induced by fracture network deformation and explicitly resolved in the FEMDEM grid) and microscopic closure (controlled by microscale roughness and implicitly captured by the JCM) as given by

$$b_m = \begin{cases} b_0 + w & , w \geq 0 \\ b_0 - v & , w < 0 \end{cases}$$

(4.47)

where w is the mesoscopic normal separation of fracture joint elements as shown in Fig. 4.1, and v is the microscopic accumulative closure derived from the incremental formulation, i.e. Eq. (4.46). The first part of the piecewise function corresponds to the scenario that the fracture joint element is mesoscopically opened, while the second part models the condition that the two opposite walls of the fracture are in contact at the scale of FEMDEM discretisation.
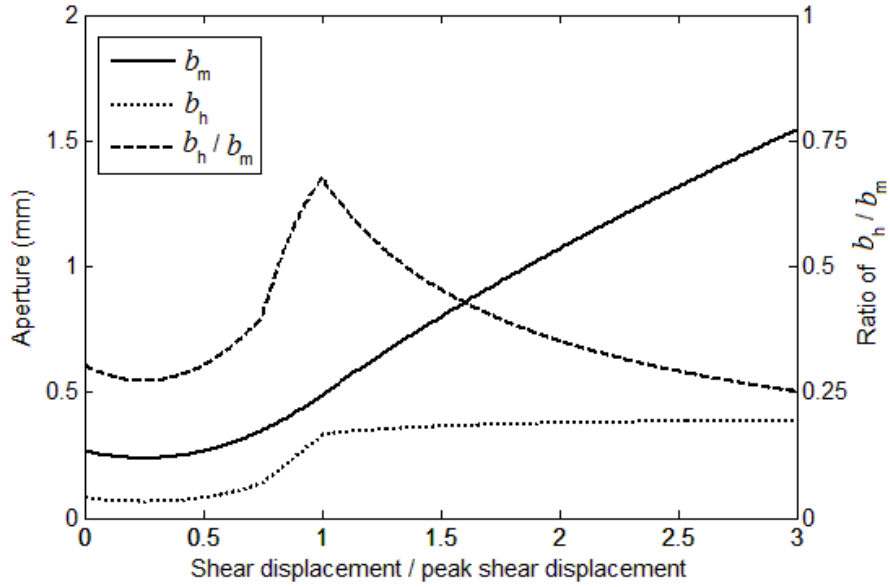
Fig. 4.5 Variation of mechanical aperture, hydraulic aperture and their ratio for a fracture with length of 0.5 m, JRC = 15 and JCS = 120 MPa during a shearing process with an assumed compressive normal stress of 10 MPa (note: the x-axis is normalised by the peak shear displacement).

The hydraulic aperture b_h defined as an equivalent aperture for laminar flow is derived based on an empirical relation with the mechanical aperture [Olsson and Barton, 2001]:

$$b_h = \begin{cases} b_m^2 / JRC^{2.5} & , \ u/u_p \leq 0.75 \\ b_m^{1/2} JRC_{mob} & , \ u/u_p \geq 1.0 \end{cases} \tag{4.48}$$

where JRC_{mob} is the mobilised JRC due to the roughness degradation and can be estimated using Table 4.1 or the power-base empirical relation, i.e. Eq. (4.36). A linear interpolation is used to determine the value of hydraulic aperture in the transition phase, i.e. $0.75 < u/u_{peak} < 1.0$, of Eq. (4.48) [Olsson and Barton, 2001]. As shown in Fig. 4.5, in the pre-peak phase, asperities of rough walls contract first with closed small voids and increased contact areas, which leads to a slight decline in the mechanical aperture and the ratio of hydraulic aperture to mechanical aperture, i.e.

b_h/b_m. Thereafter, the fracture walls begin to dilate with asperities not destroyed yet and both mechanical and hydraulic apertures exhibit an increasing trend. In the post-peak stage, where asperities get worn and damaged, the mechanical aperture continues to increase. However, the reduction of joint porosity associated with gouge production results in a decreased ratio of b_h/b_m, and the hydraulic aperture seems to reach a plateau under further shear displacement. It has to be mentioned that this empirical equation between the hydraulic and mechanical apertures was derived based on the hydromechanical shear experiments of granite rock joints. In this thesis, such a relationship is assumed also applicable to sedimentary rocks for generic investigations.

4.4.3 Coupling between JCM and FEMDEM

The JCM and FEMDEM modules are combined to achieve compatibility with respect to both stress and displacement fields. The displacement fields of JCM and FEMDEM are linked through Eq. (4.47), while the stress fields are coupled in both normal and tangential directions along the fracture interface. Normal stress of a joint element is extracted from adjacent finite elements of the FEMDEM solid model using

$$\sigma_n = \mathbf{n}^T \cdot \boldsymbol{\sigma} \cdot \mathbf{n} \tag{4.49}$$

where $\boldsymbol{\sigma}$ is the Cauchy stress tensor of the finite element located on the opposite fracture walls, and $\mathbf{n} = [n_x, n_y]^T$ is the outward unit normal vector of the finite element edge. By substituting the incremental value of normal stress and shear displacement into the JCM formulation, i.e. Eq. (4.46), the incremental normal displacement can be solved with the aperture further derived from Eq. (4.47). Friction angle between two rough fracture walls is often larger than the residual friction angle due to the effect of asperities [Barton and Choubey, 1977]. The friction coefficient also varies during the progression of shearing as a result of roughness degradation [Olson and Barton, 2001]. Mobilised friction coefficient μ_{mob} of each fracture joint element can be calculated using its current parameters (see Eq. (4.33)) as given by:

$$\mu_{mob} = \tan\left[JRC_{mob} \log_{10}\left(\frac{JCS_n}{\sigma_n}\right) + \phi_r \right] \tag{4.50}$$

The updated friction coefficient is transferred to the FEMDEM solver in each time step for calculation of the tangential friction force between a contactor and a target edge as given by Eq. (4.23).

4.5 Verification and calibration

The empirical constitutive laws are implemented in the FEMDEM framework at the joint element scale, but the consistency between the simulated macroscopic fracture behaviour and the empirical formulations requires a detailed verification and will most likely benefit from further calibration. The consistency between the empirical formulations and best-fit representations of the laboratory experiments has been reported in the literature, most notably by the extensive work of Barton, Bandis and co-workers. Clearly, it is important to recognise these best-fit relationships do not include the error and scatter in results which will have been presented. However, in spite of these errors being compounded, the combined empirical relations as set out provide the best estimate of the various mechanical dependencies on fracture wall microscale roughness. Hence, the task here is to check whether the new proposed numerical implementation of the combined JCM-FEMDEM (that computes the integrated displacement-force history from the incremental expressions) can reproduce with sufficient accuracy the predictions of the empirical equations designed to cover a wide range of fractures, rock properties and stress conditions. In this sense, the "validity" of the numerical model will be examined by comparing numerical results with the empirical solutions, i.e. Eq. (4.33) for the shear stress, the integral of Eq. (4.38) for the dilational displacement, and Eq. (4.25b) for the normal closure.
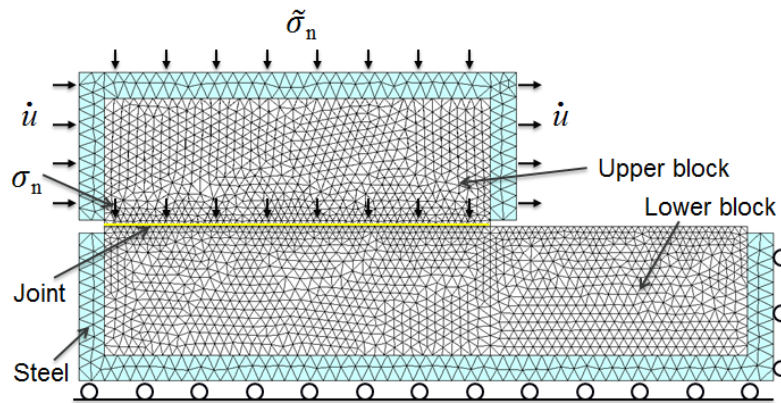
Fig. 4.6 Numerical model setup for the direct shear test of a joint sample under a constant normal stress condition. The normal stress $\tilde{\sigma}_n$ applied on the top of the shear box is designed to generate a constant normal stress $\sigma_n \equiv 24.5$ kPa on the joint surface by considering the gravitational forces of the upper block and shell. The shearing of the two fracture walls is controlled by the constant velocity boundary condition applied on the upper half of the shear box.

The model setup is based on the physical experiment conducted by Bandis [1980] using a series of cast replicas of natural joint surfaces prepared in different sizes, i.e. 6 cm, 12 cm, 18 cm and 36 cm. The material used for casting joints in the laboratory was made from the mixture of silver sand, alumina, barites and water. The density of the analogue material was 1850 kg/m^3 and the Young's modulus was 0.8 GPa. The Poisson's ratio was not provided in the reference [Bandis, 1980], so a typical value of 0.3 is assumed for the numerical model. As shown in Fig. 4.6, the specimen consists of an upper portion and a longer lower portion, and is placed in a shear box made of steel having a density of 8030 kg/m^3, a Young's modulus of 190 GPa and a Poisson's ratio of 0.3. The bottom and right sides of the lower steel shell are constrained by the roller boundary conditions, while the upper one is free to move. The normal stress $\tilde{\sigma}_n$ applied on the top of the shear box is designed to generate a constant normal stress $\sigma_n \equiv 24.5$ kPa on the joint surface with the consideration of the gravitational forces of the upper block and the steel shell. The shearing of the two fracture walls is controlled by the velocity boundary condition applied on the upper half of the shear box. The input joint properties for the numerical models of different sized joints were based on the smallest sample, i.e. $L_0 = 6$ cm, $JRC_0 = 15.0$, $JCS_0 = \sigma_c = 2$ MPa, and $\phi_r = 32°$ (the properties of the larger joints will be scaled up using Eq. (4.28) and (4.29) based on their actual lengths identified by the algorithm as described in section 4.4.1). The penalty term p for the specimen is chosen to be 20 times that of the Young's modulus [Mahabadi, 2012], i.e. $p = 16$ GPa. The damping coefficient η is assigned to be the theoretical critical value, i.e. $\eta = 2h (E\rho)^{1/2}$, where h is the element size, to reduce dynamic oscillations.

The numerical shear stress is derived as the quotient between the total tangential contact force integrated for all upper wall nodes and the length of the joint sample. In contrast to both the indirect measurement method which is used in laboratory testing of shear strength (i.e. by monitoring the horizontal forces loaded on the shear box in the laboratory [Bandis, 1980]), and the method adopted for the numerical modelling of an explicit roughness profile [Karami and Stead, 2008; Bahaaddini et al., 2014], in the proposed JCM-FEMDEM framework the tangential force acting on the joint surface is directly extracted from the contact algorithm and emerges by virtue of the forces recorded by the joint element data structure. It also gives an unbiased measurement of the joint frictional forces as it samples the forces (and stresses) where they need

to be known to have been correctly implemented, rather than deducing them from averaged values at the specimen boundaries. Obviously, monitoring the boundary forces is the only method available for laboratory determination of these shearing properties of joint surfaces.
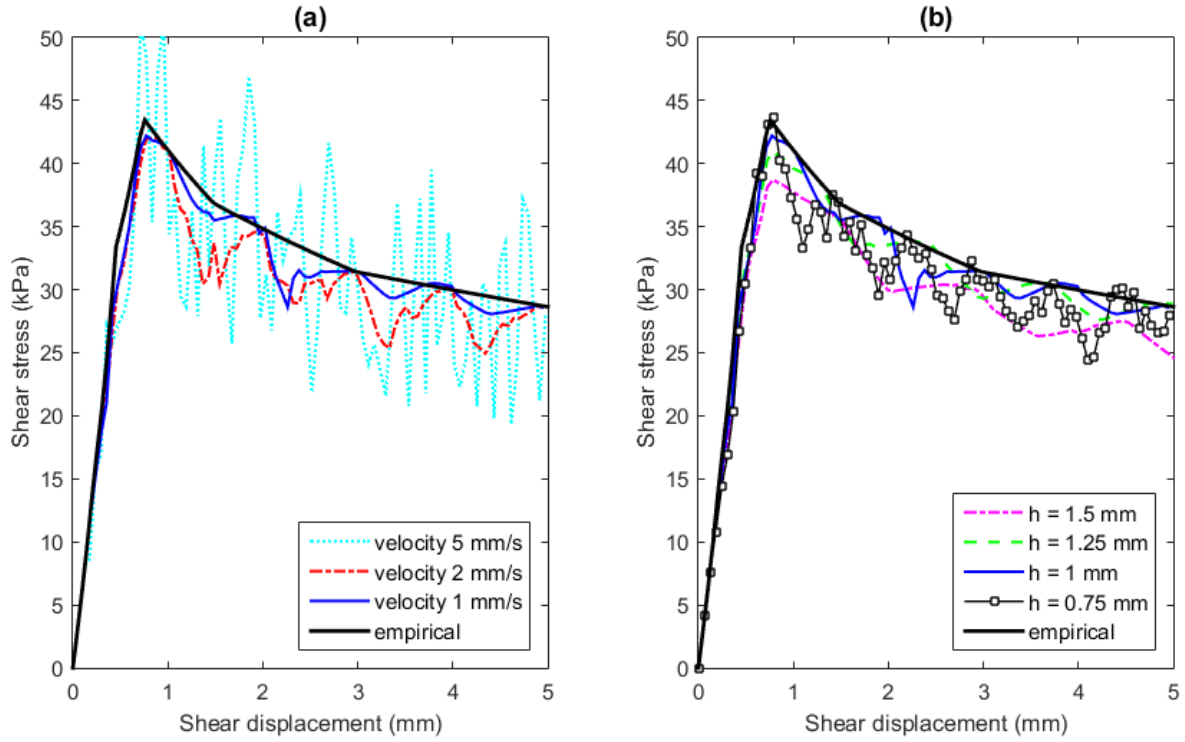
Fig. 4.7 Assessment of velocity and mesh sensitivities by comparing the numerical results with the empirical best-fit for the shear stress-shear displacement behaviour. (a) The numerical models are discretised by the same mesh configuration with an element size $h = 1$ mm along the joint, but conditioned with different velocity boundary conditions. (b) The numerical models are discretised by different mesh configurations with various element sizes h along the joint, but sheared under the same velocity condition of 1 mm/s.

The sensitivity of the shear stress-shear displacement behaviour to the loading velocity is shown in Fig. 4.7a. The numerical models discretised by the same very fine mesh with an element size of 1 mm along the joint are loaded by different shearing velocities ranging from 1 to 5 mm/s. The numerical plot exhibits an oscillatory form, which is possibly attributed to the dynamic effect of the explicit time integration scheme for modelling the shear experiment processes which are actually performed at loading rates associated with quasi-static deformation, i.e. the numerical model cannot sufficiently reach equilibrium during the shearing. However, it

can be seen that, as the velocity decreases, the oscillation amplitude is dramatically reduced and the numerical curve gradually approaches the empirical one. A velocity of 1 mm/s, however, requires a runtime of approximately 50 hours on a desktop computer equipped with an Intel Core E5-1620@3.70GHz and is therefore considered to be an appropriate value for simulating the quasi-static condition. Although 1 mm/s is still orders of magnitude larger than that of the original shear experiment, the loading rate in the numerical models is considered to be quite slow given the very small time step of 8×10^{-8} s/step (i.e. more than 1×10^{6} iterations are executed during every 0.1 mm displacement). The selected very high damping coefficient also helps suppress dynamic vibrations. The effect of mesh size on the shear stress is assessed by comparing the modelling results with different element sizes along the joint, i.e. 1.5 mm, 1.25 mm, 1 mm and 0.75 mm (Fig. 4.7b) under the same shearing velocity of 1 mm/s. With the refinement of the mesh, the numerical curve tends to converge to the target empirical solution. More interestingly, the wavelength of the oscillating numerical curves seems to correspond to the element size, possibly due to the use of constant-strain triangular finite elements and the transition between positions with perfectly overlapped opposing wall nodes (corresponding to the wave peaks) during the shearing. It implies that an element size close to a value of the peak shear displacement (i.e. 0.74 mm for the 6 cm specimen according to Eq. (4.34) [Barton et al., 1985]) divided by an integer number may more accurately capture the peak strength behaviour, as demonstrated by the curve of the numerical model with an element size of 0.75 mm in Fig. 4.7b.

Based on the results of the sensitivity analysis, the models of larger joint sizes, i.e. 12 cm, 18 cm, and 36 cm, are also built with the element sizes chosen as 1 mm, 1.5 mm, and 2.0 mm, respectively (corresponding to their distinct peak shear displacement values of 1.10 mm, 1.39 mm, and 2.06 mm). The models are all sheared under the same loading velocity of 1 mm/s and the same constant normal stress of 24.5 kPa. Apart from the waviness in the numerical plots, the similarity between the empirical and numerical curves of shear stress-shear displacement (Fig. 4.8a) is evident and is a reasonable justification that the implementation of the JCM-FEMDEM model has been verified. The numerical predictions for the joint dilational behaviour fit well to the empirical values (Fig. 4.8b), indicating that the implemented joint constitutive model

performs well in the numerical simulation. During the shearing process, the joint specimens exhibit a certain contraction in the pre-peak stage and a considerable dilation in the post-peak stage. It is reassuring that the scale effects on joint shearing behaviour observed in the laboratory test have been largely captured by the numerical model. With the increase of the joint sample size, the value of peak shear displacement increases, a transition from a "brittle" to "plastic" shear failure mode occurs, and a higher dilational displacement is generated.
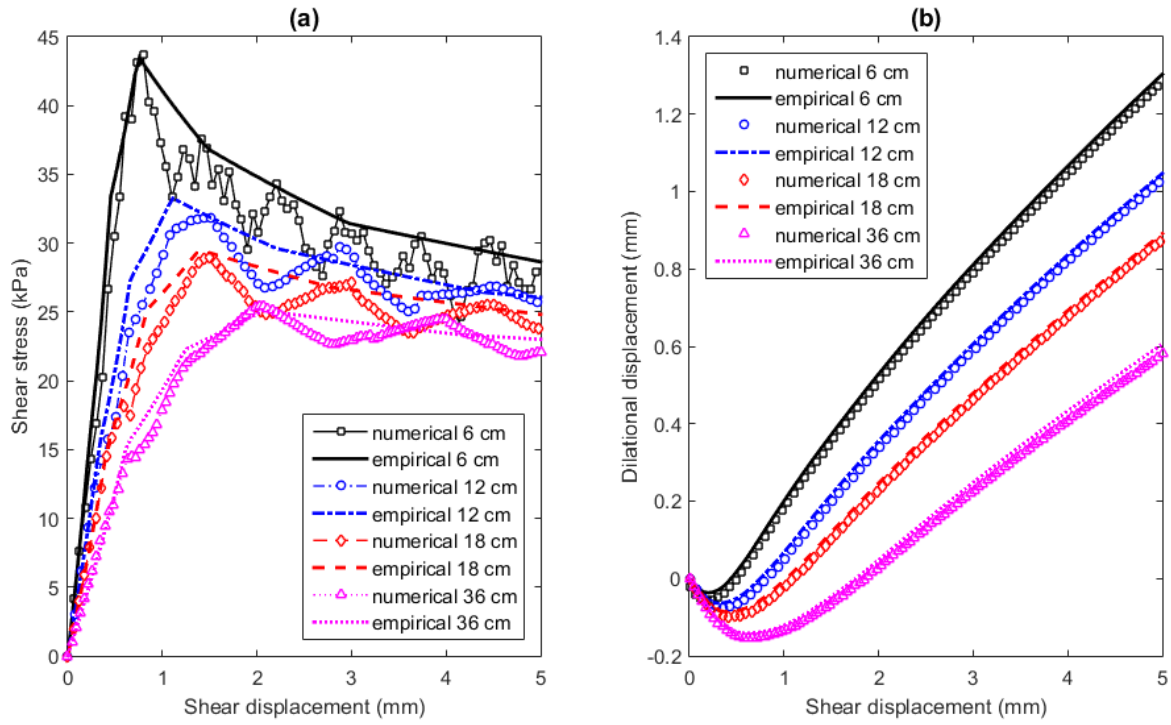
Fig. 4.8 (a) Shear stress-shear displacement curves and (b) dilational displacement-shear displacement curves obtained from the numerical models and the empirical formulations for joint samples with different sizes (i.e. 6 cm, 12 cm, 18 cm and 36 cm) in the direct shear test with a loading velocity of 1 mm/s under a constant normal stress $\sigma_n \equiv 24.5$ kPa.

In order to also examine the numerical model with respect to normal closure, the 6 cm joint sample is loaded with a normal stress gradually increased up to a value of 1 MPa, which is still smaller than the uniaxial compressive strength (i.e. $\sigma_c = 2$ MPa) of the analogue material and therefore will not cause breakage in the intact blocks. No shearing condition is imposed for this test of normal closure. As shown in Fig. 4.9, the numerical model also gives consistent results with the empirically calculated values, showing that the implementation of the empirical trends

for joint aperture closure is near perfect for this investigated JRC and idealised loading conditions.
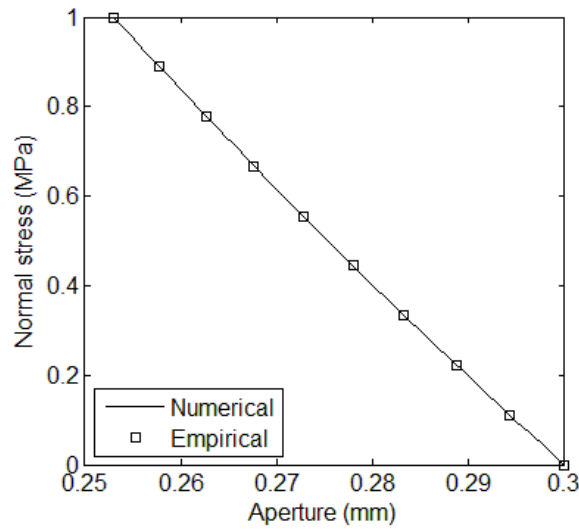
Fig. 4.9 The numerical and empirical results of the closure of the fracture aperture of the 6 cm joint sample under a normal stress gradually increased up to a value of 1 MPa.

4.6 Discussion

The consistency of the numerical results with the empirical solutions demonstrates the performance of the combined JCM-FEMDEM formulation for capturing realistic shear strength and normal closure behaviour of single fractures, although it is recognised that it would be ideal to further test the model over a parameter space with different JRC, JCS, normal stresses etc. The observation of the relation between the oscillation wavelength and the element size inspires an idea for future research to employ unstructured adaptive meshes for the initial choice of mesh appropriate to each individual fracture with distinct length and therefore specific peak shear displacement. Dynamic remeshing may also be developed if the effect of variable normal stress on peak shear displacement (i.e. Eq. (4.35)) is to be considered. The underlying mechanism of such a repetitive oscillatory form also requires a more detailed study in the future, as there is considerable interest in stick-slip phenomena during shearing.

The addition of the JCM module to the FEMDEM framework permits the simulation of the sophisticated shearing behaviour of pre-existing rough fractures based on experimentally derived constitutive laws. Unlike the work conducted with an explicit representation of the fracture roughness profile [Karami and Stead, 2008; Bahaaddini et al., 2014] that models the underlying

process of asperity failure and roughness degradation, the proposed method integrates the well-established joint constitutive laws directly as the criteria for implicit microscale modelling and can be advantageous in applications for large scale engineering problems. However, the discrete modelling approaches based on an explicit time marching scheme may all suffer from potential dynamic effects in numerical experiments. Although a large damping coefficient can help significantly attenuate the dynamic oscillation and approximate a quasi-static condition [Mahabadi, 2012; Tatone and Grasselli, 2015], further development in computational formulation and efficiency (e.g. implicit solution, and parallel computing) is still required to more realistically represent the physical conditions in laboratory experiments.

4.7 Concluding remarks

To conclude, a joint constitutive model that captures the overall behaviour of the micro-mechanical phenomena of compressed and/or sheared individual fractures as observed in laboratory experiments was implemented in the finite-discrete element analysis framework for geomechanical modelling of fractured rocks. The combined JCM-FEMDEM model is able to achieve compatibility for both the fracture and intact rock matrix fields with respect to stress and displacement. The numerical model exhibits realistic shear strength and displacement characteristics with the recognition of the fracture size effect, which was demonstrated by a comparison with the experimentally derived empirical solutions. The numerical model can be applied to simulate the complex behaviour of natural fracture networks under in-situ stresses including fracture opening, closing, shearing, dilatancy and new crack propagation, which will be demonstrated in the following chapters. It has to be mentioned that, the complete formulation of the JCM model presented in this chapter represents a relatively new work finished in the late stage of the PhD. Hence, only Chapter 8 and 9 are based on the latest version of the JCM that can consider scale-dependent roughness properties and mobilised shear strength of natural fractures. The other chapters (i.e. Chapter 5-7) are based on an early simplified JCM model that uses constant JRC and JCS parameters and a constant dilation angle for the calculation of aperture closure and dilatancy. Furthermore, the code in Chapter 5-7 uses a generalised energy release rate G for brittle failure, whereas mode I and mode II failure types are characterised by separate energy release rates G_I and G_II in the model used in Chapter 8 and 9.

5 Hydromechanical modelling of 2D fracture networks

5.1 Introduction

To characterise the geometrical attributes of a target natural fracture system that cannot be directly observed or sampled, an analogue fracture network (AFN) obtained from geological mapping of a "similar" rock mass can be used. The rock outcrop analogues often involve complicated intersections, terminations, bends and segmentations. Many studies have used mapped analogues to investigate the geomechanical and/or hydraulic behaviour of fractured rocks [Zhang and Sanderson, 1996; Sanderson and Zhang, 1999; Leckenby et al., 2005; Belayneh et al., 2006; Latham et al., 2013]. However, complete geometrical description of a natural fracture system is always difficult due to its 3D nature and the limited access to all information. Hence, stochastic discrete fracture networks (DFNs) are often used to approximate real discontinuity structures [Dershowitz and Einstein, 1988]. However, its potential to provide poor representations of real fracture systems is a widely-recognised disadvantage [Odling 1992; Berkowitz and Hadad, 1997], which can lead to significantly biased results in flow simulation [Odling and Webman, 1991; Belayneh et al., 2009].

Apart from fracture geometries, the fluid flow in fractured rocks is also greatly influenced by fracture apertures that are strongly related to geomechanical conditions [Rutqvist and Stephansson, 2003]. Some fractures with an unfavourable orientation for closure or a critical orientation for shear can become the major pathways for fluid migration while others may contribute little [Barton et al., 1995; Zoback, 2007]. The semi-analytical solution [Pollard and Segall, 1987; Olson, 2003] for a highly eccentric ellipse or ellipsoid representation of a fracture, based on linear elastic fracture mechanics, permits a calculation of the fracture opening under in-situ stresses through a simple formulation. However, the analytical solution is based on the assumption that fractures are straight, poorly interconnected and in their critical/subcritical state for propagation, which oversimplifies the mechanical complexity and stress heterogeneity of highly disordered geological systems with interconnected and/or curved fractures. As can be seen in Chapter 4, the FEMDEM method offers a whole new technology to solve the deformation of complex fracture networks under in-situ stresses. Thus, in this chapter, it is used

to evaluate stress effects on fluid flow in fracture networks and examine whether stochastic DFNs seem to oversimplify predictions for their more realistic analogue counterparts. Note that, for concision, the term "DFN" in this chapter refers to a stochastically-generated fracture network, while "AFN" refers to a geologically-mapped fracture network, which is slightly different from the nomenclature in Chapter 3.

5.2 Geological and stochastic fracture networks

5.2.1 AFN extraction
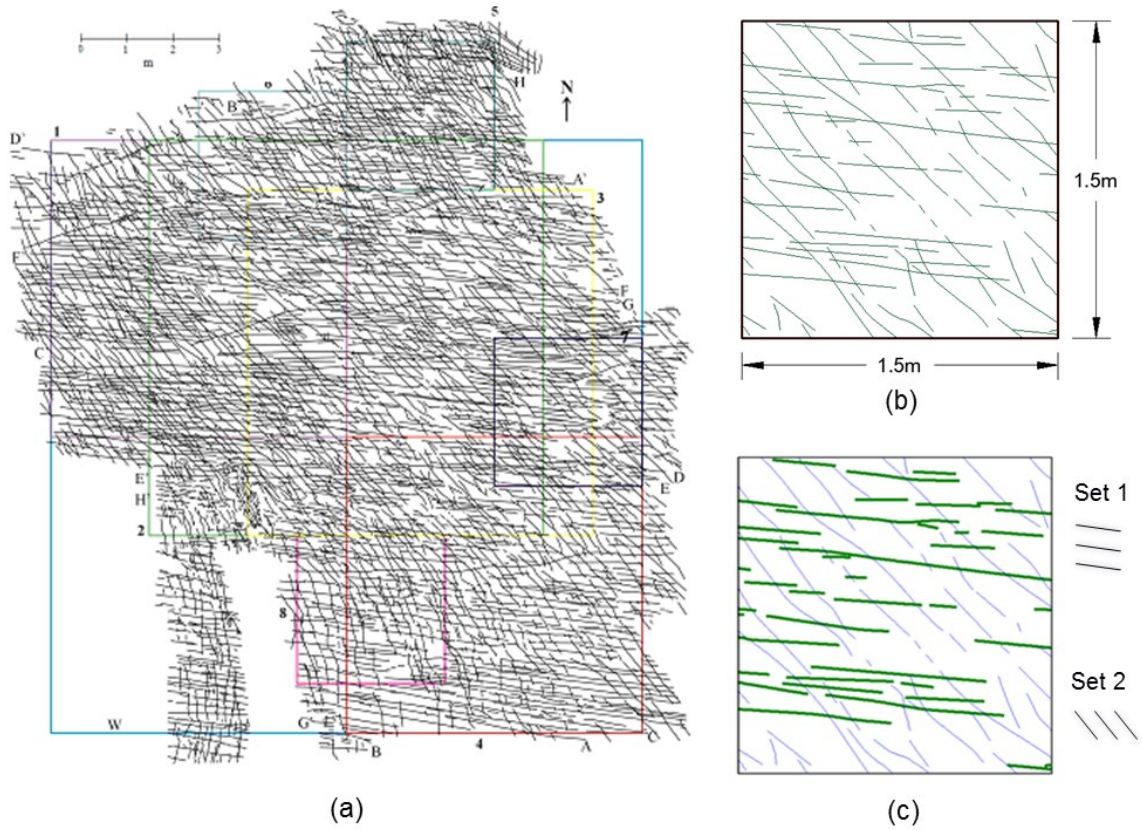
Fig. 5.1 (a) An outcrop of ~12 × 12 m at Kilve on the southern margin of the Bristol Channel Basin (after Belayneh et al. [2009]). (b) The extracted 1.5 m × 1.5 m analogue pattern. (c) Fracture clustering by fuzzy K-means algorithm.

The analogue fracture pattern is based on an outcrop map located at Kilve on the southern margin of the Bristol Channel Basin (Fig. 5.1a) [Belayneh et al., 2009]. This outcrop pattern has an intermediate fracture density and is quite close to the geometrical percolation threshold [Masihi and King, 2007]. As such, it may be considered as a particular case with properties not necessarily of networks with very high percolating characteristics. In this geological site, two

oblique sets of vertical, layer-normal fractures were formed extensionally and filled with calcite minerals, striking approximately 100° and 140°, respectively. The extracted AFN pattern is considered particularly well suited to being represented by random DFNs because the fracture sets are very distinct, cross-cut with few terminations and are generally straight. Two-dimensional analysis is conducted in this study.

5.2.2 AFN statistics required in the DFN construction

Statistical analysis is conducted by employing a suite of methods to derive characteristic parameters of the AFN fracture pattern, including identification of fracture sets and measurement of fracture geometrical attributes such as orientation, length and density. The statistics will be used for the generation of equivalent DFNs based on the random Poisson DFN model.

(a) Fracture set identification

Fractures formed during the same geological evolution commonly share similar properties (e.g. preferential orientation), so it is of great importance to cluster fractures reasonably into groups before further statistical analysis. The fuzzy K-means algorithm [Hammah and Curran, 1998] is used to automatically cluster analogue fractures into two sets based on their orientations (Fig. 5.1c). The orientation of a curved fracture is determined by the length-weighted average of all its segments.

(b) Fracture orientation

The rose diagrams of orientation data further validate the result of fracture set identification (Fig. 5.2a&d). In this study, orientation statistics are interpreted with a discrete probability distribution, through which DFNs are bootstrapped to share the same fracture orientation dataset with the original AFN to enhance their similarity.

(c) Fracture density

Location of fractures is represented by their barycentres, which are defined as the midpoints of the fracture traces. The concept of "fracture density cells" is introduced to analyse the spatial characteristics of natural fractures [Xu and Dowd, 2010]. The whole domain is divided into a series of sub-regions with fracture density (i.e. the number of fractures per unit area) calculated separately. A non-homogeneous point map is created to account for the spatial heterogeneity of the AFN system (Fig. 5.2b&e).

(d) Fracture length

A chi-squared goodness of fit test is made to determine the best probability distributions for the AFN fracture lengths. The negative exponential, gamma and lognormal distributions are involved in the hypothesis test under a significance level of 5% and the negative exponential distribution is found to give the best fit to the length data. Sampling errors caused by the censoring bias in window sampling have been corrected using the method proposed by Kulatilake and Wu [1984] (Fig. 5.2c&f).
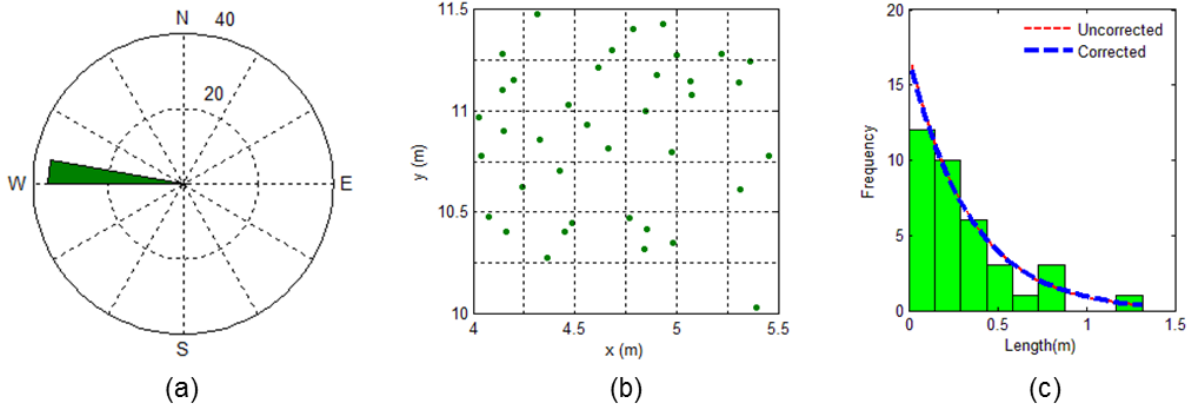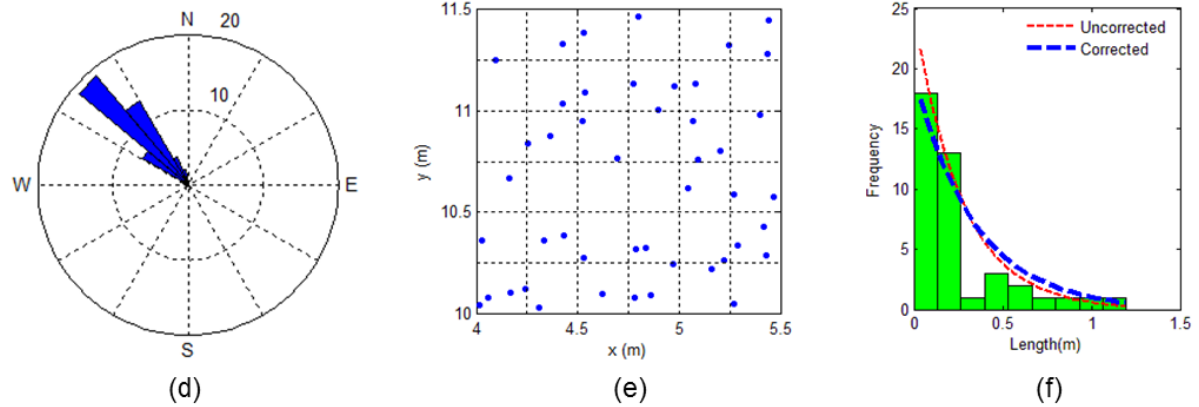
Fig. 5.2 Statistics of the AFN pattern: (a) orientation, (b) barycentres and (c) length distribution of fracture set 1, and (d) orientation, (e) barycentres and (f) length distribution of fracture set 2.

5.2.3 Stochastic DFN realisations

A stochastic DFN model is constructed with criteria commonly used to build networks for normal hydrogeological calculations, but in addition, further constraints are imposed to improve the network quality. A DFN is created by three steps. (i) Fracture locations are simulated first using a randomly generated point pattern. Barycentres are seeded uniformly in each density cell

using the marked Poisson point process with density values matched to the AFN non-homogeneous map. (ii) The second step is the modelling of the geometry of individual fractures, in which orientation and length parameters are generated independently according to their probability distributions. (iii) The final step is the quality examination of the randomly created DFN realisations. In this study, the examination focuses on fracture length, connectivity and hydraulic conductivity. If either of them fails, the generation process is repeated automatically.

To consider the potential censoring effects on DFN fracture lengths, a chi-squared test is implemented to check whether the final DFN pattern has the same length distribution as the AFN. The average number of intersections per fracture is measured as the connectivity index of a fracture network [Hestir and Long, 1990]. If the relative difference between the AFN and a DFN is smaller than 5%, the two models are considered to be equivalent with respect to this connectivity index.

Furthermore, the conductivity parameter η proposed by Leung and Zimmerman [2012] for fracture only flow is used to assess the hydraulic equivalence. The parameter η was developed from flow simulations based on random two-dimensional fracture networks. It was found to have a linear correlation with the hydraulic conductivity of fracture networks that were assigned with a uniform aperture distribution. The parameter η that is a combination of crack mean density ε_{mean} and segment density ρ_{seg} incorporates the information of both length and connectivity of a fracture network. The definitions of ε_{mean}, ρ_{seg} and η are given by

$$\varepsilon_{mean} = \frac{n}{A}\left(\frac{\overline{l}}{2}\right)^2 \tag{5.1}$$

$$\rho_{seg} = \frac{n_{seg}}{A} = \frac{n + 2n_{node}}{A} \tag{5.2}$$

$$\eta = \sqrt{A\varepsilon_{mean}\rho_{seg}} = \frac{n\overline{l}}{2}\sqrt{\frac{1 + 2n_{node}/n}{A}} \tag{5.3}$$

where n is the total number of fractures, A is the model area, $\overline{l}$ is the arithmetic mean of all fracture lengths and n_{node} is the number of intersection nodes in a fracture network. The parameter η is used to enhance the similarity between DFN realisations with the original AFN. If

η calculated for a DFN and for the original AFN are similar at the 95% confidence level, they are expected to exhibit similar hydraulic behaviour under the assumption of constant aperture.

Fig. 5.3 shows ten DFN realisations that passed this similarity examination. Hence with this further tuning, the scene is set for geomechanical deformation of the various networks. It should be noted that DFN7 was arbitrarily selected to give a visual comparison between the AFN and DFN models in the following sections. The quantitative analyses, however, are based on the results of all ten DFNs (given by mean values with error bars representing ±1 standard deviation).
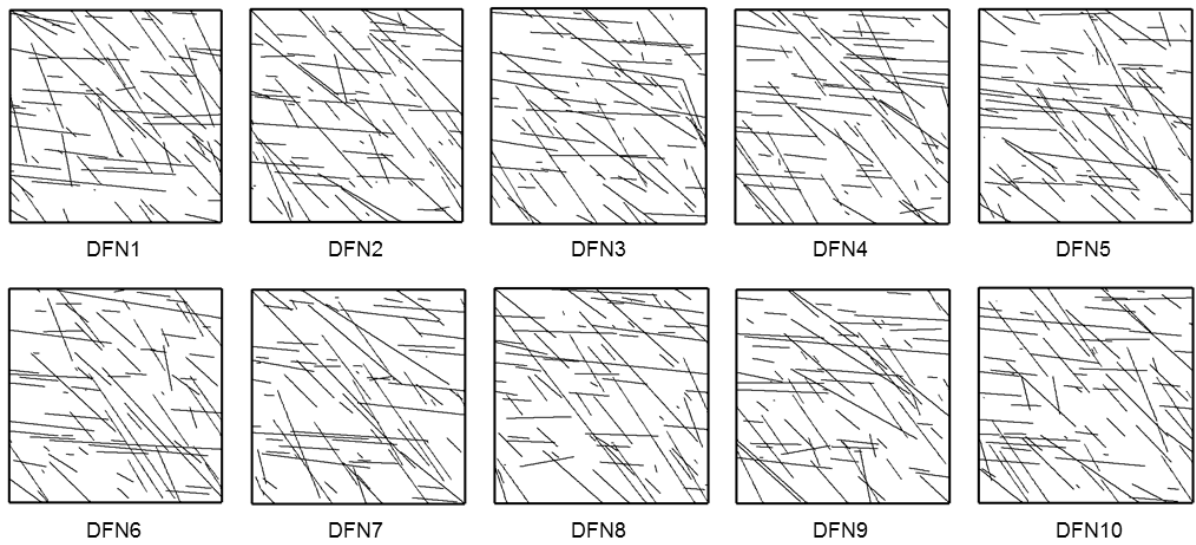
Fig. 5.3 Multiple stochastic DFN realisations.

5.3 Hydromechanical modelling

5.3.1 Geomechanical experiment

As shown in Fig. 5.4, a series of plane strain geomechanical experiments is designed with biaxial effective stresses ($\sigma'_1 = 10$MPa, $\sigma'_3 = 5$MPa) applied at a range of angles (0°, 30°, 60°, 90°, 120° and 150°) (i.e. the strike-slip faulting regime with σ'_2 being vertical). Assumed typical material properties of limestone [Lama and Vutukuri, 1978; Barton and Choubey, 1977] are given in Table 5.1. Geomechanical modelling is conducted on the original AFN and the DFN equivalents using the FEMDEM solver. Far-field stresses are applied at the boundaries of the domain from an unstressed state with all fractures having a constant initial aperture. The models adjust to a new deformed state under in-situ stresses loaded by different orientations. In this

research, the fracture behaviour is modelled using a simplified joint constitutive law assuming constant JRC and JCS parameters and a constant dilation angle.
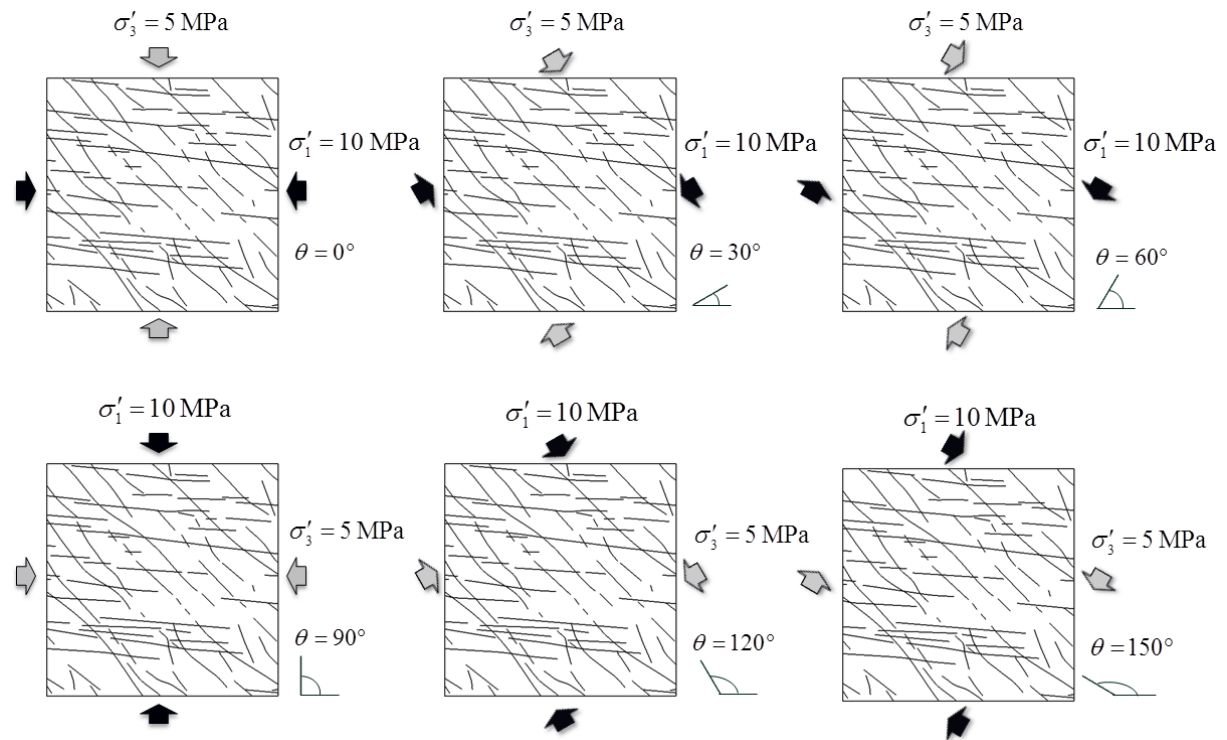
Fig. 5.4 Far-field stresses are applied at a range of angles to the fractured rock.

Table 5.1 Material properties of the fractured limestone.

Properties	Value
Bulk density ρ (kg/m3)	2700
Young's modulus E (GPa)	30
Poisson's ratio υ	0.27
Tensile strength f_t (MPa)	2.5
Internal friction angle ϕ_i (º)	31
Cohesion c (MPa)	5
Energy release rate G (J·m^{-2})	200
Residual friction angle ϕ_r (º)	31
JCS (MPa)	120
JRC	15
Dilation angle ϕ_d (º)	5
Initial mechanical aperture b_0 (mm)	0.3

5.3.2 Fluid flow modelling

Single-phase steady state flow of incompressible fluid with constant viscosity through porous media, in absence of sources and sinks, is governed by the continuity equation and Darcy's law. The mass balance of fluid is given by

$$\nabla \mathbf{u} = 0 \tag{5.4}$$

where $\mathbf{u}$ is the superficial fluid velocity given by Darcy's law:

$$\mathbf{u} = -\frac{\mathbf{k}}{\mu} \nabla P \tag{5.5}$$

where μ is the dynamic viscosity, P is the fluid pressure and $\mathbf{k}$ is the permeability tensor of the porous medium. For isotropic material, the permeability scalar k is used instead.

The fluid flow domain $\mathbf{\Omega}$ is composed of two overlapping subdomains, namely the fracture domain $\mathbf{\Omega}_f \in \mathbf{R}^1$ and the matrix domain $\mathbf{\Omega}_m \in \mathbf{R}^2$. The deformed fractures in response to the loading of effective in-situ stresses are extracted from the geomechanical simulation. Fracture geometries are derived as the median lines in between opposite fracture walls and apertures are determined from the joint constitutive model. Another unstructured grid is created with matrix bodies discretised into finite elements and fractures segmented into lower dimensional line elements [Paluszny et al., 2007]. The fluid pressure equation is solved by the finite element method and the continuity equation is calculated by the finite volume method [Geiger et al., 2004]. A constant permeability k_m is assigned to matrix elements, whereas fracture permeability is characterised using piecewise hydraulic apertures obeying the cubic law, i.e. $k_i = b_i^2/12$ [Witherspoon et al., 1980], where k_i is the permeability of the ith line element, and b_i is its corresponding hydraulic aperture. By combining Eq. (5.4) and Eq. (5.5), a fluid field can be described by

$$\nabla \cdot (k \nabla p) = 0 \tag{5.6}$$

In the finite element system, each element e_i is assigned with constant material properties. Spatial integration over the bounded domain $\mathbf{\Omega}$ gives

$$\left[\sum_{e_i} \int_{\mathbf{\Omega}_m} \nabla \mathbf{N}^T k_m \nabla \mathbf{N} d\mathbf{\Omega} + \sum_{e_i} b_i \int_{\mathbf{\Omega}_f} \nabla \mathbf{N}^T k_i \nabla \mathbf{N} d\mathbf{\Omega} \right] \mathbf{p} = 0 \tag{5.7}$$

where $\mathbf{N}$ is the shape function of each element and $\mathbf{p}$ is the nodal pressure. The nodal pressure is resolved by the algebraic multigrid methods for systems (SAMG) [Stüben, 2001]. The fluid velocity field is calculated from the gradient of the pressure field based on linear interpolation at

the midpoints of finite element edges, i.e. nodes of the finite volume grid. The interstitial fluid velocity field is continuous between adjacent node-centred finite volumes, although discontinuous between two finite elements [Geiger et al., 2004]. By applying a prescribed macroscopic pressure differential on each pair of opposite boundary surfaces with no-flow conditions on the remaining ones parallel to the flow direction (Fig. 5.5), the equivalent permeability of a fractured porous medium can be computed based on the integration of the fluid flux over the node-centred finite volumes along model boundaries [Lang et al., 2014].
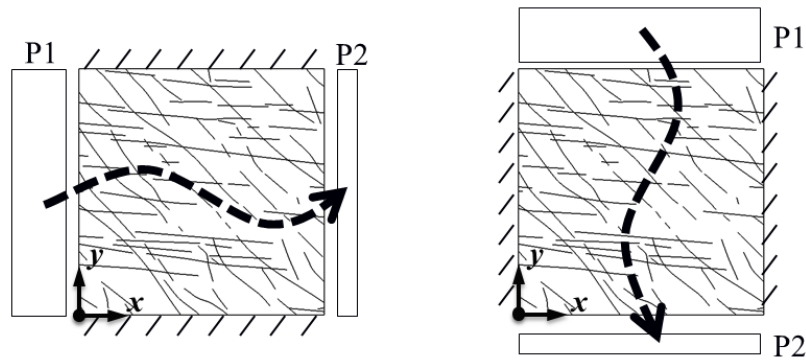
Fig. 5.5 Calculation of equivalent permeability based on single-phase steady state flow under a pressure differential imposed on each pair of opposite boundaries while the remaining ones are impervious.

5.4 Results

5.4.1 Stress heterogeneity
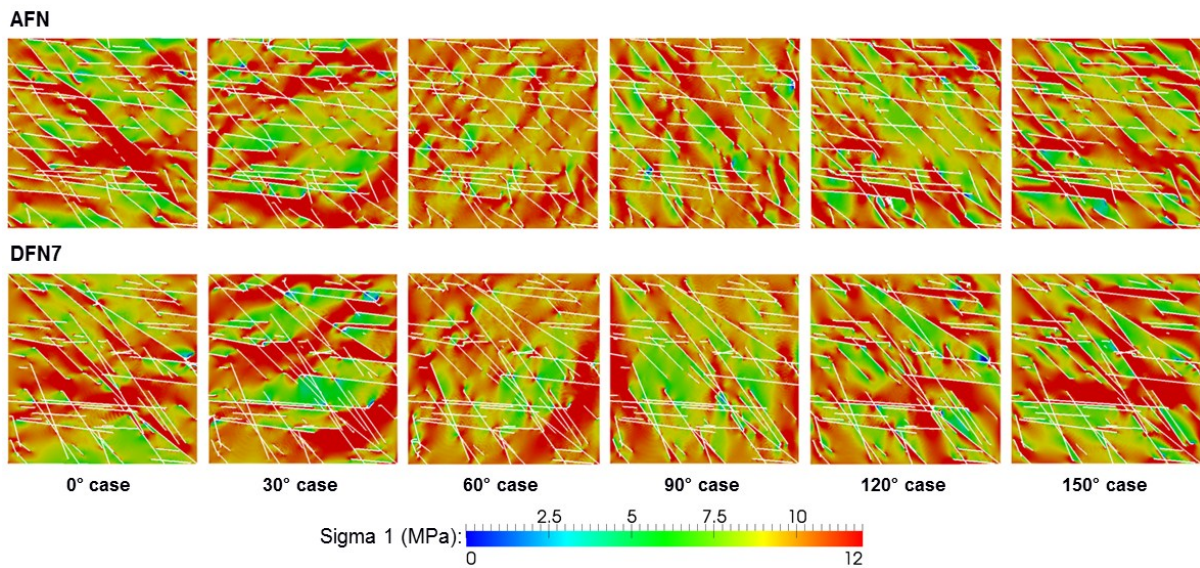
Fig. 5.6 Contours of the local maximum principal stress of the AFN and DFN7.

Fig. 5.6 shows the distribution of local maximum principal stress in the deformed models of the AFN and one DFN (i.e. DFN7). The high compressive stress bands are likely to trend along the orientation of applied maximum far-field stress, but will be considerably influenced by the spatial organisation of fractures as well. For example, in the 0° case, the bands attempt to align with the x-direction, but often have to comply with the shape of internal matrix blocks.
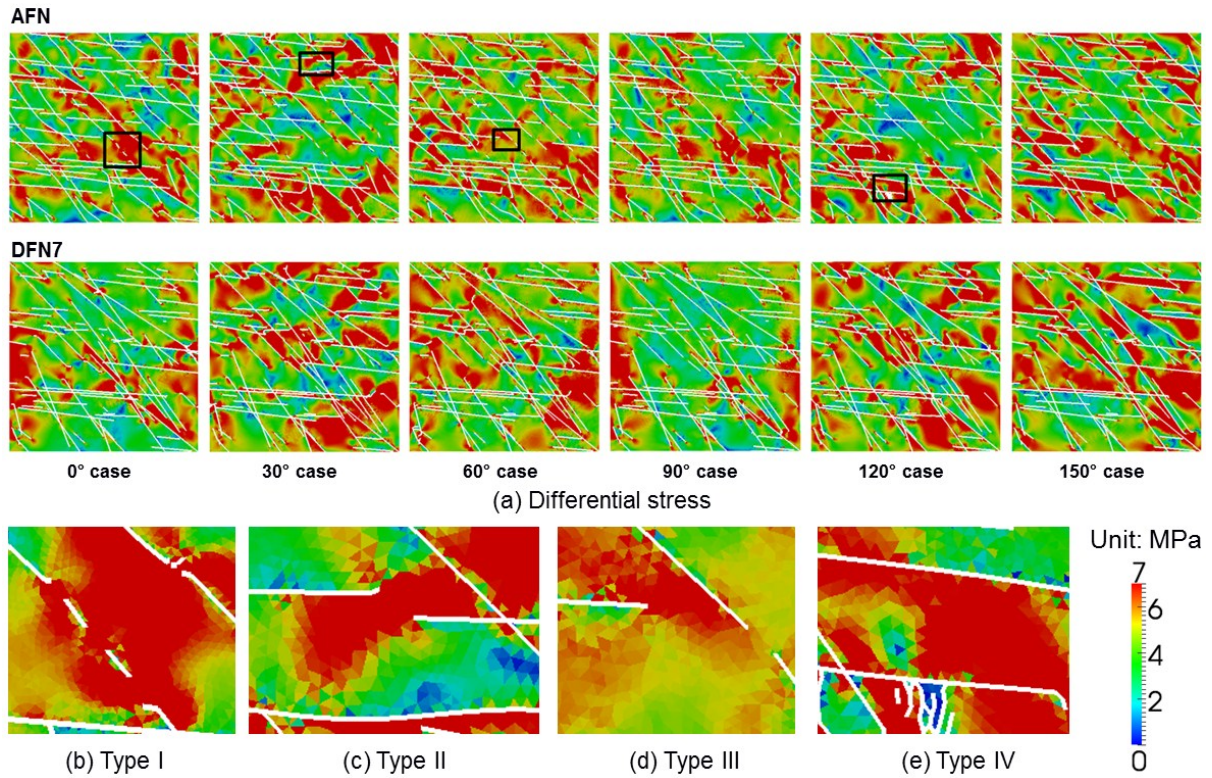
Fig. 5.7 (a) Contours of the differential stress of the AFN and DFN7. (b)-(e) Four types of circumstances for differential stress concentration in the AFN model (corresponding locations are sequentially marked in (a)).

The heterogeneity of differential stress is presented in Fig. 5.7a. The stress contours of the two models appear to have similar overall colour zonation in each scenario, although they display distinct features in detail. For example, in the AFN model, high differential stress concentration appears to usually occur under four types of circumstances related to fractures with high shear stress: (i) the unpenetrated area between coplanar or quasi-coplanar fractures (Fig. 5.7b), (ii) the rock bridge between offset, nearly parallel fractures (Fig. 5.7c), (3) the intact region between the tip of a fracture and a close non-parallel fracture (Fig. 5.7d), and (4) the

matrix block between nearly parallel fractures (Fig. 5.7e). Corresponding locations of these subareas are sequentially marked in Fig. 5.7a.

The sensitivity of differential stress distribution to the change of far-field stress orientation is also dramatic. Based on the Mohr circle analysis (Fig. 5.8), an explanation is given for the variation of stress heterogeneity pattern in different stress angle scenarios. In the 0° and 90° cases, as can be derived from Fig. 5.8, high shear stress occurs in fractures of Set 2, with a moderate normal stress across them, which leads to several high local differential stress scenarios such as the Type I concentration circumstance related to Set 2 (Fig. 5.7b). In the 30° and 120° cases, Set 1 affords higher shear stress and the bands of high differential stress are observed to be distributed more as if related to fractures in this set (Fig. 5.7c&e). In the 60° and 150° cases, both sets get relatively high shear stress between fracture walls and high differential stresses locate in places related to both sets (Fig. 5.7d).
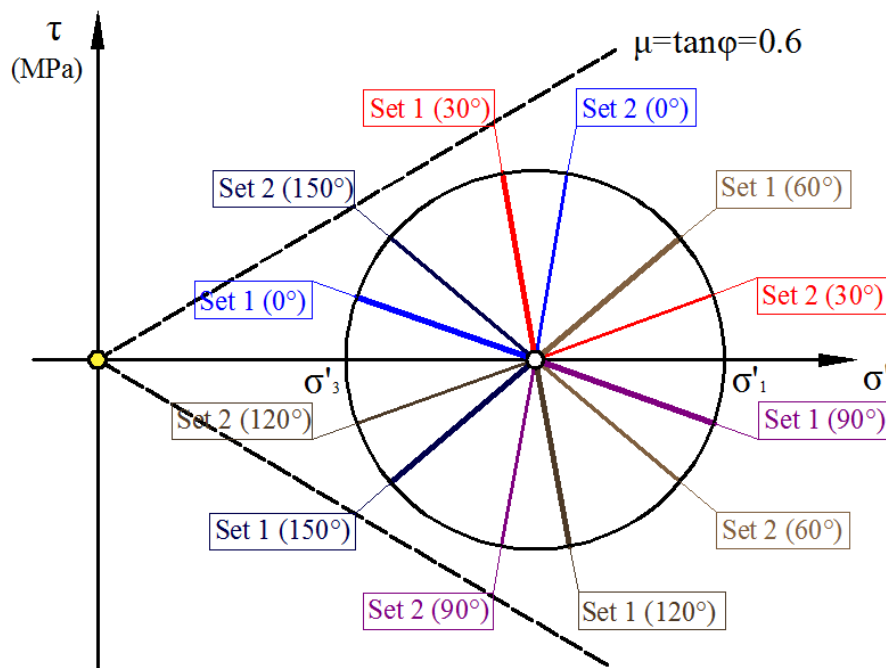
Fig. 5.8 Mohr circle analysis.

In general, the AFN and DFN models show approximately equal area for high maximum principal stress and differential stress. In some cases, two models even present significantly similar patterns (e.g. the 30° case), whereas they look quite different in some other cases (e.g. the 90° case). This phenomenon might be caused by the shortcoming of the point-based spatial

representation of fractures in the stochastic DFN modelling, which can hardly reflect the complex relationships between natural fractures (e.g. the spacing between fractures in the same set). In the AFN, fractures in Set 2 have nearly uniform spacing while fractures in Set 1 exhibit local clustering. Although a non-homogeneous density cell map is used, it is still difficult to accurately capture these specific features in the random process. The unrealistic spacing distribution in the DFNs may contribute to the difference in stress distribution with the AFN. Furthermore, the Poisson DFN model is difficult to accommodate the Type I circumstance for differential stress concentration. In short, the DFN geometries which lack self-organised spatial relations of geologically formed natural fractures may lead to certain biases when being used to study the stress heterogeneity in fractured rocks.

5.4.2 Shear displacement
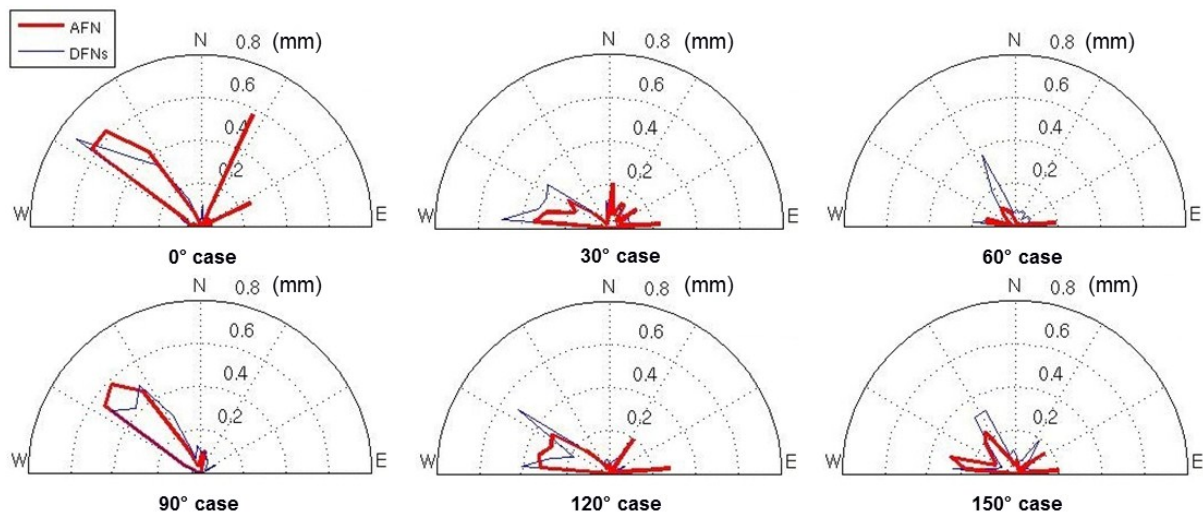
Fig. 5.9 Rose diagrams of length-weighted shear displacement of the AFN and DFNs (mean value of the ten DFN realisations).

The applied deviatoric in-situ stress field, although below critical levels in general, is sufficient to locally trigger sliding of fracture walls in the fracture network. Rose diagrams of length-weighted shear displacement in the AFN and DFNs (mean value of the ten realisations) reveal great similarity, especially with respect to the orientation of maximum values (Fig. 5.9). Analysis based on the Mohr circle (Fig. 5.8) provides some interpretations to the rose diagrams. For the 0° and 90° cases, Set 1 is suppressed in shear while Set 2 is quite active. For the 30° and 120° cases, Set 1 is highly active in shear while Set 2 stays quite suppressed. For the 60° case,

both sets are quite suppressed at unfavourable orientation for shear. However, for the 150° case, both sets are prone to ease of sliding, although with medium magnitude since the shear stress is not very high. High shear displacement often happens in pre-existing fractures with favourable orientations, but also it accompanies newly propagated cracks which usually grow obliquely from the tips of pre-existing ones. Shear displacement develops with large magnitudes along large fractures or around isolated matrix blocks. The rose diagrams indicate that DFN fractures seem to be slightly more active in sliding, which might be attributed to the straight line simplification in DFN models.

5.4.3 Hydraulic aperture
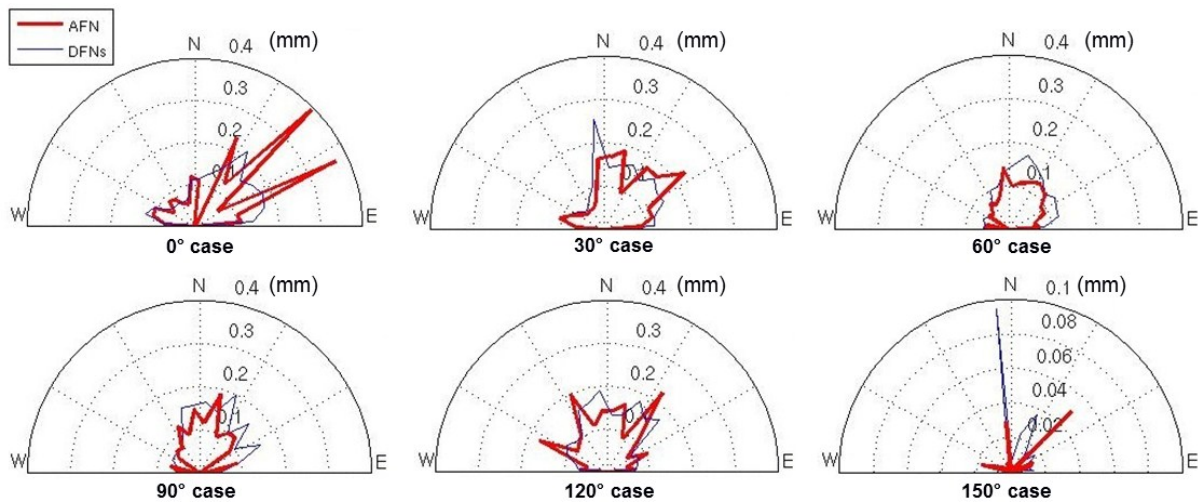
Fig. 5.10 Rose diagram of length-weighted hydraulic aperture of the AFN and DFNs (mean value of the ten DFN realisations).

Rose diagrams of hydraulic aperture shows that the highest value is likely to occur in the direction of wing cracks (Fig. 5.10). Pre-existing fractures under lower compressive normal stress also shows higher hydraulic aperture. For example, in the 30° case, fractures in Set 1 are less compressed and higher hydraulic aperture is observed. It can be noted that the AFN and DFNs show certain similarity in the rose pattern under different boundary conditions.

5.4.4 Fracture propagation

Fracture propagation is simulated as the explicit separation between the edges of adjacent unstructured finite elements [Munjiza, 2004]. Sliding of pre-existing fracture walls can engender stress concentration near the fracture tips and induce the formation of wing cracks or secondary

cracks [Willemse and Pollard, 1998]. The initiation of new cracks is greatly correlated to the shearing of pre-existing fractures, which has been observed in the numerical simulation. For the 0° and 90° cases, most new cracks accompany activation of Set 2, which is favourably oriented for shearing (Fig. 5.11a&d). For the 30° and 120° cases, new fracturing happens mainly at the tips of fractures in Set 1, which has favourable orientation for sliding (Fig. 5.11b&e). For the 60° and 150° cases, both sets are almost equally suppressed or activated, which leads to similar opportunities for the two sets to develop breakage (Fig. 5.11c&f). It is noticed that the orientation of wing cracks varies with the orientation of far-field stresses and seems to follow the direction of the maximum principal stress.

| (a) 0° | (b) 30° | (c) 60° | (d) 90° | (e) 120° | (f) 150° |
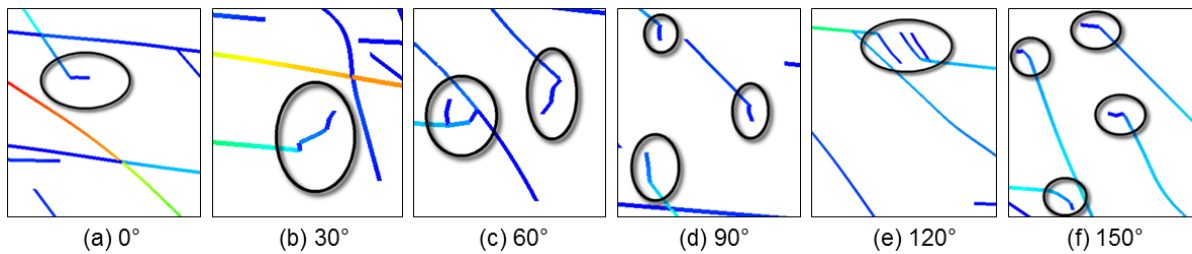
Fig. 5.11 Wing crack propagation at the fracture tips of the AFN model in different stress angle cases.

5.4.5 Connectivity state

The connectivity nature of a fracture pattern can be characterised by the properties of clusters, in which member fractures intersect to form connected sub-networks. Fracture propagation may connect pre-existing fractures in different clusters and result in larger occupations. Quantitative assessment of the connectivity state of fracture patterns involves the distribution analysis of cluster mass, which is defined as the total length of all member fractures in a cluster [Odling, 1992]. The AFN and DFNs show certain similarity in their cluster frequency and proportion distributions. In both models, most clusters occupy smaller sizes (<0.32m) and only a few clusters develop with larger sizes (>10m) (Fig. 5.12a), whereas the largest clusters constitute a greater mass proportion in fracture patterns as illustrated in Fig. 5.12b. The DFNs appear to have more small-sized clusters (0.01-0.03m) and the AFN pattern has more medium-sized ones (0.03m-0.32m), which leads to greater sharpness in the AFN's cluster mass frequency distribution (Fig. 5.12a). Interestingly, these differences in connectivity between the two models remain, even though they are initially prescribed with statistically equal numbers of

fracture intersection nodes. However, the magnitude of the difference between deterministic and stochastic networks is not as significant as for the results shown in the research by Odling [1992], which might be attributed to the tuning process.
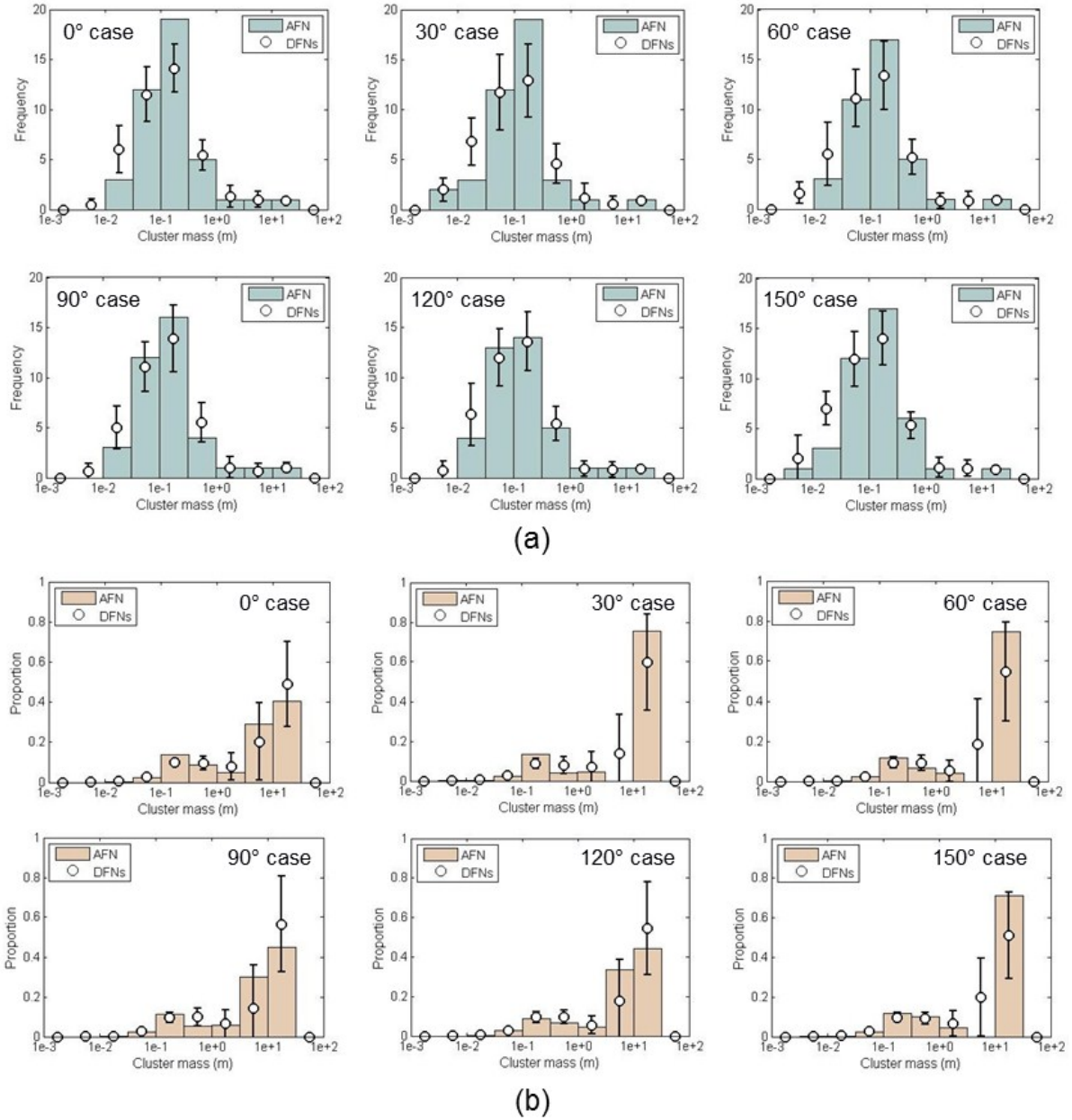
Fig. 5.12 (a) Cluster mass frequency distribution and (b) cluster mass proportion distribution of the AFN and DFNs in different cases.

5.4.6 Average geomechanical response

Four indicators are used to measure the average geomechanical response of the rock models under various boundary conditions. First, as shown in Fig. 5.13a, the AFN and DFNs exhibit

certain similarity in the sensitivity of shear behaviour to the orientation change of applied far-field stresses. For example, the lowest value occurs in the 60° case, in which both fracture sets are suppressed for shearing. However, DFNs seem to accommodate higher average shear displacement than the AFN. This might be attributed to the straight line assumption in DFN models, so that the artificial fractures tend to slide more easily than natural fractures with extra resistance from curvature.
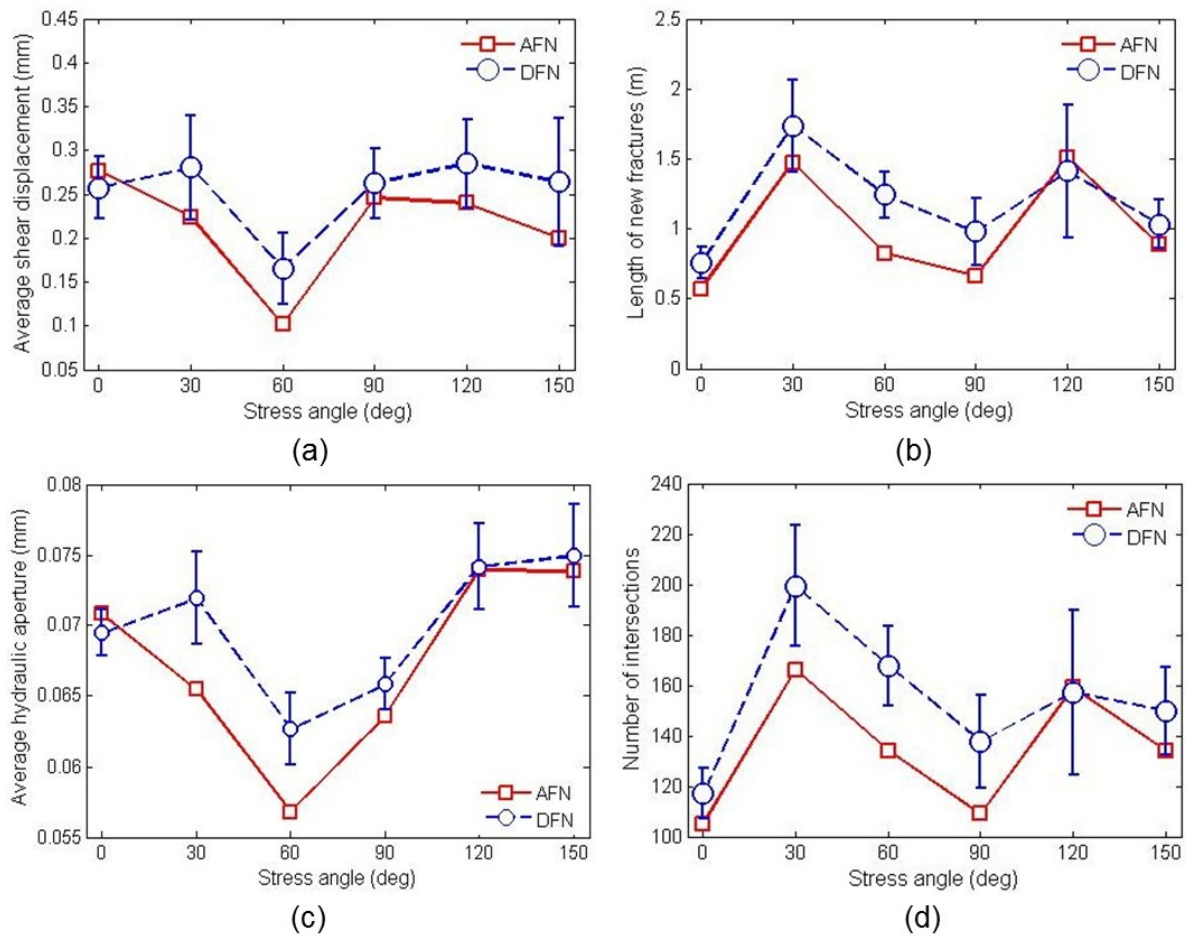
Fig. 5.13 Variation of different indicators according to the change of boundary stress angle: (a) overall average shear displacement, (b) length of new fractures (c) overall average hydraulic aperture, and (d) number of "T" and "X" intersection nodes.

More fracture propagation is also observed in the DFN models (Fig. 5.13b). Unlike the AFN pattern which was formed in geological conditions with stress relief under certain failure mechanisms, artificially generated DFN fractures are considered likely to require more breakage to adapt to a given geomechanical environment. As mentioned before, new crack development is

related to the shearing of pre-existing fractures. Maximum length of new fractures occurs in the 30° and 120° cases, in which Set 1 is highly active for shearing (see the Mohr circle in Fig. 5.8). However, in the 0° and 90° cases, the active Set 2 doesn't lead to much fracture evolution.

Higher average hydraulic aperture occurs in the 120° and 150° cases (Fig. 5.13c) in which both sets are under relatively lower normal stress. On the contrary, the average hydraulic aperture in the 60° case is the lowest due to the highly confining experienced by both sets. Discrepancy of average hydraulic aperture between AFN and DFNs is significant in the 30° and 60° cases, in which Set 2 is highly compressed. This might be caused by the fact that the geometrical features of Set 2, such as curvature, spacing and coplanarity, are not precisely characterised in the DFN models. Hence, fractures of Set 2 in the AFN and DFN models exhibit different normal closure and shear dilation behaviours.

The number of intersection nodes (both "T" and "X" types) (Fig. 5.13d) shows similar variation with the length of new fractures (Fig. 5.13b). This indicator is likely to be controlled by the degree of new crack growth and the orientation preference for propagation. The DFNs tend to have more intersection nodes than the AFN because of more crack growth in DFNs, although they are constrained with a statistically equal number of intersections before stress loading.

5.4.7 Inherent permeability

Before investigating the stress effects on the permeability of the fracture networks, it is important to calculate the inherent permeability of the undeformed AFN and DFNs, which is determined by the fracture network geometry [Zhang and Sanderson, 1996]. Single-phase steady state flow simulation is conducted on all eleven fracture networks where a uniform aperture distribution (0.05 mm) and matrix permeability ranging from 0.1 to 10 mD has been assumed. As shown in Fig. 5.14, a good match on macroscopic permeability between the unstressed AFN and DFNs is noticed, unlike the permeability results observed by Belayneh et al. [2009] showing differences of several orders of magnitude. This might be due to the tuning by using the conductivity parameter η in the DFN generation. However, it is worth drawing attention to the small discrepancy that still exists. This is because the anisotropic effect of dominant fracture orientations was not included in the formulation of the η parameter. The derivation of the parameter η as an indicator of connectivity is based on the assumption of nominally isotropic

DFN networks with a uniform coverage for fracture orientations, i.e. the effect of fracture sets was not considered. Thus, the significant anisotropy of the AFN pattern is not well represented by the DFN realisations: DFNs show lower permeability in the x-direction while higher permeability in the y-direction. Another possible reason is the planarity assumption (straight line in 2D) in DFN modelling. Straight fractures of Set 1 in the DFNs have larger extensions than the curved fractures in the AFN, although they are conditioned with the same length distribution. This makes DFN fractures of Set 1 easier to connect with other fractures and induce higher permeability in the y-direction, whereas the permeability in the x-direction is accordingly weakened. Furthermore, the discrepancy may also be caused by the biased representation of spatial organisation and the uncorrelated relations between different geometrical properties (i.e. density, length, location and orientation) in the DFN models.
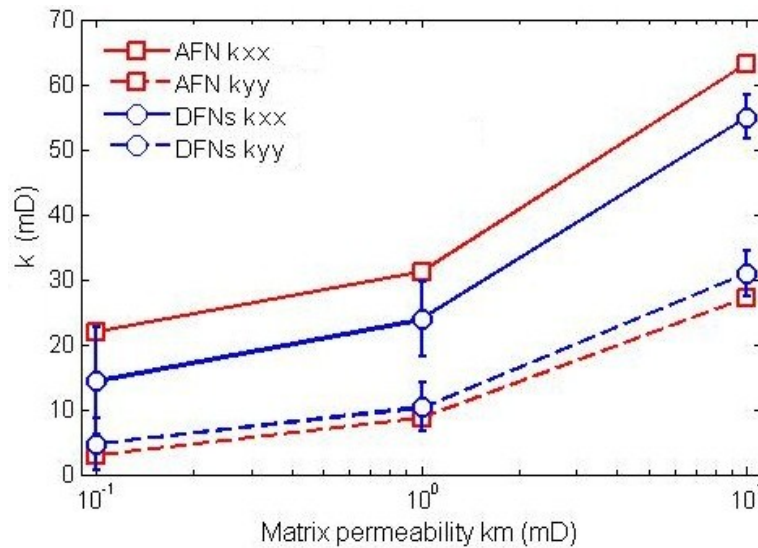
Fig. 5.14 Inherent permeability of the AFN and DFNs assigned with a constant aperture (0.05 mm).

5.4.8 Stress-dependent permeability

The equivalent permeability of the fractured rocks is calculated based on a series of steady state flow computation, in which matrix permeability k_m is assumed to be 0.1, 1 and 10 mD, respectively (Fig. 5.15). It can be noted that the equivalent permeability is much larger than the matrix permeability, implying that fractures play a significant role for fluid flow across the fractured rock models with the assumed matrix permeability.
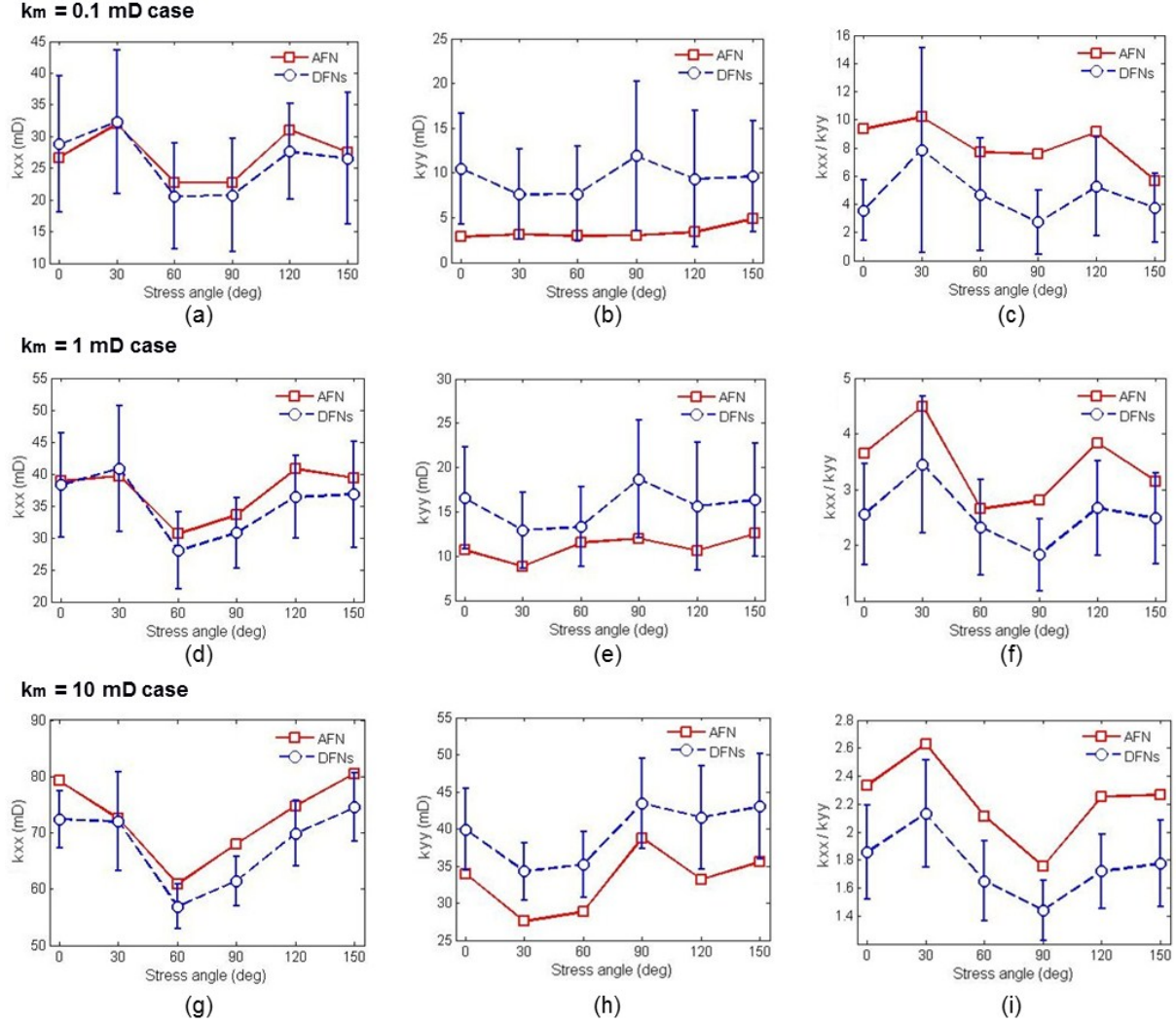
Fig. 5.15 Equivalent permeability (a) in the x direction k_{xx}, (b) in the y direction k_{yy} and (c) the permeability anisotropy ratio k_{xx}/k_{yy} of the AFN and DFNs with the matrix permeability $k_m = 0.1$ mD in various stress angle cases. Variation of (d) k_{xx}, (e) k_{yy} and (f) k_{xx}/k_{yy} for $k_m = 1$mD. Variation of (g) k_{xx}, (h) k_{yy} and (i) k_{xx}/k_{yy} for $k_m = 10$ mD.

The 0°, 30° and 150° cases show higher permeability in the x-direction because of the smaller normal compression in Set 1 (Fig. 5.8), which serves as the main fluid pathways in the x-direction. Fracture propagation sub-parallel to the x-direction may also contribute to the higher permeability. The 120° case also shows relatively high permeability in the x-direction, which can be attributed to the high hydraulic aperture (see Fig. 5.13c) and more fracture propagation (see Fig. 5.13b) in this scenario. The 90° case exhibits the highest permeability in the y-direction as the result of relatively smaller normal compressive stress in Set 2 (see Fig. 5.8) and the favourable propagating orientation (see Fig. 5.11d). In keeping with expectation from simple

mechanical considerations, it is inferred that models are more permeable along the direction of the maximum principal far-field stress, while suppressed for fluid flow in the direction of the minimum principal far-field stress. The AFN and DFNs show quite similar permeability in the x-direction, whereas the DFNs are more permeable than the AFN in the y-direction.

The high variability in the DFN results (error bar of $\pm$ ~30-50%) implies that significant uncertainty may exist in the Poissonian DFN method. This is of course not new and the need for multiple realisations in DFN modelling is widely recognised. It is of interest to further analyse the sensitivity of the equivalent permeability of stressed rocks to the matrix permeability. In the $k_m = 0.1$ mD case, larger error bars are involved since the uncertainty effect of stochastic models is amplified when flow is more dominated by fractures. As k_m increases, the inconsistency between the AFN and DFNs seems to become slightly larger in the x-direction since more fractures participate in transporting fluids with more matrix-fracture transfer, and the bias caused by DFN geometries becomes more significant.

5.5 Discussion

Table 5.2 presents the values of some important geomechanical and hydraulic properties of the AFN and ten DFNs. The results of each network model (AFN or DFN) under different stress orientations are averaged, while the mean values and standard deviations for multiple DFN realisations are further calculated. The ratio between a DFN and the AFN is calculated individually for each stress orientation scenario and further averaged for each DFN realisation. Mean values as well as corresponding spread for multiple DFN realisations are finally obtained, as shown by the last column of Table 5.2. Under in-situ stresses, which are often ignored in conventional reservoir simulations based on data of fracture traces on outcrops, the two types of fracture networks (i.e. AFN and DFN) present certain differences in geomechanical response. The artificially generated straight lines seem to require greater opening, sliding and new fracture propagation to adapt to a geomechanical environment. Stress concentration can be quite different in local areas because of the fracture-dependent heterogeneity effect, which results in distinct fracture propagation and coalescence patterns in the DFNs. This can generate considerable uncertainty in the connectivity properties of DFNs. The effects of geomechanical changes, e.g. stress heterogeneity, opening and sliding of fracture walls, distribution of connected clusters as

well as propagation of new cracks, could potentially lead to a significant impact on the overall hydraulic properties of the DFNs. The mean permeability of multiple DFNs shows a reasonably good match with that of the AFN in the x-direction while a notable discrepancy can be observed in the y-direction. This implies that in the relatively easy percolating direction, after adjustment to the geomechanical stress environment, these artificially created DFN models have, in a sense, converged to the geologically evolved fracture system. However, the DFNs lead to a significant bias in the y-direction, the direction observed to be near to the critical percolating state, due to the connectivity change induced by more fracture propagation and new intersections. Thus, the DFN might be susceptible to exaggerating the ease of flow when fracture networks are just below the percolating threshold.

Table 5.2 Values of key geomechanical and hydraulic properties of the AFN and ten DFNs.

		AFN	DFN	DFN/AFN
Shear displacement		0.215 mm	0.252 ± 0.019 mm	1.229 ± 0.108
Length of new fractures		0.988 m	1.192 ± 0.121 m	1.262 ± 0.111
Number of intersection nodes		134	155 ± 12	1.156 ± 0.083
Hydraulic aperture		0.067 mm	0.070 ± 0.001 mm	1.040 ± 0.016
k_{xx}	$k_{\mathrm{m}} = 0.1$ mD	27.100 mD	26.090 ± 8.192 mD	0.960 ± 0.292
	$k_{\mathrm{m}} = 1$ mD	37.137 mD	35.172 ± 6.691 mD	0.945 ± 0.170
	$k_{\mathrm{m}} = 10$ mD	72.624 mD	67.844 ± 5.242 mD	0.9344 ± 0.068
k_{yy}	$k_{\mathrm{m}} = 0.1$ mD	3.366 mD	9.415 ± 6.083 mD	2.892 ± 1.764
	$k_{\mathrm{m}} = 1$ mD	11.026 mD	15.573 ± 5.710 mD	1.417 ± 0.492
	$k_{\mathrm{m}} = 10$ mD	32.975 mD	39.558 ± 5.695 mD	1.204 ± 0.162
k_{xx}/k_{yy}	$k_{\mathrm{m}} = 0.1$ mD	8.266	4.636 ± 3.220	0.560 ± 0.366
	$k_{\mathrm{m}} = 1$ mD	3.429	2.550 ± 0.870	0.746 ± 0.243
	$k_{\mathrm{m}} = 10$ mD	2.224	1.761 ± 0.306	0.792 ± 0.130

When using random DFNs to estimate the permeability of a fractured rock, apertures are often assigned based on certain statistical distributions, e.g. uniform, lognormal or power law distribution [de Dreuzy et al., 2001a, 2001b, 2002; Min and Jing, 2003; Baghbanan and Jing, 2007; Leung and Zimmerman, 2012]. It is often assumed that fractures with longer extensions

accommodate larger apertures [Pollard and Segall, 1987; Vermilye and Scholz, 1995; Olson, 2003]. However, geomechanical effects may induce a significantly different aperture distribution in which a long fracture with unfavourable orientation may exhibit quite a small aperture caused by high normal compression [Zhang and Sanderson, 1996; Min et al., 2004b; Latham et al., 2013]. To further demonstrate the effects of geomechanically-induced aperture variability, the undeformed DFN networks are assigned with different statistical aperture distributions (i.e. uniform, lognormal and power law distributions), while the substituted distribution parameters are deduced from the hydraulic aperture data of the stressed AFN model. Furthermore, for models with a lognormal or power law aperture distribution, fracture apertures and lengths are positively correlated, i.e. longer fractures are paired with larger apertures. Table 5.3 summarises the permeability results of the stressed AFN, stressed DFNs and the non-geomechanical DFNs with statistically distributed apertures. By comparing with the stressed AFN model which is considered to be a real world system by virtue of its accurate topology characterisation and realistic aperture distribution [Latham et al., 2013], it is clear that the DFN models attributed with equivalent constant apertures (uniform distribution) show much higher permeability in both x and y directions, and tend to exaggerate the conductivity of the fracture system. The DFNs with a lognormal or power law aperture distribution show lower permeability in both directions, which might be due to the inaccurate fitting by these statistical distributions. Another reason for their lower permeability might be due to no consideration of fracture propagation in the non-geomechanical DFNs. The stressed DFNs seem to give a closer estimation to the real world on account of geomechanical modelling, which also provides a stress-dependent aperture distribution for further calculation of the permeability of fractured rocks [Min et al., 2004b]. Hence, if geomechanical effects are ignored and aperture distribution is assumed unrealistically, the flow simulation based on DFN realisations may produce misleading results.

The validity of DFN models have been examined based on a specific fracture pattern with an intermediate fracture density quite close to the geometrical percolation threshold. However, to achieve a more general conclusion, further investigation is required based on a more saturated or sparser pattern of fractures. A spectrum illustrating the correlation between fracture density and how close DFNs are to an AFN is expected to be valuable. Another limitation of this research is

that only one in-situ stress ratio ($\sigma'_1/\sigma'_3 = 2$) was considered for a fractured rock stressed to a level below its critical state at a depth <1 km. Higher stress ratios (e.g. ≥3) are expected to trigger more significant shear dilatancy and flow localisation [Sanderson and Zhang, 1999; Min et al., 2004b; Baghbanan and Jing, 2008] as well as increase connectivity caused by crack propagation [Latham et al., 2013].

Table 5.3 Comparison of the permeability results of the stressed AFN, stressed DFNs and non-geomechanical DFNs with statistically distributed apertures ($k_m = 1$ mD).

	Stressed AFN	Stressed DFNs	DFNs with statistical aperture distribution		
			Uniform	Lognormal	Power law
k_{xx} (mD)	37.137	35.172 ± 6.691	47.123 ± 19.487	18.727 ± 5.028	19.509 ± 4.763
k_{yy} (mD)	11.026	15.573 ± 5.710	18.135 ± 9.758	8.120 ± 2.563	8.640 ± 2.754

5.6 Concluding remarks

To conclude, this research used an outcrop analogue to evaluate the uncertainties of DFN representations for hydromechanical modelling of naturally fractured rocks. Ten discrete fracture networks were created randomly based on the statistics from the analogue pattern. Several additional constraints were included during DFN generation to enhance the equivalence of DFNs to the original pattern. By applying in-situ stresses at different angles to the fractured rocks, their geomechanical response was modelled using the FEMDEM method. Important disparities were noticed on several geomechanical aspects, including stress heterogeneity, fracture wall shearing, aperture development, crack propagation and network connectivity. The hydraulic comparison was made by conducting steady state flow simulation based on the fracture networks with stress-induced variable apertures. For this specific fracture network, the deformed DFNs were found to take on the hydraulic permeability of the deformed AFN but only in the direction with an initially good connectivity state. A significant discrepancy was observed for flow in the direction associated with a poor percolation state. Further investigation showed that a fracture network with statistically distributed apertures may have great biases for calculating the permeability of a fractured rock. The main factors determining the quality of DFNs for hydromechanical modelling of a natural fracture system are considered to be its accuracy in describing the geologically formed topology and geomechanically induced apertures.

6 Upscaling of 2D fracture network models

6.1 Introduction

Geomechanical modelling of the development of fracture patterns and apertures achieved on a scale spanning the laboratory specimen to perhaps a few meters is becoming relatively accurate with the latest mechanical models such as those based on the combined finite-discrete element method (FEMDEM) [Munjiza, 2004; Munjiza et al., 2011; Latham et al., 2013; Mahabadi et al., 2014b; Lei et al., 2014]. Many important geological phenomena can be modelled in FEMDEM numerical experiments, such as reactivation of shear on pre-existing fracture walls, propagation of new cracks and variation of aperture distribution. Due to the limits of processing power, it is currently impossible to extend this accuracy to macroscale simulation. Hence, upscaling is required to understand and evaluate important subsurface properties of large-scale naturally fractured rocks based on models established at a smaller scale.

Disordered geological media often exhibit significant scale invariance and self-similarity [Barton, 1995; Odling, 1997; Berkowitz et al., 1999; Bour et al., 2002; Lei and Wang, 2016]. Nontrivial power law scaling, including fractal properties, was observed in natural fracture systems [Bonnet et al., 2001], which often does not have a representative elementary volume (REV). An important feature of the fractal geometry and power law methods is the absence of the need for a characteristic length scale [Bonnet et al., 2001]. An understanding of the scaling behaviour of natural fracture systems opens the possibility that hydromechanical properties of a macroscale fractured rock may be estimated based on the characterisation of its crucial features from a relatively smaller sampled model [Zimmerman and Main, 2004].

Scaling of rock permeability has been extensively studied based on compilation of in-situ measurement data [Brace, 1980, 1984; Clauser, 1992; Neuman, 1994; Renshaw, 1998]. Three measurement scales of permeability were distinguished: the laboratory scale (1-10 cm), the borehole or in-situ scale (1 m-1 km), and the regional scale (1-100 km) (Fig. 6.1) [Clauser, 1992]. Increase of permeability from the laboratory to the borehole scale was observed, since laboratory tests are usually based on unfractured core specimens [Brace, 1980, 1984]. However, from the borehole to the regional scale, although an increasing permeability trend was reported [Brace,

1980, 1984; Neuman, 1994], so too was a plateau with no increase or a decrease [Clauser, 1992; Renshaw, 1998] (Fig. 6.1). Rather than focusing on the broad spectrum of scales where the transition behaviour depends on many complex factors (e.g. seismically visible faults, multiple rock types and even karst features), the scope of this study is chosen to be on the in-situ scale (say, 1-100 m), where flow is often dominated by fractures [Clauser, 1992], and focus on the mechanisms by which permeability of fractured rock may vary with the modelling scale over this range.
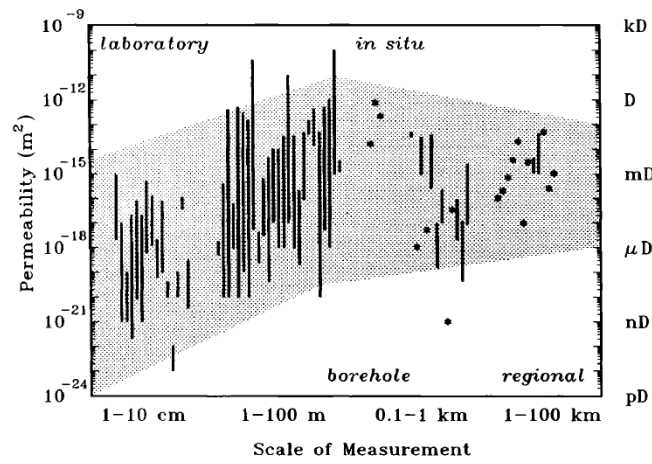
Fig. 6.1 Permeability of crystalline rocks and characteristic scale of measurements [Clauster, 1992].

Much work using discrete fracture networks (DFNs) has focused on flow in random fractal patterns where, by neglecting geomechanical constraints, fluid transport has been modelled in networks with apertures assumed either constant [Leung and Zimmerman, 2012; de Dreuzy et al., 2001a], or statistically distributed and correlated with trace lengths [de Dreuzy et al., 2001b, 2002; Klimczak et al., 2010]. The scaling of network connectivity is dominated by the relationship between the fractal dimension and the power law length exponent [Berkowitz et al., 2000; de Dreuzy et al., 2001a; Darcel et al., 2003a], whereas the scaling of permeability is further governed by the transmissivity distribution of individual fractures [de Dreuzy et al., 2001b, 2002; Davy et al., 2006; Klimczak et al., 2010]. However, since geomechanically-constrained apertures vary intimately with a locally varying stress field, it is an open question whether the appearance of scale invariants of network topology has useful implications for predicting equivalent flow properties over the ~100 m block and larger, e.g. 1 km, scales.

The objective of this study is to develop a 2D fracture network upscaling method to estimate hydromechanical properties of larger-scale natural fracture systems that can be based on a small sized model. There are two distinct developments needed: (i) to construct the network topology on large domains conditioned by the data from smaller outcrops obeying a self-referencing scheme, and (ii) to apply geomechanical constraints to derive realistic apertures for each fracture at the outcrop scale and to propose a mechanism to preserve such aperture realism in larger scales.

6.2 Scaling properties of a natural fracture system

The outcrop of a natural fracture system was mapped at Kilve on the southern margin of the Bristol Channel Basin covering approximately 225 m^2 (Fig. 6.2a) [Belayneh et al., 2009]. Tectonic displacement along normal faults underlying the rift system induced porosity reduction and excess fluid pressure [Belayneh et al., 2009]. During such tectonic evolution process, two oblique sets of vertical, layer-normal fractures were formed extensionally and filled with calcite minerals, striking approximately 100° (Set 1) and 140° (Set 2), respectively (note that the vein thickness will not be used for this study when deriving fracture apertures for flow prediction). The fractured limestone layer (~26 cm thick) is sandwiched between almost impervious shales and the joint sets are layer bound [Belayneh et al., 2009]. An important feature of this outcrop system is that the fracture sets are very distinct and cross-cut with few abutting relationships. 2D analysis is used here, while some potential 3D effects will be discussed in section 6.6.

The outcrop map represents a limited range of trace data of the actual fracture system controlled by the image resolution (~0.05 m) and the mapped domain size (~12 m). To eliminate the effect of irregular boundaries of the whole outcrop pattern (with unmapped areas inside the domain), a squared subarea of size $L = 6$ m containing ~1,000 fractures is extracted (Fig. 6.2b) as a sample of the fracture system to measure its scaling properties. Since it is very expensive in CPU time to compute very large domains given the current processing power [Latham et al., 2013; Lei et al., 2014], a smaller domain of size $L = 2$ m is selected for geomechanical modelling (section 6.4) and also serves as the source for network upscaling (section 6.5). The larger area ($L = 6$ m) will be used for checking the upscaled fracture networks generated from the source pattern ($L = 2$ m) using the proposed new approach (section 6.3.5).
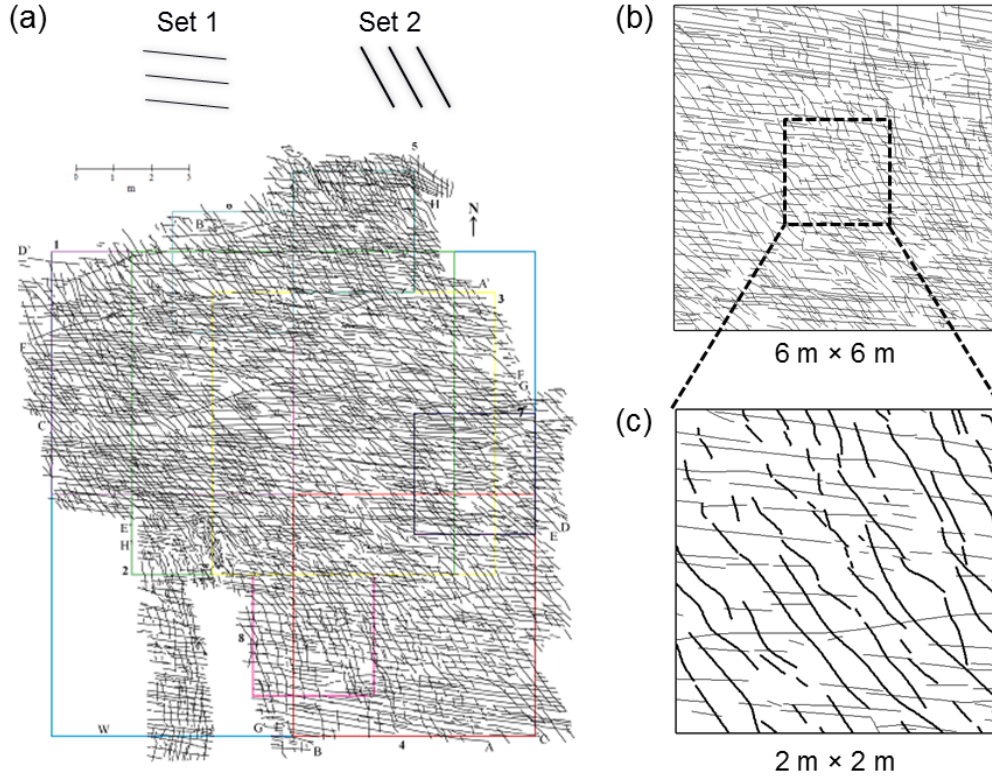
Fig. 6.2 (a) The outcrop pattern mapped at Kilve on the southern margin of the Bristol Channel Basin [Belayneh et al., 2009]. (b) Extracted 6 m × 6 m pattern for analysis of scaling properties. (c) Extracted 2 m × 2 m pattern for geomechanical modelling and as the source for network upscaling (light lines represent Set 1 and bold lines represent Set 2).

6.2.1 Spatial distribution

The fractal dimension D (or the correlation dimension D_c) describes the spatial distribution of fractures. The correlation dimension D_c can be calculated using a two-point correlation function [Bour and Davy, 1999] as defined by

$$C_2(r) = \frac{1}{N^2} N_d(r) \sim r^{D_c} \tag{6.1}$$

where N is the total number of fracture barycentres (i.e. midpoint of each fracture trace), and N_d is the number of pairs of barycentres whose separation is smaller than r. For a fractal population, $C_2(r)$ is expected to scale with r following a power law trend and its exponent gives the value of D_c. Fig. 6.3 illustrates the scaling of $C_2(r)$ with r for the selected 6 m × 6 m pattern, where a power law trend is manifest for over two decades on the bilogarithmic diagram. By employing least squares analysis, D_c is estimated to be 2.0. Due to the fact that $D_c \leq D \leq 2.0$ (i.e. Euclidean

dimension) [Bonnet et al., 2001], D is also equal to 2.0, implying that the network of fracture barycentres exhibits a homogeneous filling of the 2D space and is nonfractal.
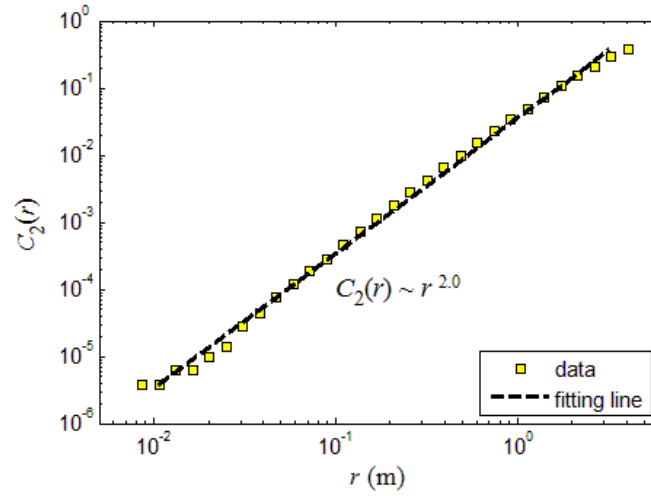
Fig. 6.3 Calculation of the two-point correlation function $C_2(r)$ as a function of r. The slope of the least squares fitting line for data points $(r, C_2(r))$ on the bilogarithmic diagram gives an estimate of the correlation dimension $D_c \approx 2.0$.

6.2.2 Length distribution

The density distribution of fracture lengths (i.e. trace lengths) can be described by the power law model [Bour et al., 2002; Davy et al., 2010] as given by

$$n(l,L) = \alpha L^D l^{-a} \qquad \text{for } l \in [l_{min}, l_{max}] \qquad (6.2)$$

where $n(l, L)dl$ gives the number of fractures with sizes l belonging to the interval $[l, l + \mathrm{d}l]$ ($\mathrm{d}l$ $<< l$) in an elementary volume of characteristic size L, a is the power law length exponent, D is the fractal dimension, and α is the density term. The equation is valid irrespective of D [Bour et al., 2002], even for the studied nonfractal pattern. The exponent a can be derived from either the cumulative distribution or density distribution of fracture lengths. However, a comparison between the two derivations of a is considered useful [Davy, 1993]. The observed data of fracture lengths is often biased due to the truncation (resolution limitation) and censoring effects (incomplete sampling) [Bonnet et al., 2001]. A lower cut-off of 0.3 m (i.e. 5% × L [Odling, 1997]) is used to eliminate the truncation effect. In the cumulative distribution analysis, the censoring effect is corrected using the Kaplan-Meier method [Odling, 1997]. By employing least squares fitting, the cumulative exponent c is estimated to be 1.45 and the length exponent is

therefore calculated as $a = c+1 = 2.45$ (Fig. 6.4a). The cumulative distribution may suffer from an additional intrinsic bias, i.e. the finite size effect [Pickering et al., 1995]. In the density distribution analysis, the censoring effect is corrected by removing fractures that intersect the sampling boundaries [Bour et al., 2002]. To account for the density perturbation from the artificial deletion, an effective system size is estimated as the square root of the coverage area of remaining fractures and used for the calculation of the density term α, given an assumption that the proportion of the coverage area to the squared space is equal to the ratio between the total length of remaining fractures and the total length of all sampled fractures. The length exponent a estimated from the density distribution has a slightly lower value of 2.37, and the density term α is calculated to be 3.28 (Fig. 6.4b). The density distribution was recommended more appropriate for characterising the length scaling behaviour [Davy, 1993; Bonnet et al., 2001] and is adopted for later analysis.
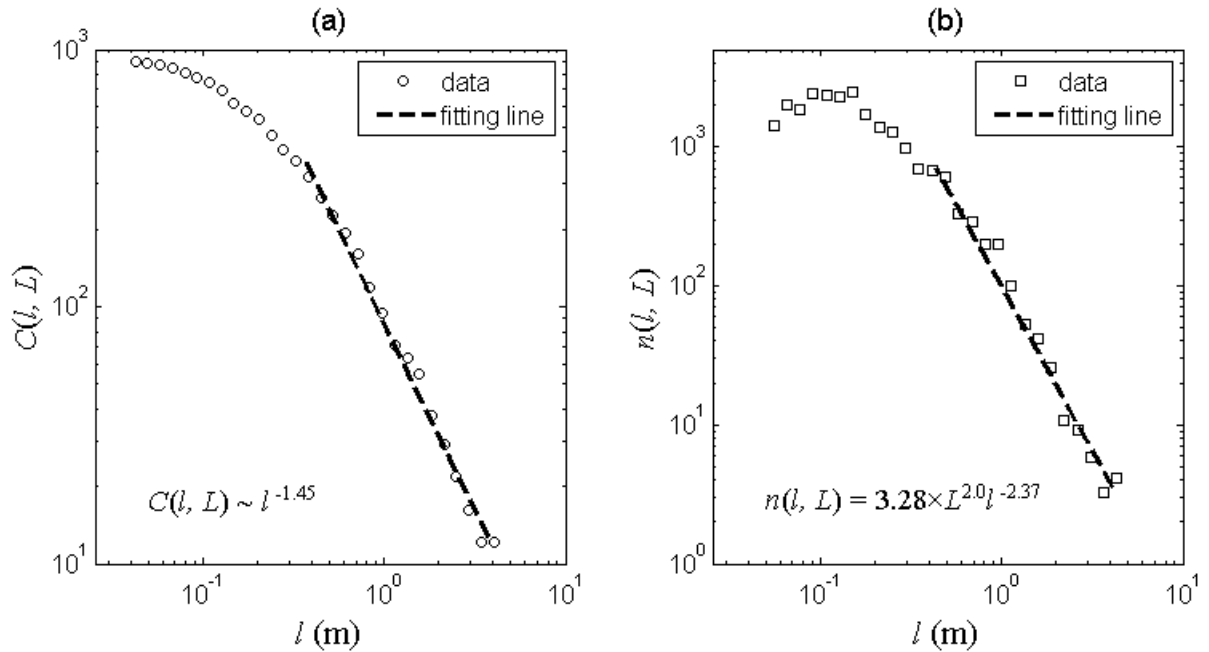
Fig. 6.4 (a) The cumulative distribution, and (b) density distribution of fracture lengths of the studied pattern having a size of $L = 6$ m. A lower cutoff of 0.3 m (i.e. 5% $\times$ L) is used to eliminate the truncation effect. By correcting the censoring effect using the Kaplan-Meier method [Odling, 1997], the cumulative distribution gives an estimate of the length exponent $a = 1.45+1 = 2.45$. After removing fractures that intersect sampling boundaries and correcting the system size, the density distribution gives the length exponent $a = 2.37$ and the density term $\alpha = 3.28$.

6.2.3 Density, intensity and connectivity

If a fracture system ideally obeys the power law length distribution, its fracture density γ (i.e. number of fractures per unit area) can be derived from the integral of the density function of fracture lengths [Darcel et al., 2003a], while the fracture intensity P_{21} (i.e. total length of fractures per unit area) can be derived based on the first moment of the density distribution of fracture lengths as [Darcel et al., 2003a]

$$P_{21} = \frac{1}{L^2} \int_{l_{\min}}^{l_{\max}} n(l, L) l \, dl = \frac{\alpha L^{D-2} (l_{\min}^{-a+2} - l_{\max}^{-a+2})}{a-2} \tag{6.3}$$

Due to the broad range of fracture lengths, the percolation behaviour of the fracture network is determined by two parts that describe the contribution from smaller and larger fractures [Bour and Davy, 1997] as given by

$$p(l, L) = \int_{l_{\min}}^{L} \frac{n(l, L) l^D}{L^D} \, dl + \int_{L}^{l_{\max}} n(l, L) \, dl \tag{6.4}$$

For the studied network with $a < D+1$, if $l_{\min}$ is sufficiently small, the first integral of Eq. (6.2) is controlled by the upper bound L [Berkowitz et al., 2000], which means the connectivity is only slightly dependent on $l_{\min}$. The critical system size L_c (or the connection length) corresponding to the percolation threshold can be further calculated as [Berkowitz et al., 2000]

$$L_c = \left[(D+1-a)(a-1) \frac{p_c}{D\alpha} + l_{\min}^{D+1-a} \frac{(a-1)}{D} \right]^{\frac{1}{D+1-a}} \tag{6.5}$$

for $a > 1$ and $a \neq D+1$. The percolation threshold p_c is a scale-independent parameter with a value ranging between 5.6 and 6.0 [Bour and Davy, 1997]. Here, L_c is calculated to be ~0.80 m and found marginally influenced by the given $l_{\min}$ (i.e. 0.05 m). Another feature of the scenario of $a < D+1$ is that, if the fracture density γ is fixed, the network connectivity will increase with scale, i.e. the fracture network is well-connected at larger scales ($L \gg L_c$) [Davy et al., 2006]. For measurements based on a finite-sized domain, $l_{\max}$ is likely to be controlled by the domain size L, and consequences of such an effect will be discussed in section 6.6.

6.2.4 Displacement and length correlation

Fractures often exhibit displacements perpendicular and/or parallel to the discontinuity surface. They are termed aperture and shear displacement, respectively, and referred as fracture

displacement attributes here.

The relation between shear displacements and fracture lengths has been extensively studied in the literature based on field measurement. By assuming a perfect positive correlation, a general form of shear displacement-length correlation law [Bonnet et al., 2001] is given by

$$\delta_{max} \sim l^{n_1} \tag{6.6}$$

where δ_{max} is the maximum shear displacement of an individual fracture, l is the fracture length, and n_1 is the correlation exponent. A simple linear relation is predicted by the linear elastic fracture mechanics (LEFM) theory [Pollard and Segall, 1987]. A plane strain model taking account of inelastic deformation of faults also suggests $n_1 = 1.0$ [Cowie and Scholz, 1992a]. A degree of consistency has been observed between the linear scaling predictions and field measurements [Cowie and Scholz, 1992a, 1992b; Dawers et al., 1993; Scholz et al., 1993; Kim and Sanderson, 2005; Schultz et al., 2008]. However, a range of values for n_1 have also been reported, such as 0.5 [Fossen and Hesthammer, 1997], 1.5 [Gillespie et al., 1992], and 2.0 [Walsh and Watterson, 1988]. Variation of n_1 is controlled by numerous factors including lithology, growth mechanism of faults as well as their interaction and reactivation [Bonnet et al., 2001; Kim and Sanderson, 2005].

The correlation between fracture apertures and trace lengths has also been widely investigated [Vermilye and Scholz, 1995; Walmann et al., 1996; Renshaw and Park, 1997; Olson, 2003; Schultz et al., 2008]. Supposing a power correlation is also valid [Bonnet et al., 2001], apertures can then be related to fracture lengths as

$$b_{max} \sim l^{n_2} \tag{6.7}$$

where b_{max} is the maximum aperture of an individual fracture, l is the fracture length, and n_2 is the correlation exponent. The exponent n_2 was proposed to range between 0.5 and 2.0 [Bonnet et al., 2001; Neuman, 2008]. A square root sublinear scaling law was derived by incorporating subcritical and critical fracture propagation criteria into LEFM analysis [Olson, 2003] and is given by

$$b_{max} = \frac{K_{Ic}(1-\upsilon^2)}{E\sqrt{\pi/8}} l^{0.5} \tag{6.8}$$

where K_{Ic} is the mode I fracture toughness, E is the Young's modulus, and υ is the Poisson's

ratio. For plane strain conditions, K_{Ic} is related to the energy release rate G by

$$G = K_{\text{Ic}}^2 \left(\frac{1-\upsilon^2}{E} \right) \tag{6.9}$$

By assuming fracture opening shape to be elliptical in nature, the average aperture b_{avg} can be related to b_{max} [Olson, 2003] as

$$b_{\text{avg}} = \frac{\pi}{4} b_{\text{max}} = \sqrt{\frac{\pi G(1-\upsilon^2)}{2E}} l^{0.5} \tag{6.10}$$

The square root model shows good agreement with field observations [Walmann et al., 1996; Olson, 2003; Schultz et al., 2008; Klimczak et al., 2010]. However, variation of n_2 still exists due to the interaction among fractures in the actual geological environment [Hatton et al., 1994; Vermilye and Scholz, 1995; Renshaw and Park, 1997].

In reality, the scaling exponents (i.e. n_1 and n_2) are not only determined by topological attributes, but also influenced by geomechanical constraints, e.g. the magnitude and orientation of in-situ stresses. In this research, the scaling exponents will be derived based on geomechanical modelling of a fractured rock under in-situ stress conditions. For simplicity, fractures are associated with no initial phase of shearing, whereas initial apertures are assigned a priori using Eq. (6.8) to model rupture-induced initial opening. A further application of assumed far-field stresses using the FEMDEM geomechanical model will illustrate the accommodation of closure, opening, shearing and dilatancy in the fracture system and introduce variability to the distribution of displacement attributes (section 6.4.1). The resulting stress-dependent distribution is to be preserved in a scaled and coupled way during the formation of growth networks (section 6.4.2 and 6.4.3).

6.3 Fracture network growth model

6.3.1 Growth lattice

By assuming the fracture system fills progressively larger and larger Euclidean space domains in a repeatable process, a novel scheme is developed to grow the geologically-obtained fracture pattern together with its spatially variable displacement attributes (i.e. fracture aperture and shear displacement) into larger scales using a growth lattice (Fig. 6.5b). There are two types of cells in a growth lattice: the source cell (SC) that is the reference for network growth, and the

growth cell (GC) that is a clone of the SC sharing common geostatistics. Here, the source cell corresponds to the 2 m × 2 m outcrop sample. Important characteristics of the source network will be retained during a growth process: (i) at the population level, fracture density and spatial distribution are matched by GCs to the SC; (ii) at the individual fracture level, various properties including orientation, length, segmentation, curvature, and displacements are preserved. The fractures are classified into censored (partially sampled) and uncensored (completely observed) types (Fig. 6.5a), each of which requires distinct means for extrapolation. Boundary constraints are applied along the cell periphery to guarantee topological connectivity. The growth procedure is implemented separately for each set due to the intrinsic difference in their geostatistical properties.
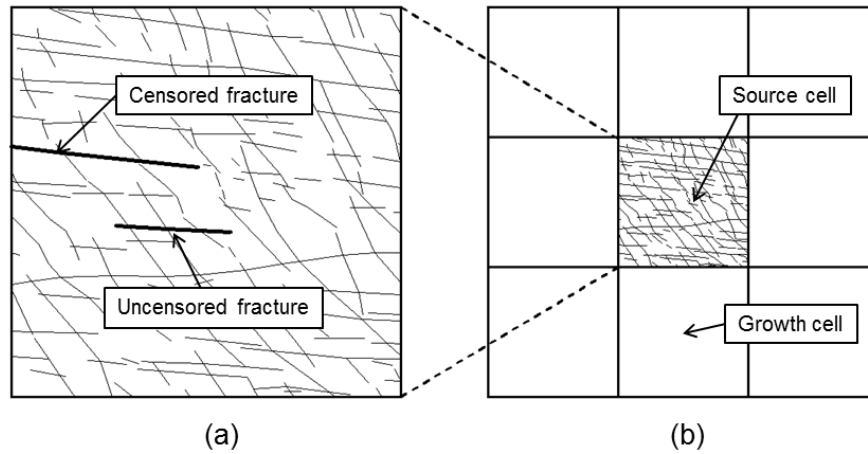
Fig. 6.5 (a) The source cell pattern involving censored and uncensored fractures, and (b) a growth lattice consisting of one source cell and eight growth cells.

6.3.2 Source cell geostatistics

Methods of statistics are applied to the source pattern to interpret its topological complexity in a quantitative way. Location of censored fractures is measured based on the distribution of censoring nodes, through which partially sampled fractures are truncated by the SC boundary. Spatial organisation of uncensored fractures is characterised by the distribution of their barycentres, based on a physically reasonable assumption that barycentre is likely to be the initial nucleus position for idealised symmetrical crack development [Bour et al., 2002]. Two exclusion parameters, i.e. exclusion radius and spacing, are computed for each barycentre based on its spatial relationship with other nuclei (Fig. 6.6). The exclusion radius of a barycentre is the

distance with the closest counterpart, while exclusion spacing is measured by projecting the point cloud to a line perpendicular to the mean orientation of the fracture set. The procedure allows the preservation of fracture barycentre spatial distribution. The SC spatial information is synthesised into a mathematical expression given by

$$X_i = \chi\left(\varepsilon_n, \varepsilon_r, \varepsilon_s\right)$$ (6.11)

where X_i corresponds to the location of the barycentre of the ith source fracture, ε_n, ε_r, ε_s denote the probability density functions (PDFs) for the distribution of spacing of censoring nodes, exclusion radius and spacing of barycentres, respectively, determined from a series of nonparametric Kolmogorov-Smirnov (K-S) hypothesis tests.
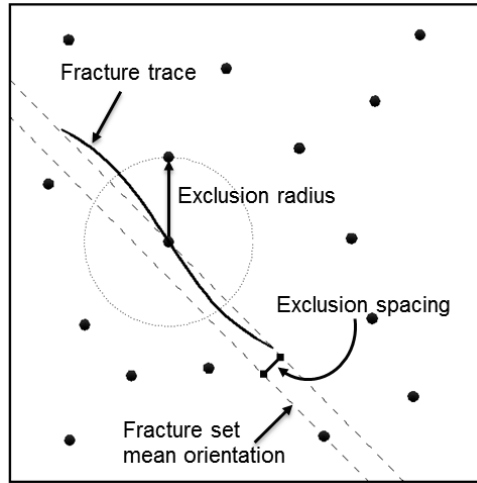
Fig. 6.6 Barycentre map for characterising fracture exclusion radius and spacing.

Characteristics of individual fractures are also statistically quantified for various key respects. The property, priority degree, is measured for each fracture based on the ratio of its length to the size of the SC domain. For example, a censored fracture with a ratio greater than 1.0 is potentially a traversing fracture in larger scales and is associated with a high priority. The number of segments of each source fracture is counted and will be used later to determine the duration of the discrete-time sequence for each random walker (section 6.3.3). Curvature of multi-segment fracture traces is governed by the inflection nature as well as orientation dispersion (Fig. 6.7). It is a property that can greatly influence the tortuosity of migration path for subsurface flow [Ronayne and Gorelick, 2006]. The number of inflection points, $\tilde{n}$, is counted for each naturally bent fracture by identifying the concavity sign transition based on the second

derivatives of the non-uniform rational basis spline (NURBS) in the 2D Cartesian coordinate system. Hypothesis tests are conducted to choose an optimal distribution (e.g. uniform, normal, lognormal, exponential, gamma) for segmental lengths, orientations, shear displacements and apertures with their truncated PDFs denoted as $g_i(l)$, $h_i(\theta)$, $u_i(\delta)$ and $v_i(b)$, respectively, for the ith source fracture. For development of $u_i(\delta)$ and $v_i(b)$, see section 6.4.1. The segmental statistical properties are measured independently for each source cell fracture to account for their length-dependency and inter-correlation. For example, a longer fracture is prone to be more bent (see Fig. 6.2c) and have greater trajectory variation, i.e. greater dispersion in segmental orientation, for the reason that it occupies larger space and the growth path can be more influenced by stress heterogeneity and other existing fractures. Furthermore, the aperture and shear displacement may be greatly affected by the degree of curvature.
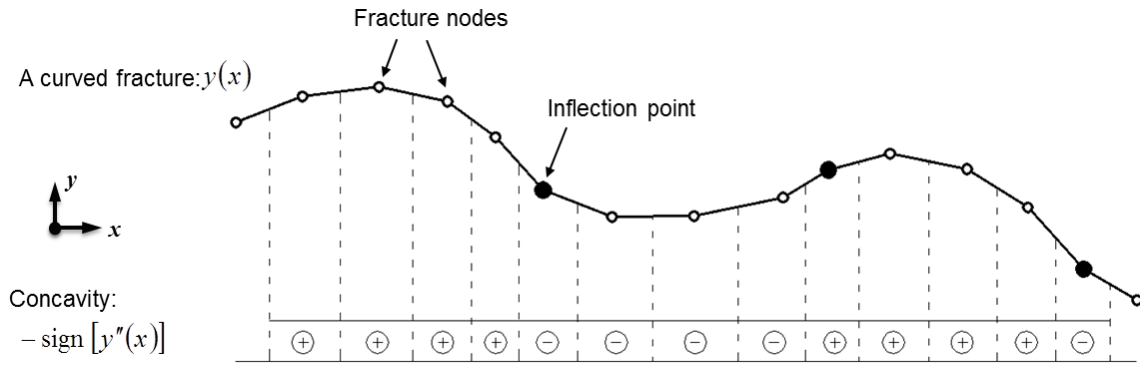
Fig. 6.7 Characterisation of the curvature of a multi-segment fracture NURBS based on the transition between concavity and convexity.

6.3.3 Growth of fractures

(a) Growth formulation

The nucleation process of fractures in GCs, according to the self-referencing scheme, is governed by the spatial information model of the source sample as

$$X_i^0 = \chi(\varepsilon_n, \varepsilon_r, \varepsilon_s) \qquad (6.12)$$

where X_i^0 is the position of a random nucleus for the ith growth fracture. Propagation of fractures from nuclei is simulated through discrete-time random walks in a polar coordinate system [Kaye, 1994], in which a fracture is traced by variable jumps from one position to another as time proceeds:

$$X_i^{t+1} = X_i^t + \Delta X_i^t \tag{6.13}$$

where $t \in \{0,1,2\dots,T_i\}$ is the discrete time in sequence, T_i corresponds to the prospective number of segments of the ith growth fracture, X_i^t is the position of the walker at the time t, and ΔX_i^t is the increment for the next step governed by a multivariate distribution given by

$$f_i\!\left(\Delta X_i^t\right) = g_i(l)\,h_i\!\left(\theta \mid \lambda^t \theta^t \geq \lambda^t \theta^{t-1}\right) \tag{6.14}$$

where l and θ are two independent random variables for segmental length and orientation, respectively, which are generated in a bootstrapping process based on the corresponding source fracture statistics, and λ^t is a sign variable indicating the current concavity state that switches from plus to minus or vice versa if the walker passes an inflection point that is associated to the discrete time sequence through a Bernoulli process with a success probability of $\tilde{n}/(T+1)$. Amplitude of a curved trace is modelled by a conditional distribution, i.e. the second part of the right hand side of Eq. (6.14), so that the orientation variable monotonically increases or decreases in each period between inflection nodes, with the degree of curvature controlled by the standard deviation. Fracture displacement variables, i.e. δ and b, are stochastically generated using the probability functions $u_i(\delta)$ and $v_i(b)$, and automatically assigned to each segment as walkers parade.

In the numerical implementation, growth of censored and uncensored fractures in GCs is achieved in different ways due to their distinct sampling features. Nuclei of censored fractures are seeded along lattice edges, while barycentrer of uncensored fractures are spawned inside cell domains. In each growth region, censored fractures are grown ahead of uncensored ones and will place constraints for barycentre nucleation. Geological arrest model is not included in this growth scheme on account of the cross-cutting feature of the source pattern, which means that each random walk is an independent process.

(b) Growth of censored fractures

Following the self-referencing scheme, GCs are prescribed to share a similar window censoring condition to the SC due to the same occupation area in the 2D Euclidean space. Censoring nodes are randomly seeded along lattice edges, except those belonging to the central SC (Fig. 6.8a). Adjacent cells are constrained to have the same nodes along their identical edge to guarantee the connectivity between them, while their nonoverlapped edges are equipped with

statistically mirrored settings. A censored growth fracture in GCs evolves from a nucleus located on the lattice edge with its propagation traced by a random walker (Fig. 6.8b). The censoring nodes already connected with fractures from neighbour cells are hatched first and new fractures are forced to propagate with the priority degree retained. Other isolated censoring nodes are arbitrarily allocated with the remaining fracture statistics from SC data sets. Censored fractures are grown first in the four GCs neighbouring the SC, which can place priority constraints for the nuclei along the edges shared with other GCs located at lattice corners.
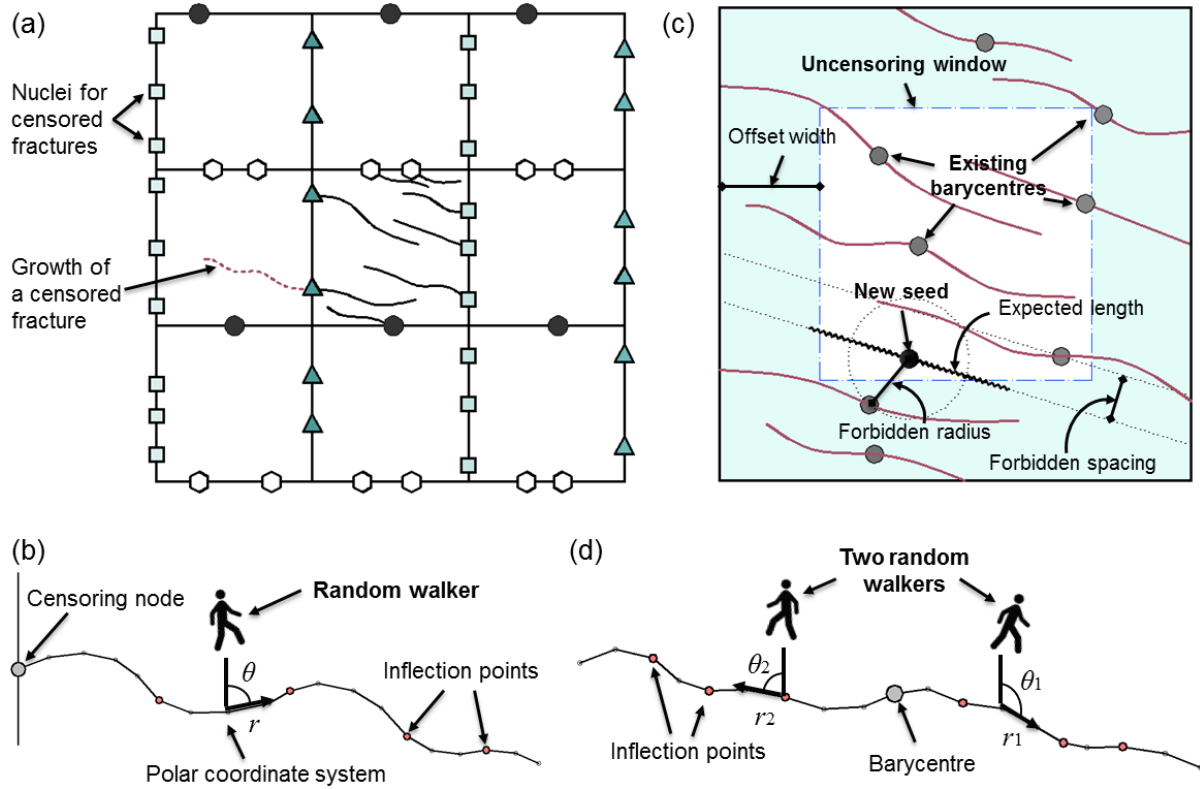
Fig. 6.8 (a) Nucleation of censored fractures by seeding censoring nodes along edges of the growth lattice, (b) propagation of a censored fracture from a censoring node simulated by a random walker, (c) nucleation of uncensored fractures by a point packing process constrained by the barycentre exclusion parameters, and (d) propagation of an uncensored fracture from its barycentre captured by two synchronised random walkers.

(c)   Growth of uncensored fractures

Nucleation of uncensored fractures is modelled by a point packing process (Fig. 6.8c). Barycentres of already generated censored fractures are identified to draw an initial barycentre map. An uncensoring window offsetting a width from the cell periphery is recognised to be the

domain for coordinate generation, where an uncensored fracture has little chance to touch cell borders. The offset width is calculated based on the expected values of the length and orientation of the current propagating fracture. Inserting a new nucleus into the barycentre cloud is constrained by the frequency distribution of exclusion parameters. The distance between a new seed and the closest existing barycentre cannot be smaller than a random variable of exclusion radius, while the minimum spacing with existing fractures also has to be larger than a stochastic value of exclusion spacing. If the new seed doesn't satisfy these criteria, it will be abandoned and another candidate will be generated. This process is repeated under an automated mechanism until the candidate can pass the examination, after which the map will be updated with the new nucleus added. An uncensored crack hatches from the barycentre nucleus and propagates as two synchronised walkers jogging towards opposite directions (Fig. 6.8d).

6.3.4 Recursive cell culture

A recursive cell culture scheme is implemented to extrapolate fracture networks into larger lattices under a self-referencing scheme (Fig. 6.9). The recursive formulation is given by

$$\begin{cases} Cell_n = f_{\text{growth}}(Cell_{n-1}) \\ Cell_0 = \text{initial SC} \end{cases} \tag{6.15}$$

where the nth order cell is grown from the n-1th order cell which serves as the source cell in the nth phase, f_{growth} is the growth function based on random walks in the nine-grid lattice, and the 0th order cell corresponds to the initial SC. In each growth phase, censored fractures from different cells are connected, followed by establishment of a new SC geostatistical library based on the larger network for next phase cell culture.

$Cell_n$ $Cell_{n-1}$ $Cell_1$ $Cell_0$

f_{growth} f_{growth} f_{growth}
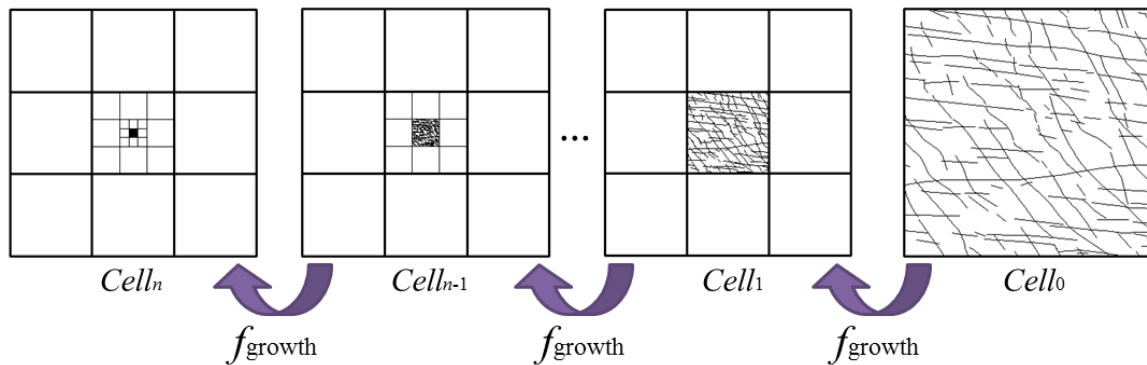
Fig. 6.9 Recursive cell culture scheme.

6.3.5 Validity of growth networks

To examine the validity of growth networks for representing larger fracture systems, a comparison is made at a system scale of $L = 6$ m between the original analogue fracture network (AFN) from outcrop mapping (Fig. 6.10a), ten realisations of growth fracture network (GFN) cultivated from the central $L = 2$ m source pattern (Fig. 6.10b), and ten realisations of pure Poissonian discrete fracture network (DFN) (Fig. 6.10c). A Poissonian DFN is created by the following steps: (i) generating fracture barycentres using a Poisson process with the barycentre density equal to that of the AFN, (ii) sampling random lengths conditioned by the power law statistics obtained in section 6.2, (iii) assigning fracture orientations (uncorrelated with lengths) using a bootstrapping process from the orientation data of the AFN, and (iv) deleting the fracture portions that are outside the domain. The Poissonian DFN is constrained to statistically have the same (98% confidence interval) fracture intensity P_{21} as the AFN. Observation of Fig. 6.10 highlights some interesting differences in visual appearances. The AFN and GFN appear subtly different, since the central $L = 2$ m source cell does not fully feature the characteristics of the original AFN, such as the relatively long and straight Set 1 fractures as can be seen in the top left region of Fig. 6.10a as well as the significant swing in orientation of Set 2 from the lower left to the top right corner. However, the much disordered appearance of Fig. 6.10c is in stark contrast to the other two, possibly due to the uncorrelation between lengths and orientations in the DFN system [Odling, 1992]. A quantitative comparison is further given as shown in Table 6.1.

(a)   (b)   (c)
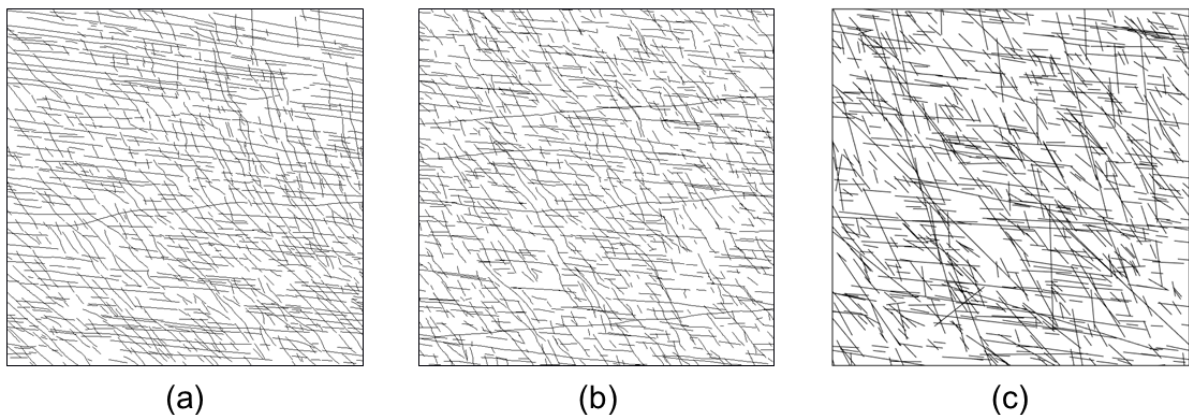
Fig. 6.10 Fracture patterns (domain size $L = 6$ m) of (a) the analogue fracture network (AFN), (b) one of the ten growth fracture network (GFN) realisations, and (c) one of the ten Poissonian discrete fracture network (DFN) realisations.

In Table 6.1, the fractal dimension D is derived from the two-point correlation function, length exponent a is estimated from the density distribution of fracture lengths, fracture intensity P_{21} is calculated using Eq. (6.3) and percolation parameter p is computed from Eq. (6.4). Intersection density ω is measured as the number of intersection nodes per unit area. It can be noted that the GFN realisations show quite similar results to the AFN, although certain discrepancy still exists. The AFN has a slightly higher P_{21} value than GFNs possibly caused by intrinsic heterogeneity of geological media and potential scale-dependency of P_{21} (a further discussion is given in section 6.6). The GFNs have a fractal dimension approximately equal to 2, indicating that the nonfractality of the barycentre spatial distribution is preserved. Larger length exponent (i.e. fewer long fractures) in the GFNs is probably a result of the sampling bias of the limited source data as already observed in the visual comparison. However, the Poissonian DFNs seem to slightly overestimate several important properties, e.g. p and ω. Fig. 6.11 further compares the spacing distribution of the three types of networks measured by placing twenty scanlines along the North-to-South direction and the East-to-West direction, respectively, for each pattern. It seems that the AFN exhibits a "lognormal-like" spacing distribution, while the DFNs tend to have an "exponential-like" distribution since there is no constraint for very close barycentres in the Poisson process. The GFNs tend to present a more realistic spacing distribution under the control of the exclusion parameters, although certain discrepancies still exist probably in relation to the bias in predicting the length distribution. Generally, the growth patterns exhibit quite a good match to the actual fracture system regarding geometric properties.

Table 6.1 Comparison between the analogue fracture network (AFN), growth fracture networks (GFNs), and Poissonian discrete fracture networks (DFNs) with the domain size $L = 6$ m.

Properties	AFN	GFNs	DFNs
Fractal dimension D	2.00	1.96 ± 0.04	1.92 ± 0.08
Length exponent a	2.37	2.54 ± 0.05	2.55 ± 0.05
Fracture intensity P_{21} (m^{-1})	11.23	10.67 ± 0.04	11.28 ± 0.11
Percolation parameter p	12.14	11.55 ± 0.26	13.44 ± 1.52
Intersection density ω (m^{-2})	23.81	23.79 ± 0.64	27.11 ± 9.09
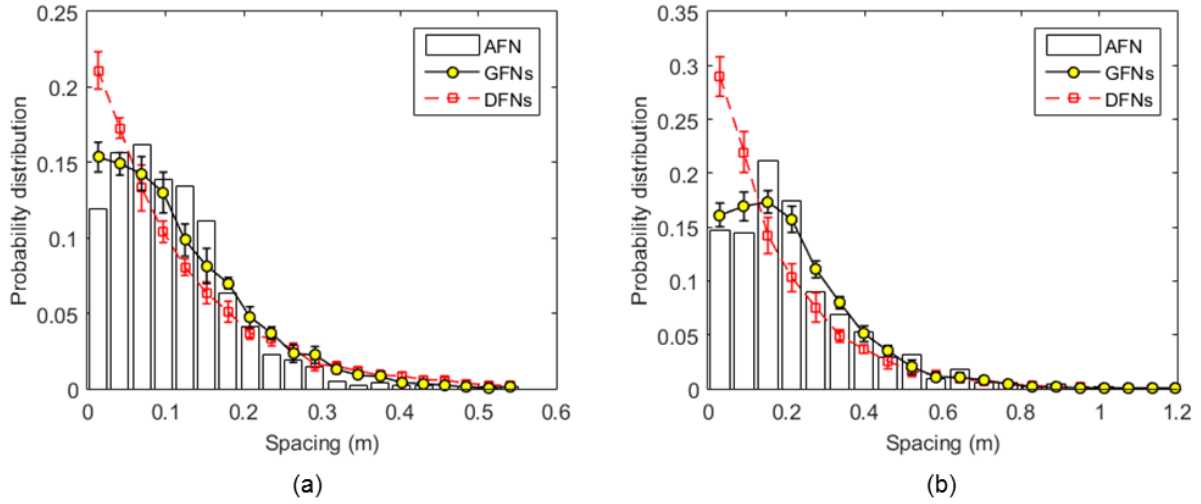
Fig. 6.11 Spacing distribution of the AFN, GFNs, and DFNs measured by placing twenty scanlines along (a) the North-to-South direction and (b) the East-to-West direction, respectively, for each fracture pattern.

6.4 Characterisation of fracture attributes

Fracture displacement attributes, i.e. aperture and shear displacement, of hierarchical rock structures exhibit significant stress-dependency [Min et al., 2004b; Baghbanan and Jing, 2008; Latham et al., 2013; Lei et al., 2014] and scale-dependency [Hatton et al., 1994; Walmann et al., 1996; Renshaw and Park, 1997; Bonnet et al., 2001; Kim and Sanderson, 2005; Neuman, 2008]. Geomechanical modelling is conducted on the 2 m × 2 m rock sample to obtain realistic distribution of fracture attributes, which will be transformed into larger networks following proper scaling laws.

6.4.1 Stress-dependency of fracture attributes

A plane strain numerical experiment is designed with biaxial effective stresses applied by different ratios, i.e. a hydrostatic stress case with $\sigma'_x/\sigma'_y = 1$, and a deviatoric stress case with $\sigma'_x/\sigma'_y = 2$, given that $\sigma'_y \equiv 5$ MPa. Material properties of limestones vary widely, and those of a type of limestone deemed to be typical [Lama and Vutukuri, 1978] are chosen as given in Table 6.2. To eliminate artificial shock, far-field stresses are applied at the model boundaries by a ramping stage from an unstressed state, and the fractured limestone adjusts to a new deformed state under the two different stress scenarios considered. Stress effect on the variability of fracture attributes is characterised in two aspects [Lei et al., 2014]: (i) opening and shearing caused by network-scale fracture and matrix interaction under applied far-field stresses (referred

to here as mesoscopic effect), and (ii) closure and dilation governed by fracture-scale roughness under local compressive stress and shearing movement (referred to as microscopic effect). The fracture behaviour is modelled by a simplified joint constitutive model with a constant dilation angle and no consideration of the fracture size effect on the JRC and JCS parameters.

Table 6.2 Material properties of the fractured limestone.

Properties	Value
Bulk density ρ (kg/m3)	2700
Young's modulus E (GPa)	30
Poisson's ratio υ	0.27
Tensile strength f_t (MPa)	7
Internal friction angle ϕ_i (º)	45
Cohesion c (MPa)	15
Residual friction angle ϕ_r (º)	35
Energy release rate G (kJ·m^{-2})	1
JCS (MPa)	100
JRC	5
Dilation angle ϕ_d (º)	5
Initial mechanical aperture b_0 (mm)	0.1

As shown in Fig. 6.12a, longer fractures exhibit relatively larger apertures under the hydrostatic condition, mainly controlled by the a priori correlation with fracture lengths. However, variation is observed in the deviatoric case (Fig. 6.12b), where some quite large apertures emerge locally caused by dilational bends in curved fractures, dilational jogs at sheared intersections, and fracture openings along rotated block boundaries [Latham et al., 2013]. The influence of in-situ stress ratio on shear displacement distribution is more significant. In the hydrostatic case, all fractures are suppressed for shearing (Fig. 6.12c), whereas considerable sliding occurs in the deviatoric condition (Fig. 6.12d), especially associated with Set 2 due to its favourable orientation.
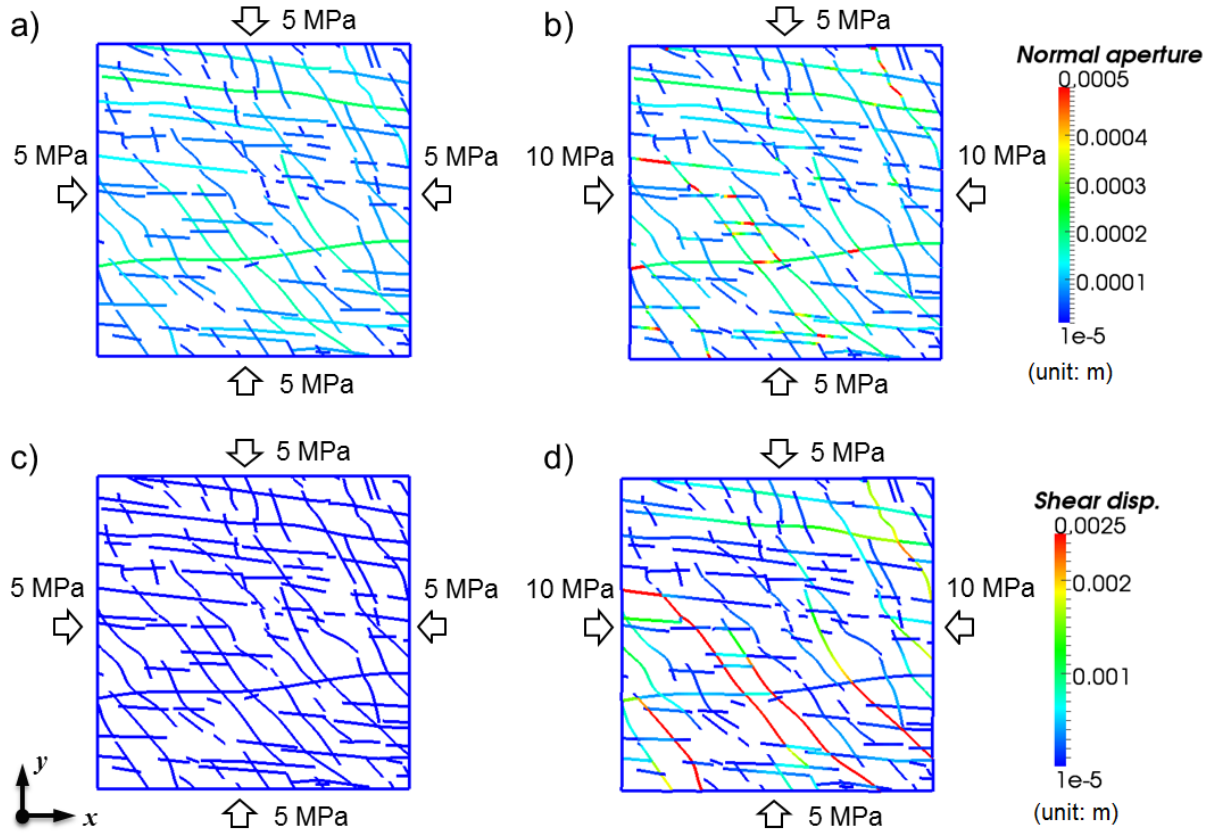
Fig. 6.12 Aperture distribution of the fractured rock in response to different biaxial stress conditions: (a) a hydrostatic case with $\sigma'_x = 5$ MPa and $\sigma'_y = 5$ MPa, and (b) a deviatoric case with $\sigma'_x = 10$ MPa and $\sigma'_y = 5$ MPa. Shear displacement distribution of the fractured rock in (c) the hydrostatic case and (d) the deviatoric case.

6.4.2 Scale-dependency of fracture attributes

The scaling exponents, i.e. n_1 and n_2, of fracture attributes can be derived by statistical correlation analysis and are found greatly influenced by the in-situ stress state. As shown in Fig. 6.13a, fracture apertures in the hydrostatic case experienced significant closure from their initial values. However, deformed apertures still tend to follow a power law relation with fracture lengths, believed to be mainly caused by the a priori square root correlation. The non-linear relation between aperture closure and fracture length (as can be seen from Eq. (4.25)-(4.27)) adjusted the exponent n_2 to be 0.568 in the hydrostatic condition. Geomechanically-induced variability under deviatoric stresses is well captured and a higher exponent is obtained, i.e. $n_2 = 0.635$. The higher exponent can be possibly attributed to the tendency that a longer fracture may generate more openings due to more locally curving parts of the fractures (where it is easier to form dilational bends) and more intersections with other fractures (where it is easier to

accommodate dilational jogs). Shear displacements also show a power law trend with scale (Fig. 6.13b). Fractures under the deviatoric condition are associated with a much higher exponent (n_1 = 1.148) than those under the hydrostatic condition (n_1 = 0.406). Such aperture and shear displacement scale-dependencies produced by the geomechanical model are considered important and realistic for these unique scenarios.
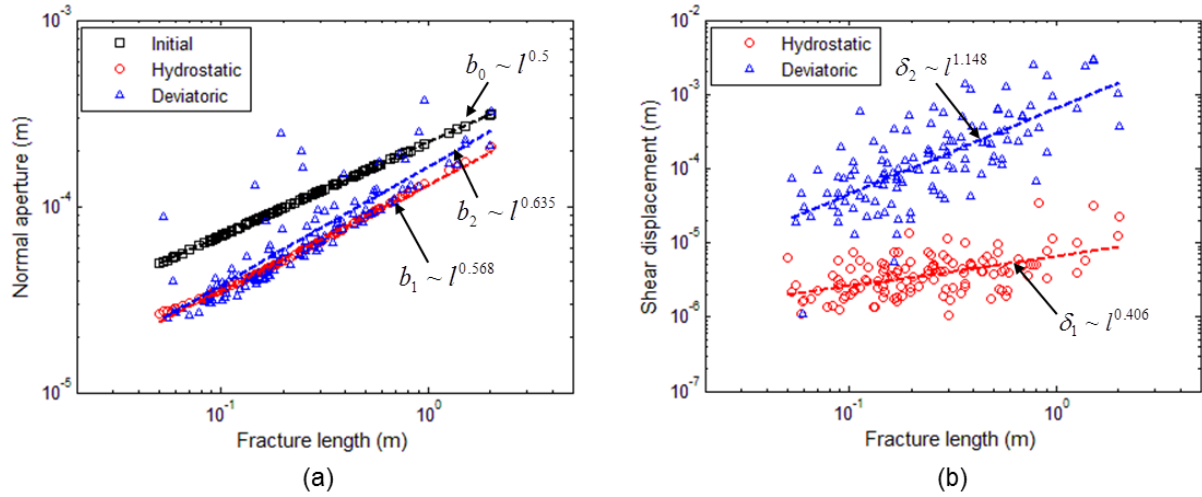
Fig. 6.13 (a) Correlation between length-weighted average apertures and fracture lengths, and (b) correlation between length-weighted average shear displacements and fracture lengths of the 2 m × 2 m fractured rock under different in-situ stress conditions.

During the formation of growth networks, when some fractures are connected with each other via cell boundaries to form a longer fracture, their displacement attributes will be upgraded by multiplying a scaling factor ζ deduced from Eq. (6.6) and (6.7):

$$\zeta = \frac{l_l^n}{l_s^n} = \left(\frac{l_l}{l_s}\right)^n \tag{6.16}$$

where l_s is the length of a shorter fracture which will connect with other shorter fractures to form a longer one with length l_l, and n is the scaling exponent to be substituted by n_1 or n_2 for shear displacement or aperture, respectively. The upgrading operation is implemented automatically in each growth phase.

6.4.3 Coupling of fracture attributes with a fracture dilation model

For each growth network, its scaled aperture and shear displacement can be mechanically coupled according to a fracture dilation model [Asadollahi and Tonon, 2010] to account for

shear-induced dilational displacement b_s given by

$$b_s = \begin{cases} \frac{1}{3}u\left(\frac{2u}{u_p}-1\right)\tan\left[JRC\log_{10}\left(\frac{JCS}{\sigma'_n}\right)\right] & , u \leq u_p \\ \int_{u_p}^{u}\tan\left[JRC\log_{10}\left(\frac{JCS}{\sigma'_n}\right)\left(\frac{u_p}{u}\right)^{0.381}\right]du + b_{s,peak} & , u > u_p \end{cases} \quad (6.17)$$

where u is the fracture shear displacement, u_p is the peak shear displacement, $b_{s,peak}$ is the dilational value at u_p, and σ'_n is the effective normal stress applied on fracture walls. The peak shear displacement u_p is a stress- and scale-dependent parameter that can be estimated using an empirical relation, i.e. Eq. (4.35) [Asadollahi and Tonon, 2010]. Normal stress σ'_n is estimated using the Mohr circle equation:

$$\sigma'_n = \frac{1}{2}\left(\sigma'_x + \sigma'_y\right) + \frac{1}{2}\left(\sigma'_x - \sigma'_y\right)\cos 2\theta + \tau'_{xy}\sin 2\theta \quad (6.18)$$

where σ'_x and σ'_y are the values substituted from the applied far-field stresses, τ'_{xy} is equal to 0, and θ is the intersection angle between the normal of fracture plane and the positive x direction. The integral part in Eq. (6.17) is numerically approximated by the quadratic solution of the three-point Simpson's rule. In the hydrostatic case, not surprisingly, dilational effect scarcely exists since $\delta_s << \delta_{peak}$.

Mechanical aperture b_m is derived as the summation of the dilational displacement and the scaled normal aperture. Hydraulic aperture b_h, defined as an equivalent aperture for laminar flow between smooth parallel plates, may exhibit a complicated non-linear correlation with mechanical aperture [Barton et al., 1985; Olsson and Barton, 2001]. For simplicity, hydraulic aperture in this research is treated equally to mechanical aperture, which tends to overestimate flow rates by a roughness-dependent factor ≤ 2 [Matthäi and Belayneh, 2004]. However, this bias is considered not to have a significant influence for the focus of this study which is the trend by which permeability is likely to change over length scales.

6.5 Multiscale growth networks with stress- and scale-dependent apertures

6.5.1 Multiscale growth network realisations

Multiscale growth networks with stress- and scale-dependent apertures are constructed through the recursive cell culture scheme based on the stressed 2 m × 2 m Kilve analogue sample. Fig. 6.14 presents one realisation set of multiscale growth patterns, in which important features

of natural fracture systems are modelled including non-planarity, segmentation, local clustering, and spanning fractures. Fig. 6.15 shows the normalised density distributions of fracture lengths of this realisation set and it seems that the data can be fitted by a power law with an exponent $a \approx 2.6$.
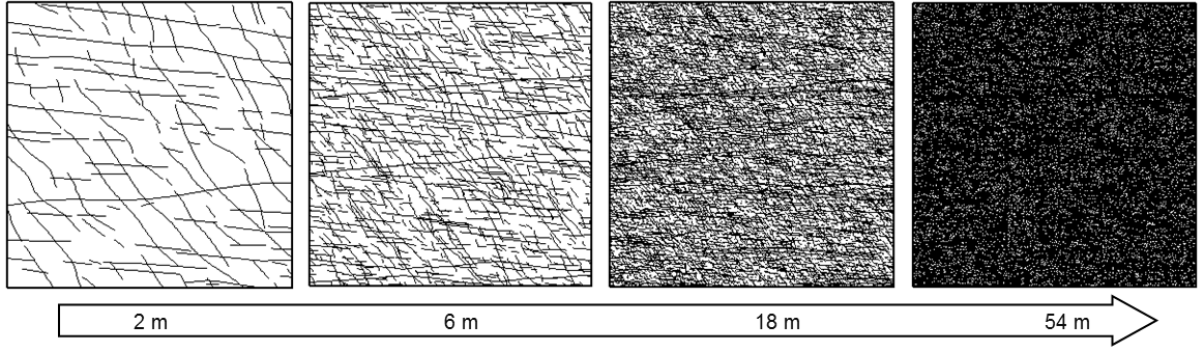
Fig. 6.14 Multiscale growth realisations achieved by the recursive cell culture scheme.
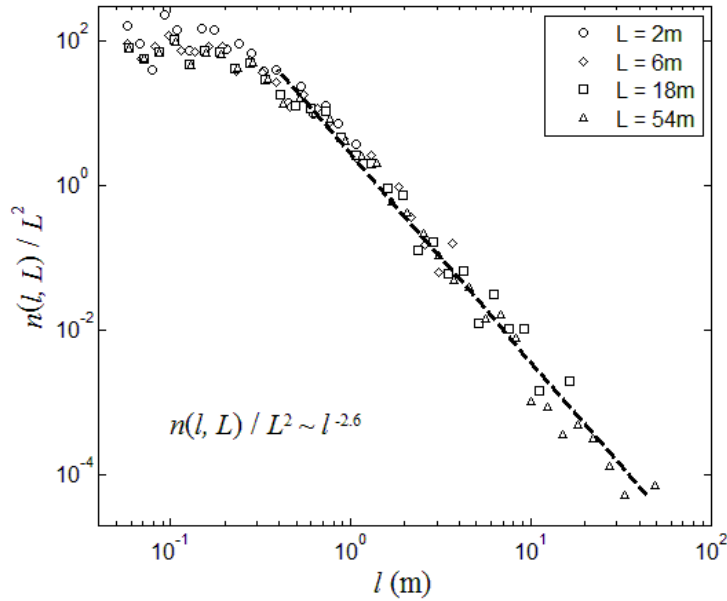
Fig. 6.15 Normalised density distributions of fracture lengths of a realisation set of multiscale growth networks.

Important properties of multiscale growth networks (ten realisations for each stress condition) are summarised in Table 6.3. Variation of fracture density caused by crack propagation is neglected due to its minor effect. Topological attributes are averaged for all realisations, while stress-dependent parameters (e.g. aperture, porosity) are listed separately for each stress scenario. Fractal dimension $D \approx 2$ over all scales indicates that the homogeneous

filling feature is retained by the growth model. The networks at larger scales show relatively higher length exponent, implying the existence of certain biases tending to underestimate the existence of longer fractures under the repetitive assumption of the proposed method, which has also resulted in the scale-invariance of P_{21} and intersection density ω (consequences and possible solutions will be discussed in section 6.6). Percolation parameter p increases with the system size since more large fractures are involved as a result of extrapolating censored fractures in larger domains. Rock porosity ϕ, defined as the fraction of aperture space over total rock volume, increases with scale as a result of scaled and coupled displacement attributes.

Table 6.3 Properties of multiscale growth network realisations.

Properties	2 m	6 m	18 m	54 m
Fractal dimension D	1.98	1.95 ± 0.04	1.97 ± 0.01	1.96 ± 0.01
Length exponent a	2.43	2.54 ± 0.11	2.59 ± 0.11	2.66 ± 0.12
Fracture intensity P_{21} (m^{-1})	10.84	10.77 ± 0.06	10.72 ± 0.07	10.68 ± 0.07
Percolation parameter p	7.48	11.32 ± 0.57	13.94 ± 0.94	14.43 ± 1.63
Maximum fracture length (m)	2.01	6.04 ± 0.00	18.11 ± 0.01	54.34 ± 0.03
Intersection density ω (m^{-2})	25.00	23.69 ± 0.59	23.72 ± 0.36	23.96 ± 0.36
Hydrostatic Stress Condition				
Fracture porosity ϕ (%)	0.110	0.125 ± 0.020	0.131 ± 0.034	0.133 ± 0.035
Harmonic mean aperture (mm)	0.062	0.064 ± 0.000	0.066 ± 0.000	0.066 ± 0.001
Geometric mean aperture (mm)	0.090	0.097 ± 0.001	0.100 ± 0.001	0.101 ± 0.001
Arithmetic mean aperture (mm)	0.124	0.165 ± 0.004	0.205 ± 0.012	0.253 ± 0.026
Deviatoric Stress Condition				
Fracture porosity ϕ (%)	0.160	0.229 ± 0.006	0.263 ± 0.016	0.273 ± 0.019
Harmonic mean aperture (mm)	0.058	0.063 ± 0.001	0.065 ± 0.001	0.066 ± 0.001
Geometric mean aperture (mm)	0.093	0.116 ± 0.002	0.128 ± 0.002	0.134 ± 0.002
Arithmetic mean aperture (mm)	0.166	0.296 ± 0.061	0.435 ± 0.055	0.628 ± 0.078

The equivalent aperture for each fracture population is calculated using the generalised

f-mean function given by:

$$\bar{b}_{\mathrm{h}}^3 = f^{-1}\left(\sum_{i=1}^{n} w_i f\left(b_{\mathrm{h}i}^3\right)\right) \qquad (6.19)$$

where n is the total number of fractures, $w_{\mathrm{i}} = l_i/l_{\mathrm{tot}}$ is the length-based weight of the ith fracture, $b_{\mathrm{h}i}$ is the hydraulic aperture of the ith fracture, and $f = x$, $1/x$, or $\ln(x)$ corresponds to arithmetic, harmonic, or geometric mean, respectively. Arithmetic mean treats fractures as connected in parallel and tends to give an upper bound, while harmonic mean assumes fractures as connected in series and tends to provide a lower bound [de Marsily, 1986; Zimmerman and Bodvarsson, 1996; Ronayne and Gorelick, 2006; Leung and Zimmerman, 2012]. Permeability of 2D heterogeneous media is more likely to be governed by the geometric mean of local fracture permeability that follows a lognormal or power law distribution [de Marsily, 1986; de Dreuzy et al., 2002]. The aperture of each individual fracture, i.e. $b_{\mathrm{h}i}$ in Eq. (6.19), is derived as the harmonic mean of its segmental apertures since fracture segments are connected in series in the 2D scenario. Growth realisations of different stress cases are associated with a close value for harmonic mean aperture, whereas the deviatoric case shows slightly higher geometric mean and remarkably larger arithmetic mean aperture compared to the hydrostatic case.

6.5.2 Flow in multiscale fractured rocks

Fluid flow in the growth networks is modelled by single-phase flow simulation based on the hybrid finite element-finite volume method (FEFVM) [Paluszny et al., 2007]. Fractures are segmented into lower dimensional line elements, which are embedded in a uniform matrix material discretised by an unstructured finite element grid [Paluszny and Matthäi, 2010]. Matrix permeability k_{m} of fractured hydrocarbon reservoirs ranges between 1 mD and 1 D [Matthäi and Belayneh, 2004]. A lower bound value, i.e. $k_{\mathrm{m}} = 1 \times 10^{-15}$ m^2, is adopted here. Fracture permeability k_{f} is characterised using piecewise hydraulic apertures obeying the cubic law (i.e. $k_{\mathrm{f}} = b_{\mathrm{h}}^2/12$), with a harmonic mean value (lower bound) derived to be ~3 × 10^{-10} m^2. In the highly connected disordered media, flow is dominated by fractures due to the large fracture-matrix permeability contrast, i.e. $k_{\mathrm{f}}/k_{\mathrm{m}} > 10^5$-$10^6$ [Matthäi and Belayneh, 2004]. By applying a prescribed macroscopic pressure differential on each pair of opposite boundaries, the fluid pressure and velocity fields are resolved with equivalent permeability of the different sized

domains further computed [Lang et al., 2014].
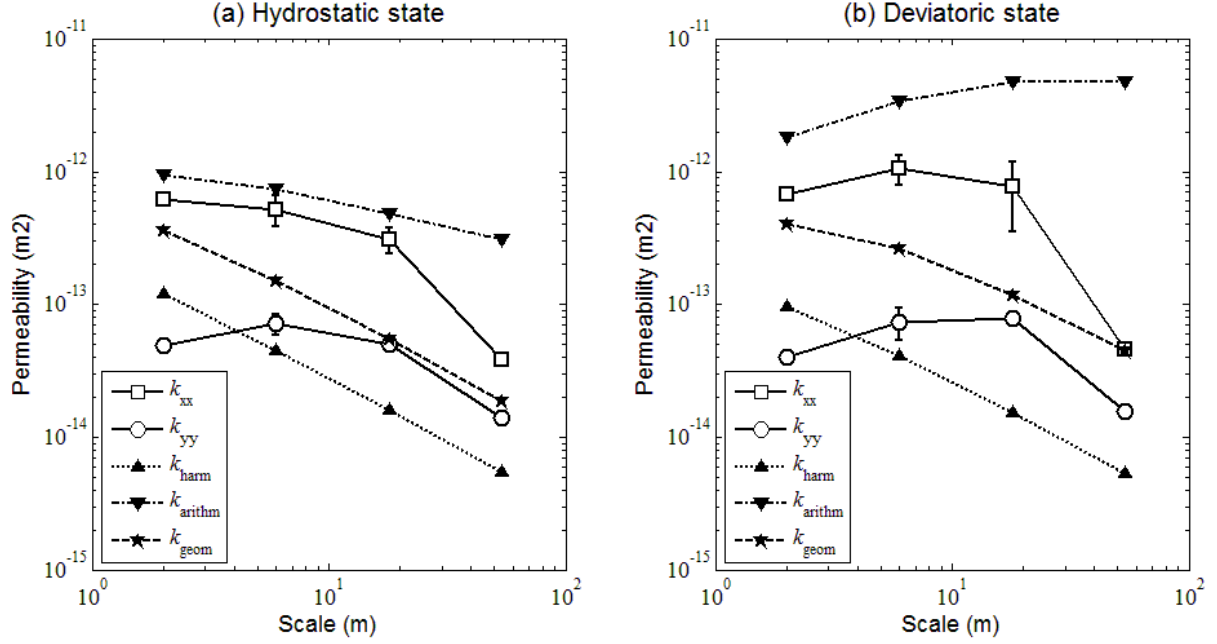
Fig. 6.16 Equivalent permeability k_{xx} and k_{yy} computed from the flow simulation, and analytical permeability k_{harm}, k_{arithm}, k_{geom} calculated by substituting the harmonic, arithmetic and geometric mean apertures into Eq. (6.20), under the applied (a) hydrostatic and (b) deviatoric stress conditions.

Fig. 6.16 shows the permeability scaling trend of the ten sets of growth realisations in both x and y directions (error bars represent ±1 standard deviation). It can be noted that the equivalent permeability is always at least one order of magnitude larger than the matrix permeability (i.e. 1 × 10^{-15} m^2), which verifies the expected fluid partitioning behaviour, i.e. fracture-dominated flow. With the scale increasing, the permeability of the deviatoric case displays an upward trend at the small and intermediate scale (<10-20 m) and a continued downward trend at larger scales (>20 m), whereas the permeability of the hydrostatic case mainly shows a downward trend except a slight increase in the y direction at the small scale (<10 m). Fracture networks under the deviatoric condition appear to possess higher permeability due to their wider apertures.

Two factors are considered to dominate the permeability scaling trend: (i) the length exponent a that governs the connectivity scaling of a fracture population [Berkowitz et al., 2000; Darcel et al., 2003a], and (ii) the correlation exponents n_1 and n_2 which regulate the transmissivity scaling of each individual fracture [de Dreuzy et al., 2002; Neuman, 2008]. For the studied case of $2 < a < D+1$, with the increase of domain size L, the number of fractures

larger than L (i.e. traversing fractures) increases as $\sim L^{-a+D+1}$ [Davy et al., 2006], whereas the relative percentage of such fractures decreases as $\sim L^{-a+D-1}$. Thus, a global downward trend might be expected for rock permeability at large scales [Renshaw, 1998; Klimczak et al., 2010]. The flow behaviour is also significantly affected by the distribution of variable apertures, which leads to diversity of fluid-flow structures [de Dreuzy et al., 2001b] and permeability scaling trends [Klimczak et al., 2010]. Under a higher boundary stress ratio, longer fractures play a more important role for fluid migration due to their lower resistance [Tsang and Neretnieks, 1998] in association with wider apertures that are correlated with fracture length. Hence, at small scales, a permeability increase occurs in the deviatoric case attributed to the considerable contribution from long fractures. However, a global decreasing trend is inevitable due to the decreasing probability of traversing fractures at larger scales, with shorter fractures carrying a heavier role for fluid transport. In the hydrostatic stress case, the equivalent permeability mainly declines with the increased scale, because the slightly scaled apertures with no shear-induced dilation do not endow long fractures with highly conductive capability compared to the decreased relative frequency of long fractures whose length follows the power law.

The trend of rock permeability with scale may be further explained by the flow structure transition zone between the connecting scale and the channelling scale [de Dreuzy et al., 2001a, 2001b; Davy et al., 2006]. The connecting scale L_c (or the connection length) is where the fracture network shifts from disconnected to connected, while the channelling scale ξ (i.e. the correlation length in the percolation theory) is where the flow structure transforms from extremely channelled to distributed. As shown in Fig. 6.17, for growth networks in the deviatoric case, the connection length L_c seems to be at a scale <2 m, which is consistent with the predicted value of ~0.80 m in section 6.2.3, and the channelling scale ξ is at 20-50 m. Within the transition zone (i.e. system size from L_c to ξ), the flow structure is made up of a number of quite independent, multi-path, multi-segment channels [Tsang and Neretnieks, 1998; de Dreuzy et al., 2001a], under the preference of fluid to flow in least resistance paths in the disordered system of finite-sized, curved fractures. This tortuosity feature has significant impact on effective flow properties [Ronayne and Gorelick, 2006] and may become even more crucial when the considered rock volume exceeds the channelling scale ξ, after which the percentage of

domain-sized fractures decreases and flow begins to exhibit dispersive behaviour, like in a homogeneous porous medium [de Dreuzy et al., 2001a; Davy et al., 2006].

West to East:
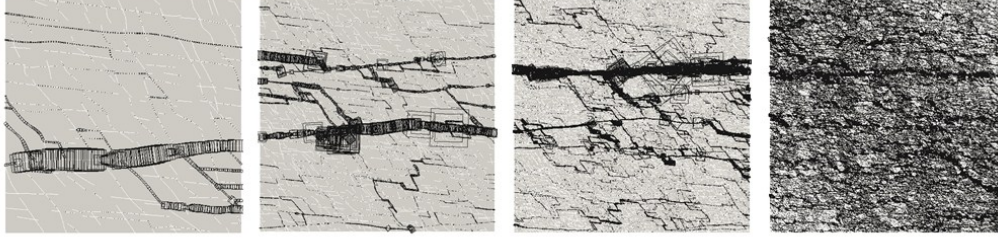
North to South:
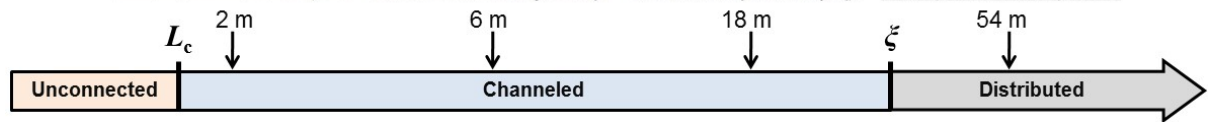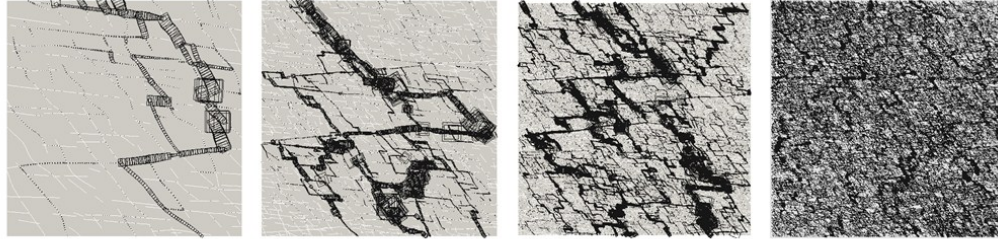
Fig. 6.17 Flow structure transition from extremely channelled to distributed in multiscale growth networks under the deviatoric stress condition (boxes illustrate the main pathways of the flow structure).

For comparison with the flow modelling, an analytical solution for rock mass permeability k_{analy} can also be computed by assuming idealised orthogonal fractures fully penetrating the system domain and ignoring the flow in the matrix [Matthäi and Belayneh, 2004]

$$\left(L - \frac{b_h l_{tot}}{L}\right) k_{analy} = b_h \frac{b_h^2}{12} \tag{6.20}$$

where l_{tot} is the total length of all fractures in the $L \times L$ squared domain, b_h is the network equivalent aperture that can be substituted by the harmonic, arithmetic or geometric mean, corresponding to the analytical permeability, k_{harm}, k_{arithm}, k_{geom}, respectively. It is reassuring to note that, the equivalent permeability is quite well bounded by the harmonic and arithmetic solutions, while the median trend is better tracked by the geometric one (Fig. 6.16). Highly conductive fractures with long lengths and wide apertures capable of transmitting fluid across long distances seem to behave more like an "in parallel" connected network [Leung and Zimmerman, 2012], so k_{xx} is better captured by the upper bound at small scales, where channels

mainly constituted by very long fractures dominate the flow. However, at large scales, fluid has to migrate through less conductive branches to reach the opposite boundary due to the proportional reduction of longer fractures, which makes the fracture population act more like an "in series" connected network and k_{xx} tends to approach the lower bound. The equivalent permeability in the y direction k_{yy} mainly exhibits closer values to the lower limit due to the inherent zigzag feature of the North-to-South flow structure. Indeed, the mechanism of network alteration from "parallel" to "series" is equivalent to the essence of flow structure transition from "channelled" to "distributed". Geometric mean seems to elegantly trace the median trend of equivalent permeability, irrespective of the anisotropic flow features, although it cannot capture the mechanism of channelling-induced permeability increase at smaller scales. Due to the fact that equivalent aperture of harmonic mean is not sensitive to the ratio of far-field stresses (Table 6.3), magnitudes of equivalent permeability under the prescribed hydrostatic and deviatoric conditions tend to converge at larger scales but with intrinsic anisotropy retained (Fig. 6.16). At even larger scales (e.g. >100 m) with upscaling based on the original 2 m × 2 m source cell, the fractured rock probably behaves like a porous medium [Long et al., 1982] with a lower REV permeability conjectured. However, the repetition assumption might not be valid at that scale since many complex larger-scale factors (e.g. seismically visible faults, multiple rock types and even karst features) will be involved [Clauser, 1992], which is out of the scope of this study.

6.6 Discussion

The stress- and scale-dependent properties of fracture attributes were modelled using the FEMDEM model for an interconnected fracture system. The results provide estimates of the length correlation exponents caused by fracture reactivations and interactions in response to applied in-situ stresses. The exponent n_1 for the correlation of shear displacements to fracture lengths varies from ~0.5 under a hydrostatic state to >1.0 under a deviatoric condition. The classical analytical solutions based on, e.g. the linear elastic model [Pollard and Segall, 1987] or the post-yield model [Cowie and Scholz, 1992a, 1992b] cannot fully account for the displacement-length relationship observed here. One possible reason is that these analytical formulations assume that fractures are poorly interconnected and purely straight, which oversimplifies the topological complexity of natural fracture systems involving cross-cutting,

segmentation and curvature. A second is that these classical solutions apply to fractures at a critical state for propagation, which is not the general state of interest. The stress-dependent behaviour of fracture apertures in this work was also captured by synthesising both microscopic and mesoscopic effects, and a higher exponent n_2 is induced under the deviatoric stress condition. The exponent n_2 for the aperture to length relationship was found greatly controlled by the a prior square root correlation [Olson, 2003], whose universality may require further validation. Furthermore, more stress scenarios might need to be explored to examine the power law relation between aperture and length.

In the actual field measurements of a natural fracture system based on a finite-sized window sampling, observed maximum fracture length l_{max} may increase with the system size L. By assuming $n(l, L)$ ideally obeys the power law, fracture intensity P_{21} at a certain scale can be roughly calculated by substituting $l_{max} \approx L$ into Eq. (6.3):

$$P_{21}(L) \approx \frac{\alpha L^{D-2}(l_{min}^{-a+2} - L^{-a+2})}{a-2} \tag{6.21}$$

which implies that P_{21} is scale dependent and increases with L for the studied scenario of $2 < a < 3$. If the domain size L is large enough, P_{21} approaches a constant value determined by l_{min}. Scale-dependency of intersection density ω might also be nontrivial [Darcel et al., 2003a]. The proposed growth method that assumes growth cells share the same length distribution as the source cell can be seen as a first-order approximation to the real fracture system. Potentially important heterogeneity, e.g. when considering a source pattern that visually seems in some ways different to the pattern in a neighbour region, cannot be accounted for in such growth models based on only one source pattern, and this source cell selection problem has already been recognised in section 6.3.5. When solving real problems, extraction of source patterns from different locations might be necessary, and by doing so the lower and upper bounds of permeability may be informatively obtained based on growth modelling results from multiple sources. Discrepancy in length exponent of the multiscale growth networks may also be attributed to this space repetition hypothesis. However, such deviation is considered not to dramatically change the permeability scaling trend since length exponent is still kept in the regime of $2 < a < 3$. To more realistically model the natural heterogeneity, a tuning mechanism

can be introduced by using a prescribed power law density distribution of lengths to adjust the growth results. Correlation between fracture position and length that have been reported [Bour and Davy, 1997; Darcel et al., 2003c] is also an important influence to be incorporated. Development of such modules will be the next step of this research and a validation may be conducted based on some outcrop patterns over several scales, e.g. in [Bour et al., 2002]. Interesting directions for future work arising from this growth methodology include modelling of networks having different fractal dimensions (e.g. $1 < D < 2$) and length exponents (e.g. $1 < a < 2$ and $a > 3$) [de Dreuzy et al., 2001a], development of a random walk algorithm for hierarchical patterns involving sequential formation and geological arrest [Paluszny and Matthäi, 2010; Davy et al., 2010, 2013], and upscaling realistic apertures derived from direct (two-way) hydromechanical coupling, where the effect of pore fluid pressure on aperture evolution can be more realistically captured [Rutqvist and Stephansson, 2003].

Another limitation of this research is that 2D analysis was used to model the actual 3D fracture systems. The finite layer thickness may influence the fracture growth process and leads to the existence of a characteristic length that defines the transition of scaling behaviour [Bonnet et al., 2001]. The role of bedding interfaces can also have important 3D effects on the hydromechanical behaviour of the layered rock. For example, apertures vary considerably for extensional layer-normal joints affected by delamination or variable interface slip. Fractures may propagate across the bedding interface, depending on layer mechanical properties, local stress fields and finite strains. Potentially dominant role of flow in the bedding planes due to delamination between the limestone and the shales and focused flows in such cross-cutting fractures may also be essential. To achieve 3D geomechanical modelling, a newly developed 3D crack propagation model [Guo et al., 2015, 2016] will be employed to capture the brittle deformation response including local concentrations of critically high tensile or differential stresses, together with realistic fracture opening and shearing behaviour on both pre-existing and newly propagated fractures (see Chapter 8). Such capability opens the way to modelling 3D flows in geomechanically realistic fractured layers as well as channelised flow in comminuted fracture intersections and bedding planes, based on which a 3D network upscaling method may be further developed to statistically estimate rock mass properties in larger scales.

6.7 Concluding remarks

To conclude, a new approach to upscaling 2D fracture network models was proposed for preserving geostatistical and geomechanical characteristics of a smaller-scale "source" fracture pattern. The scaling properties of an outcrop system were examined in terms of the spatial organisation and length distribution using fractal geometry and power law relations. The fracture pattern was observed to be nonfractal with the fractal dimension $D \approx 2$, while its length distribution tends to follow a power law with the exponent $2 < a < 3$. To introduce a realistic distribution of fracture aperture and shear displacement, the FEMDEM geomechanical model was applied to simulate the response of a 2 m × 2 m fractured rock sample under in-situ stresses. A novel scheme accommodating discrete-time random walks in recursive self-referencing lattices has been developed to nucleate and propagate fractures together with their stress- and scale-dependent attributes into larger domains up to 54 m × 54 m. Advantages of this approach include preserving the non-planarity of natural cracks, capturing the existence of long fractures, retaining the realism of variable apertures, and respecting the stress-dependency of displacement-length correlations. Hydraulic behaviour of multiscale growth realizations was modelled by single-phase flow simulation, where distinct permeability scaling trends were observed for different in-situ stress scenarios. A transition zone was identified where flow structure shifts from extremely channelled to distributed as the network scale increases. The observed stress effects on the scaling behaviour of fracture attributes and rock permeability demonstrate the importance of incorporating geomechanical analysis when upscaling fracture network models for reservoir simulation.

7 Hydromechanical modelling of an idealised 3D persistent fracture network

7.1 Introduction

Effects of stress on the permeability of fractured rocks have been widely investigated using 2D fracture network models [Zhang and Sanderson, 1996; Min et al., 2004b; Baghbanan and Jing, 2008; Latham et al., 2013; Lei et al., 2014]. However, the 3D nature of fluid flow in fractured rocks under polyaxial (i.e. true-triaxial) stress conditions remains poorly understood. In reviewing the literature on fluid flow in fractures, there appears to be two distinct research focuses which depend on the chosen scale of study. The first scale is at the level of the individual fracture in which the surface roughness is described in detail [Witherspoon, 1980; Tsang and Witherspoon, 1981; Barton et al., 1985; Olsson and Barton, 2001], and the second scale is at the level of the fracture network with emphasis on the overall properties [Dershowitz et al., 2000; Pouya and Fouché, 2009; Lang et al., 2013]. Each aspect needs methods adapted to mechanisms for the given scale and appropriate for their analysis and interpretation. Up to now, there are very few attempts to bridge these two scales in 3D numerical modelling, with an exception of recent work by de Dreuzy et al. [2012] that combined the effects of fracture-scale heterogeneity and the network-scale topology in fluid flow modelling of 3D discontinuity systems. However, mechanical stress that has a vital impact on the variability of aperture fields were assumed to be uniform and isotropic across their model, regardless of the effects of fracture orientation and interaction which are known to be highly significant.

In this chapter, a stress-induced variable aperture model is implemented into the 3D FEMDEM geomechanical model which can resolve explicit DFN geometries. The combined formulation is applied to investigate the flow heterogeneity in an idealised 3D persistent fracture network caused by both fracture-scale roughness and network-scale interaction effects under polyaxial stress conditions. This research will mainly focus on the stress effect, whereas the complexity of scale effects and the possible existence of an REV are beyond the scope of this study. Persistent fracture sets are used here to remove the intricacy associated with fracture propagation – a topic which will be covered in the next chapter.

7.2 Numerical method

7.2.1 Solid modelling

The persistent discrete fracture network is integrated into the 3D FEMDEM model [Munjiza, 2004] to simulate the geomechanical behaviour of 3D fractured rocks under polyaxial (true-triaxial) in-situ stresses. The rock mass dissected by a persistent fracture population (Fig. 7.1a) is represented by an unstructured grid system (Fig. 7.1b) involving a discretisation of matrix domain using four-noded tetrahedral elements and a configuration of fracture interfaces using six-noded joint elements. A joint element is formed by two triangular faces that belong to opposite volumetric finite elements and are associated with separate nodes but having coincident initial coordinates. Kinetics of the multi-block geological system is governed by the Cauchy linear momentum equation, i.e. Eq. (4.5). Fracture propagation is not modelled since only persistent fracture networks are considered in this study.
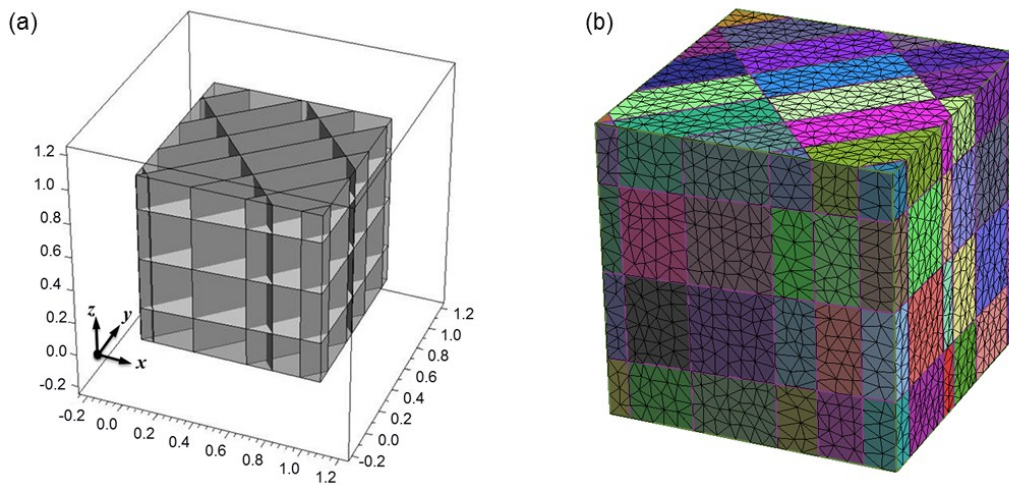
Fig. 7.1 Representation of (a) a fractured rock embedded with a persistent fracture network using (b) an unstructured grid.

Fracture space represented by separated interfaces of deformed solids in the mechanical model is transformed to lower dimensional surfaces associated with variable equivalent apertures for fluid flow. The aperture model presented here is aimed to capture the change in fluid conduits caused by the applied in-situ stresses to the rock mass skeleton. The aperture characterisation procedure includes identification of 3D fracture system topologies (as described below) and calculation of variable hydraulic apertures (see Chapter 4). Note that the fracture behaviour in

this chapter is modelled using a simplified joint constitutive model (JCM) model assuming constant joint roughness coefficient (JRC) and joint wall compressive strength (JCS) parameters and a constant dilation angle.

The generic search algorithm for 2D fracture network topologies as described in Chapter 4 is extended for 3D systems, where a fracture is dissected into several block facets (polygonal shape) bounded by the intersections with many other fractures. Each block facet is further discretised into a number of connected joint elements in the FEMDEM grid system. Connectivity analysis (Fig. 7.2) is first implemented for each joint element to recognise its three continuously connected neighbours (i.e. sharing the same edge with identical nodes). If the edge of a joint element is located on model boundaries or fracture intersections, it is considered having no neighbour via that edge and a value of '-1' is assigned numerically.
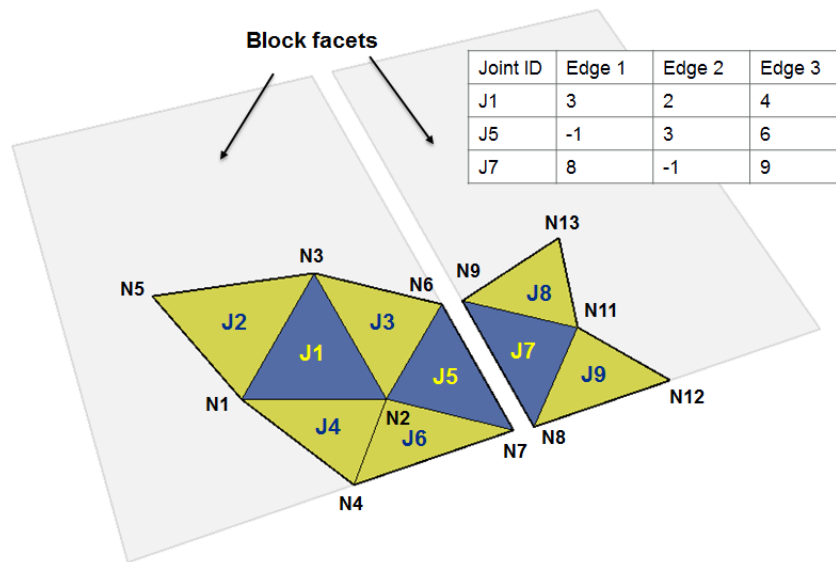
Fig. 7.2 Connectivity analysis of fracture joint elements.

Identification of isolated block facets is achieved based on a ternary-tree data structure (Fig. 7.3), in which a joint element is represented by a tree-node that has one parent tree-node (except the 1st level tree-node) and three child tree-nodes corresponding to its three neighbours. A breadth-first search (BFS) is conducted to recognise connected components (i.e. joint elements belonging to the same facet) by scanning the built ternary-tree structure, where previously visited tree-nodes or unreal neighbour tree-nodes are marked to be dead (i.e. empty nodes in Fig. 7.3) and will not grow in further searching loops.
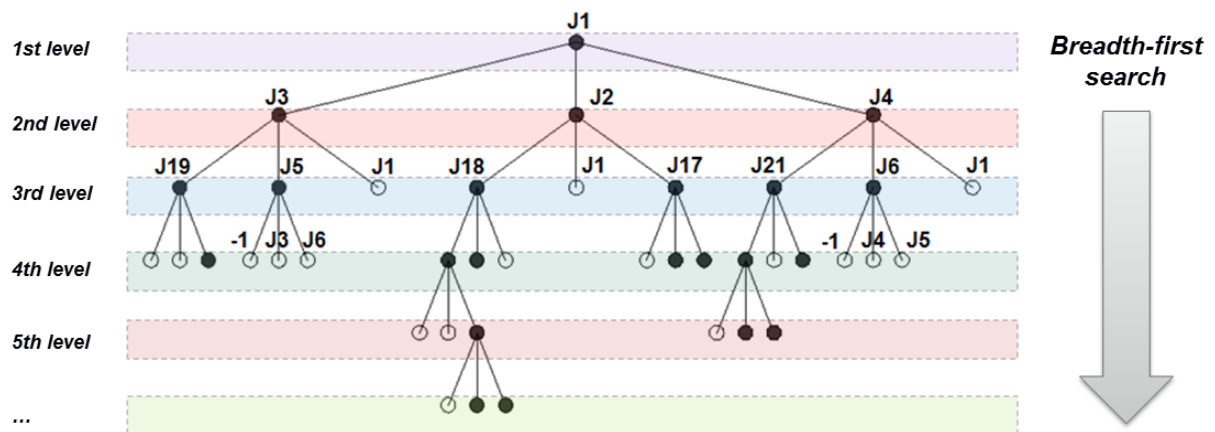
Fig. 7.3 Identification of a block facet by breadth-first search (BFS) based on a ternary-tree data structure representing the topological connectivity of joint elements.

Isolated block facets represented by multiple ternary-trees are further combined based on their connectivity and coplanarity state to form corresponding discrete fractures (Fig. 7.4). The 3D fracture space bounded by opposite fracture walls in the solid model is transformed into a lower dimensional system represented by the median surfaces between deformed facing walls with calculated variable apertures.
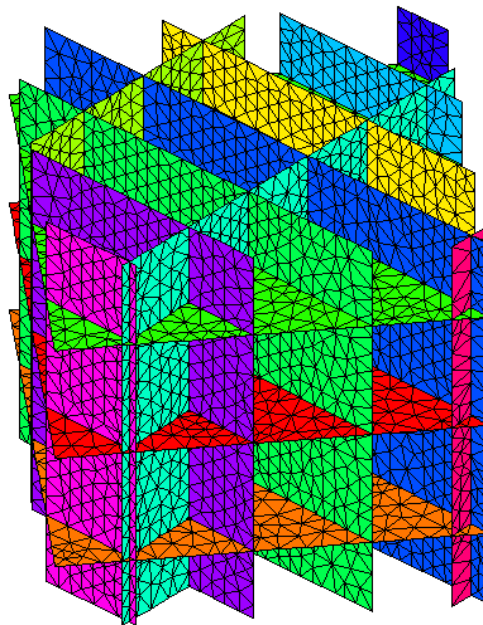
Fig. 7.4 Identified discrete fractures formed by combined block facets.

7.2.2 Fluid flow modelling

Single-phase steady state flow of incompressible fluid with constant viscosity through

porous media, in absence of sources and sinks, is governed by the continuity equation and Darcy's law, which are reduced to a Laplace equation as

$$\nabla \cdot (k \, \nabla p) = 0 \tag{7.1}$$

where k is the intrinsic and isotropic permeability of the porous medium with local variability permitted, and p is the fluid pressure solved at nodes of unstructured finite element grids by employing the standard Galerkin method. The element-wise constant barycentric velocity is resolved based on the pressure gradient vector field by applying Darcy's law given by

$$\mathbf{u}^e = -\frac{k^e}{\mu} \nabla p^e \tag{7.2}$$

where $\mathbf{u}^e$ is the vector field of element-wise constant velocities, p^e is the local element pressure field, μ is the constant fluid viscosity, and k^e is the local permeability of a matrix volumetric element with an assumed constant value or a lower dimensional fracture element having a variable value related to the local hydraulic aperture obeying the cubic law for laminar flow between parallel plates. By applying a prescribed macroscopic pressure differential on each pair of opposite boundary surfaces with no-flow conditions on the remaining ones parallel to the flow direction, pressure diffusion is solved for all fracture and matrix elements of the entire domain. The equivalent permeability tensor of the fractured media is computed using element volume weighted averaging of pressure gradients and fluxes for elements e within a restricted subvolume V of the flow region away from the borders to eliminate boundary effects [Lang et al., 2014]

$$\frac{1}{V} \sum_e \int_{V^e} u_j^e dV^e = \frac{k_{ij}}{\mu} \frac{1}{V} \sum_e \int_{V^e} \frac{\partial p^e}{\partial x_i} dV^e \tag{7.3}$$

where u_j^e is the element-wise barycentric velocity in the j direction, $\partial p^e/\partial x_i$ is the element pressure gradient along x_i, and k_{ij} are the components of the symmetric second-rank permeability tensor $\mathbf{k}$:

$$\mathbf{k} = \begin{bmatrix} k_{xx} & k_{xy} & k_{xz} \\ k_{yx} & k_{yy} & k_{yz} \\ k_{zx} & k_{zy} & k_{zz} \end{bmatrix} \tag{7.4}$$

whose eigenvectors give the maximum, medium and minimum principal equivalent permeability, i.e. k_{max}, k_{med}, and k_{min}, respectively.

7.3 Numerical experiment setup

7.3.1 Persistent fracture network

The discontinuity system of a periodically fractured limestone involves three orthogonal sets of persistent fractures with their geological data given by Table 7.1. The two vertical sets are oblique at 45° to the model boundaries where far-field horizontal stresses are to be applied. In this study, dispersion of fracture orientation is ignored to avoid treating finite elements with extremely high aspect ratios caused by intersection between sub-parallel fractures from the same set. All fractures are assumed through-going (i.e. only persistent fractures are modelled), tending to provide an upper limit for rock deformability and permeability. In reality, such idealised persistent networks might still be representative of some special scenarios involving highly fractured "non-strata bound" sedimentary rock. Assumed material properties for this fractured limestone are given in Table 7.2 [Bandis et al., 1983; Lama and Vutukuri, 1978]. Due to the limits of current processing power, the numerical computation is technically constrained to consider only a relatively small scale virtual experiment and a 0.5 m × 0.5 m × 0.5 m cube-shaped rock sample is extracted for analysis here (Fig. 7.5).

Table 7.1 Geological data of the discontinuity system with three orthogonal sets of persistent fractures.

Fracture sets	Dip (°)	Dip direction (°)	Spacing (m)
Set 1	90	45	0.050
Set 2	90	315	0.075
Set 3	0	0	0.100

Table 7.2 Material properties of the fractured limestone.

Properties	Value
Bulk density ρ (kg/m3)	2700
Young's modulus E (GPa)	30
Poisson's ratio υ	0.27
Friction angle ϕ_r (º)	31
JCS (MPa)	120
JRC	15
Initial mechanical aperture b_0 (mm)	0.3
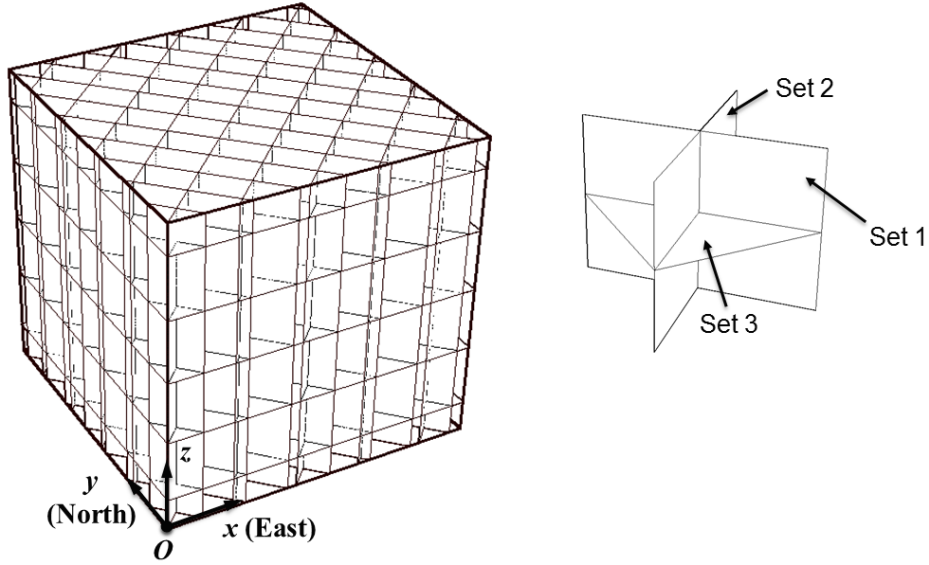
Fig. 7.5 A 0.5 m × 0.5 m × 0.5 m fracture network with three orthogonal sets of persistent fractures.

7.3.2 Procedure for numerical experiment
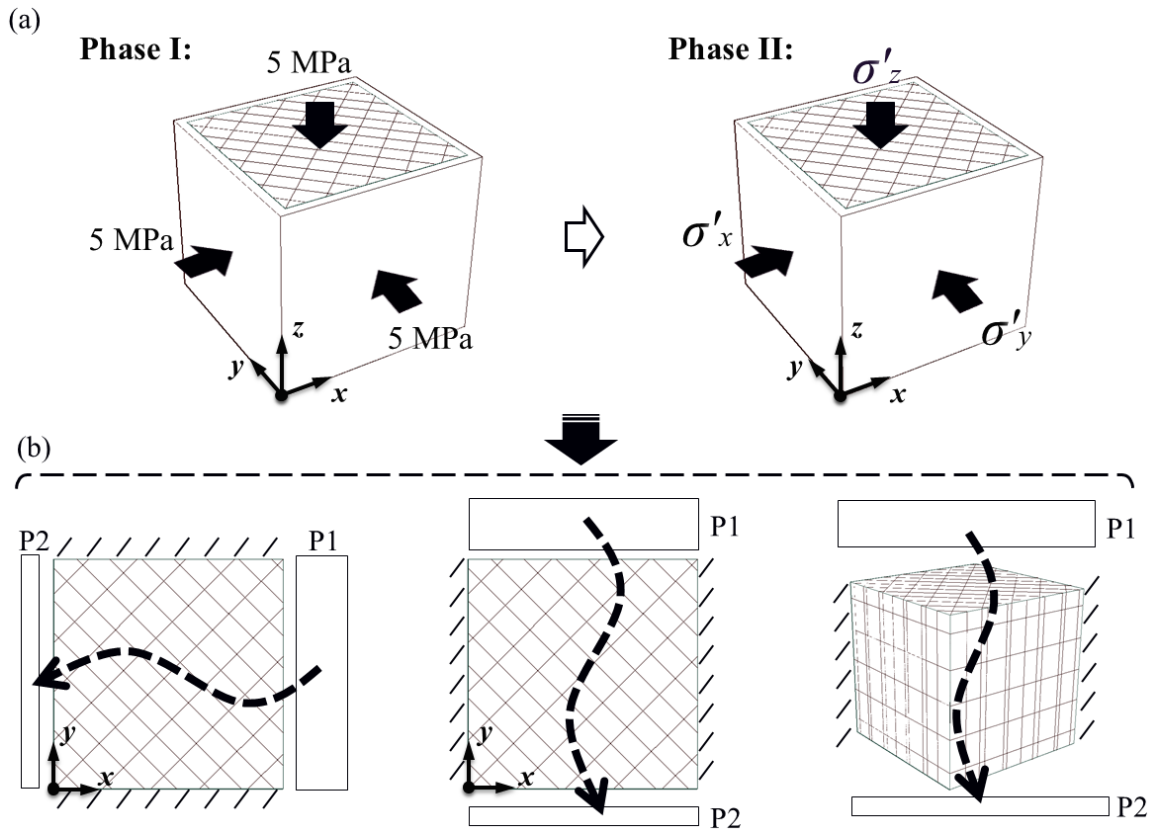
Fig. 7.6 Procedure for the numerical experiment: (a) mechanical modelling with polyaxial stress conditions loaded by two phases, and (b) calculation of the equivalent permeability based on single-phase steady state flow through the stressed sample under a prescribed macroscopic pressure differential imposed on each pair of opposite boundary surfaces while the remaining ones are impervious.

The fractured rock is considered to be at a depth of ~350 m with a pore fluid pressure ratio (i.e. the ratio of pore fluid pressure to lithostatic stress) equal to 0.45, producing an overburden effective stress of 5 MPa. The rock sample is designed to be surrounded by a hollow-box shaped buffer zone having a width of 0.025 m and a reduced Young's modulus of 0.3 GPa. The buffer material has no physically corresponding substance in a realistic rock mass. It is introduced purely as a means to create boundary conditions that have a less distorting effect in the corner regions of the main volume domain of interest. The effect of the buffer zone is to provide a semi-free displacement boundary constraint to accommodate potential large slipping in such persistent system. The bottom of the model is fixed in the vertical direction, to accommodate the body force effect, but has no constraint for movements in the horizontal plane (i.e. "roller" boundary condition).

Table 7.3 Loading scheme for the geomechanical experiment.

σ'_x	σ'_y	σ'_z	σ'_y/σ'_x
Phase I (lithostatic stress condition):			
5	5	5	1.0
Phase II (deviatoric stress conditions):			
5	5	10	1.0
5	10	10	2.0
5	11	10	2.2
5	12	10	2.4
5	13	10	2.6
5	14	10	2.8
5	15	10	3.0
5	20	10	4.0

The solid model is loaded in two consecutive phases (Fig. 7.6a and Table 7.3). First, an isotropic stress field ($\sigma'_x = \sigma'_y = \sigma'_z = 5$ MPa) is imposed to consolidate the rock sample under the effective lithostatic stress. Second, a series of deviatoric stress conditions is further loaded with a fixed $\sigma'_x = 5$ MPa, various $\sigma'_y = 5\text{-}20$ MPa, and an increased $\sigma'_z = 10$ MPa to consider the evolution of corresponding strike-slip tectonic regimes under an enhanced overburden stress

(Table 7.3). More stress conditions are explored for the horizontal stress ratio between 2.0 and 3.0 where the state is approaching the theoretical value for frictional sliding on ideally oriented pre-existing fracture walls (i.e. a ratio of 3.1) given that the friction coefficient equals to 0.6 [Zoback, 2007]. Though, in the field, observed stress ratios are generally less than 2.0, values larger than this is used for the sake of studying the effect from typical to extreme conditions to bring out clearly the system behaviour. A larger ratio may also represent conditions close to an excavation or fluid injection point. In any case, the simulations may correspond to laboratory measurements where such stress ratios may be imposed. Single-phase steady state fluid flow through the deformed fracture network with stress-induced variable apertures is further modelled by imposing the classical permeameter boundary condition: two opposite boundary surfaces of the cube have fixed heads while the four orthogonal boundaries parallel to the flow direction are impervious (Fig. 7.6b).

7.4 Results

7.4.1 Fracture apertures
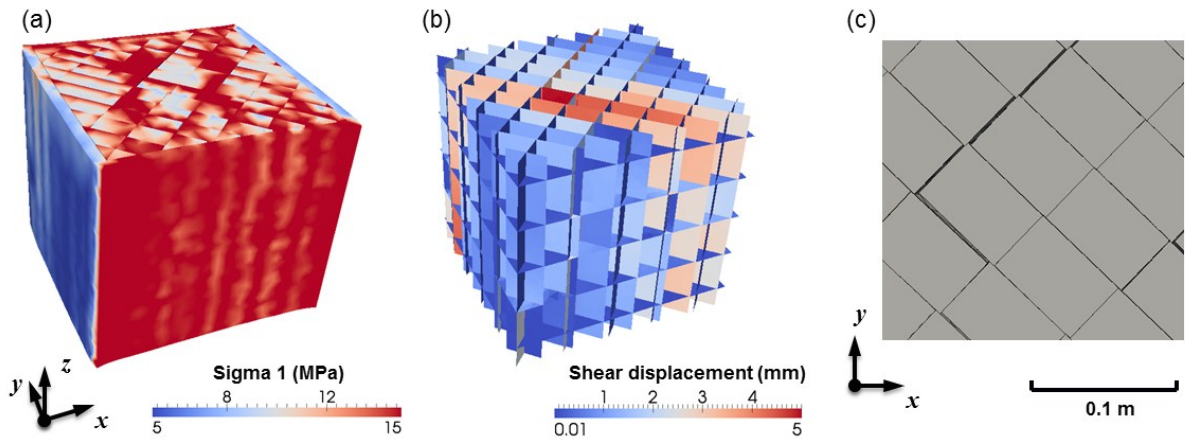
Fig. 7.7 (a) Distribution of differential stress in the matrix blocks, (b) distribution of fracture shear displacement in log scale, and (c) fracture openings caused by block rotations (observed from the top of the model) of the fractured rock under the polyaxial stress condition of $\sigma'_x = 5$ MPa, $\sigma'_y = 15$ MPa, and $\sigma'_z = 10$ MPa.

The model that has arrived at equilibrium under the initial isotropic stress condition further adjusts to a new deformed state when various polyaxial stress fields are loaded. The stress ratio

of σ'_y/σ'_x triggers stress heterogeneity in the matrix blocks (Fig. 7.7a), shear displacements along the two vertical sets (Fig. 7.7b), and even mesoscopic fracture openings caused by block rotations if the stress ratio is high enough (Fig. 7.7c).

Hydraulic aperture of the stressed fracture networks is calculated as the summation of mesoscopic opening caused by fracture interaction and block rotation, and microscopic aperture governed by the surface roughness nature. Effect of stress generates significant fracture-scale heterogeneity for the distribution of hydraulic apertures in single fractures. Fig. 7.8 shows the heterogeneous aperture contour of a vertical fracture extracted from the network under the deviatoric stress condition with $\sigma'_y/\sigma'_x = 3$. Very large apertures are clustered in some local areas, which seem to be connected and form a slightly diverted vertical channel from the top to the bottom of the model.
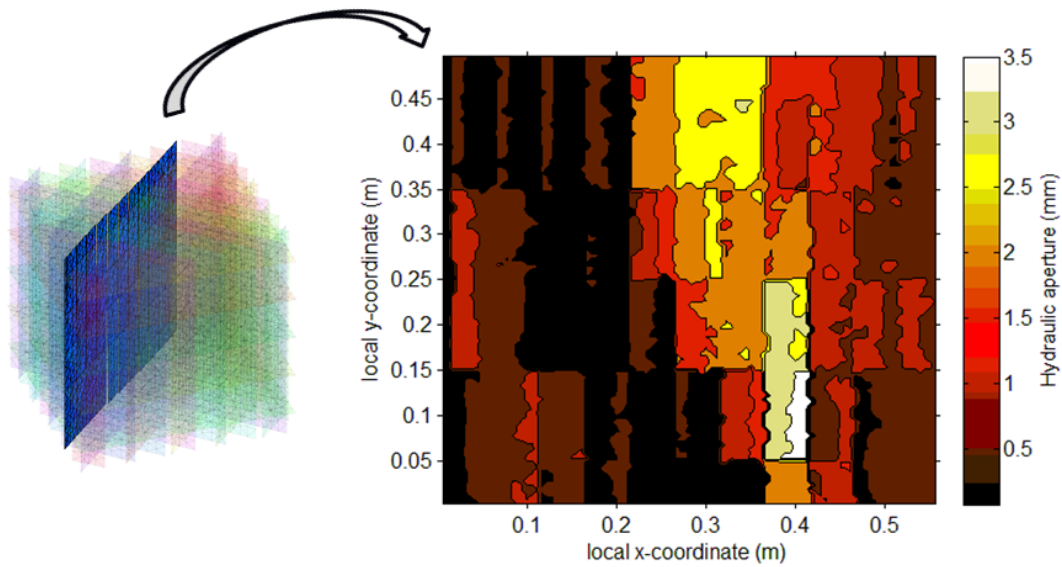
Fig. 7.8 Distribution of hydraulic aperture within a single fracture under the polyaxial stress condition of $\sigma'_x = 5$ MPa, $\sigma'_y = 15$ MPa, $\sigma'_z = 10$ MPa.

Fig. 7.9 shows the network-scale distribution of hydraulic apertures in log scale under different polyaxial stress conditions. In the stress case of $\sigma'_y/\sigma'_x = 1$, hydraulic apertures are uniformly distributed and exhibit quite low magnitude in such an isotropic stress field. With the increase of the far-field stress ratio, heterogeneity of fracture apertures begins to emerge and develop. Especially in cases of $\sigma'_y/\sigma'_x \geq 3$, very large hydraulic apertures are localised in some fractures of the two vertical sets that are favourably oriented for shearing.
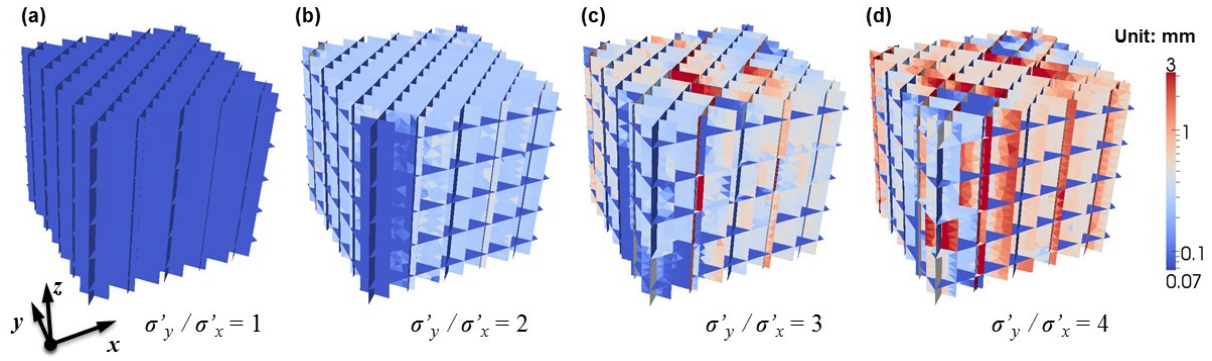
Fig. 7.9 Distribution of hydraulic apertures in the fracture network under various polyaxial stress conditions: (a) $\sigma'_y/\sigma'_x = 1$, (b) $\sigma'_y/\sigma'_x = 2$, (c) $\sigma'_y/\sigma'_x = 3$, (d) $\sigma'_y/\sigma'_x = 4$, given that $\sigma'_x = 5$ MPa and $\sigma'_z = 10$ MPa.
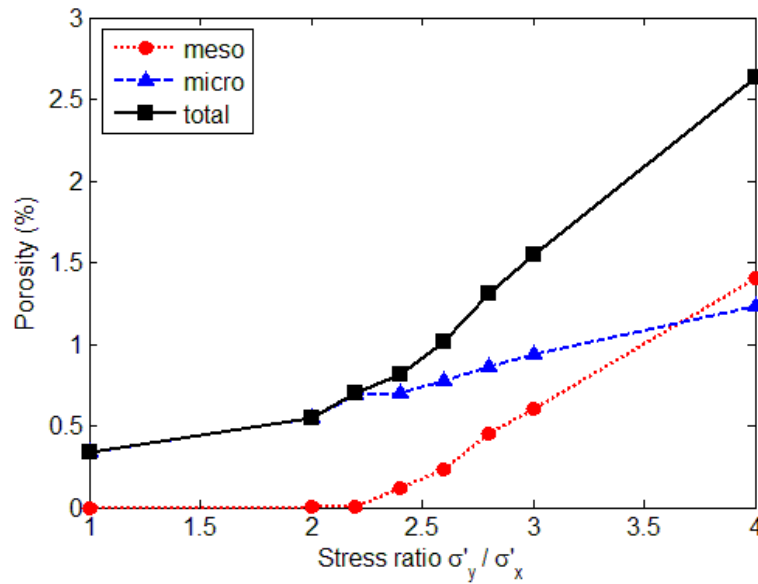
Fig. 7.10 Fracture porosity of the fractured rock under various polyaxial stress conditions: the three curves represent the porosity induced by mesoscopic effects, microscopic effects and the value of total porosity, respectively.

Fracture porosity is calculated as the proportion of fracture hydraulic aperture space to the total rock mass volume. The contributions from mesoscopic and microscopic effects are distinguished to isolate the sources of hydraulic apertures under different stress conditions (Fig. 7.10). In the case with a low stress ratio, e.g. $\sigma'_y/\sigma'_x < 2.5$, fracture porosity is mainly dominated by the microscopic roughness effect. As the stress ratio increases, the microscopic component exhibits moderate increase due to shear dilatancy, while the mesoscopic counterpart begins to

manifest itself by a dramatic growth. As a result, the total porosity shows a continuous increasing trend under the increased differential stress ratio. It seems that the microscopic and mesoscopic porosity components as well as the total porosity display a positive linear relation with the stress ratio when $\sigma'_y/\sigma'_x > 2.5$.

7.4.2 Equivalent permeability

Matrix permeability k_m is assumed to have a low value, i.e. 1×10^{-15} m^2, to produce a high fracture-matrix permeability contrast and impose a condition close to fracture-only flow. Poroelastic effect of the Biot-type coupling between pore fluid pressure and solid elastic stress [Rutqvist and Stephansson, 2003] is only modelled for a particular scenario with the Biot coefficient equal to 1.0. The equivalent permeability of the fractured rock under various polyaxial stress conditions is derived from the steady state flow simulation, where a subvolume is conservatively chosen with a distance of 10% of the model size away from the nearest domain boundaries. As shown in Fig. 7.11, the increased stress ratio of σ'_y to σ'_x leads to considerable increase over several orders of magnitude in the diagonal of the permeability tensor, i.e. components, k_{xx}, k_{yy}, and k_{zz}. A transition regime with steep permeability increase occurs when the far-field stress ratio is approaching the critical threshold (i.e. 3.1) [Zoback, 2007].
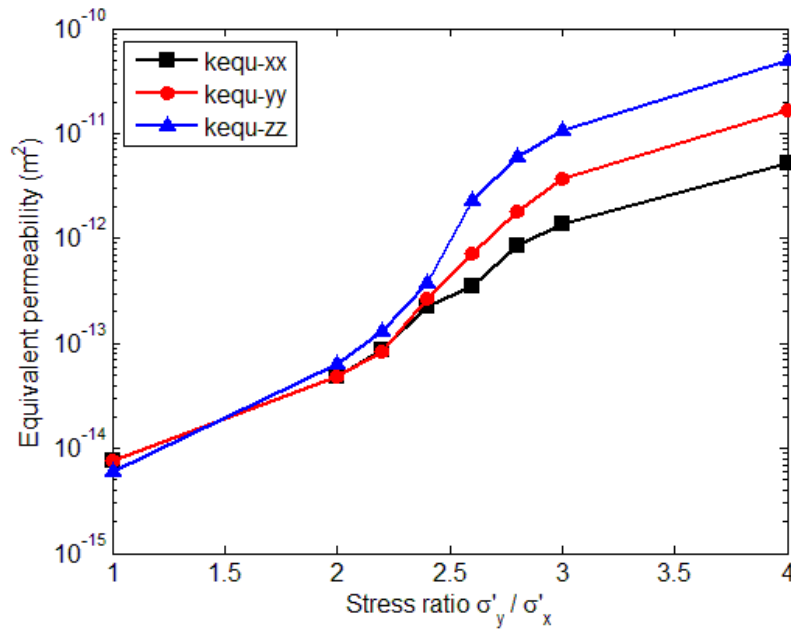
Fig. 7.11 Equivalent permeability of the fractured rock under various polyaxial in-situ stress conditions.
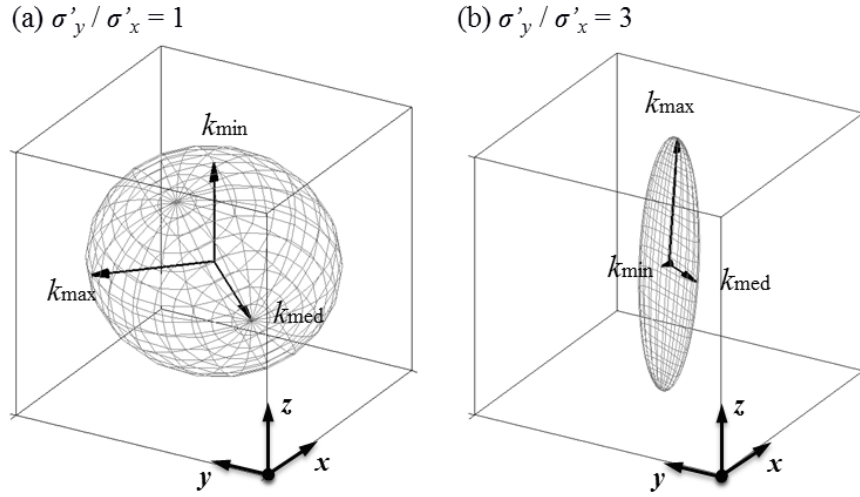
Fig. 7.12 Ellipsoid visualisation, after normalisation with respect to k_{max}, of the permeability tensor of the fractured rock under different polyaxial stress conditions: (a) $\sigma'_x = 5$ MPa, $\sigma'_y = 5$ MPa, $\sigma'_z = 10$ MPa, (b) $\sigma'_x = 5$ MPa, $\sigma'_y = 15$ MPa, $\sigma'_z = 10$ MPa. Note k_{max} in (b) is >1000 times k_{max} in (a).
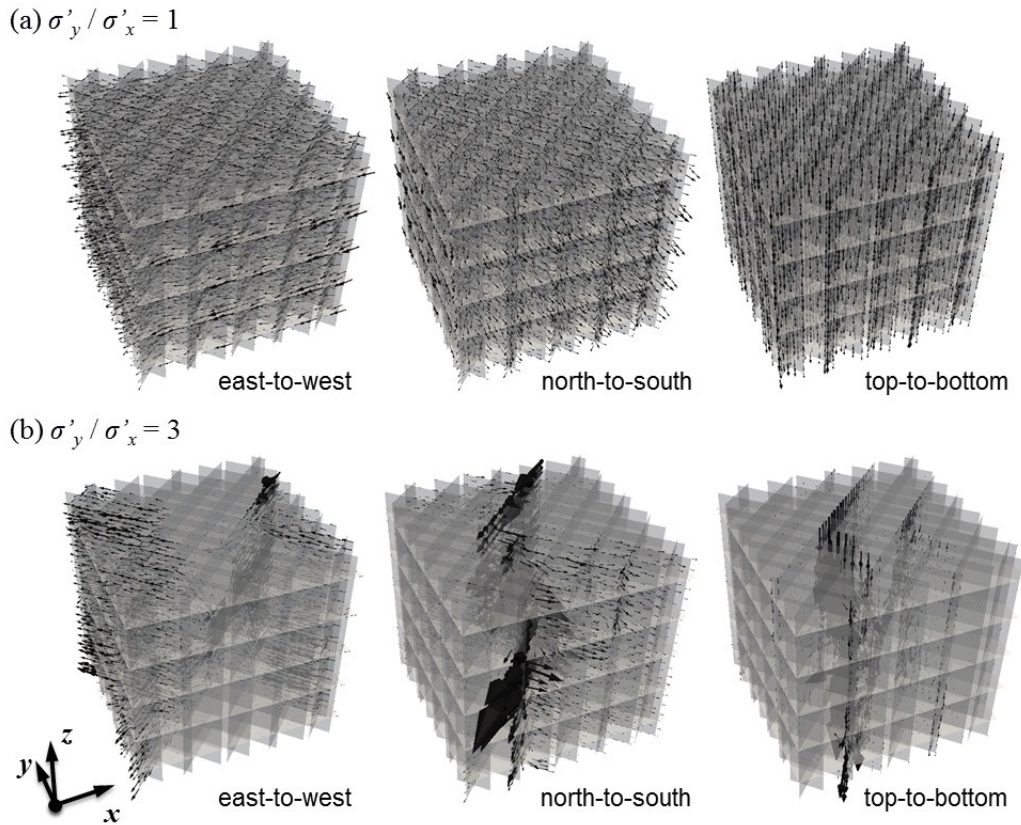
Fig. 7.13 Flow pathways in the fractured rocks under different polyaxial stress conditions: (a) $\sigma'_x = 5$ MPa, $\sigma'_y = 5$ MPa, $\sigma'_z = 10$ MPa, (b) $\sigma'_x = 5$ MPa, $\sigma'_y = 15$ MPa, $\sigma'_z = 10$ MPa (note the flow arrow sizes representing local flux magnitudes in the flow simulation of the case $\sigma'_y/\sigma'_x = 3$ are scaled down by a factor that is 20, 50, and 100 times the one of the case $\sigma'_y/\sigma'_x = 1$ for east-to-west, north-to-south, and top-to-bottom pattern, respectively).

The permeability tensor is visualised as a triaxial ellipsoid with three semi-principal axes indicating the magnitudes of maximum, medium, and minimum principal permeability, i.e. k_{max}, k_{med}, and k_{min}, respectively (Fig. 7.12). Normalisation is performed with respect to corresponding k_{max} since the absolute values span several orders of magnitude. In the case of $\sigma'_y/\sigma'_x = 1$, the permeability tensor ellipsoid is quite isotropic, despite of the intrinsic anisotropy in fracture geometries. In the case with higher stress ratios, e.g. the one of $\sigma'_y/\sigma'_x = 3$, significant permeability anisotropy is induced by the deviatoric stress acting with respect to the favourably oriented vertical fractures, resulting in a very high permeability in the subvertical direction.

The increased far-field stress ratio also leads to considerable change in flow patterns as illustrated by Fig. 7.13. In the case of $\sigma'_y/\sigma'_x = 1$, fluid spreads through the whole network due to the quite uniformly distributed apertures. However, in the case of $\sigma'_y/\sigma'_x = 3$, fluid flow is localised in some zigzag-shaped pathways corresponding to the large aperture channels formed by parts of some fractures of the two vertical sets.

7.5 Discussion

Stress-induced heterogeneity of hydraulic apertures of a 3D persistent fracture network has been modelled with consideration of both fracture-scale and network-scale effects. In cases with lower stress ratio, fracture porosity is mainly controlled by the fracture-scale microscopic roughness effect. With the increase of stress ratio, pre-existing fractures were reactivated for shearing and matrix blocks were mobilised into rotation and sliding at the mesoscale, which created some large openings along block boundaries. As a result, even in the persistent fracture, local hydraulic apertures can vary greatly, as shown in Fig. 7.8. The formation of large aperture channels due to such network-scale mechanical interactions leads to significant flow localisation and dramatic increase of overall hydraulic conductivity. The transition stage of permeability with steep growth that occurred when the far-field stress ratio is approaching the critical threshold (Fig. 7.11) shows consistency with the results of 2D fracture network modelling [Min et al., 2004b].

The results of the case under a critically stressed state, e.g. $\sigma'_y/\sigma'_x = 3$, are of particular interest. First, the shear displacement is extremely heterogeneous, in spite of being given such regular geometrical configurations of fracture sets. The system finds equilibrium by activating

sliding with local extremes of shear displacement as highlighted in Fig. 7.7b. Locally, the sliding on the two vertical sets has created large aperture channels parallel to the active fractures (Fig. 7.8), which shows consistency with the field observation from boreholes that critically stressed faults with favourable orientations appear to have much higher hydraulic conductivity [Zoback, 2007]. The result supports what is already known of the strike-slip faulting regime, that significantly higher permeability can be anticipated in the vertical direction associated with localised flow along displacing and dilating fractures [Sibson, 1994; Sanderson and Zhang, 1999]. This raises the question of whether the imposed boundary conditions with orthogonally applied stresses and semi-free displacement constraints are the most appropriate for modelling mechanical behaviour of the rock sample with such persistent fractures and whether the localisation effect is exaggerated by considering a domain with such few idealised fractures. However, some fundamental mechanisms captured in this idealised fractured rock model, e.g. stress-induced fracture dilation, block rotation and flow localisation, would probably exist in more complicated systems having arbitrarily shaped and oriented fractures, which has been proven in many 2D models [Zhang and Sanderson, 1996; Min et al., 2004b; Baghbanan and Jing, 2008; Latham et al., 2013; Lei et al., 2014].

The high sensitivity of equivalent permeability (Fig. 7.11 and 7.12) and flow structure (Fig. 7.13) to the polyaxial stress condition indicates that special attention is required when the in-situ stress state of rock masses is significantly perturbed resulting from natural or human activities. For example, unloading effects during the excavation of underground infrastructures may cause significant stress redistribution surrounding the openings (see Chapter 9); injections and extractions of fluids during oil/gas reservoir production can significantly change the pore fluid pressure level and further vary the effective stress state of rock masses; multiple complex factors (e.g. underground excavation, radioactivity-induced heat transfer, and glaciation loading) can engender remarkable changes on the geomechanical condition of nuclear waste repositories. Such irreversible perturbations may lead to intensive fault reactivation, dramatic flow enhancement, and severe construction risk. Needless to say, the modelling methods employed in this study can also be applied to investigate more permeable matrix rock scenarios. The extreme nature of the flow anisotropy would be somewhat ameliorated by modelling a rock system with a

more permeable matrix material. However, the realism of the "persistent-only" fracture model with no new fracturing adopted here may come into question as such a rock mass with weak sedimentary rock properties may be weak enough to locally propagate new fractures before the exceptionally high in-situ stress ratios considered here could be generated.

Unlike some other conventional 3D upscaling methods in the literature [Snow, 1969; Oda, 1985, 1986; Renard and de Marsily, 1997] that do not require explicit mechanical and flow simulations to compute the equivalent hydraulic properties, the proposed approach here may not be a practical solution under the limits of current processing power. This is a particular problem for applications to real reservoirs with domains spanning hundreds or thousands of metres and consisting of millions of fractures. However, this study still has important implications for upscaling permeability to grid block properties for 3D reservoir flow simulation. For example, the results obtained in this study imply that determination of an REV size, if it exists, may be a sophisticated process that requires many coupled effects to be considered in the model including not only the description of geometrical features, but also, characterisation of the geomechanical setting and changes resulting from any perturbation of the stress field. Indeed, it is recognised that there is unlikely to be an REV once a realistic system with impersistent fractures is modelled due to its intrinsic fractal nature [Bonnet et al., 2001]. The next step is to model more realistic 3D fracture networks which have pre-existing fractures of finite sizes and new fractures induced by stress concentrations (see Chapter 8).

7.6 Concluding remarks

To conclude, this chapter presented a stress-induced variable aperture model to capture the effects of polyaxial stress conditions on the flow properties of 3D persistent fracture networks. Geomechanical behaviour of the rock mass was simulated by the FEMDEM solid model, where a fracture treated as the interface between discrete matrix bodies can open, shear and dilate in the heterogeneous stress field. Under the stress condition with a relatively lower differential stress ratio, fracture apertures are mainly governed by the fracture-scale roughness effect. With the increase of the in-situ stress ratio, fractures with favourable orientations are reactivated to shear and matrix blocks bounded by the shearing fractures are promoted to rotate, which generates significant fracture openings at the block boundaries. Such fracture openings tend to be the

dominant contributor to the aperture field in high stress ratio conditions. To prepare for the flow modelling required in this work, a new discrete fracture system indexing logic was developed based on a breadth-first search of ternary-tree structures to systematically identify the 3D fracture network topology associated with the stress-induced variable apertures. Based on a series of single-phase flow simulations, the equivalent permeability of the stressed fractured rock was computed, ranging over more than three orders of magnitude with respect to the variation of the effective stress ratio. A near-isotropic permeability tensor was observed in the case with a lower stress ratio, whereas the fractured rock under a critical stress state exhibits highly anisotropic features in its permeability. Fluid flow tends to localise in some critically stressed fractures that have much higher hydraulic conductivity than other fractures which are not significantly reactivated for shearing. The large aperture channels that are optimally oriented with regard to the direction of pressure gradient provide a major pathway for fluid migration. The results of this study have important implications for upscaling permeability to grid block properties for reservoir flow simulation as well as other relevant engineering problems.

8 Hydromechanical modelling of a realistic 3D fracture network

8.1 Introduction

The stress effects on fluid flow for 2D fracture networks and an idealised 3D persistent fracture network have been investigated in the previous chapters using the 2D/3D JCM-FEMDEM model developed. In this chapter, these understandings will be extended to the scenario of geologically realistic 3D fracture networks with interconnected, impersistent and bent discontinuities. The aim of this research is to take advantage of all the relevant new FEMDEM modelling techniques in a 3D context and to investigate fluid flow in a stressed 3D fracture system without the constraint of parallel persistent discontinuities as imposed in Chapter 7.

Under in-situ stress conditions, fractures with tips that terminate in the intact rock matrix and are aligned subparallel to the maximum principal stress direction are susceptible to aperture opening and length extension driven by the high tensile stresses concentrated at their tips [Pollard and Segall, 1987]. Furthermore, the sliding of pre-existing discontinuities can also generate stress concentrations at their ends and trigger the formation of wing cracks or secondary cracks [Willemse and Pollard, 1998]. The new cracks can link pre-existing discontinuities to provide important pathways for fluid migration and enhance the connectivity and permeability of the geological formation. To simulate the complex brittle fracture process, the 3D FEMDEM solver embedded with a newly developed 3D crack propagation model [Guo et al., 2015, 2016] is used in this research. This 3D fracture model, implemented in the 3D FEMDEM code is a 3D extension of the smeared crack model (also known as the cohesive zone model) developed for the 2D FEMDEM [Munjiza et al., 1999] and based on the 3D FEMDEM framework [Munjiza, 2004; Xiang et al., 2009a] for solving solid deformation and multi-body interaction of discontinuum systems. To achieve geomechanical modelling of fracture networks, the code is extended to incorporate the 3D JCM model, the principles of which have been described in Chapter 4 and 7. By including the roughness effects of fractures via the 3D JCM approach, it is possible to capture the mechanical behaviour of rough fractures including degraded shear strength and nonlinear normal/shear displacement characteristics. Deformation of 3D discrete

fracture networks and stress-induced aperture changes are computed. The hydraulic behaviour of the stressed fractured rock is then modelled using single-phase steady state fracture-matrix flow with the equivalent permeability further derived (see section 7.2.2 for the governing equations). This research will focus on the stress effects. The complexity of scale effects and the possible existence of an REV are also potentially of great significance, which are, however, beyond the scope of this study.

8.2 Numerical method

The principles of the 3D FEMDEM approach for solving stress, deformation and interaction as well as fracture propagation in discontinuous solid media are similar to those of the 2D FEMDEM as presented in Chapter 4. Below, only the small adaptions found to be necessary for the 3D formulation are described.

The combined fracture-matrix solid system of a 3D fractured rock is represented by a discontinuous discretisation of the model domain using four-noded tetrahedral finite elements and six-noded joint elements embedded between the facets of neighbouring tetrahedra. Each tetrahedral element is connected with four joint elements and each joint element is linked to two tetrahedral volumes. There are two types of joint elements: cohesive (i.e. unbroken) joint elements and fracture (i.e. broken) joint elements. Cohesive joint elements are constructed by a detachment algorithm based on the original continuous configuration between tetrahedral elements in the matrix domain, whereas fracture joint elements are generated based on the initial overlapping surfaces of opposite tetrahedral elements located on pre-existing discontinuities. The joint elements (either broken or unbroken) are created and inserted between the facets of tetrahedral element pairs before the numerical simulation and no further remeshing process is performed during later computations. Fig. 8.1 presents a schematic illustration of two generic scenarios where two tetrahedral elements are neighbours in 3D space. In the first example, two tetrahedral elements, i.e. $N_1N_2N_3N_4$ and $N_5N_6N_7N_8$, are linked by a fracture joint element i.e. $N_1N_4N_3$-$N_7N_6N_5$, which is located on the plane of a pre-existing discontinuity. In the second example (b), two tetrahedral elements, i.e. $N_1N_2N_3N_4$ and $N_9N_{10}N_{11}N_{12}$, are connected by a cohesive joint element i.e. $N_2N_3N_4$-$N_{10}N_{11}N_9$, which is inside the intact rock matrix.
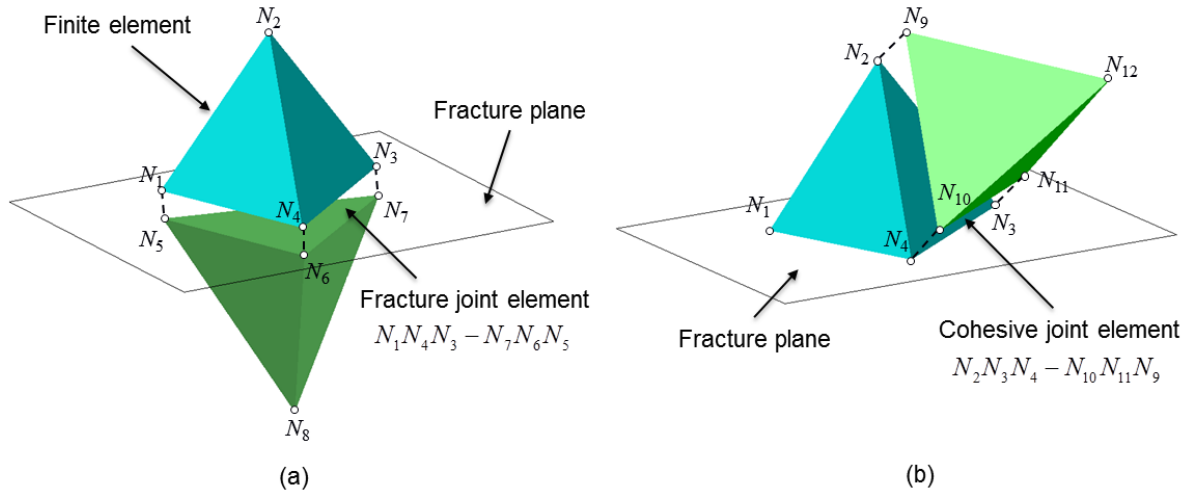
Fig. 8.1 Two tetrahedral finite elements linked by (a) a fracture joint element or (b) a cohesive joint element in 3D FEMDEM.
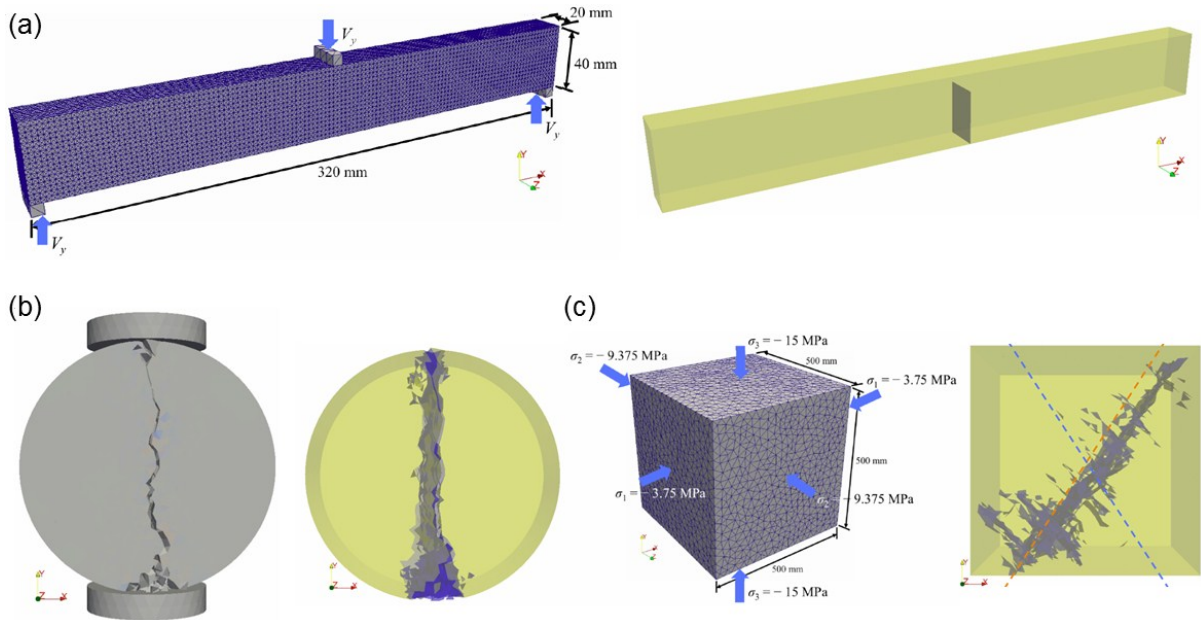
Fig. 8.2 The capability and validity of the 3D FEMDEM formulation embedded with a smeared crack model for capturing the fracturing of brittle/quasi-brittle materials have been demonstrated based on (a) three-point bending tests, (b) Brazilian disc tests, and (c) polyaxial compression tests [Guo, 2015].

The deformation of the bulk material is captured by the linear-elastic constant-strain tetrahedral finite elements with the impenetrability enforced by a penalty function and the continuity constrained by the constitutive relation for cohesive joint elements [Munjiza et al., 1999], while the interaction of matrix bodies through discontinuity interfaces is simulated by the penetration calculation [Munjiza et al., 2000] along fracture joint elements. Propagation of new

173

fractures is modelled by the transition of cohesive joint elements to fracture joint elements in a 3D unstructured grid system. The capability and validity of a smeared crack model implemented in the 3D FEMDEM for capturing the fracturing of brittle/quasi-brittle materials have been demonstrated based on a series of (a) three-point bending tests, (b) Brazilian disc tests, and (c) polyaxial compression tests (Fig. 8.2) [Guo, 2015].

The topology of a 3D fracture network (discretised into a system of fracture joint elements) is identified using the ternary-tree search algorithm (see section 7.2.1). Each block facet (i.e. isolated fracture patch bounded by the intersections with other fractures or model boundaries) is treated as an individual fracture having size-dependent roughness properties with their deformation characterised by the combined JCM-FEMDEM formulation (see section 4.3&4.4).

8.3 Numerical experiment setup

8.3.1 A 3D fractured layer with realistic joint sets
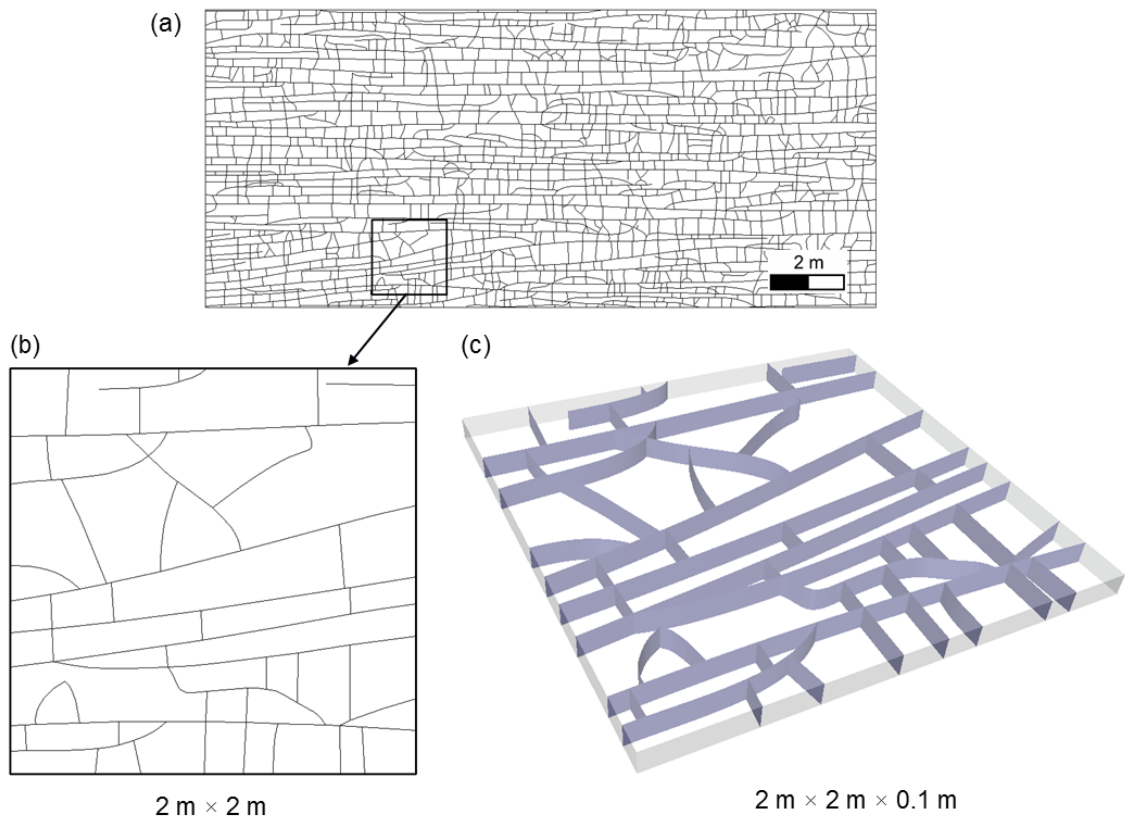
Fig. 8.3 (a) An 18 m × 8 m fracture network mapped at the limestone exposure at the south margin of the Bristol Channel Basin, UK [Belayneh and Cosgrove, 2004], (b) a 2 m × 2 m fracture pattern is selected and (c) extruded with a height of 10 cm (i.e. bed thickness) to build the 3D fractured layer geometry.

The fracture network used in this research is based on the outcrop map (Fig. 8.3a) of a limestone bed located at Kilve on the southern margin of the Bristol Channel Basin, UK [Belayneh and Cosgrove, 2004]. The fractured limestone bed (10 cm thick) is sandwiched between almost impervious shales and the vertically dipping joints are layer bound (do not extend into the neighbouring shales). The joint network exhibits a ladder pattern consisting of two major sets. The E-W striking set (Set 1) that formed in an early stage contains "through-going" (or persistent) fractures. The N-S striking set (Set 2) developed later and is characterised by short joints abutting the fractures of Set 1. It can be noted that this highly hierarchical joint pattern is featured by "T" and "X" type fracture nodes with only a few "I" type nodes (i.e. "dead-end" fracture tips). Considering the very expensive runtime of 3D FEMDEM simulations, a 2 m × 2 m pattern (Fig. 8.3b) is selected from the original 18 m × 8 m analogue for geomechanical computations. The extracted 2D network is extruded by 10 cm (i.e. the thickness of the layer) to build a 3D geometry (Fig. 8.3c). Assumed material properties for this fractured limestone are given in Table 8.1 [Bandis et al., 1983; Lama and Vutukuri, 1978].

Table 8.1 Material properties of the fractured limestone.

Properties	Value
Bulk density ρ (kg/m3)	2700
Young's modulus E (GPa)	30
Poisson's ratio υ	0.27
Tensile strength f_t (MPa)	7
Internal friction angle ϕ_i (°)	26.6
Cohesion c (MPa)	15
Mode I energy release rate G_I (J·m^{-2})	100
Mode II energy release rate G_{II} (J·m^{-2})	400
Residual friction angle ϕ_r (°)	31
Laboratory sample length L_0 (m)	0.2
JCS$_0$ (MPa)	169
JRC$_0$	9.7
Initial mechanical aperture b_0 (mm)	0.194

8.3.2 Procedure for numerical experiment

		σ'_x (MPa)	σ'_y (MPa)	σ'_z (MPa)
Case A		5	5	10
Case B		5	10	10
Case C		10	5	10
Case D		5	15	10
Case E		15	5	10
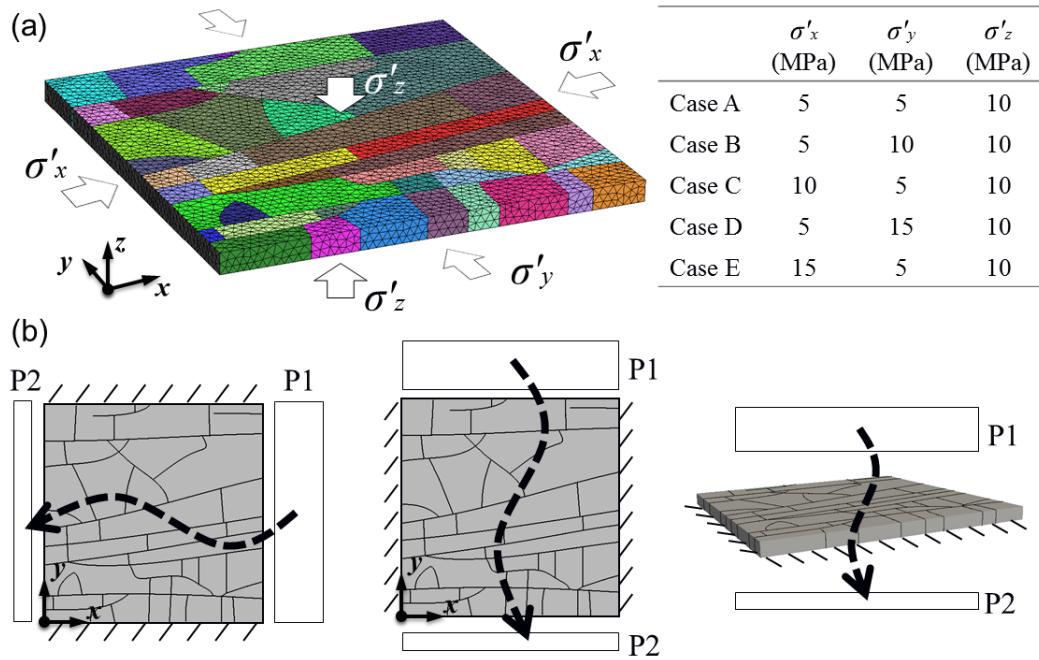
Fig. 8.4 Procedure for the numerical experiment: (a) geomechanical modelling with polyaxial stresses applied on the boundaries of the problem domain (2 m × 2m), and (b) calculation of the equivalent permeability based on single-phase steady state fluid flow through the stressed layer under a prescribed macroscopic pressure differential imposed on each pair of opposite boundaries while the remaining ones are impervious.

The fractured limestone is considered to be at a depth of ~700 m with a pore fluid pressure ratio (i.e. the ratio of pore fluid pressure to lithostatic stress) equal to 0.45, producing an overburden effective stress of 10 MPa (i.e. $\sigma'_z \equiv 10$ MPa). The gravitational body forces are neglected for this thin-bedded layer. The problem domain containing intersected pre-existing fractures is discretised by an unstructured mesh with an average element size of ~3.0 cm (Fig. 8.4a). Geomechanical behaviour of the fractured layer in response to polyaxial (true-triaxial) effective stresses is simulated using the 3D FEMDEM model. The effect of pore fluid pressure is assumed to be a second-order factor for aperture development and is not included in the simulation. The poroelastic effect of the Biot-type coupling between pore fluid pressure and solid elastic stress is only modelled for a particular scenario with the Biot coefficient for the solid skeleton compressibility equal to 1.0. A series of in-situ stress conditions explore with the following horizontal stress ratios: $\sigma'_x/\sigma'_y = 1/3, 1/2, 1, 2, 3$ (Fig. 8.4a). Single-phase steady state

fluid flow through the deformed fracture network with stress-induced variable apertures is further modelled by imposing the classical permeameter boundary condition: two opposite boundary surfaces of the rectangular volume domain have fixed heads while the four orthogonal boundaries parallel to the flow direction are impervious (Fig. 8.4b). Matrix permeability k_m is assumed to have a low value, set here at 1×10^{-15} m^2, to produce a high fracture-matrix permeability contrast and impose a condition close to fracture-only flow.

8.4 Results

8.4.1 Stress heterogeneity

The fractured rocks arrived at equilibrium and exhibit distinct stress heterogeneity patterns under different polyaxial stress conditions. The distribution of maximum principal stresses in Case A loaded by an isotropic horizontal stress condition (i.e. $\sigma'_x = \sigma'_y = 5$ MPa) is quite uniform and dominated by the overburden stress (i.e. $\sigma'_z = 10$ MPa) (Fig. 8.5a). With the increase of the stress ratio (either σ'_y/σ'_x or σ'_x/σ'_y), stress heterogeneity begins to emerge and escalate, with the contour of maximum principal stresses being organised to follow the direction of the applied maximum horizontal stress (Fig. 8.5b-e).
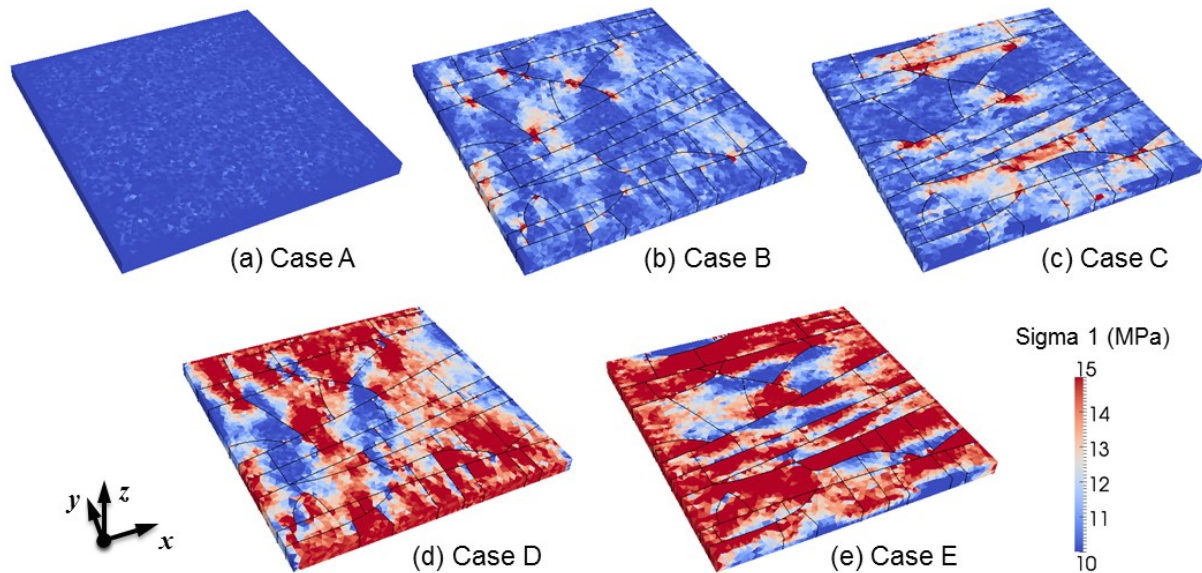
Fig. 8.5 Distribution of maximum principal stresses in the fractured layer under different polyaxial stress conditions: (a) Case A, $\sigma'_x = 5$ MPa, $\sigma'_y = 5$ MPa; (b) Case B, $\sigma'_x = 5$ MPa, $\sigma'_y = 10$ MPa; (c) Case C, $\sigma'_x = 10$ MPa, $\sigma'_y = 5$ MPa; (d) Case D, $\sigma'_x = 5$ MPa, $\sigma'_y = 15$ MPa; (e) Case E, $\sigma'_x = 15$ MPa, $\sigma'_y = 5$ MPa.

Note $\sigma'_z = 10$ MPa for all cases.

8.4.2 Shear displacement

The joint network in Case A is associated with very low (or almost zero) shear displacements under the isotropic horizontal stress field (Fig. 8.6a). However, an increased horizontal stress ratio triggers and intensifies the sliding of pre-existing fractures (Fig. 8.6b-e). In Case B and D, the maximum horizontal stress is applied in the y direction, which accommodates moderate shearing along some bent fractures in Set 2, which are also oblique to σ'_y. However, in Case C and E, much higher shear displacements occur and concentrate in some through-going fractures of Set 1 which are striking oblique to the applied maximum horizontal stress σ'_x. Hence, the occurrence of high shear displacements is not only related to the orientation of fractures, but also their connectivity and persistence. The truncated fractures of Set 2 are more suppressed for shearing, because they are constrained by intact blocks at their ends and the shearing forces tend to be dissipated by the through-going fractures of Set 1. However, the fractures of Set 1 that penetrate the whole domain create much easier weakness zones to localise sliding and accommodate the applied bulk differential stresses, with no displacement constraints from intact rocks at their ends. The high shear displacements in Case C-E are expected to create larger dilations and apertures in the fractures.
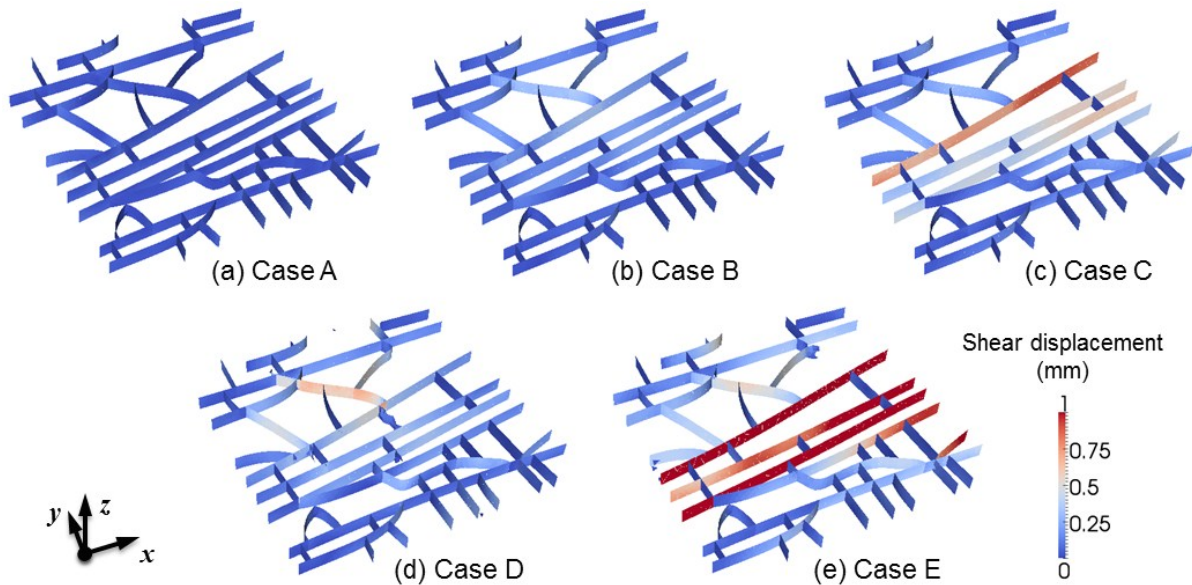
Fig. 8.6 Distribution of shear displacements in the joint network of the fractured layer under different polyaxial stress conditions.

8.4.3 Crack propagation

Propagation of new cracks only appeared in Case D and E, both of which are associated with a high horizontal stress ratio of 3. In Case D, several minor cracks grew from "T" intersections, where the fractures of Set 2 abut the ones of Set 1. The new cracks that developed from the tips of fractures that are subparallel to the y direction seem to be governed by mode I tensile failure, while the cracks that extended from oblique fractures are more induced by mode II shear failure. More interestingly, one quite long new crack initiated and propagated from the middle of a persistent fracture of Set 1 and was mainly driven by tensile failure. It links another fracture of Set 1 and exhibits an "abutting" characteristic quite similar to that of the natural joint sets. This fracturing process is considered to be related to the stress-induced bending of the rock block that the new crack penetrated. In Case E, less fracturing occurred. One crack nucleated from the bending point of a tortuous fracture and propagated generally following the direction of the maximum horizontal stress σ'_x. Surprisingly perhaps, the two joints (close to the back of the layer) which are subparallel to σ'_x and associated with "dead-end" tips did not propagate. Actually, the minimum principal stresses at their tips were found in a compressive state and far from reaching the rock tensile strength.
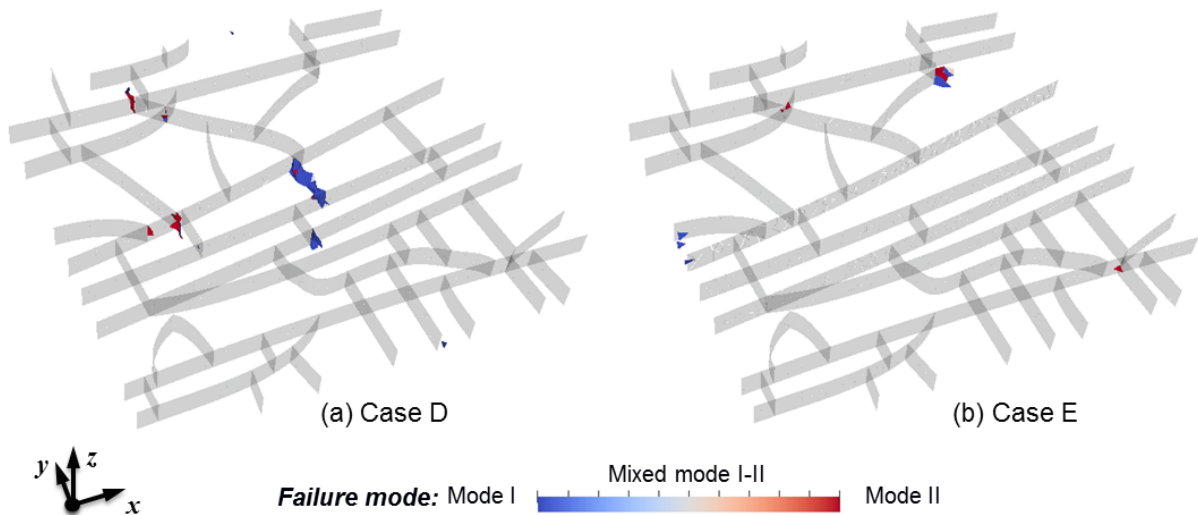
Fig. 8.7 Propagation of new cracks under the stress conditions with a high stress ratio: (a) Case D, σ'_y/σ'_x = 3, and (b) Case E, σ'_x/σ'_y = 3 (note: geometries in transparent gray colour represent the pre-existing fractures).

8.4.4 Hydraulic apertures

Fig. 8.8 shows the distributions of hydraulic apertures on a logarithmic scale under different polyaxial stress conditions. In Case A, hydraulic apertures are almost uniformly distributed. The relatively smaller apertures in some short fracture sections are probably related to their higher scaled JRC_n and JCS_n values (see Eq. (4.28) and (4.29)). With the increase of the horizontal stress ratio, heterogeneity of fracture apertures develops with some very large apertures localised at the fractures associated with high shear displacements. Note that the initial mechanical apertures of all fractures were assigned a constant value of 0.194 mm (see Table 8.1) before the boundary stress loading. However, due to the nonlinear relation between the mechanical and hydraulic apertures (see Eq. (4.48)), the initial hydraulic apertures vary for different fractures with various sizes and JRC_n values and are in a range of 0.020-0.242 mm (larger values for larger fracture sections).
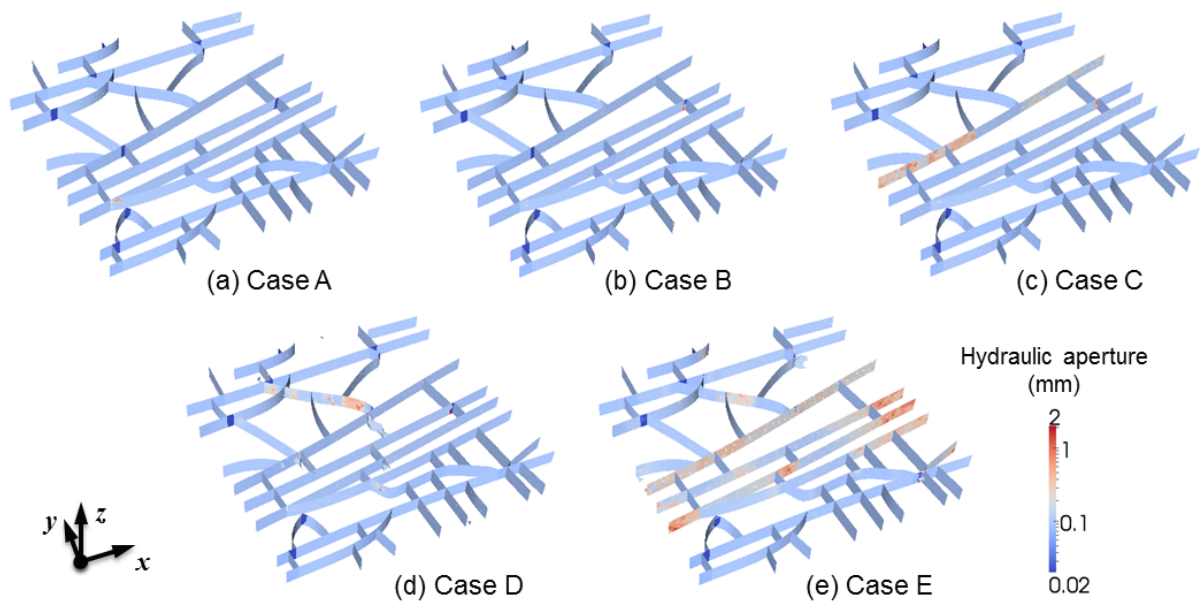
Fig. 8.8 Distribution of hydraulic apertures in the joint network of the fractured layer under different polyaxial stress conditions.

8.4.5 Fluid pathways

The fractured layer under different polyaxial stress conditions also exhibits different vertical flow patterns as illustrated in Fig. 8.9. In Case A and B, fluid uniformly passes through all joints of the network due to the quite homogeneous aperture distribution. In Case C-E, fluid flow is

localised in some parts of fractures corresponding to the large aperture channels formed in bent (Fig. 8.9d) or persistent (Fig. 8.9c&e) fractures.
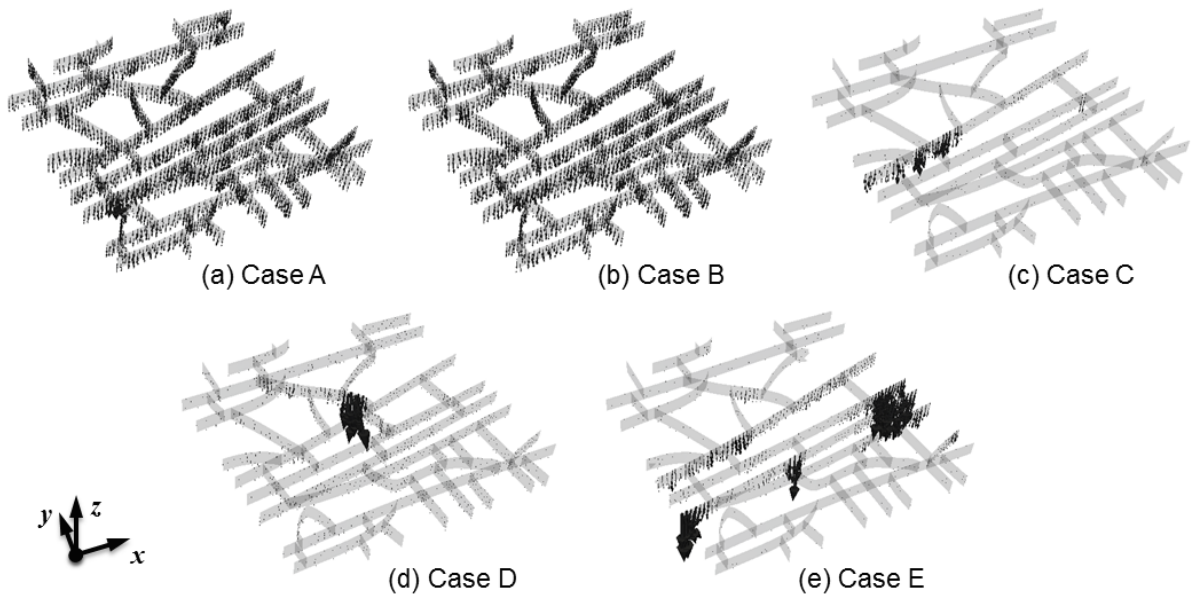
Fig. 8.9 Pathways for vertical flow in the joint network of the fractured layer under different polyaxial stress conditions (note the flow arrow sizes representing local flux magnitudes in the flow simulation of Case C-E are scaled down by a factor 10 times the one of Case A&B).

8.4.6 Equivalent permeability

The equivalent permeability of the fractured rock under various polyaxial stress conditions is derived from steady state flow simulations, where a subvolume is conservatively chosen with a distance of 10% of the model size away from the nearest domain boundaries. The bed-normal permeability, i.e. k_{zz}, of the fractured layer is about one order of magnitude larger than the horizontal components, i.e. k_{xx} and k_{yy} (Fig. 8.10). Note that k_{xx} is larger than k_{yy} due to the better connectivity of the joint pattern in the x direction, i.e. the strike direction of the dominant persistent fractures. It can be noticed that the equivalent permeability of the fractured rock exhibits distinct stress-dependent behaviour in the x and y directions. The permeability is much more sensitive to an increased stress ratio of σ'_x/σ'_y (Set 1 is more reactivated for shearing) (Fig. 8.10b) than to an increased ratio of σ'_y/σ'_x (Fig. 8.10a). Such an anisotropic stress dependency of the permeability is clearly related to the inherent anisotropy of the joint network geometries. Furthermore, the bed-normal permeability k_{zz} seems to be more sensitive to the variation of

geomechanical loading than k_{xx} and k_{yy}. It can be seen that the permeability contrast of k_{zz}/k_{yy} in Case E (i.e. $\sigma'_x = 15$ MPa, $\sigma'_y = 5$ MPa) spans over almost two orders of magnitude. The results demonstrate that both the magnitude and orientation of the far-field stresses have significant influence on the permeability of the fractured layer embedded with an anisotropic joint network.
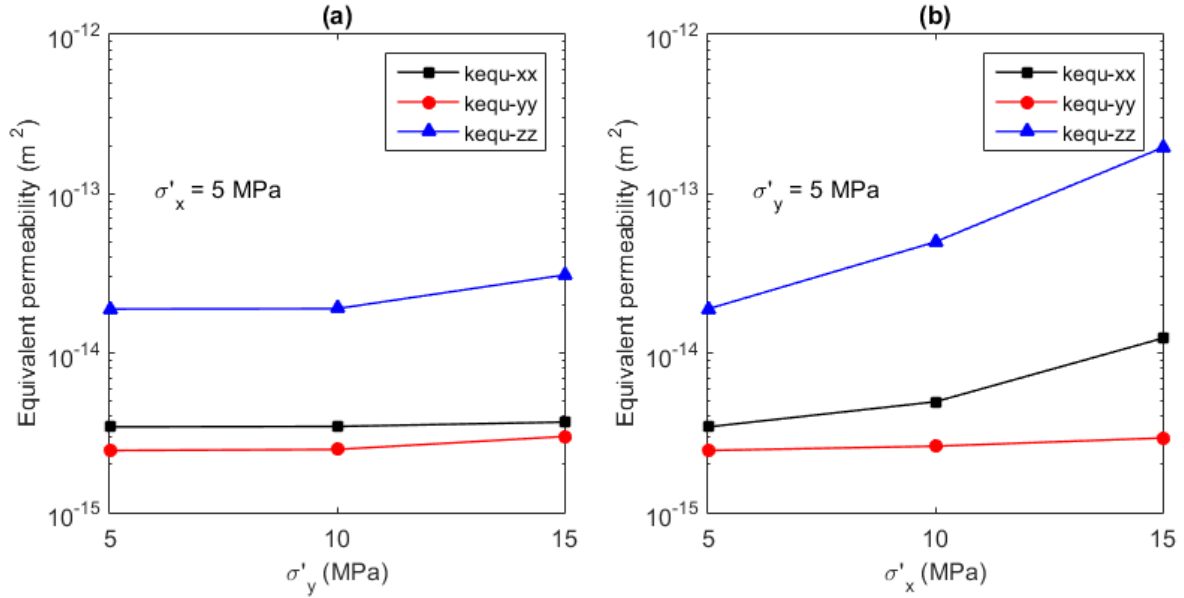
Fig. 8.10 Variations of the equivalent permeability of the fractured layer under (a) an increased σ'_y while $\sigma'_x \equiv 5$ MPa, or (b) an increased σ'_x while $\sigma'_y \equiv 5$ MPa.

8.5 Discussion

Stress-controlled variability of fracture apertures in a realistic 3D joint network of a sedimentary layer has been modelled based on the 3D JCM-FEMDEM model developed and combined with a crack propagation model. Under applied far-field stresses, pre-existing fractures can open, close, shear and dilate, which is dominated by the heterogeneous stress field in the rock. New fractures can also nucleate and propagate, which is governed by mode I, mode II and mixed-mode brittle failure. Compared to the results of Chapter 7 based on an idealised 3D persistent fracture network, the permeability of this fractured layer is less sensitive to the differential stress ratio. One explanation is that most fractures in this quite orthogonal joint pattern trend along or perpendicular to the applied far-field stresses, so that fractures here are less active for shearing than the persistent joint sets in Chapter 7 which are 45° oblique to the horizontal stresses. Furthermore, the matrix blocks of the limestone layer are partially bounded

by some impersistent joints and tend to be more difficult to rotate due to more significant interlocking effects between blocks.

Despite the great capability of the developed 3D simulation tool, some limitations may still exist. For example, the joint behaviour was modelled based on an empirical formulation that assumes isotropic roughness properties for each individual fracture. However, both laboratory and numerical experiments have revealed that fracture apertures evolve anisotropically on the fracture plane under shearing and form more pronounced channels in the direction perpendicular to the shear displacement [Yeo et al., 1998; Koyama et al., 2006]. Such an anisotropic effect may result in even higher bed-normal permeability and more localised vertical flow in the studied sedimentary layer. To simulate it, a 3D anisotropic joint constitutive model, e.g. the one proposed by Jing et al. [1994], needs to be implemented into the 3D FEMDEM formulation. Another limitation is that initial apertures were assumed constant for the joint network. The important correlation with fracture sizes can be considered by using a linear [Pollard and Segall, 1987] or sublinear [Olson, 2003] scaling relation, while the intrinsic heterogeneity of fracture wall asperities can be modelled based on fractal or self-affine assumptions [Thompson and Brown, 1991; Oron and Berkowitz, 1998].

In the current research, the stress-induced localisation of vertical flow was visually compared based on the flux patterns of the joint network under different stress conditions. To more quantitatively characterise the heterogeneity, the multifractal method [Sanderson and Zhang, 1999, 2004] can be used to calculate the evolution of the generalised fractal dimension as an indicator of the degree of flow heterogeneity. The vertical flow under a high horizontal stress ratio is expected to exhibit more significant multifractal features. Extensions of this 3D work also include hydromechanical modelling of a fractured multilayer system where the fluid flow in bedding planes may also be stress-dependent and can influence the vertical flow behaviour. Another avenue for future work is the analysis of more general 3D fracture networks with oriented fractures more indicative of crystalline rocks.

8.6 Concluding remarks

To conclude, this chapter presented a study of the stress/deformation and fluid flow in a 3D sedimentary layer embedded with a realistic joint network under various polyaxial stress

conditions. Geomechanical behaviour of the fractured layer was simulated by the 3D JCM-FEMDEM code integrated with a crack propagation model. Important rock and fracture responses have been captured including the opening/closing, shearing, dilation of pre-existing fractures and the propagation of new fractures into intact rocks driven by stress concentrations. Under a high stress ratio, these geomechanical characteristics resulted in strongly heterogeneous distributions of stresses, shear displacements and fracture apertures. Based on a series of single-phase flow simulations, the flux field and equivalent permeability of the stressed fractured rock were derived. The cases examined were all based on a low matrix permeability assumption although the methodology is equally applicable to rock with higher matrix flows contributing to the equivalent permeability. The vertical fluid flow is quite uniformly distributed under an isotropic horizontal stress condition, but tends to be localised in only a few fractures associated with high shear displacements as the stress ratio increases. The equivalent permeability was observed to have an anisotropic stress dependency attributed to the inherent anisotropy of the fracture network geometries. The results of this study have important implications for upscaling permeability to grid block properties for reservoir flow simulation and exploring mineral deposits for the mining industry.

9   Further application to excavation damaged zone modelling

9.1 Introduction

Subsurface rocks embedded with naturally occurring fractures are often encountered in engineering excavations for tunnel construction, hydrocarbon extraction, mining operations, geothermal production and deep geological disposal of radioactive waste. Underground and surface excavations that reload and perturb the rock mass from an initially equilibrated geological system can engender stress redistribution and generate tension, compression and shear in different parts around the opening [Read, 2004]. Such perturbations to the in-situ stress field are expected to trigger the creation of an excavation disturbed zone (EdZ) and/or excavation damaged zone (EDZ) [Hudson et al., 2009]. For crystalline rocks, EdZ corresponds to the region where only reversible elastic deformation has occurred, whereas EDZ refers to the region where irreversible deformation involving new crack propagation has developed [Tsang et al., 2005]. Furthermore, progressive failure in rocks can lead to an excavation failed zone (EFZ) featured by wedge failure, spalling and even rockbursting at the periphery of an underground cavity [Martin and Christiansson, 2009; Hoek and Martin, 2014]. In the context of nuclear waste repositories in crystalline rocks, predication of EFZ depth and position is critical for safety management during the excavation stage and/or the open-drift stage, while understanding of EdZ/EDZ properties has important implications for assessing the long-term performance involved with radionuclide migration and mineral dissolution problems [Tsang et al., 2005]. A schematic of possible envelopes of EdZ, EDZ and EFZ in an intact rock is shown in Fig. 9.1a, while the potential influence of pre-existing fractures on the envelope geometries is depicted in Fig. 9.1b. It is clear that study of the interaction between man-made openings and pre-existing fractures as well as newly-propagating cracks is a nontrivial issue for relevant engineering activities.

Progressive failure of intact rocks has been extensively studied using various numerical models, such as the damage mechanics-based finite element model [Tang, 1997], the bonded-particle DEM model [Potyondy and Cundall, 2004], the elasto-plastic cellular automaton model [Feng et al., 2006], the FEMDEM model incorporating microscale heterogeneity

[Mahabadi et al., 2014b] and strength anisotropy [Lisjak et al., 2014a; Lisjak et al., 2014b]. Geomechanical behaviour of naturally fractured rock masses represented by explicit DFNs has also been widely modelled based on the block-type DFM method [Min and Jing, 2003], the bonded-particle DEM method [Mas Ivars et al., 2010; Harthong et al. 2012], and the FEMDEM model [Latham et al., 2013; Lei et al., 2014, 2015a, 2015b]. In reviewing the literature, it seems that numerical analysis of EdZ/EDZ has mainly focused on crack initiation and propagation in intact rocks. Only a few attempts have been made to address the geomechanical study of the effect of pre-existing joints or faults, recognised to be an important and nontrivial problem [Hudson et al. 2009]. This problem was identified as a "bottleneck" issue for EdZ/EDZ research [Tsang et al. 2005], but it has not been adequately investigated in the past decade. In this chapter, the FEMDEM method that can capture the reactivation of pre-existing discontinuities and the propagation of new cracks will be used to simulate the mechanical evolution of disturbed or damaged zones. The research will focus on the excavation stage of an underground tunnel in a specific fractured crystalline rock and study the progressive rock mass collapse in an extreme case where no artificial support is introduced. The crystalline rock is assumed to have incompressible grains, i.e. the modulus of grains is much larger than that of the rock, which leads to a Biot-Willis coefficient of 1.0. Geomechanical response of the fractured rock is modelled based on the concept of Terzaghi's effective stress law, whereas the transient dissipation of pore fluid pressure as well as the dynamic poroelastic coupling is beyond the scope of this study.
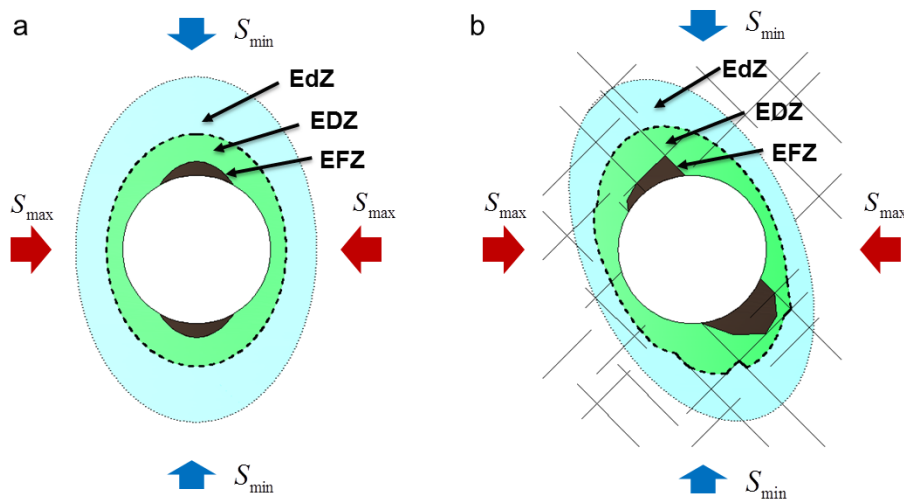
Fig. 9.1 Schematics of (a) the possible envelopes of EdZ, EDZ and EFZ in an isotropic intact rock under far-field stresses S_{max} and S_{min}, and (b) alteration of the envelopes caused by pre-existing fractures.

9.2 Verification and calibration of the numerical model

The numerical model developed in Chapter 4 is employed to simulate the deformation of rock materials, fracturing of intact rocks and shearing of rough fractures involved in the EDZ evolution around tunnel excavations. Before applying the numerical model to solve such a complex problem, it might be useful to examine the performance of the developed geomechanical model in representing the different aspects of rock/fracture behaviour. Numerical verification can be conducted by comparing a numerical solution with an analytical one to examine if the computer code can match results for the particular condition in the realm of the analytical solution. However, due to the complexity of natural geological systems, no numerical model can be fully verifiable in such heterogeneous material systems [Oreskes et al., 1994]. Hence, calibration of a computational code is often a necessary procedure to achieve empirically adequate consistency between input parameters and output properties to investigate a particular behaviour [Potyondy and Cundall, 2004; Tatone and Grasselli, 2015]. Verification and/or calibration of the FEMDEM model is presented here with respect to simulating the stress distribution of an elastic solid and the progressive failure of intact rocks, while the verification/calibration for rough fracture shearing has been presented in Chapter 4.

9.2.1 Elastic stress distribution

Stress distribution around a circular opening in 2D infinite elastic solid under given far-field principal stresses can be described by a closed-form analytical solution [Jaeger et al., 2007]:

$$\sigma_{\theta\theta} = \frac{1}{2}(S_x + S_y)\left[1+\left(\frac{r_o}{r}\right)^2\right] - \frac{1}{2}(S_x - S_y)\left[1+3\left(\frac{r_o}{r}\right)^4\right]\cos 2\theta \tag{10.1a}$$

$$\sigma_{rr} = \frac{1}{2}(S_x + S_y)\left[1-\left(\frac{r_o}{r}\right)^2\right] + \frac{1}{2}(S_x - S_y)\left[1-4\left(\frac{r_o}{r}\right)^2+3\left(\frac{r_o}{r}\right)^4\right]\cos 2\theta \tag{10.1b}$$

$$\tau_{r\theta} = -\frac{1}{2}(S_x - S_y)\left[1+2\left(\frac{r_o}{r}\right)^2-3\left(\frac{r_o}{r}\right)^4\right]\sin 2\theta \tag{10.1c}$$

where S_x and S_y are the far-field principal stresses that align along the x and y axis, respectively, r_o is the radius of the circular opening, $\sigma_{\theta\theta}$, σ_{rr} and $\tau_{r\theta}$ are the stresses in the (r, θ) polar coordinate system. The local maximum and minimum principal stresses σ_1 and σ_2 at any point of (r, θ) of the solid medium can be derived from:

$$\sigma_{1,2} = \frac{\sigma_{\theta\theta} + \sigma_{rr}}{2} \pm \sqrt{\left(\frac{\sigma_{\theta\theta} - \sigma_{rr}}{2}\right)^2 + \tau_{r\theta}^2} \qquad (10.2)$$

Assuming $r_o = 1$ m, $S_x = 2$ MPa, $S_y = 1$ MPa, the distributions of σ_1 and σ_2 near the circular opening are as illustrated in Fig. 9.2a&b.
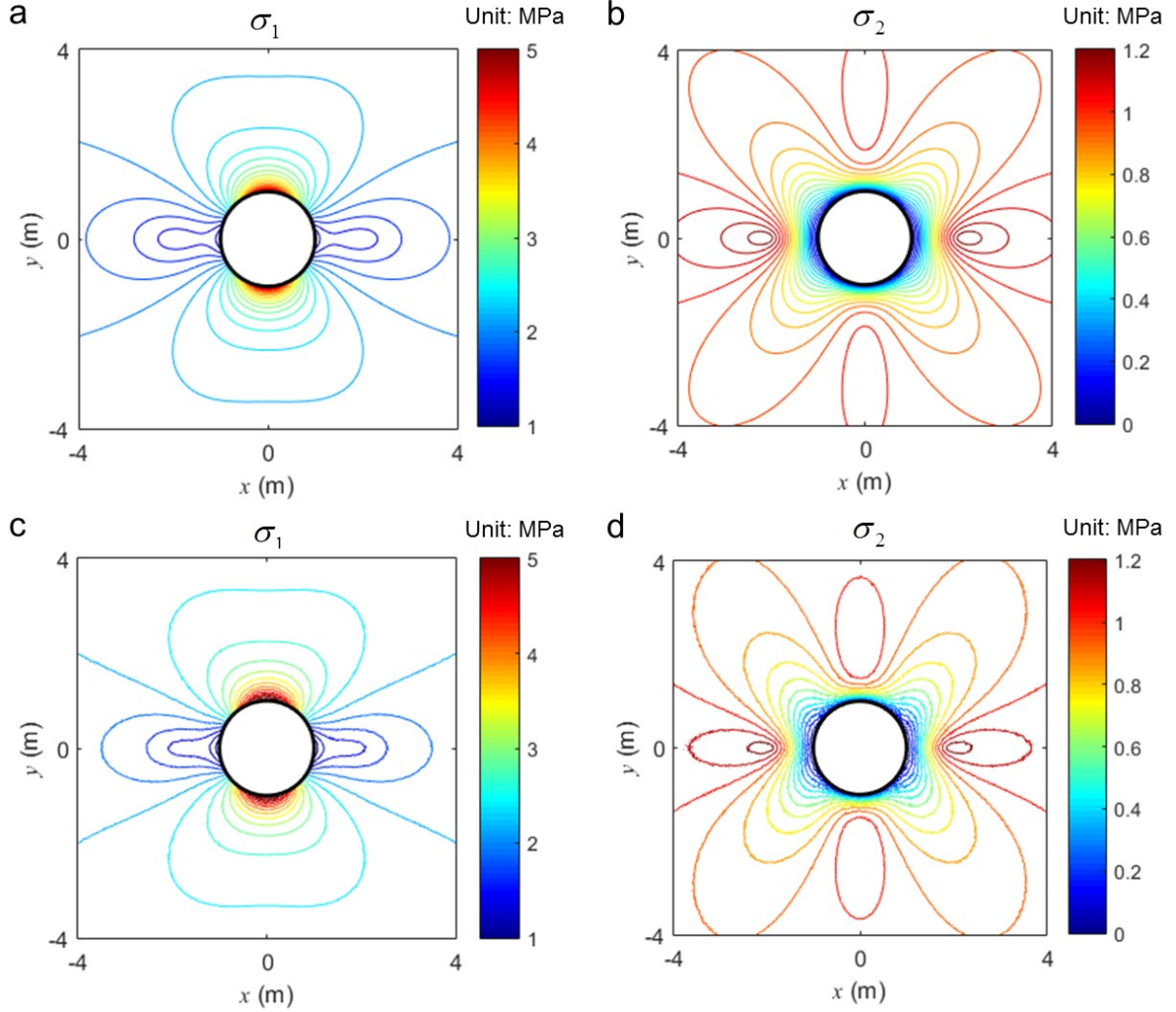
Fig. 9.2 Distribution of (a) maximum principal stress σ_1 and (b) minimum principal stress σ_2 derived by the analytical solution for an infinite elastic plate having a circular hole with a radius of 1 m under far-field stresses $S_x = 2$ MPa and $S_y = 1$ MPa, and the numerical results of (c) σ_1 and (d) σ_2 obtained from the FEMDEM model based on a finite-sized domain of 20 m × 20 m (only the near field, i.e. -4 m $\leq x$ and $y \leq 4$ m, is shown here).

To verify the FEM part of the FEMDEM method used for capturing the elastic stress field, a 20 m × 20 m model is built with a circular opening of $r_o = 1$ m at the centre of the domain.

Far-field stresses $S_x = 2$ MPa, $S_y = 1$ MPa are applied to the boundaries of the squared domain along the x and y directions, respectively. The function of fracturing is switched off in this simulation. An unstructured mesh with an element size of ~0.05 m is used. Fig. 9.2c&d show the numerically obtained distributions of σ_1 and σ_2 in the near field (i.e. -4 m $\leq x$ and $y \leq 4$ m). The analytical and numerical solution fields exhibit quite similar patterns, while the slight discrepancy of the contours is caused by the effect of the finite-sized domain used in the numerical model. The consistency is further demonstrated by comparing the maximum and minimum circumferential stresses $\sigma_{\theta\theta,max}$ and $\sigma_{\theta\theta,min}$ around the opening for a range of far-field stress ratios, i.e. $S_x/S_y = 1$-5 given $S_y \equiv 1$ MPa (Fig. 9.3).
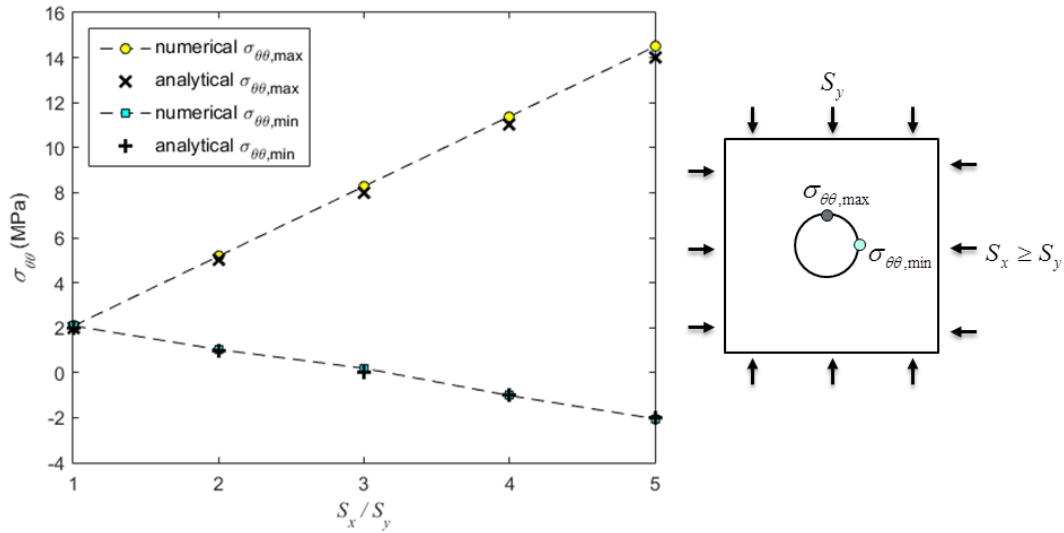
Fig. 9.3 Maximum and minimum circumferential stresses around a circular opening under a range of far-field stress ratios, i.e. $S_x/S_y = 1$-5 given $S_y \equiv 1$ MPa, calculated by the analytical and numerical models.

9.2.2 Fracturing of intact rocks

The capability of the FEMDEM approach for modelling intact rock fracturing process is demonstrated by 2D plane stress virtual experiments for the uniaxial compressive strength (UCS) test (Fig. 9.4a) and Brazilian disc (BD) test (Fig. 9.4b). The UCS test is based on a rectangular specimen of 75 mm × 150 mm and the BD test uses a circular disc having a diameter of 120 mm. Material properties assigned for the modelling are based on the data of the Borrowdale Volcanic Group (BVC) rock at the Sellafield area, Cumbria, England [Nirex, 1997a], as given in Table 9.1. The model domains are discretised by unstructured meshes with element size $h \approx 1$ mm. The specimens are loaded by two rigid platens moving inward at a constant velocity of $v/2 = 0.05$ m/s.

The friction coefficient between the platen and specimen is set to be 0.1. The penalty term p is chosen to be 100 times that of the Young's modulus, i.e. $p = 8400$ GPa. The damping coefficient η is assigned to be the theoretical critical value, i.e. $\eta = 2h\ (E\rho)^{1/2} \approx 3 \times 10^4$ kg/m·s, to reduce dynamic oscillations. The temporal integration scheme is set to have a very small time step of 1×10^{-9} s in order to accommodate instability induced by the large penalty term. The selected model setup parameters are considered to be in the appropriate range for capturing the laboratory-scale fracturing process [Mahabadi, 2012; Tatone and Grasselli, 2015].
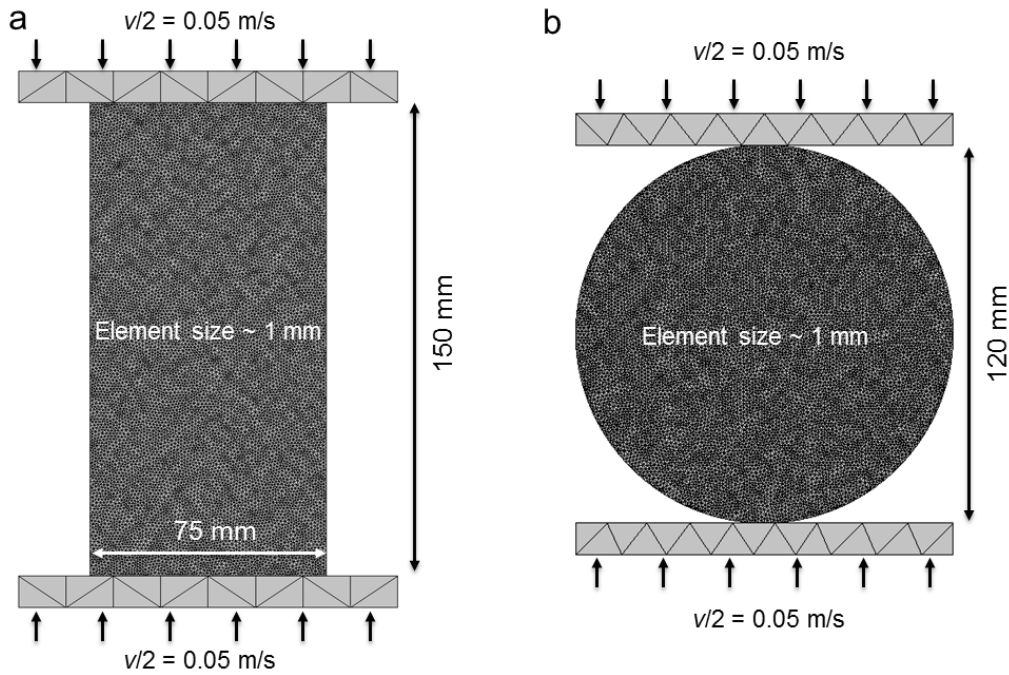
Fig. 9.4 Model setup for (a) the uniaxial compressive strength (UCS) and (b) the Brazilian disc (BD) tests.

Table 9.1 Assumed material properties of the laboratory-scale rock specimens.

Parameter	Value
Bulk density ρ (kg/m3)	2750
Young's modulus E (GPa)	84.0
Poisson's ratio υ	0.24
Tensile strength f_t (MPa)	11.6
Internal friction angle ϕ_i (º)	31.0
Cohesion c (MPa)	44.5
Residual friction angle ϕ_r (º)	24.9
Uniaxial compressive strength UCS (MPa)	157.0

A calibration can be used to derive an appropriate combination of energy release rates (i.e. G_I and G_{II}) for consistency between simulated strength properties (e.g. indirect tensile strength, UCS) obtained from the numerical specimens and the input strength parameters that serve as the calibration targets. Note that the relation between c, ϕ_i and the target UCS value can be based on the Mohr-Coulomb failure criterion as given by

$$\mathrm{UCS} = \frac{2c}{\tan\left(45° - \phi_i / 2\right)} \tag{10.3}$$

The axial stress in the UCS test is calculated as the ratio between the applied load at the top boundary of the specimen and the width of the specimen. The indirect tensile stress σ_t in the BD test is derived as

$$\sigma_t = \frac{2F}{\pi D t} \tag{10.4}$$

where F is the load applied by the top platen, D is the diameter of the disc, and t is the sample thickness that is assumed to be 1.0 in 2D. Following the procedure proposed by [Tatone and Grasselli, 2015], a series of numerical experiments are designed with the energy release rates G_I ranging from 50 to 1000 J/m^2 and G_{II} ranging from 500 to 5000 J/m^2. As shown in Fig. 9.5a and b, the surfaces representing the simulated UCS and BD strength as a function of energy release parameters can be constructed based on linear interpolation. The intersection polylines between the interpolated surface and the plane of target UCS or BD strength represent the scenario where a combination of G_I and G_{II} can approximately reproduce the target values. The intersection point of the UCS and BD polylines (Fig. 9.5c) defines the unique combination of $G_I = 327.6$ J/m^2 and $G_{II} = 2367.7$ J/m^2 that tends to yield correct UCS and BD strength in the laboratory-scale experiment.

The results of the UCS and BD tests with the finalised energy parameters are presented in Fig. 9.6. In the UCS test, the failure of the specimen is dominated by propagating mode II cracks that form inclined shear planes and the macroscopic UCS strength value is 156.9 MPa. In the BD test, the disc contains diametric tension cracks and exhibits an indirect tensile strength of 11.6 MPa. Furthermore, the emergent elastic modulus measured as the slope of the stress-strain curve of the UCS test exhibits a value of ~80.0 GPa, which indicates that the selected penalty term is adequately large to capture precisely the rock deformation behaviour. It should be noted that

mesh sensitivity (e.g. size and orientation) analysis is not included here, but may be necessary if the model is used for solving real problems due to the inherent dependency of the cohesive zone calculation on the prescribed grid discretisation.
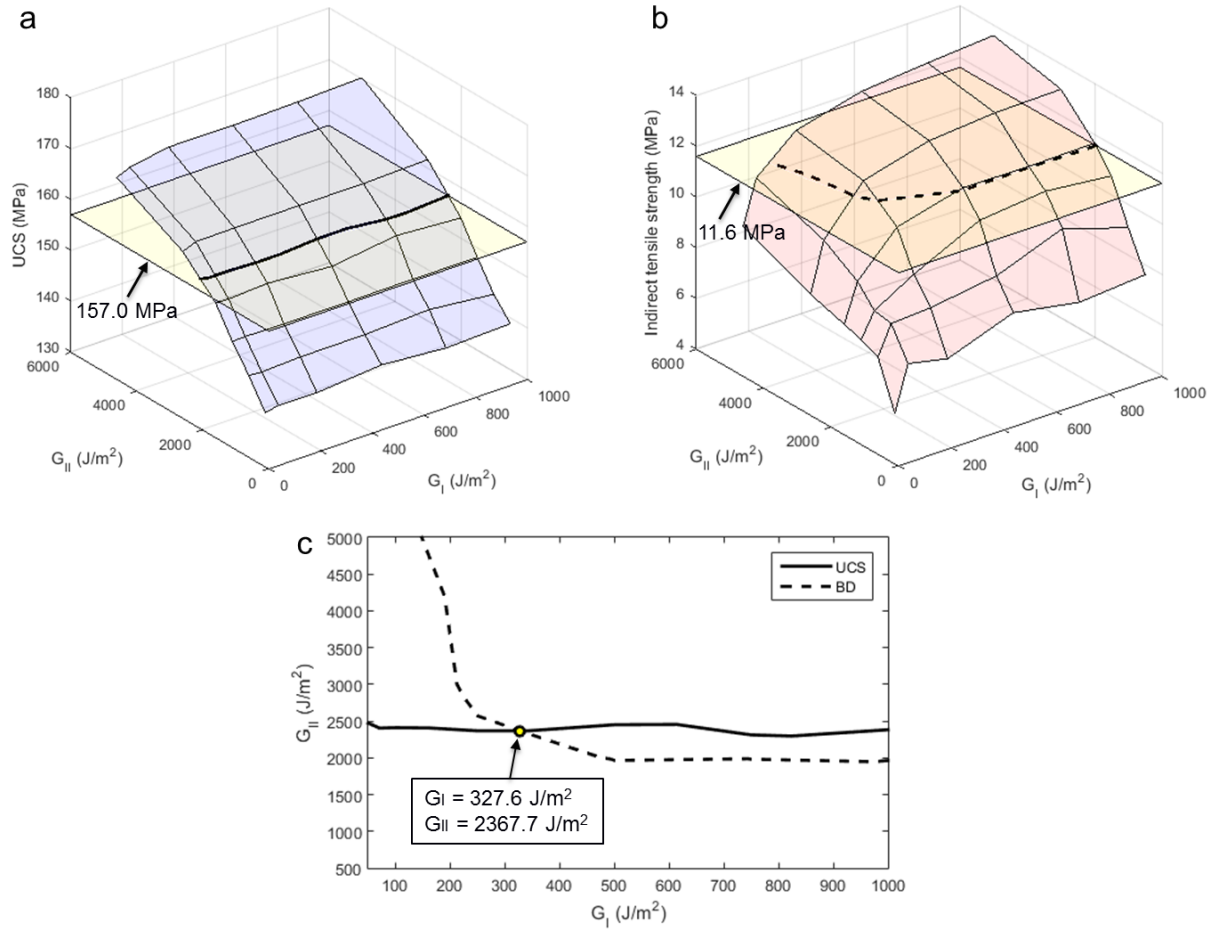
Fig. 9.5 Calibration of energy release rates for simulating intact rock failure based on the procedure proposed by Tatone and Grasselli [2015]: (a) Simulated uniaxial compressive strength (UCS) as a function of energy release rates G_I and G_{II} and the intersection polyline with the plane of target UCS (i.e. 157.0 MPa), (b) Simulated indirect tensile strength as a function of energy release rates G_I and G_{II} and the intersection polyline with the plane of target tensile strength (i.e. 11.6 MPa), (c) The intersection point of the projected 2D UCS intersection polyline and BD polyline defines the calibrated combination of G_I and G_{II}.

The value of calibrated G_{II} is in the typical range of shear fracture energy release rate [Cox and Scholz, 1985], whereas the value of G_I that corresponds to a fracture toughness K_{IC} of 5.4 MPa·m$^{1/2}$ for a plain strain condition is significantly higher than the value (1.6-1.7 MPa·m$^{1/2}$)

predicted using the empirical correlation proposed by Gunsallus and Kulhawy [1984] and also exceeds the typical range measured for crystalline rocks in the laboratory experiments [Atkinson and Meredith, 1987; Latham, 1998]. Obviously, this calibration procedure [Tatone and Grasselli, 2015] is able to produce a self-consistent model in terms of numerical aspects, but the physical realism of the calibrated parameters may require further studies.
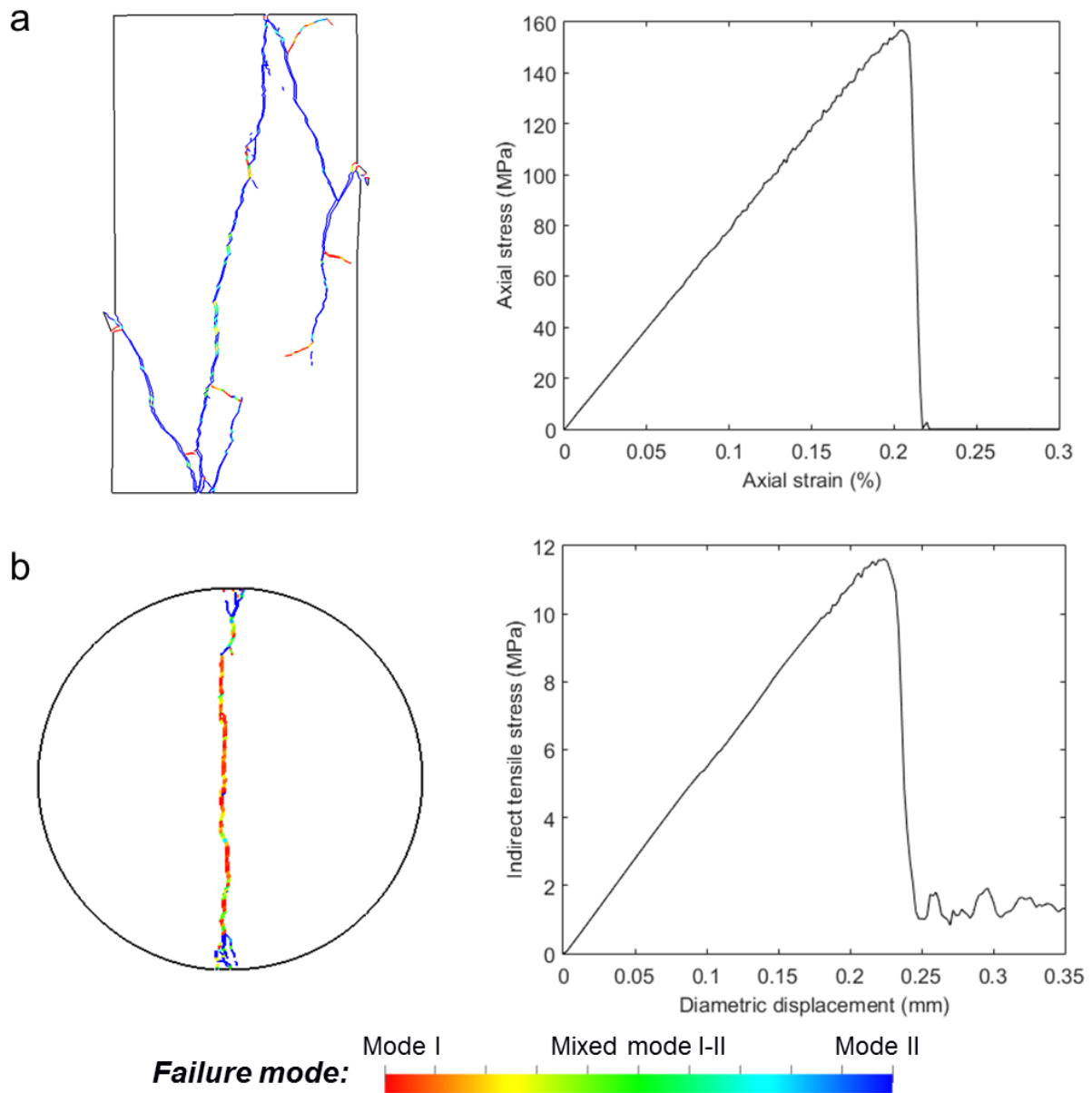
Fig. 9.6 (a) The fracture pattern and stress-strain curve of the calibrated UCS test. (b) The fracture pattern and stress-displacement curve of the calibrated BD test.

9.3 Numerical experiment setup

9.3.1 Rock properties and in-situ stresses

The numerical experiment of a hypothetical repository is based on the site characterisation of a geological formation at the Sellafield area, Cumbria, England, conducted by the UK Nirex Limited [Nirex, 1997a, 1997b]. The host medium is a thick sequence of Ordovician volcaniclastic rocks. The intact rock properties used in the field-scale model are presented in Table 9.1. The joint properties were characterised based on a laboratory sample with size L_0 equal to 0.3 m, which gives $JCS_0 = 112.2$ MPa and $JRC_0 = 3.85$ [Kobayashi et al., 2001]. The in-situ stresses can be empirically calculated by [Nirex, 1997a]:

$$S_v = 0.0294 \, y + 0.26622 \qquad (10.5a)$$

$$S_H = 0.03113 \, y + 1.88747 \qquad (10.5b)$$

$$S_h = 0.01996 \, y + 0.31619 \qquad (10.5c)$$

where S_v is the vertical overburden stress (MPa), S_H is the maximum horizontal stress (MPa), S_h is the minimum horizontal stress (MPa), and y is the depth (m). The orientation of S_H is 340º from the North. Pore fluid pressure P_f is assumed to be hydrostatically distributed with the water table located at the ground surface. Since the Biot-Willis coefficient is assumed to be 1.0, the effective stress components can be calculated by subtracting P_f from the total stress components. Fig. 9.7a shows the magnitudes of in-situ stresses and pore fluid pressure at different depths and Fig. 9.7b further depicts the variation of lateral effective stress ratio, i.e. S'_H/S'_v and S'_h/S'_v. A series of numerical experiments corresponding to three different depths, i.e. 250 m, 500 m and 1000 m (Table 9.2), will be explored in the following sections.

Table 9.2 Effective in-situ stresses at the selected depth scenarios

Depth (m)	S'_v (MPa)	S'_H (MPa)	S'_h (MPa)	S'_H/S'_v	S'_h/S'_v
250	5.15	7.20	2.84	1.40	0.55
500	10.03	12.52	5.36	1.25	0.53
1000	19.80	23.15	10.41	1.17	0.52
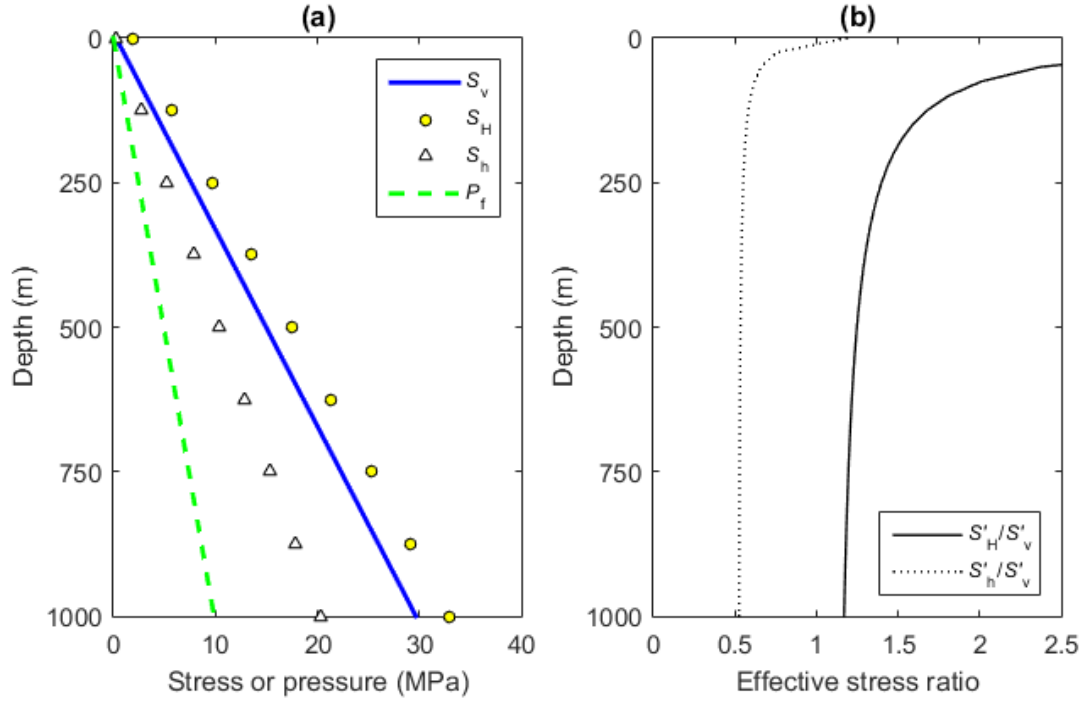
Fig. 9.7 (a) Distribution of in-situ stresses and pore fluid pressure, and (b) effective stress ratios at different depths.

9.3.2 Fracture networks

Four sets of fractures were observed in the field with their mean dips/dip-directions given as 8º/145º, 88º/148º, 76º/21º, 69º/87º, respectively [Min et al., 2004a]. Dispersion of fracture orientations is not included in this study since uncorrelation between lengths and orientations was found to result in unrealistic patterns [Blum et al., 2005]. The field measurement gives a limited range of trace lengths between 0.5 m and 250 m, i.e. the minimum length $l_{min} = 0.5$ m and the maximum length $l_{max} = 250$ m. As shown in Fig. 9.8a, a power law fracture length distribution has been fitted to the field data [Nirex, 1997b], with the cumulative distribution given by

$$N = \gamma\, l^{-C} \tag{10.6}$$

where N is the number of fractures per unit area (m²) having a length larger than l, γ is a density constant, C is the exponent of the cumulative distribution of fracture lengths. The field data can be plausibly modelled by a range of combinations of γ and C, resulting in different fracture density scenarios. A low density case with $\gamma = 1.25$ and $C = 2.0$ is adopted here for creating DFN realisations. Fracture lengths are sampled by using the following equation [Min et al., 2004a]:

$$l = \left(l_{\min}^{-C} + F\left(l_{\max}^{-C} - l_{\min}^{-C}\right)\right)^{-1/C} \tag{10.7}$$

where F is a random number uniformly distributed in the range of $0 \leq F \leq 1$. The distribution of fracture barycentres is modelled by a Poisson process. Four sets of fractures are also assumed to have equal density, because no available data exists for treating them individually [Blum et al., 2005]. Two 2D cross-sections are chosen through the host rock oriented at 340º and 250º from the North, respectively, corresponding to the plane of S_V-S_H and that of S_V-S_h. The generated DFN patterns, denoted as DFN1 and DFN2 (Fig. 9.8b), will be used for the modelling of a hypothetical excavation in the crystalline rock under the corresponding 2D stress field. Since significant modifications have been made when interpreting the field data, the results presented here cannot be used to directly infer the condition of the real system at Sellafield.
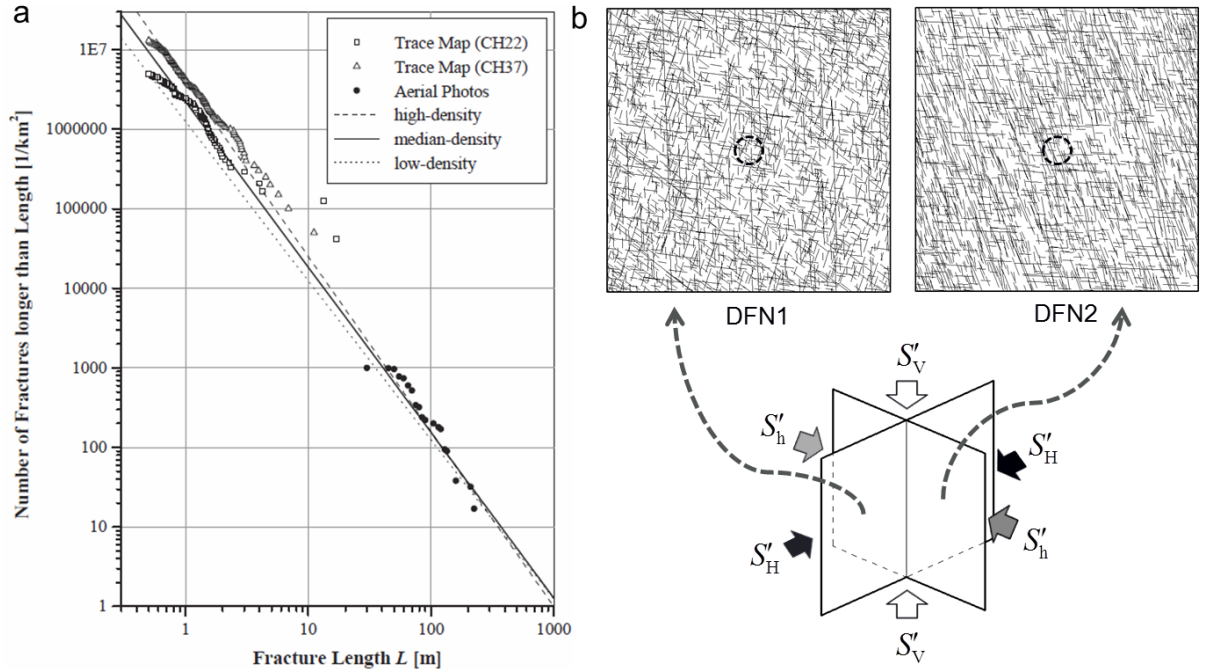
Fig. 9.8 (a) Distribution of fracture lengths mapped at Sellafield that can be fitted by a power law cumulative distribution (after Blum et al. [2005]), and (b) the 20 m × 20 m discrete fracture network (DFN) generated in the cross-section plane oriented 340º (DFN1) or 250º (DFN2) from the North (dashed circles represent the tunnels advancing in two different directions).

9.3.3 Model discretisation and boundary conditions

The 20 m × 20 m fractured rock domain embedded with one of the DFN networks is discretised by an unstructured mesh with pre-existing discontinuities represented by a series of

prescribed overlapping edges (but with separated nodes) of triangular finite elements. An increased element size ($h \approx 5.0$ cm) is used to constrain the modelling to affordable runtime for the field-scale simulation, while retaining an acceptable degree of accuracy. Variations of simulated strength properties induced by the decrease of mesh resolutions can be evaluated through a recalibration when solving real problems. For simplicity, such procedure is not included in this study and the calibrated parameters (e.g. G_I and G_{II}) based on the laboratory-scale specimens are adopted with no change. A discussion about this effect and potential solutions is given in section 9.6. The EDZ behaviour captured in the field-scale models can be, therefore, mainly used for qualitative assessment.

The hypothetical circular tunnel with a diameter of 2 m is placed at the centre of the field-scale model and the response to stresses is simulated for a range of tunnel depth scenarios. The distance from the tunnel centre to the model boundary is five times the tunnel diameter, for which the boundary effect is considered minor. The bottom of the model is constrained by a roller boundary condition (i.e. no displacement in the y direction) in order to accommodate the body force effect. The boundary stress σ_y that is applied to the top of the model is set equal to the effective overburden stress, i.e. S'_v, of the studied depth. The lateral stress σ_x is imposed uniformly (i.e. gravity-induced gradient is neglected) to the left and right model boundaries with the magnitude defined by the maximum or minimum effective horizontal stress, i.e. S'_H or S'_h, depending on the chosen cross-section. The pre-existing fractures are represented with no initial phase of shearing before the phases of far-field stress application. The plain strain numerical experiment is designed with multiple sequential deformation-solving phases [Lisjak et al. 2014a, 2014b]: (i) intact rock and rock mass fractures are deformed from an unstressed state to accommodate equilibrium under geological far-field stresses; this includes applying an initial ramping stage to avoid sudden violent failure, (ii) the circular core is relaxed in a process that mimics the progressive unloading effects during tunnelling face advancement; this is achieved by gradually reducing the deformation modulus of the excavated circular area, (iii) rock materials inside the excavated area are removed after which an interior free surface is created with no tunnel support introduced, and (iv) an EDZ progressively evolves around the unsupported opening; this may involve intensive new cracking that links pre-existing discontinuities. Here,

the relaxation phase is mainly introduced for the purpose of avoiding unrealistic artificial shocks that can arise by instant removal of excavation materials. The final EDZ patterns do not correspond to the eventual completely collapsed state, which requires unacceptable excessive runtime, but all models are ceased at the same point of simulation time for comparison.

9.4 Results

9.4.1 Rock mass failure

Fig. 9.9 presents the simulation results of the excavation in the rock mass model of DFN1 at the depth of 1000 m. The model first reaches the equilibrium state under the effective far-field stresses of S'_v = 19.80 MPa and S'_H = 23.15 MPa and the gravitational forces (Fig. 9.9a). The fractured rock medium exhibits remarkable homogeneity for the initial in-situ stress condition that is close to isotropic (S'_H/S'_v = 1.17). With the relaxation of core rocks, stress concentrations begin to appear in the fictitiously softening materials as well as the rocks surrounding the tunnel (Fig. 9.9b). After the removal of the rocks inside the tunnel (Fig. 9.9c), the model continues to solve for the consequent evolution of the excavation damaged zone (EDZ) around the man-made opening, i.e. the zone where irreversible deformation involving new crack propagation has developed (Fig. 9.9d). The perturbation to the in-situ stress field caused by the excavation is dramatic. An interior low stress zone (stress loosing zone) is formed surrounding the tunnel boundary, where intensive rock mass failure develops as a result of structurally-governed kinematic instability (e.g. key blocks) and stress-driven breakage (e.g. wing cracks). The stress loosing zone seems to have a long axis along the direction of the minimum principal stress (i.e. S'_v) in this 2D plane. A self-organised exterior high stress zone (stress arching zone) is promoted at a certain distance to the tunnel periphery, where compression arches seem to evolve along the direction of the maximum principal stress (i.e. S'_H). In contrast, the DFN2 model at the depth of 1000 m exhibits significant heterogeneity under the far-field stresses (S'_v = 19.80 MPa, S'_h = 9.41 MPa) and the gravitational forces, before any artificial perturbation is introduced (Fig. 9.10a). After the removal of rocks in the tunnel, a stress loosing zone is created in the near-field of the excavation and also tends to follow the direction of the minimum principal stress, i.e. S'_h (Fig. 9.10d). An exterior stress arching zone is also vertically formed along the maximum principal stress, i.e. S'_v, especially at the right hand side of the tunnel (the marked asymmetry).

More interestingly, the high-stress contours of these arching zones seem to be microscopically constrained by the pre-existing fractures in the local areas (Fig. 9.9d and Fig. 9.10d).
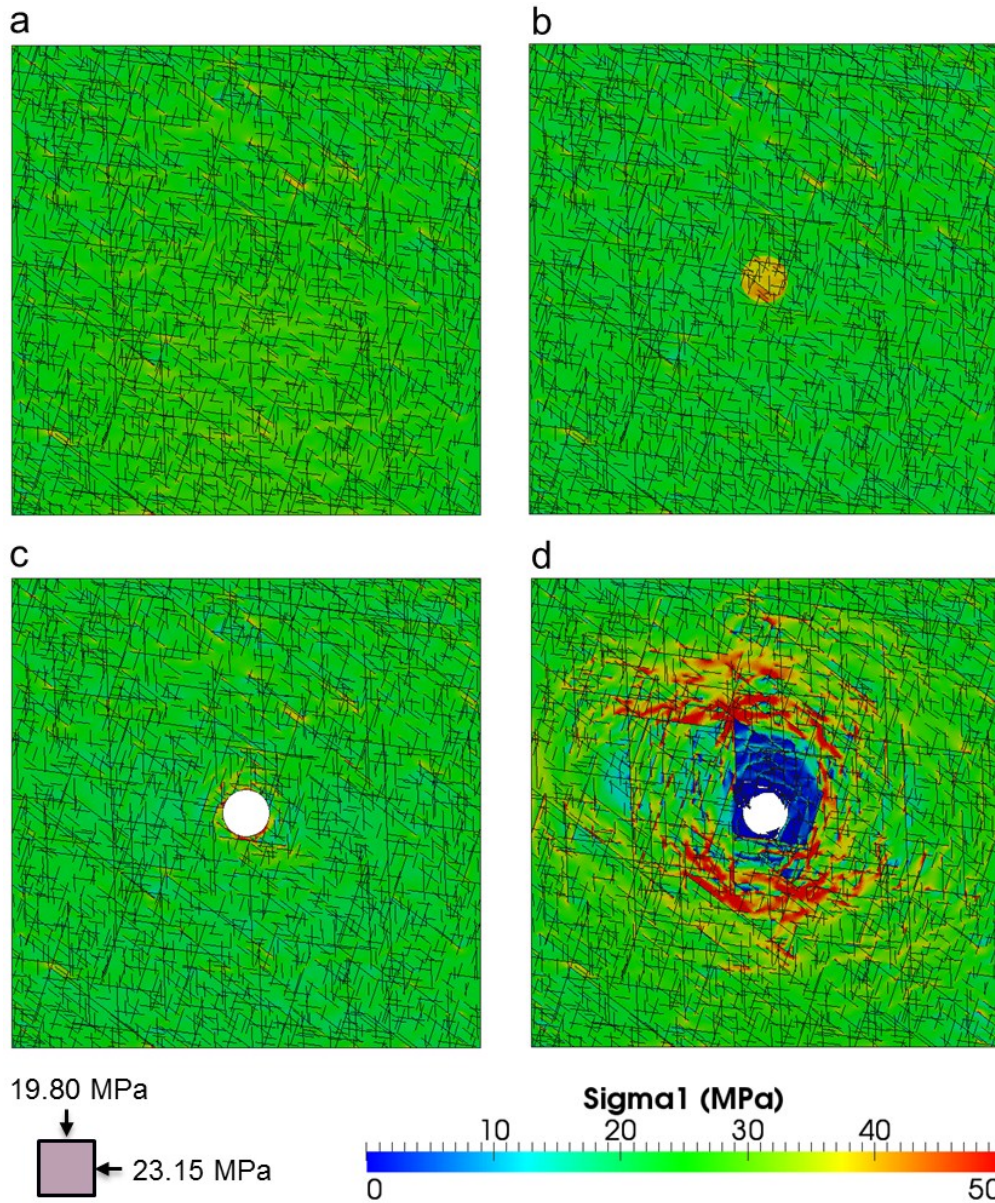
Fig. 9.9 Rock mass failure around the tunnel excavation in the 20 m × 20 m DFN1 rock mass model at the depth of 1000 m. The numerical experiment is a sequence of different phases: (a) force equilibration under the geological in-situ stress condition that pertains before the excavation, (b) central core relaxation during the excavation, (c) physical removal of materials inside the tunnel after the excavation, and (d) evolution of the excavation damaged zone around the unsupported opening (note: black lines represent the pre-existing discontinuities in the geological formation, and the colour contours represent the maximum principal stress distribution).
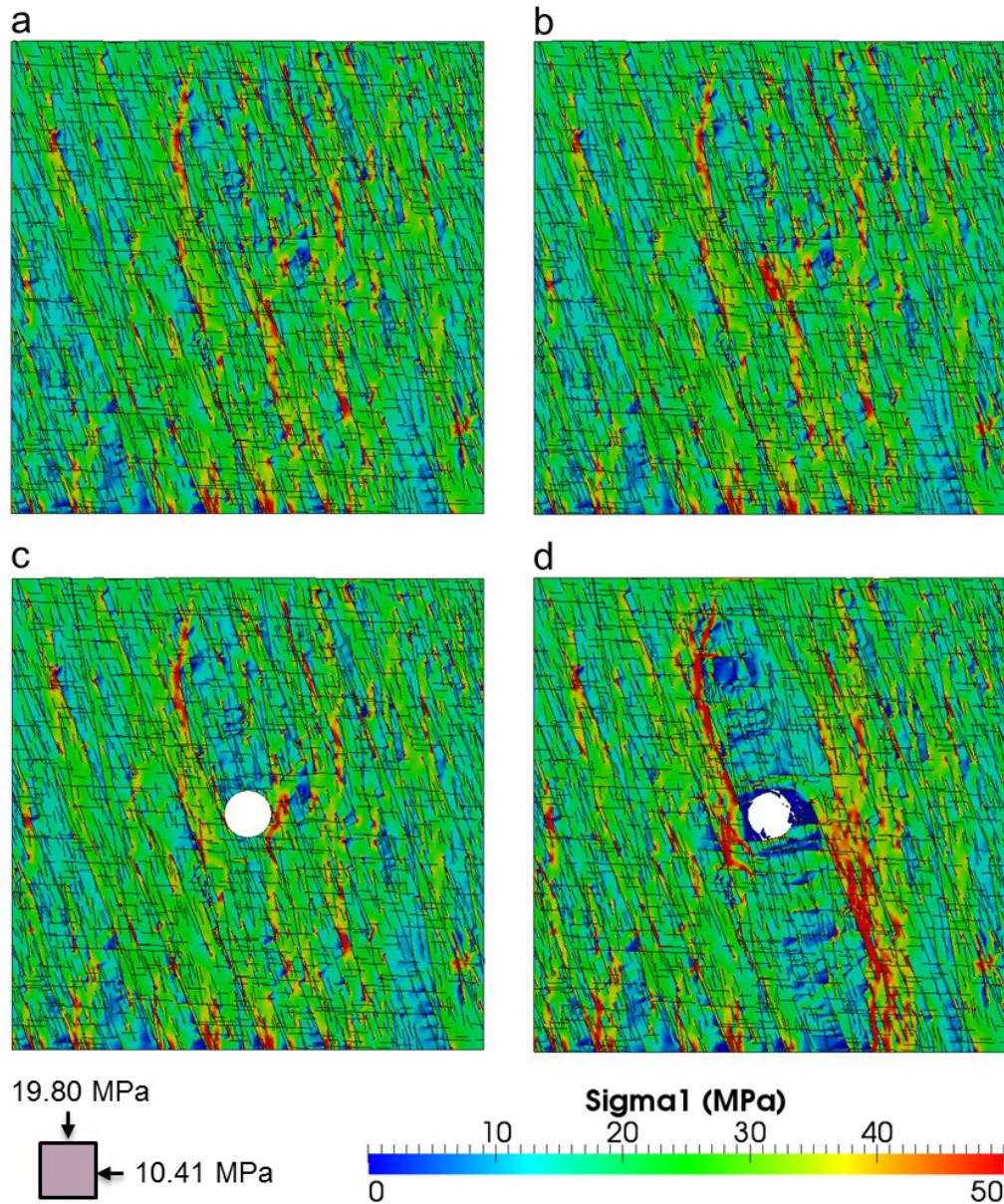
Fig. 9.10 Rock mass failure around the tunnel excavation in the 20 m × 20 m DFN2 rock mass model at the depth of 1000 m.

Fig. 9.11 shows the near-field fracture development around the tunnel excavation in the two DFN models of various depth scenarios. For the depth of 250 m, quite few new cracks emerge in both networks and the rock can almost remain stable except slight structurally-governed falling of rock pieces. For the depth of 500 m, slightly more new cracks are generated in both DFN networks. However, for the scenario of 1000 m depth, extensive tension-dominated new cracks assembled with a few shear-dominated ones also created. The propagation of these new cracks tends to follow the direction of the maximum principal stress in each DFN model, i.e. horizontally in DFN1 and vertically in DFN2. The new cracks in DFN1 are concentrated in the

rock above the tunnel top or under the invert (Fig. 9.11c), whereas fracturing in DFN2 mainly occurs in the lateral space (Fig. 9.11f).

DFN1

(a) 250 m   (b) 500 m   (c) 1000 m

DFN2

(d) 250 m   (e) 500 m   (f) 1000 m

shear-dominated new cracks: ■ (blue)   pre-existing fractures: ■ (green)
tension-dominated new cracks: ■ (red)   boundary of the excavation: ■ (black)
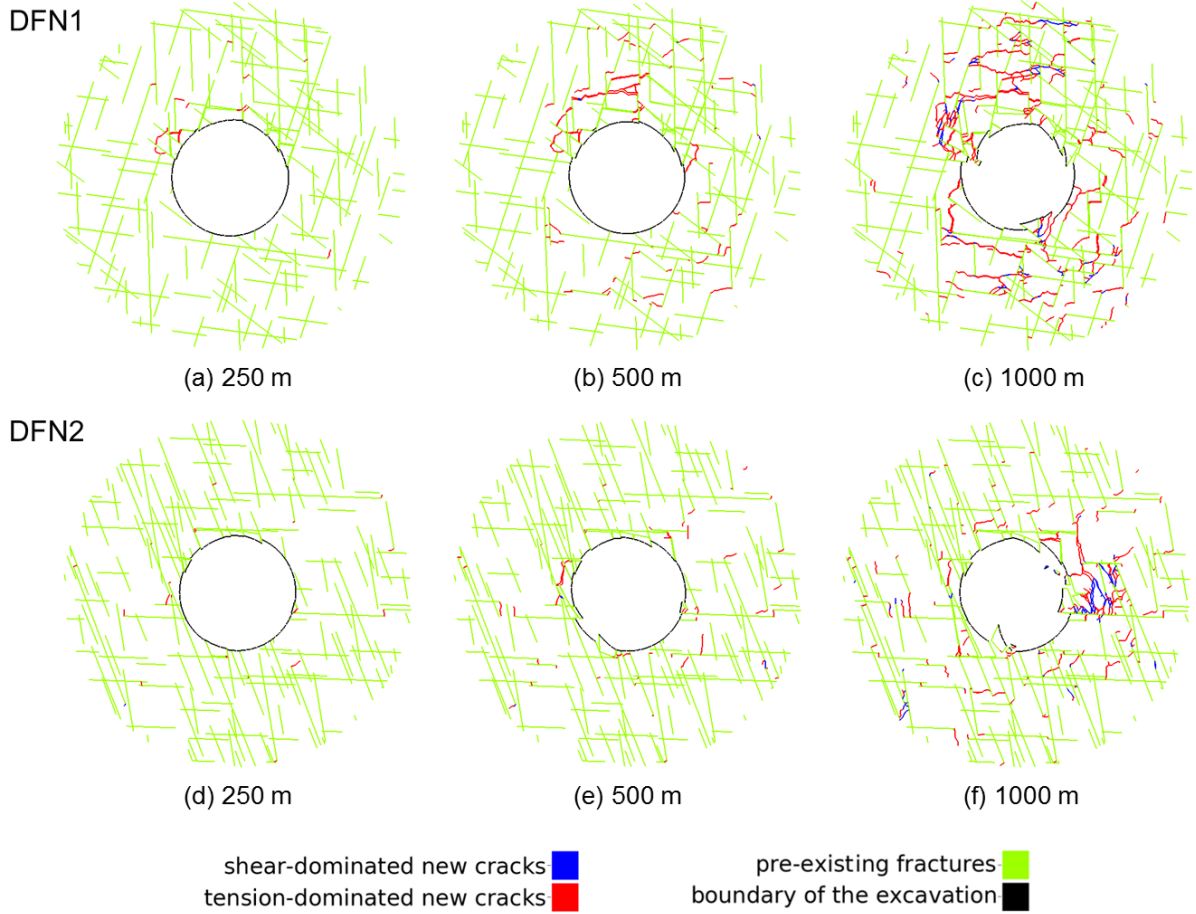
Fig. 9.11 Fracture development at the near-field to the excavation boundary in the DFN models at various depths. Shear-dominated new cracks correspond to the broken joint elements with the failure mode indicator $1.0 \leq m \leq 1.5$, while tension-dominated new cracks correspond to the case with $1.5 < m \leq 2.0$.

9.4.2 Shear reactivation

Fig. 9.12 illustrates the distribution of shear displacement in the two DFN models at various depths, in which high displacement values are highlighted in darker tones. It can be seen that, at the shallow depth (i.e. 250 m), only very long fractures exhibit high shear displacement. As the depth increases, more fractures including some small ones close to the tunnel are reactivated for shearing. The shear displacement magnitudes of sets in DFN1 seem more isotropic (i.e. three sets are sheared by a quite equal degree), while the shearing in DFN2 is localised mainly in subvertical fracture sets and displays relatively higher displacement magnitudes. Such shearing

phenomena may be attributed to the quite isotropic stress fields for DFN1 and the high differential stress conditions for DFN2 in addition to the specialisations of their fracture geometries.

DFN1

(a) 250 m   (b) 500 m   (c) 1000 m
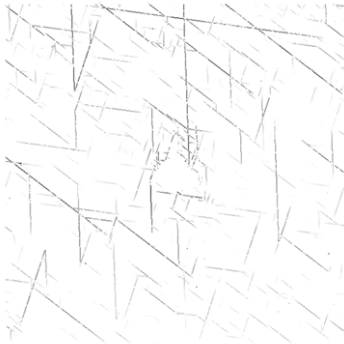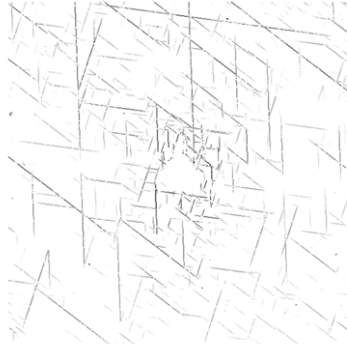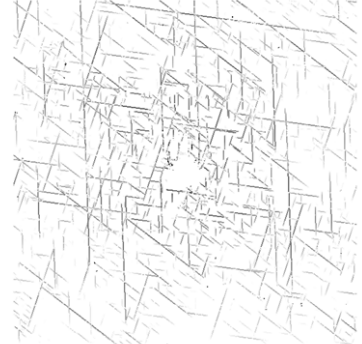
DFN2

(d) 250 m   (e) 500 m   (f) 1000 m
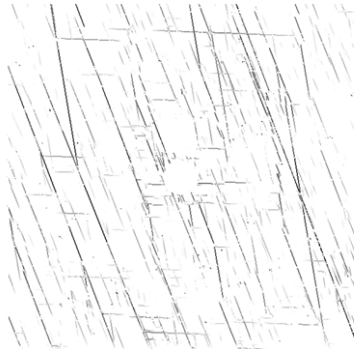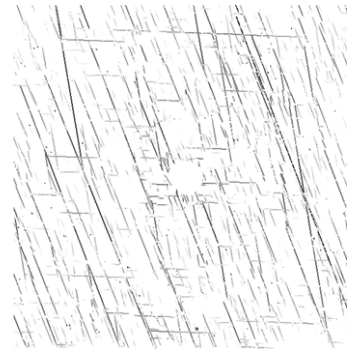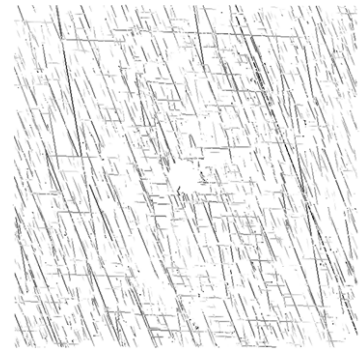
Shear displacement (mm)
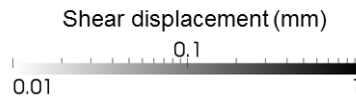
Fig. 9.12 Shear displacement along pre-existing and propagating fractures in the DFN models at various depths.

9.4.3 Characterisation of the excavation damaged zone (EDZ)

The geometrical properties of these specific cases of EDZ are characterised using an ellipse that has a minimal volume to cover the area with excavation-induced new crack propagation at an assumed confidence level (i.e. 90%). With the increase of depth, the extent of the EDZ ellipses in DFN1 is gradually enlarged with the aspect ratio attenuated (Fig. 9.13a-c). To further explore the spatial heterogeneity and directional variation of the damage developed inside the ellipse, the frequency of new broken joint elements is counted based on a polar coordinate

system of gridding and is represented using a graphic rose with colour bands showing the ranges of distance to the tunnel centre. The direction of the rose with the longest spoke corresponds to the direction with the greatest new damage. As shown by Fig. 9.13d-f, major damage direction seems to be the vertical direction in DFN1 and the spatial extent of the damage expands with the increased depth (more new cracks with larger distances to the tunnel centre emerge).
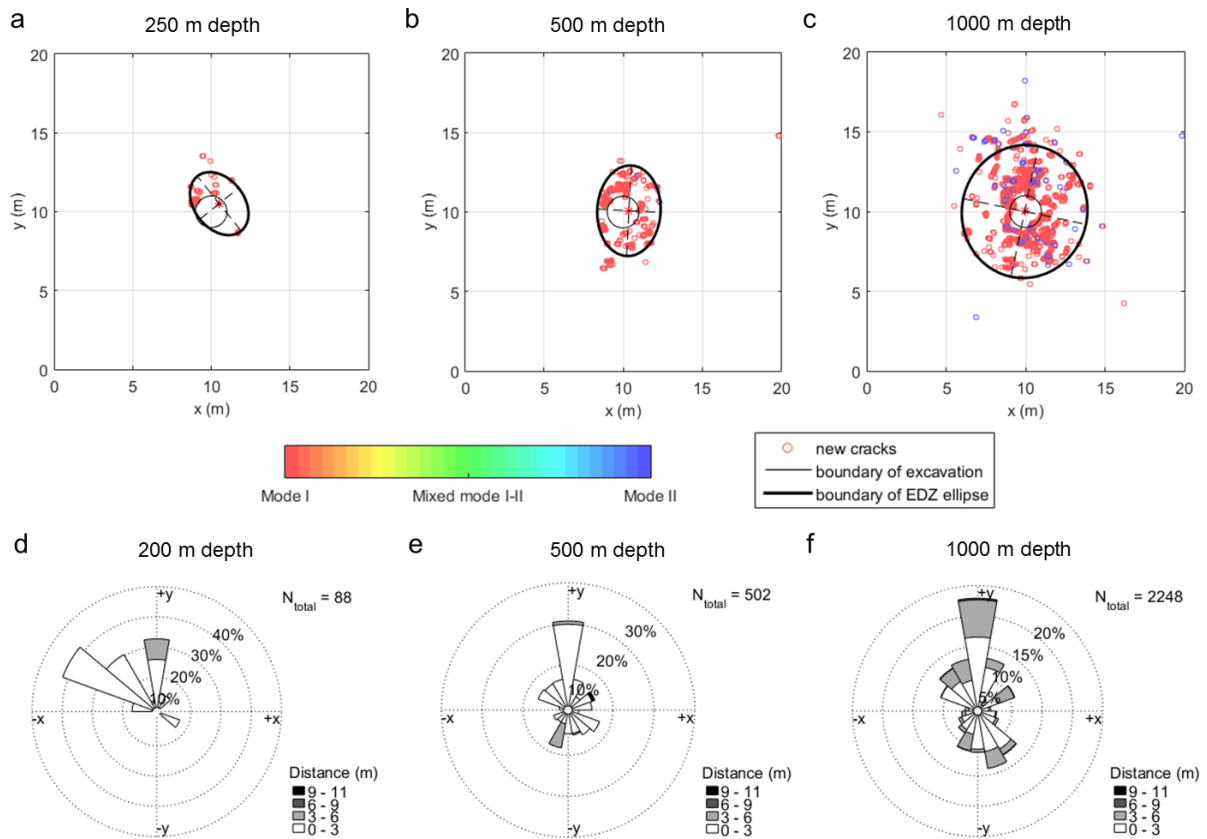
Fig. 9.13 Ellipses of the EDZ that covers 90% excavation-induced broken joint elements of the DFN1 model at the depth of (a) 250 m, (b) 500 m and (c) 1000 m; the rose diagram for the directional frequency of new cracks of the DFN1 model at the depth of (d) 250 m, (e) 500 m and (f) 1000 m (note: the colour bands show the ranges of distance from new crack centroids to the tunnel centre).

For the DFN2 model, the EDZ ellipses cover almost the whole modelling domain but with extremely sparse cracking (Fig. 9.14a-c). Such uniformly distributed damage is probably attributed to the relatively higher stress ratio that engenders more shear displacements and transmits the influence to a larger region. The rose diagrams for DFN2 indicate that the dominant damage orientation (especially close to the tunnel) tends to be along the horizontal axis, i.e. the

direction of S'_h (e.g. Fig. 9.14f). Apart from new cracking propagation, the sliding along rough fractures is also an important indicator of the damage evolution in the rock with naturally formed discontinuities. A more in-depth understanding of the EDZ characteristics may benefit from the consideration of these two effects based on some means of calculating the energy partitioning by fracturing and shearing. Modelling of the energy dissipated by the frictional sliding of rough fractures with a varying frictional coefficient and the propagation of new fractures requires further code development and is beyond the scope of this study, but might be achieved by introducing the acoustic emission model [Lisjak et al., 2013] in the future.
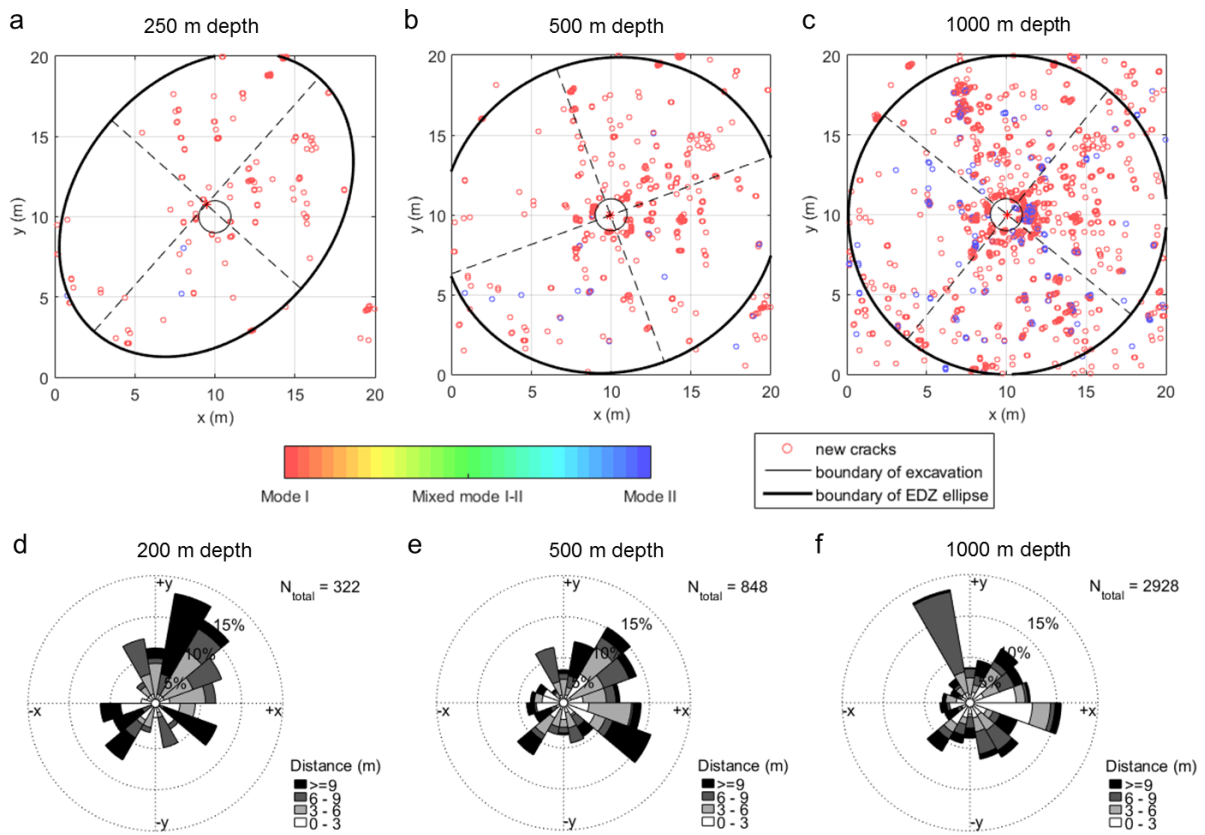
Fig. 9.14 Ellipses of the EDZ that covers 90% excavation-induced broken joint elements of the DFN2 model at the depth of (a) 250 m, (b) 500 m and (c) 1000 m; the rose diagram for the directional frequency of new cracks of the DFN2 model at the depth of (d) 250 m, (e) 500 m and (f) 1000 m.

9.4.4 Influence of stress on new crack propagation

The influence of in-situ stresses on new crack propagation is explored by analysing the relationship between the maximum principal stress or differential stress ratio and the total length

of excavation-induced new cracks (Fig. 9.15). Regardless of the topologies of pre-existing fractures (i.e. for both DFN1 and DFN2), a quite monotonic increase of new crack propagation occurs with the enhanced maximum principal stress level. However, there is no clear correlation between the background principal stress ratio (i.e. $\sigma_{max}/\sigma_{min}$) and new fracturing, at least in the modelled scenarios. Needless to say, it is the imposition of zero confinement at the tunnel wall that introduces the differential stresses that drive the deformation and these are higher when at greater depths, completely masking any differences inherited from the slight differences in background tectonic principal stresses.
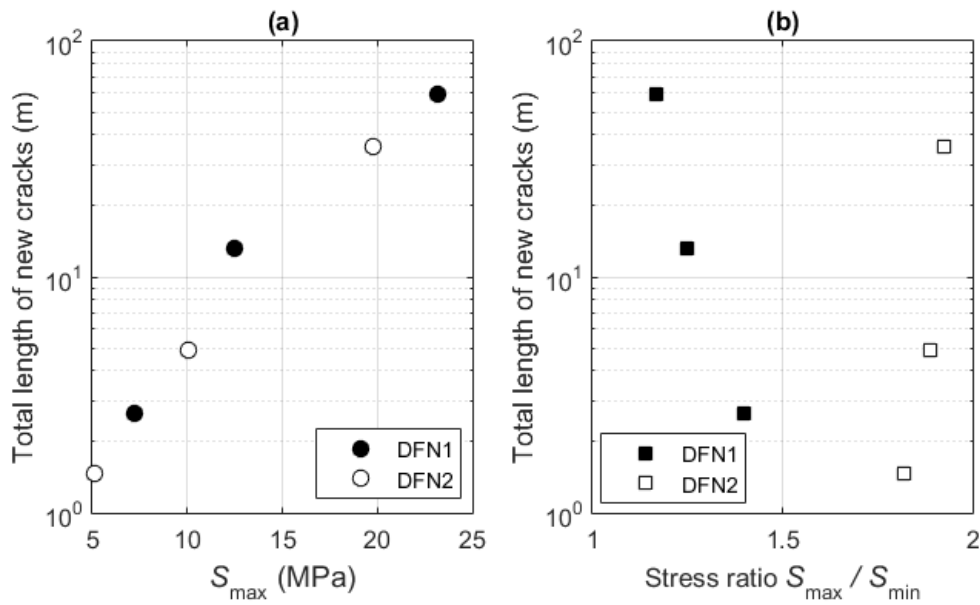
Fig. 9.15 (a) The relation between maximum principal stress σ_{max} and the total length of excavation-induced new cracks, and (b) the relation between principal stress ratio $\sigma_{max}/\sigma_{min}$ and the total length of excavation-induced new cracks for the two DFN models at various depths.

9.5 Discussion

The progressive rock mass failure around a geometrically idealised tunnel in a crystalline fractured rock is modelled by using 2D FEMDEM analysis. The characteristics of the EDZ were found significantly affected by the in-situ stresses and pre-existing fractures. Excavation in the condition of a higher maximum principal stress tends to generate more irreversible damage, i.e. new cracks and shear displacements, in the host rock. The ellipses of the EDZ featured by new fracturing around a circular opening are influenced by the pre-existing fractures and exhibit a

slightly oblique orientation to the far-field stresses. However, to draw a general conclusion, simulations based on multiple DFN realisations are important when solving real problems. Special care is also required when designing the boundary stresses applied to the FEMDEM model, since the actual in-situ stress field can be complex and distorted by tectonic factors, and the pore fluid pressure in the subsurface can be quite different from the hydrostatic linear prediction (especially in sedimentary and metamorphic terrains). Furthermore, the anisotropic nature of intact rock materials is also a nontrivial issue if the deforming and fracturing behaviour is to be more realistically simulated, especially for transversely isotropic rocks, e.g. shales [Lisjak et al., 2014a]. Integration of a rock support system module in the FEMDEM formulation may be important for calculating the safety of the concrete lining that prevents the surrounding rock from freely displacing and falling [Lisjak et al., 2014b]. It is also interesting to develop techniques for modelling acoustic emissions and/or microseismic events that can be used to describe EDZ features and compare with field measurement [Cai et al., 2007; Lisjak et al., 2013]. One unresolved issue in this study is related to the cohesive zone model: the mesh size dependency of model properties as has been mentioned in section 9.3.3 and also pointed out by Lisjak et al. [2014a]. Except for the possible solution of conducting field-scale recalibrations when solving real problems, development of a scale independent cohesive constitutive model or at least a universal scaling law could be very useful. Furthermore, the computational efficiency issue caused by setting a very small time step when using a very large penalty term to reproduce accurate deforming response [Mahabadi, 2012] may be overcome by introducing some non-penetration algorithms for computing multi-body interactions, e.g. the impulse-based method [Paluszny et al., 2013; Tang et al., 2013, 2014].

In this research, deformation of the solid was determined by the skeletal effective stresses, whereas the dynamic impact of local internal fluid pressure (e.g. fluid pressure dissipation near the excavation boundary) was not explicitly included. The immersed shell method [Viré et al., 2015] and the multiphase flow modelling [Su et al., 2015] that have been recently developed in the research group at Imperial College will be coupled with the FEMDEM geomechanical models to capture the complex two-way coupling processes involving the transient response of rock solid and fluid flow as well as the dynamic fluid-solid interaction. The long-term evolution

of EDZ around a nuclear waste repository is a multi-physical problem that is governed by a complex thermal-hydromechanical-chemical coupling process [Rutqvist et al., 2002; Hudson et al., 2009] and development of approaches for modelling such coupled phenomena are keenly anticipated.

Another limitation of this research is that 2D analysis was used to model the tunnel excavation and associated rock mass failure, whereas, in real tunnels, the rock mass fracture system deforms in 3D and the tunnelling is a time-dependent 3D process. There might be a way that the core relaxation process can be correlated with the advancing speed of the tunnelling face in 3D rock space by employing field measurement to calibrate the 2D FEMDEM simulation. However, it is essential to develop a 3D model if the fractured rock in response to phased excavation is to be realistically simulated. First, the pre-existing fractures are 3D geometries and can be arbitrarily oriented. Second, the propagation of new cracks is also a 3D problem in nature, which is not restricted in only one plane or manageable with plane strain assumptions, except in some peculiar cases, e.g. sedimentary rock with strong bedding features under larger parallel extensional tectonic forces. Third, the actual excavation method (e.g. top-heading and bench method) in tunnel construction is an extremely complex 3D process that involves significant interaction along the tunnel longitudinal axis [Read, 2004; Si et al., 2015]. In addition, the stress in the rock is also a 3D heterogeneous field [Lei et al., 2015b], where its three principal components can simultaneously affect the deformation of intact rocks and propagation of new fractures [Mahabadi, 2014a]. To achieve 3D geomechanical modelling, the 3D FEMDEM model combined with the joint constitutive model and crack propagation model (as has been used in Chapter 8) will be employed to capture the brittle deformation response including local concentrations of critically high tensile or differential stresses, together with realistic fracture shearing behaviour on pre-existing and newly propagated fractures. Evolution of the 3D EDZ around a tunnel excavation can be, therefore, captured by simulating the actual construction procedure. However, such a sophisticated simulation will be highly restrained by the extremely expensive computational cost.

The FEMDEM model that captures the dynamics of rock mass failure goes beyond the conventional key block theory that mainly includes static topological analysis [Zhang and Lei,

2013, 2014]. Compared to some other discrete modelling approaches such as the block-type DEM method [Min and Jing, 2003; Noorian-Bidgoli et al., 2013] and the particle-based DEM model [Potyondy and Cundall, 2004; Mas Ivars et al., 2010; Harthong et al., 2012], the proposed FEMDEM framework is able to model the realistic fracturing behaviour of brittle rocks governed by fundamental fracture mechanics principles associated with self-consistent strength and fracture energy parameters [Lisjak and Grasselli, 2014]. The key advantages of this work to the previous FEMDEM-based EDZ studies [Lisjak et al., 2014a, 2014b] is the capability of simulating the complex topology and sophisticated shearing of pre-existing fractures in addition to the brittle fracturing, which allows a more realistic modelling of the EDZ evolution in naturally fractured rocks. Furthermore, the detailed attention given to fracture aperture and connectivity of all pre-existing and new fractures can help to underpin simulation of hydromechanically coupled flow behaviour for the various phases in the life cycle of a nuclear waste repository.

9.6 Concluding remarks

To conclude, in the scope of 2D analysis, a workflow based on the hybrid FEMDEM method has been developed for modelling the underground excavation for nuclear waste disposal in geological formations with pre-existing discontinuities. The geomechanical model can capture the deformation of intact rock matrix, the heterogeneity of local stress fields, the reactivation of pre-existing discontinuities, and the propagation of new cracks induced by tensile, shear or mixed-mode brittle failure. A calibration was first conducted based on the laboratory-scale UCS and Brazilian disc tests to assign the most appropriate parameters for use in the numerical model in order to achieve a consistency between simulated macroscopic rock strengths and input microscopic mechanical properties. A joint constitutive model is also applied to pre-existing fractures to take into account the effect of asperity degradation and the scale-dependency of fracture roughness. A 2D numerical study of a circular tunnel excavation opened in two alternative heading directions in a fractured crystalline rock was conducted. The two cross-sections correspond to the two planes of far-field principal stresses. As the DFNs are based on real data for a specific site, the DFNs appropriate for analysis in each tunnel section have different fracture directional properties. An EDZ around the unsupported man-made opening is

formed by the coalescence of pre-existing discontinuities caused by new crack propagation in response to the excavation process. Excavation in the condition of a higher maximum principal stress tends to generate more irreversible damage in the host rock. The ellipses characterising the extent of the EDZ around a circular opening is influenced by the pre-existing fractures and exhibits a slightly oblique orientation to the far-field stresses. The results of this study have important implications for designing stable underground openings for nuclear waste repositories as well as other engineering facilities which are intended to generate minimal damage in host media.

10 Conclusions and future work

10.1 Summary of the present research

This thesis presented a systematic study of the geometry, geomechanics and fluid flow properties of natural fracture networks. After a brief background introduction of rock fractures in nature and associated engineering problems (Chapter 1), the thesis first presented an "appetiser" study of the statistics and tectonism of a multiscale natural fracture system to enhance the understanding of the geometrical complexity and underlying mechanisms of natural fracture networks (Chapter 2). From a literature review of discrete fracture network (DFN) models that were used to simulate the geomechanical and hydromechanical behaviour of natural fracture systems (Chapter 3), it became clear that several important outstanding issues were needed to be addressed, according to which the rest of the thesis was structured. A joint constitutive model (JCM) was implemented into the finite-discrete element method (FEMDEM) to simulate the complex mechanical behaviour of natural fractures associated with intrinsic surface asperities (Chapter 4). The JCM-FEMDEM model was applied to capture the geomechanical response of 2D natural and stochastic fracture networks at a metric scale with the consequences on their equivalent permeability further analysed (Chapter 5). An upscaling approach was developed to estimate the hydromechanical properties of larger scale fracture systems based on the metric scale simulation results (Chapter 6). The numerical model was extended to 3D to calculate the stress-dependent permeability of an idealised persistent fracture network (Chapter 7) and a realistic fractured sedimentary layer (Chapter 8). The capability of the developed JCM-FEMDEM model was further demonstrated through a vivid example of modelling the progressive rock mass failure around an excavation in a geological formation with pre-existing discontinuities (Chapter 9). Based on the observations and results of these studies, the following conclusions were made.

1. A natural fracture network is the result of the superposition of multiple fracture sets each linked to a separate tectonic event. The driving force for fracture formation may be dissipated at the end of a tectonic episode when the system becomes connected. However, the "effective" connectivity can successively be reduced by cementation of early

fractures and reestablished by subsequent cracking. In addition, the connectivity anisotropy may also permit additional cracking in directions which have a poorer percolation state. Thus, the "apparent" connectivity measured for fracture networks regardless of their internal sealing conditions may be highly variable depending on the intensity of previous crack-seal cycles and can indicate a state well above or close to the percolation threshold (Chapter 2).

2. Compared to other continuum or discontinuum approaches, the FEMDEM model provides a powerful tool to calculate the stress and deformation of rock matrix and solve the translation, rotation and interaction of multiple discrete solids. In such a computational scheme, pre-existing fractures can be treated as the internal boundaries of rock volumes. The FEMDEM approach also gives a natural solution route to capturing the fracturing process in rock governed by fracture mechanics principles (Chapter 3&4).

3. The FEMDEM formulation was extended to integrate a JCM model to better mimic the non-linear constitutive behaviour of natural fractures associated with intrinsic surface roughness. The combined JCM-FEMDEM model is able to achieve compatibility for both the fracture and matrix fields with respect to stress and displacement. The numerical model exhibits realistic shear strength and displacement characteristics with the recognition of fracture size effects. This extended FEMDEM model can be applied to simulate the complex behaviour of natural fracture networks under in-situ stresses including fracture opening, closing, shearing, dilatancy and new crack propagation (Chapter 4).

4. Important disparities may exist between a natural fracture network and its Poisson DFN equivalents in terms of geomechanical and hydromechanical properties. The two types of fracture networks exhibit significant differences with respect to stress heterogeneity, fracture wall shearing, aperture development, crack propagation and network connectivity. The stressed Poisson DFNs were found to take on the permeability of the stressed AFN but only in the direction with a good connectivity state. A considerable discrepancy was observed for flow in the direction associated with a poor percolation condition (Chapter 5).

5. The stress condition has significant influences on the mechanical behaviour of natural fractures including opening/closing, sliding, dilatancy, and can result in a very heterogeneous aperture distribution in a fracture network (Chapter 5-8). Stress-driven new cracks can also link pre-existing fractures to form critical fluid pathways and enhance the connectivity of the network (Chapter 5&8). Such geomechanically induced characteristics can also affect the fluid flow in the discontinuity system. Under a high stress ratio condition, the fluid flow can be highly localised in some large aperture channels created by block rotations and/or shear dilations (Chapter 7&8). The equivalent permeability varies with the rotation of the stress field (Chapter 5&8) and the change of the stress ratio (Chapter 7&8). As the stress ratio increases, the permeability of a fracture network can vary over several orders of magnitude. The permeability tensor under a critical stress state (i.e. with a high stress ratio that exceeds a certain threshold) can be much more anisotropic than that of a low stress ratio condition (Chapter 7).

6. The scaling behaviour of the fractured rock permeability relies on the connectivity scaling of the fracture system (related to its geometrical distribution) and the transmissivity scaling of individual fractures (related to the aperture distribution). Distinct permeability scaling trends were observed for fracture networks under different in-situ stress conditions. Based on the analysis of a simulated multiscale fracture system, the flow structure was observed to be scale-dependent and shift from extremely channelled to distributed as the modelling scale increases (Chapter 6).

7. The EDZ around an underground excavation in fractured rocks is formed by the coalescence of pre-existing discontinuities induced by new crack propagations in response to the engineering perturbations. Excavation in the condition of a higher maximum principal stress tends to generate more irreversible damage in the host rock. The EDZ characteristics, e.g. the spatial extent of the failure area and the anisotropy of the excavation-induced damage, are influenced by both the distribution of pre-existing natural fractures and the condition of far-field stresses (Chapter 9).

8. The observed effects of fractures and stresses on the rock mass properties (e.g. strength, deformation and permeability) illustrated the importance of integrating explicit DFN

representations and conducting geomechanical computations for more meaningful assessments of the hydromechanical behaviour of naturally fractured rocks (Chapter 5-9).

10.2 Original contributions

The original contributions of this thesis are summarised as below:

1. A tectonic interpretation was presented to explain the pattern formation and connectivity evolution of a multiscale natural fracture system (Chapter 2). This work proposed an answer to the open question—Are natural fracture networks well or poorly connected?

2. A JCM model that captures the rough wall interaction behaviour of individual fractures associated with asperity characteristics was implemented into the FEMDEM framework for simulating the geomechanical behaviour of fractured rocks (Chapter 4). In addition to capturing realistic fracture behaviour with respect to normal closure, shear strength and dilatancy, the key novel feature of this formulation is its capability of capturing the important size effect of fracture wall properties through a systematic characterisation of fracture network topologies.

3. The 2D FEMDEM model embedded with a JCM module was applied to simulate the geomechanical behaviour of a natural fracture network and its stochastic DFN equivalents at a metric scale (Chapter 5). This research comprehensively examined the validity of the Poisson DFN model in representing a 2D naturally fractured rock with respect to geomechanical and hydrological properties under in-situ stress conditions.

4. A new approach to upscaling 2D fracture network models was proposed for preserving geostatistical and geomechanical characteristics of a smaller scale fracture system (Chapter 6). A novel scheme accommodating discrete-time random walks in a recursive self-referencing lattice was developed to populate fractures together with their stress- and scale-dependent attributes into larger domains. Advantages of this approach include preserving the non-planarity of natural cracks, capturing the existence of long fractures, retaining the realism of variable apertures, and respecting the stress-dependency of displacement-length correlations.

5. The JCM model was also integrated into the 3D FEMDEM formulation to simulate the geomechanical behaviour of 3D natural fracture systems. The stress effects on fluid flow

in 3D were investigated for an idealised persistent fracture network (Chapter 7) and a realistic sedimentary layer with impersistent joint sets (Chapter 8). To the best knowledge of the author, the 3D work represents a first study to explore the stress-dependent permeability of 3D fracture networks based on explicit representation of fracture geometries and systematic characterisation of rock mass geomechanics.

6. The JCM-FEMDEM model was applied to simulate the EDZ evolution around a tunnel excavation in a crystalline formation with pre-existing discontinuities (Chapter 9). This research developed a workflow to incorporate explicit DFN geometries into the EDZ modelling in order to characterise the complex interactions between pre-existing fractures and new propagating cracks under excavation-induced perturbations.

10.3 Recommendations for future work

Extensions of this PhD research may include the following aspects:

1. It has been recognised as a challenging issue to create realistic DFN models for representing complex natural fracture networks with respect to important characteristics such as scaling, hierarchy, clustering and anisotropy. Some self-organised mechanisms that govern the correlation between fracture attributes and the interaction of fracture populations may be integrated to the stochastic DFN approach for more accurate representations. Furthermore, it is worth examining the validity of the conventional Poisson DFN model for capturing the hydromechanical behaviour of 3D fracture systems.

2. Enhancement of the computational efficiency seems to be an urgent task for the future development of the FEMDEM code. By implementing an implicit solver for calculating the nodal force/displacement field, the runtime may be much less than that of the current explicit temporal integration scheme. Parallel computing is also a promising technique to be employed for dealing with computations for large-scale engineering problems.

3. An extension to the current study of stress-dependent permeability of fracture networks is to simulate 3D fractured multilayer systems. Such a 3D stratified structure can be constructed by stacking different sedimentary beds, each of which is extruded from a 2D natural or stochastic fracture pattern containing finite-sized joints. The bedding plane

between adjacent layers can also be treated as a discontinuity similar to fractures. Due to the role of the bedding plane that links joints of neighbouring sedimentary units, the bed-normal permeability of the multilayer system may be very different from the one derived using the conventional hydrogeology method that assumes multiple layers are connected "in series". The stress effects on fluid flow through the layered fractured systems can be explored based on the geomechanical characterisation using the 3D JCM-FEMDEM model. Similar 3D geomechanical modelling can also be conducted on more general 3D DFNs with randomly dipping fractures that usually occur in crystalline rocks. However, the difficulty of meshing such complex geometries that may involve very small intersection angles needs to be tackled first.

4. Another planned research is to study the stress effects on the solute transport in 2D/3D fracture networks. The non-linear fracture behaviour (opening/closing, shearing and dilation) in response to applied stress conditions captured by the JCM-FEMDEM model can result in a strongly heterogeneous fluid velocity field in the fracture network and lead to some sophisticated breakthrough characteristics.

5. The 2D excavation research would benefit greatly from being extended to 3D. The natural fractures in rock are 3D geological structures and the excavation-induced new cracks also propagate in 3D space. The excavation method (e.g. top-heading and bench method) adopted in actual tunnel constructions is an extremely complex 3D process that engenders significant mechanical interactions in fractured rocks along the tunnel longitudinal axis. The developed 3D JCM-FEMDEM model will thus be used to simulate the 3D EDZ evolution around/ahead of an advancing tunnel in the future.

6. The hydromechanical modelling of fractured rocks in this thesis is based on the "effective stress" theory and mainly focused on the solid-to-fluid coupling. However, the developed 2D/3D JCM-FEMDEM formulation is well suited to extending to two-way fully-coupled simulations that allow total normal stresses to be modified by varying fluid pressure in fractures and intact rocks. An already ongoing research effort in the Imperial College group is to link the JCM-FEMDEM solver with another "in-house" code, i.e. IC-FERST (Imperial College Finite Element Reservoir Simulator), to simulate the

coupled fluid-solid processes involved in various engineering problems such as hydraulic fracturing and reservoir compaction.

7. More efforts are also needed with respect to the validation and calibration of the numerical models based on experimental data or field measurements. This can be a critical issue if the numerical models are to be used for practical applications.

References

Ackermann, R. V., and R. W. Schlische (1997), Anticlustering of small normal faults around larger faults, Geology, 25(12), 1127-1130.

Adler, P. M., and J.-F. Thovert (1999), Fractures and Fracture Networks, Kluwer Academic Publisher, Dordrecht.

Adler, P. M., J.-F. Thovert, and V. V. Mourzenko (2012), Fractured Porous Media, Oxford University Press, Oxford.

Allegre, C. J., J. L. Le Mouel, and A. Provost (1982), Scaling rules in rock fracture and possible implications for earthquake prediction, Nature, 297, 47-49.

Anders, M. H., S. E. Laubach, and C. H. Scholz (2014), Microfractures: A review, J. Struct. Geol., 69, 377-394.

Andersson, J., A. M. Shapiro, and J. Bear (1984), A stochastic model of a fractured rock conditioned by measured information, Water Resour. Res., 20(1), 79-88.

Andersson, J., and B. Dverstorp (1987), Conditional simulations of fluid flow in three-dimensional networks of discrete fractures, Water Resour. Res., 23(10), 1876-1886.

Antonellini, M. A., A. Aydin, and D. D. Pollard (1994), Microstructure of deformation bands in porous sandstones at Arches National Park, Utah, J. Struct. Geol., 16(7), 941-959.

Asadollahi, P., and F. Tonon (2010), Constitutive model for rock fractures: revisiting Barton's empirical model, Eng. Geol., 113, 11-32.

Asahina, D., J. E. Houseworth, J. T. Birkholzer, J. Rutqvist, and J.E. Bolander (2014), Hydro-mechanical model for wetting/drying and fracture development in geomaterials, Comput. Geosci., 65, 13-23.

Atkinson, B. K. (1984), Subcritical crack growth in geological materials, J. Geophys. Res. 89(B6), 4077-4114.

Atkinson, B. K., and P. G. Meredith (1987), Experimental fracture mechanics data for rocks and minerals, in Fracture Mechanics of Rock, edited by B. K. Atkinson, pp. 477-525, Academic Press, San Diego.

Baecher, G. B. (1983), Statistical analysis of rock mass fracturing, Math. Geol., 15(2), 329-348.

Baghbanan, A., and L. Jing (2007), Hydraulic properties of fractured rock masses with correlated fracture length and aperture, Int. J. Rock Mech. Min. Sci., 44(5), 704-719.

Baghbanan, A., and L. Jing (2008), Stress effects on permeability in a fractured rock mass with correlated fracture length and aperture, Int. J. Rock Mech. Min. Sci., 45, 1320-1334.

Bahaaddini, M., P. C. Hagan, R. Mitra, and B. K. Hebblewhite (2014), Scale effect on the shear behaviour of rock joints based on a numerical study, Eng. Geol., 181, 212-23.

Bai, T, and D. D. Pollard (2001), Getting more for less: The unusual efficiency of fluid flow in fractures, Geophys. Res. Lett., 28(1), 65-68.

Bai, T., D. D. Pollard, and H. Gao (2000), Explanation for fracture spacing in layered materials, Nature, 403, 753-756.

Bakun-Mazor, D., Y. H. Hatzor, and W. S. Dershowitz (2009), Modeling mechanical layering effects

on stability of underground openings in jointed sedimentary rocks, Int. J. Rock Mech. Min. Sci., 46, 262-271.

Balberg, I. and N. Binenbaum (1983). Computer study of the percolation threshold in a two-dimensional anisotropic system of conducting sticks, Phys. Rev. B, 28, 3799-3812.

Bandis, S. C. (1980), Experimental Studies of Scale Effects on Shear Strength, and Deformation of Rock Joints [PhD Thesis], University of Leeds, Leeds.

Bandis, S. C., A. C. Lumsden, and N. Barton (1981), Experimental studies of scale effects on the shear behaviour of rock joints, Int. J. Rock Mech. Min. Sci. Geomech. Abstr., 18, 1-21.

Bandis, S. C., A. C. Lumsden, and N. Barton (1983), Fundamentals of rock joint deformation, Int. J. Rock Mech. Min. Sci. Geomech. Abstr., 20, 249-268.

Barla, M., G. Piovano, and G. Grasselli (2011), Rock slide simulation with the combined finite-discrete element method, Int. J. Geomech., 12(6), 711-721.

Barton, C. A., and M. D. Zoback (1992), Self-similar distribution and properties of macroscopic fractures at depth in crystalline rock in the Cajon Pass Scientific Drill Hole, J. Geophys. Res., 97(B4), 5181–5200.

Barton, C. A., M. D. Zoback, and D. Moos (1995), Fluid flow along potentially active faults in crystalline rock, Geology, 23(8), 683-686.

Barton, C. C. (1995), Fractal analysis of scaling and spatial clustering of fractures, in Fractals in the Earth Sciences, edited by C. C. Barton, and P. R. La Pointe, pp. 141-178, Plenum Press, New York.

Barton, N. (1981), Some size dependent properties of joints and faults, Geophys. Res. Lett., 8(7), 667-670.

Barton, N. (2013), Shear strength criteria for rock, rock joints, rockfill and rock masses: problems and some solutions. J. Rock Mech. Geotech. Eng., 5, 249-261.

Barton, N., and V. Choubey (1977), The shear strength of rock joints in theory and practice, Rock Mech., 10, 1-54.

Barton, N., and S. C. Bandis (1980), Some effects of scale on the shear strength of joints, Int. J. Rock Mech. Min. Sci. Geomech. Abstr., 17, 69-73.

Barton, N., S. C. Bandis, and K. Bakhtar (1985), Strength, deformation and conductivity coupling of rock joints, Int. J. Rock Mech. Min. Sci. Geomech. Abstr., 22, 121-140.

Bear J., C.-F. Tsang, and G. de Marsily (1993), Flow and Contaminant Transport in Fractured Rock, Academic Press Inc., San Diego.

Belayneh, M, and J. W. Cosgrove (2004), Fracture-pattern variations around a major fold and their implications regarding fracture prediction using limited data: an example from the Bristol Channel Basin, in The Initiation, Propagation, and Arrest of Joints and Other Fractures, Geol. Soc. London Spec. Publ., vol. 231, edited by J. W. Cosgrove and T. Engelder, pp. 89-102, Geological Society, London.

Belayneh, M. W., S. Geiger, and S. K. Matthäi (2006). Numerical simulation of water injection into layered fractured carbonate reservoir analogs, AAPG Bull., 90(10), 1473-1493.

Belayneh, M. W., S. K. Matthäi, M. J. Blunt, and S. F. Rogers (2009). Comparison of deterministic with stochastic fracture models in water-flooding numerical simulations, AAPG Bull., 93(11),

1633-48.

Benedicto, A., M. Séguret, and P. Labaume (1999), Interaction between faulting, drainage and sedimentation in extensional hanging-wall syncline basins: example of the Oligocene Matelles basin (Gulf of Lion rifted margin, SE France), in The Mediterranean Basins: Tertiary Extension within the Alpine Orogen, Geol. Soc. London Spec. Publ., vol. 156, edited by B. Durand et al., pp. 81-108, Geological Society, London.

Berkowitz, B. (1995), Analysis of fracture network connectivity using percolation theory, Math. Geol., 27(4), 467-483.

Berkowitz, B. (2002), Characterizing flow and transport in fractured geological media: A review, Adv. Water Res., 25, 861-884.

Berkowitz, B., and A., Hadad (1997), Fractal and multifractal measures of natural and synthetic fracture networks, J. Geophys. Res., 102, 12205-12218.

Berkowitz, B., and P. M. Adler (1998), Stereological analysis of fracture network structure in geological formations, J. Geophys. Res., 103(B7), 15339-15360.

Berkowitz, B., O. Bour, P. Davy, and N. Odling (2000), Scaling of fracture connectivity in geological formations, Geophys. Res. Lett., 27(14), 2061-2064.

Bertrand, L., Y. Géraud, E. Le Garzic, J. Place, M. Diraison, B. Walter, and S. Haffen (2015), A multiscale analysis of a fracture pattern in granite: A case study of the Tamariu granite, Catalunya, Spain, J. Struct. Geol., 78, 52-66.

Billaux, D. M., J. P. Chiles, K. Hestir, and J. Long (1989), Three-dimensional statistical modelling of a fractured rock mass--an example from the Fanay-Augères mine, Int. J. Rock Mech. Min. Sci. Geomech. Abstr., 26(3-4), 281-299.

Blum, P., R. Mackay, and M. S. Riley (2009), Stochastic simulations of regional scale advective transport in fractured rock masses using block upscaled hydro-mechanical rock property data, J. Hydrol., 369, 318-325.

Blum, P., R. Mackay, M. S. Riley, and J. L. Knight (2005), Performance assessment of a nuclear waste repository: Upscaling coupled hydro-mechanical properties for far-field transport analysis, Int. J. Rock Mech. Min. Sci., 42, 781-792.

Bobet, A., A. Fakhimi, S. Johnson, J. Morris, F. Tonon, and M. Ronald Yeung (2009), Numerical models in discontinuous media: review of advances for rock mechanics applications. J. Geotech. Geoenviron. Eng., 135(11), 1547-1561.

Bonilla-Sierra, V., L. Scholtès, F. V. Donzé, and M. K. Elmouttie (2015), Rock slope stability analysis using photogrammetric data and DFN-DEM modelling, Acta Geotech., 10, 497-511.

Bonnet, E., O. Bour, N. E. Odling, P. Davy, I. Main, P. Cowie, and B. Berkowitz (2001), Scaling of fracture systems in geological media, Rev. Geophys., 39(3), 347-383.

Bour, O., and P. Davy (1997), Connectivity of random fault networks following a power law fault length distribution, Water Resour. Res., 33(7), 1567-1583.

Bour, O., and P. Davy (1998), On the connectivity of three-dimensional fault networks, Water Resour. Res., 34(10), 2611-2622.

Bour, O., and P. Davy (1999), Clustering and size distribution of fault patterns: theory and measurements, Geophys. Res. Lett., 26(13), 2001-2004.

Bour, O., P. Davy, C. Darcel, and N. E. Odling (2002), A statistical scaling model for fracture network geometry, with validation on a multiscale mapping of a joint network (Hornelen Basin, Norway). J. Geophys. Res., 107(B6), ETG4-1-ETG4-12.

Brace, W. F. (1980), Permeability of crystalline and argillaceous rocks, Int. J. Rock Mech. Min. Sci. Abstr., 17, 241-251.

Brace, W. F. (1984), Permeability of crystalline rocks: New in situ measurements, J. Geophys. Res., 89(B6), 4327-4330.

Brown, S. R., and R. L. Bruhn (1998), Fluid permeability of deformable fracture networks, J. Geophys. Res., 103(B2), 2489-2500.

Bureau de Recherches Géologiques et Minières (2011), The Geological Map of France, scale 1:250,000, http://infoterre.brgm.fr/.

Cacas, M. C., E. Ledoux, G. deMarsily, B. Tillie, A. Barbreau, E. Durand, B. Feuga, and P. Peaudecerf (1990a), Modeling fracture flow with a stochastic discrete fracture network: calibration and validation: 1. The flow model, Water Resour. Res., 26(3), 479-489.

Cacas, M. C., E. Ledoux, G. deMarsily, A. Barbreau, P. Calmels, B. Gaillard, and R. Margritta (1990b), Modeling fracture flow with a stochastic discrete fracture network: Calibration and validation: 2. The transport model, Water Resour. Res., 26(3), 491–500.

Cai, M., P. K. Kaiser, H. Moriokab, M. Minamib, T. Maejimab, Y. Tasakac, and H. Kurosec (2007), FLAC/PFC coupled numerical simulation of AE in large-scale underground excavations, Int. J. Rock Mech. Min. Sci., 44, 550-564.

Caine, J. S., J. P. Evans, and C. B. Forster (1996), Fault zone architecture and permeability structure, Geology, 24(11), 1025-1028.

Cartwright, J. A., B. D. Trudgill, and C. S. Mansfield (1995), Fault growth by segment linkage: an explanation for scatter in maximum displacement and trace length data from the Canyonlands Grabens of SE Utah, J. Struct. Geol., 17(9), 1319-1326.

Chelidze, T. L. (1982), Percolation and fracture, Phys. Earth Planet. Int., 28, 93-101.

Chilès, J. P. (1988), Fractal and geostatistical methods for modeling of a fracture network, Math. Geol., 20, 631-654.

Cho N., Martin C. D., and Sego D. C. (2007), A clumped particle model for rock, Int. J. Rock Mech. Min. Sci., 44(7), 997-1010.

Clauser, C. (1992), Permeability of crystalline rocks, Eos Trans. AGU, 73(21), 233-238.

Cowie, P. A., and C. H. Scholz (1992a), Physical explanation for the displacement-length relationship of faults using a post-yield fracture mechanics model, J. Struct. Geol., 14(10), 1133-1148.

Cowie, P. A., and C. H. Scholz (1992b), Displacement-length scaling relationship for fauls: data synthesis and discussion, J. Struct. Geol., 14(10), 1149-1156.

Cowie, P. A., C. Vanneste, and D. Sornette (1993), Statistical physics model for the spatiotemporal evolution of faults, J. Geophys. Res., 98(B12), 21809-21821.

Cowie, P. A., D. Sornette, and C. Vanneste (1995), Multifractal scaling properties of a growing fault population, Geophys. J. Int., 122, 457-469.

Cox, S. J. D., and C. H. Scholz (1985), A direct measurement of shear fracture energy in rocks,

Geophys. Res. Lett., 12, 813-816.

Cox, S. J. D., and C. H. Scholz (1988), On the formation and growth of faults: an experimental study, J. Struct. Geol., 10(4), 414-430.

Crider, J. G. (2015), The initiation of brittle faults in crystalline rock, J. Struct. Geol., 77, 159-174.

Crider, J. G., and D. C. P. Peacock (2004), Initiation of brittle faults in the upper crust: a review of field observations, J. Struct. Geol., 26, 691-707.

Cruikshank, K. M., G. Zhao, and A. M. Johnson (1991), Analysis of minor fractures associated with joints and faulted joints, J. Struct. Geol., 13(8), 865-886.

Cundall, P. A. (1971), A computer model for simulating progressive large scale movements in blocky rock systems, in Proceedings of the International Symposium on Rock Mechanics, vol. 1, pp. 129-136, ISRM, Nancy.

Cundall, P. A. (1988), Formulation of a three-dimensional distinct element model—Part I. A scheme to detect and represent contacts in a system composed of many polyhedral blocks, Int. J. Rock Mech. Min. Sci. Geomech. Abstr., 25(3), 107-116.

Cundall, P. A., and O. D. L. Strack (1979), A discrete numerical model for granular assemblies, Géotechnique, 29(1), 47-65.

Damjanaca, B., M. Boarda, M. Linb, D. Kickerb, and J. Leemb (2007), Mechanical degradation of emplacement drifts at Yucca Mountain—A modeling case study: Part II: Lithophysal rock, Int. J. Rock Mech. Min. Sci., 44, 368-399.

Darcel, C., O. Bour, P. Davy, and J.-R. de Dreuzy (2003a). Connectivity properties of two-dimensional fracture networks with stochastic fractal correlation, Water Resour. Res., 39(10), 1272.

Darcel, C., O. Bour, and P. Davy (2003b), Stereological analysis of fractal fracture networks, J. Geophys. Res., 108(B9), 2451.

Darcel, C., O. Bour, and P. Davy (2003c). Cross-correlation between length and position in real fracture networks, Geophys. Res. Lett, 30(12), 1650, doi: 10.1029/2003GL017174.

Davy, P. (1993), On the frequency-length distribution of the San Andreas fault system, J. Geophys. Res., 98, 12141-12151.

Davy, P., O. Bour, J.-R. de Dreuzy, and C. Darcel (2006), Flow in multiscale fractal fracture networks, in Fractal Analysis for Natural Hazards, Geol. Soc. London Spec. Publ., vol. 261, edited by G. Cello and B. D. Malamud, pp. 31-45, Geological Society, London.

Davy, P., R. Le Goc, and C. Darcel (2013), A model of fracture nucleation, growth and arrest, and consequences for fracture density and scaling, J. Geophys. Res. Solid Earth, 118, 1393-1407.

Davy, P., R. Le Goc, C. Darcel, O. Bour, J.-R. de Dreuzy, and R. Munier (2010), A likely universal model of fracture scaling and its consequence for crustal hydromechanics, J. Geophys. Res., 115, B10411.

Dawers, N. H., M. H. Anders, and C. H. Scholz (1993), Growth of normal faults: displacement-length scaling, Geol., 21, 1107-1110.

de Dreuzy, J.-R., P. Davy, and O. Bour (2010), Percolation parameter and percolation-threshold estimates for three-dimensional random ellipses with widely scattered distributions of eccentricity and size, Phys. Rev. E, 62(5), 5948-5952.

de Dreuzy, J.-R., P. Davy, and O. Bour (2001a), Hydraulic properties of two-dimensional random fracture networks following a power law length distribution: 1. Effective connectivity, Water Resour. Res., 37, 2065-2078.

de Dreuzy, J.-R., P. Davy, and O. Bour (2001b), Hydraulic properties of two-dimensional random fracture networks following a power law length distribution: 2. Permeability of networks based on log-normal distribution of apertures, Water Resour. Res., 37, 2079-2095.

de Dreuzy, J.-R., P. Davy, and O. Bour (2002), Hydraulic properties of two-dimensional random fracture networks following power law distributions of length and aperture, Water Resour. Res. 38(12), 1276.

de Dreuzy, J.-R., C. Darcel, P. Davy, and O. Bour (2004), Influence of spatial correlation of fracture centers on the permeability of two-dimensional fracture networks following a power law length distribution, Water Resour. Res., 40, W01502.

de Dreuzy, J.-R., Y. Méheust, G. Pichot (2012), Influence of fracture scale heterogeneity on the flow properties of three-dimensional discrete fracture networks (DFN), J. Geophys. Res. 117, B11207.

de Joussineau, G., and A. Aydin (2007), The evolution of the damage zone with fault growth in sandstone and its multiscale characteristics, J. Geophys. Res., 112, B12401.

de Marsily, G. (1986), Quantitative Hydrogeology: Groundwater Hydrology for Engineers, Academic Press, Orlando.

Dershowitz W. S, and H. H. Einstein (1988), Characterizing rock joint geometry with joint system models, Rock Mech. Rock Eng., 21, 21-51.

Dershowitz, B., P. La Pointe, T. Eiben, and L. Wei (2000), Integration of discrete feature network methods with conventional simulator approaches, SPE J., 3, 165-170.

Du Bernard, X., P. Labaume, C. Darcel, P. Davy, and O. Bour (2002), Cataclastic slip band distribution in normal fault damage zones, Nubian sandstones, Suez rift, J. Geophys. Res., 107(B7), 2141.

Dverstorp, B., and J. Andersson (1989), Application of the discrete fracture network concept with field data: Possibilities of model calibration and validation, Water Resour. Res., 25(3), 540-550.

Eberhardt, E., D. Stead, and J. S. Coggan (2004), Numerical analysis of initiation and progressive failure in natural rock slopes—the 1991 Randa rockslide, Int. J. Rock Mech. Min. Sci., 41(1), 69-87.

Ehlen, J. (2000), Fractal analysis of joint patterns in granite, Int. J. Rock Mech. Min. Sci., 37, 909-922.

Einstein, H. H., and G. B. Baecher (1983), Probabilistic and statistical methods in engineering geology. Rock Mech. Rock Eng., 16(1), 39-72.

Elmo, D., and D. Stead (2010), An integrated numerical modelling e discrete fracture network approach applied to the characterisation of rock mass strength of naturally fractured pillars. Rock Mech. Rock Eng., 43(1), 3-19.

Elmo, D., D. Stead, E. Eberhardt, and A. Vyazmensky (2013), Applications of finite element/discrete element modeling to rock engineering problems, Int. J. Geomech., 13(5), 565-580.

Engelder, T., and P. Geiser (1980), On the use of regional joint sets as trajectories of paleostress fields during the development of the Appalachian Plateau, New York, J. Geophys. Res., 85(B11),

6319-6341.

Esmaieli, K., J. Hadjigeorgiou, and M. Grenon (2010), Estimating geometrical and mechanical REV based on synthetic rock mass models at Brunswick Mine, Int. J. Rock Mech. Min. Sci., 47, 915-926.

Evans, P. H., and M. S. Marthe (1968), Microcracking and stress-strain curves for concrete in tension, Mater. Struct., 1, 61-64.

Feng, X., P. Pan, and H. Zhou (2006), Simulation of the rock microfracturing process under uniaxial compression using an elasto-plastic cellular automaton, Int. J. Rock Mech. Min. Sci., 43, 1091-1108.

Figueiredo, B., C.-F. Tsang, J. Rutqvist, and A. Niemi (2015), A study of changes in deep fractured rock permeability due to coupled hydro-mechanical effects, Int. J. Rock Mech. Min. Sci., 79, 70-85.

Follin, S., L. Hartley, I. Rhén, P. Jackson, S. Joyce, D. Roberts, and B. Swift (2014), A methodology to constrain the parameters of a hydrogeological discrete fracture network model for sparsely fractured crystalline rock, exemplified by data from the proposed high-level nuclear waste repository site at Forsmark, Sweden, Hydrogeol. J., 22(2), 313–331.

Fossen, H. and J. Hesthammer (1997), Geometric analysis and scaling relations of deformation bands in porous sandstone, J. Struct. Geol., 19, 1479-1493.

Geiger, S., A. Cortis, and J. T. Birkholzer (2010), Upscaling solute transport in naturally fractured porous media with the continuous time random walk method, Water Resour. Res., 46, W12530.

Geiger, S., and S. K. Matthäi (2014), What can we learn from high-resolution numerical simulations of single- and multi-phase fluid flow in fractured outcrop analogues?, in Advances in the Study of Fractured Reservoirs, Geol. Soc. London Spec. Publ., vol. 374, edited by G. H. Spence et al., pp. 125-144, Geological Society, London.

Geiger, S., S. Roberts, S. K. Matthäi, C. Zoppou, and A. Burri (2004), Combining finite element and finite volume methods for efficient multiphase flow simulations in highly heterogeneous and structurally complex geologic media, Geofluids, 4, 284-299.

Ghazvinian, E., M. S. Diederichs, and R. Quey (2014), 3D random Voronoi grain-based models for simulation of brittle rock damage and fabric-guided micro-fracturing, J. Rock Mech. Geotech. Eng., 6, 506-521.

Gillespie, P. A., J. J. Walsh, and J. Watterson (1992), Limitations of dimension and displacement data from single faults and the consequences for data analysis and interpretation, J. Struct. Geol., 14(10), 1157-1172.

Gillespie, P. A., J. J. Walsh, J. Watterson, C. G. Bonson, and T. Manzocchi (2001), Scaling relationships of joint and vein arrays from The Burren, Co. Clare, Ireland, J. Struct. Geol., 23, 183-201.

Golder Associate Inc. (2011) FracMan7 User Documentation, Golder Associate Inc., Seattle, Washington.

Goodman, R. E. (1976), Methods of Geological Engineering in Discontinuous Rocks, West, St Paul.

Goodman, R.E., R.L. Taylor, and T.L. Brekke (1968), A model for mechanics of jointed rock, J. Soil Mech. Found. Div., 94, 637-659.

Griffith, W. A., P. F. Sanz, and D. D. Pollard (2009), Influence of outcrop scale fractures on the effective stiffness of fault damage zone rocks, Pure Appl. Geophys., 166, 1595-1627.

Gueguen, Y., C. David, and P. Gavrilenko (1991), Percolation networks and fluid transport in the crust, Geophys. Res. Lett., 18(5), 931-934.

Gunsallus, K. L., and F. H. Kulhawy (1984), A comparative evaluation of rock strength measures, Int. J. Rock Mech. Min. Sci. Geomech. Abstr., 21, 233-248.

Guo, L. (2014), Development of a Three-dimensional Fracture Model for the Combined Finite-Discrete Element Method [PhD Thesis], Imperial College London, London.

Guo, L., J.-P. Latham, and J. Xiang (2015), Numerical simulation of breakages of concrete armour units using a three-dimensional fracture model in the context of the combined finite-discrete element method, Comput. Struct., 146, 117-142.

Guo, L., J. Xiang, J.-P. Latham, and B. Izzuddin (2016), A numerical investigation of mesh sensitivity for a new three-dimensional fracture model within the combined finite-discrete element method, Eng. Frac. Mech., doi:10.1016/j.engfracmech.2015.11.006.

Hadjigeorgiou, J., K. Esmaieli, and M. Grenon (2009), Stability analysis of vertical excavations in hard rock by integrating a fracture system into a PFC model, Tunn. Undergr. Sp. Tech., 24, 296-308.

Hammah, R. E., and J. H. Curran (1998), Fuzzy cluster algorithm for the automatic identification of joint sets, Int. J. Rock Mech. Min. Sci., 35(7), 889-905.

Hart, R., P. A. Cundall, and J. Lemos (1988), Formulation of a three-dimensional distinct element model—Part II. Mechanical calculations for motion and interaction of a system composed of many polyhedral blocks, Int. J. Rock Mech. Min. Sci. Geomech. Abstr., 25(3), 117-125.

Harthong, B., L. Scholtès, and F. Donzé (2012), Strength characterization of rock masses, using a coupled DEM-DFN model, Geophys. J. Int., 191, 467-480.

Hatton, C. G., I. G. Main, and P. G. Meredith (1994), Non-universal scaling of fracture length and opening displacement, Nature, 367, 160-162.

Hatzor, Y. H., A. A. Arzib, Y. Zaslavskyc, and A. Shapirad (2004), Dynamic stability analysis of jointed rock slopes using the DDA method: King Herod's Palace, Masada, Israel, Int. J. Rock Mech. Min. Sci., 41, 813-832.

Healy, D., Jones, R. R., and Holdsworth, R. E. (2006), Three-dimensional brittle shear fracturing by tensile crack interaction, Nature, 439, 64-67.

Hentschel, H. G. E., and I. Procaccia (1983), The infinite number of generalized dimensions of fractals and strange attractors, Physica, 8D, 435-444.

Herbert, A. W. (1996), Modelling approaches for discrete fracture network flow analysis, in Coupled Thermo-Hydro-Mechanical Processes of Fractured Media, edited by O. Stephansson, L. Jing and C.-F. Tsang, pp. 213-229, Elsevier, Amsterdam.

Hestir, K., and J. C. S. Long (1990), Analytical expressions for the permeability of random two-dimensional Poisson fracture networks based on regular lattice percolation and equivalent media theories, J. Geophys. Res., 95(B13), 21565–21581

Hoek, E. (1983), Strength of jointed rock masses, Géotechnique, 33, 187-223.

Hoek, E., and E. T. Brown (1997), Practical estimates of rock mass strength, Int. J. Rock Mech. Min.

Sci., 34(8), 1165-1186.

Hoek, E., and C. D. Martin (2014), Fracture initiation and propagation in intact rock − A review, J. Rock Mech. Geotech. Eng. 6, 287-300.

Holland, M., and J. L. Urai (2010), Evolution of anastomosing crack–seal vein networks in limestones: Insight from an exhumed high-pressure cell, Jabal Shams, Oman Mountains, J. Struct. Geol., 32, 1279-1290.

Hooker, J. N., J. F. W. Gale, L. A. Gomez, S. E. Laubach, R. Marrett, and R. M. Reed (2009). Aperture-size scaling variations in a low-strain opening-mode fracture set, Cozzette Sandstone, Colorado, J. Struct. Geol., 31, 707-718.

Horgan, G. W., and I. M. Young (2000), An empirical stochastic model for the geometry of two-dimensional crack growth in soil (with Discussion), Geoderma, 96, 263-276.

Horii, H., and S. Nemat-Nasser (1985), Compression-induced microcrack growth in brittle solids: Axial splitting and shear failure, J. Geophys. Res., 90(B4), 3105-3125.

Hudson, J. A., A. Bäckström, J. Rutqvist, L. Jing, T. Backers, M. Chijimatsu, R. Christiansson, X.-T. Feng, A. Kobayashi, T. Koyama, H.-S. Lee, I. Neretnieks, P.-Z. Pan, M. Rinne, and B.-T. Shen (2009), Characterising and modelling the excavation damaged zone in crystalline rock in the context of radioactive waste disposal, Environ. Geol., 57(6), 1275-1297.

Hunsdale, R., and D. J. Sanderson (1998), Fault distribution analysis - an example from Kimmeridge Bay, Dorset, in Development, Evolution and Petroleum Geology of the Wessex Basin, Geol. Soc. London Spec. Publ., vol. 133, edited by J. R. Underhill, pp. 299-310, Geological Society, London, doi:10.1144/GSL.SP.1998.133.01.14.

Institut National de l'Information Géographique et Forestière (1954), Aerial Analogic Photographs, No. F2543-2843 & F2742-2842, scale 1:25,000.

Irwin, G. R. (1968), Linear fracture mechanics, fracture transition, and fracture control, Eng. Frac. Mech., 1(2), 241-257.

Itasca (2013a), UDEC (Version 5.0) Manual, Itasca Consulting Group Inc., Minneapolis, USA.

Itasca (2013b), 3DEC (Version 5.0) Manual, Itasca Consulting Group Inc., Minneapolis, USA.

Itasca (2014), PFC (Version 5.0) Manual, Itasca Consulting Group Inc., Minneapolis, USA.

Jacquemyn, C., M. Huysmans, D. Hunt, G. Casini, and R. Swennen (2015), Multi-scale three-dimensional distribution of fracture- and igneous intrusion-controlled hydrothermal dolomite from digital outcrop model, Latemar platform, Dolomites, northern Italy, AAPG Bull., 99(5), 957-984.

Jaeger, J. C., N. G. W. Cook, and R. W. Zimmerman (2007), Fundamentals of Rock Mechanics (4th Edition), Blackwell Publishing, Oxford.

Jiang, Q. H., and M. R. Yeung (2004), A model of point-to-face contact for three-dimensional discontinuous deformation analysis, Rock Mech. Rock Eng., 37(2), 95-116.

Jing, L. (1998), Formulation of discontinuous deformation analysis (DDA)—an implicit discrete element model for block systems, Eng. Geol., 49, 371-381.

Jing, L. (2000), Block system construction for three-dimensional discrete element models of fractured rocks, Int. J. Rock Mech. Min. Sci., 37, 645-659.

Jing, L. (2003), A review of techniques, advances and outstanding issues in numerical modelling for

rock mechanics and rock engineering. Int. J. Rock Mech. Min. Sci., 40(3), 283-353.

Jing, L., and J. A. Hudson (2002), Numerical methods in rock mechanics, Int. J. Rock Mech. Min. Sci., 39(4), 409-427.

Jing, L., and O. Stephansson (2007), Fundamentals of discrete element methods for rock engineering: theory and applications, Elsevier, Oxford.

Jing, L., E. Nordlund, and O. Stephansson (1994). A 3-D constitutive model for rock joints with anisotropic friction and stress dependency in shear stiffness, Int. J. Rock Mech. Min. Sci. Geomech. Abstr., 31, 173-178.

Jing, L., Y. Ma, and Z. Fang (2001), Modeling of fluid flow and solid deformation for fractured rocks with discontinuous deformation analysis (DDA) method, Int. J. Rock Mech. Min. Sci., 38, 343-355.

Jing, L., K.-M. Min, A. Baghbanan, and Z. Zhao (2013), Understanding coupled stress, flow and transport processes in fractured rocks, Geosys. Eng., 16(1), 2-25.

Josnin, J.-Y., H. Jourde, P. Fénart, and P. Bidaux (2002), A three-dimensional model to simulate joint networks in layered rocks, Can. J. Earth Sci., 39, 1443-1455.

Jourde, H., E. A. Flodin, A. Aydin, L. J. Durlofsky, and X.-H. Wen (2002), Computing permeability of fault zones in eolian sandstone from outcrop measurements, AAPG Bull., 86(7), 1187-1200.

Jourde, H., P. Fenart, M. Vinches, S. Pistre and B. Vayssade (2007), Relationship between the geometrical and structural properties of layered fractured rocks and their effective permeability tensor. A simulation study, J. Hydrol., 337, 117-132.

Kachanov M. (1992), Effective elastic properties of a cracked solid: Critical review of some basic concepts, Appl. Mech. Rev., 45, 304-335.

Karami, A., and D. Stead (2008), Asperity degradation and damage in the direct shear test: a hybrid FEM/DEM approach, Rock Mech. Rock Eng., 41, 229-266.

Kattenhorn, S. A., and D. D. Pollard (2001), Integrating 3-D seismic data, field analogs, and mechanical models in the analysis of segmented normal faults in the Wytch Farm oil field, southern England, United Kingdom, AAPG Bull., 85(7), 1183-1210.

Kaye, B. H. (1994), A Random Walk Through Fractal Dimensions, VCH, Weinheim.

Kazerani, T., and J. Zhao (2010), Micromechanical parameters in bonded particle method for modelling of brittle material failure, Int. J. Numer. Anal. Methods Geomech., 34(18), 1877-1895.

Kazerani, T., Z. Y. Yang, and J. Zhao (2012), A discrete element model for predicting shear strength and degradation of rock joint by using compressive and tensile test data, Rock Mech. Rock Eng., 45(5), 695-709.

Kidan, T. W., and J. W. Cosgrove (1996), The deformation of multilayers by layer-normal compression; an experimental investigation, J. Struct. Geol., 18(4), 461-474.

Kim, Y.-I., B. Amadei, and E. Pan (1999), Modeling the effect of water, excavation sequence and rock reinforcement with discontinuous deformation analysis, Int. J. Rock Mech. Min. Sci., 36, 949-970.

Kim, Y.-S., and D. J. Sanderson (2005), The relationship between displacement and length of faults: a review, Earth-Sci. Rev., 68, 317-334.

Klerck, P. A., E. J. Sellers, and D. R. J. Owen (2004), Discrete fracture in quasi-brittle materials

under compressive and tensile stress states, Comput. Methods Appl. Mech. Eng., 193, 3035-3056.

Klimczak, C., R. A. Schultz, R. Parashar, and D. M. Reeves (2010), Cubic law with aperture-length correlation: implications for network scale fluid flow, Hydrogeol. J. 18(4), 851-862.

Kobayashi, A., T. Fujita, and M. Chijimatsu (2001), Continuous approach for coupled mechanical and hydraulic behaviour of a fractured rock mass during hypothetical shaft sinking at Sellafield, UK, Int. J. Rock Mech. Min. Sci., 38, 45-57.

Koyama, T., N. Fardina, L. Jing, and O. Stephansson (2006), Numerical simulation of shear-induced flow anisotropy and scale-dependent aperture and transmissivity evolution of rock fracture replicas, Int. J. Rock Mech. Min. Sci., 43, 89-106.

Kozicki, J., and F.-V. Donzé (2008a), A new open-source software developed for numerical simulations using discrete modeling methods, Comput. Methods Appl. Mech. Eng., 197, 4429-4443.

Kozicki, J., and F.-V. Donzé (2008b), YADE-OPEN DEM: an open source software using a discrete element method to simulate granular material, Eng. Comput., 26(7), 786-805.

Kranz, R. L. (1983), Microcracks in rocks: A review, Tectonophys., 100, 449-480.

Kulatilake, P. H. S. W., D. N. Wathugala, and O. Stephansson (1993), Joint network modelling with a validation exercise in Stripa mine, Sweden, Int. J. Rock Mech. Min. Sci. Geomech. Abstr., 30(5), 503-526.

La Pointe, P. R. (1988), A method to characterize fracture density and connectivity through fractal geometry, Int. J. Rock Mech. Min. Sci. Geomech. Abstr., 25(6), 421-429.

Lama, R. D., and V. S. Vutukuri (1978), Handbook on Mechanical Properties of Rocks: Testing Techniques and Results, Volume II, Trans Tech Publications, Clausthal.

Lambert, C., and C. Coll (2014), Discrete modeling of rock joints with a smooth-joint contact model, J. Rock Mech. Geotech. Eng., 6, 1-12.

Lang, P. S., A. Paluszny, and R. W. Zimmerman (2014), Permeability tensor of three-dimensional fractured porous rock and a comparison to trace map predictions, J. Geophys. Res., 119, 6288-6307.

Laslett, G. M. (1982), Censoring and edge effects in areal and line transect sampling of rock joint traces, Math. Geol., 14(2), 125-140.

Latham, J.-P. (1998), Assessment and specification of armourstone quality: from CIRIA/CUR (1991) to CEN (2000), in Advances in Aggregates and Armourstone Evaluation, Geol. Soc. London Spec. Publ., vol. 13, edited by J.-P. Latham, pp. 65-85, Geological Society, London.

Latham, J.-P., J. Xiang, M.W. Belayneh, H.M. Nick, C.-F. Tsang, and M.J. Blunt (2013), Modelling stress-dependent permeability in fractured rock including effects of propagating and bending fractures, Int. J. Rock Mech. Min. Sci., 57, 100-112.

Le Goc, R., C. Darcel, P. Davy, M. Pierce, and M. A. Brossault (2014), Effective elastic properties of 3D fractured systems, in Proceedings of the 1st International Conference on Discrete Fracture Network Engineering, Paper ID 142, Vancouver, Canada.

Leckenby, R. J., D. J. Sanderson, and L. Lonergan (2005), Estimating flow heterogeneity in natural fracture systems, J. Volcanol. Geotherm. Res., 148, 116-129.

Lei, Q., and X. Wang (2016). Tectonic interpretation of the connectivity of a multiscale fracture

system in limestone, Geophys. Res. Lett., 43, 1551-1558.

Lei, Q., J.-P. Latham, J. Xiang, C.-F. Tsang, P. Lang, and L. Guo (2014), Effects of geomechanical changes on the validity of a discrete fracture network representation of a realistic two-dimensional fractured rock, Int. J. Rock Mech. Min. Sci., 70, 507-523.

Lei, Q., J.-P. Latham, C.-F. Tsang, J. Xiang, and P. Lang (2015a), A new approach to upscaling fracture network models while preserving geostatistical and geomechanical characteristics, J. Geophys. Res. Solid Earth, 120, 4784-4807.

Lei, Q., J.-P. Latham, J. Xiang, and C.-F. Tsang (2015b). Polyaxial stress-induced variable aperture model for persistent 3D fracture networks, Geomech. Energ. Environ., 1, 34-47.

Leung, C. T. O., and R. W. Zimmerman (2012), Estimating the hydraulic conductivity of two-dimensional fracture networks using network geometric properties, Transp. Porous Med., 93, 777-797.

Lin, C. T., B. Amadei, J. Jung, and J. Dwyer (1996), Extensions of discontinuous deformation analysis for jointed rock masses, Int. J. Rock Mech. Min. Sci. Geomech. Abstr., 33(7), 671-694.

Lisjak, A., and G. Grasselli (2014), A review of discrete modelling techniques for fracturing processes in discontinuous rock masses, J. Rock Mech. Geotech. Eng. 6, 301-314.

Lisjak, A., Q. Liu, Q. Zhao, O. K. Mahabadi, and G. Grasselli (2013), Numerical simulation of acoustic emission in brittle rocks by two-dimensional finite-discrete element analysis, Geophys. J. Int., 195(1), 423-443.

Lisjak, A., G. Grasselli, and T. Vietor (2014a), Continuum-discontinuum analysis of failure mechanisms around unsupported circular excavations in anisotropic clay shales, Int. J. Rock Mech. Min. Sci., 65, 96-115.

Lisjak, A., D. Figi, and G. Grasselli (2014b), Fracture development around deep underground excavations: Insights from FDEM modelling, J. Rock Mech. Geotech. Eng., 6, 493-505.

Lisjak, A., B. S. A. Tatone, G. Grasselli, and T. Vietor (2014c) Numerical modelling of the anisotropic mechanical behaviour of Opalinus Clay at the laboratory-scale using FEM/DEM, Rock Mech. Rock Eng., 47(1), 187-206.

Lisjak, A., B. Garitte, G. Grasselli, H. R. Müller, and T. Vietor (2015a), The excavation of a circular tunnel in a bedded argillaceous rock (Opalinus Clay): Short-term rock mass response and FDEM numerical analysis, Tunn. Undergr. Sp. Tech., 45, 227-248.

Lisjak, A., B. S. A. Tatone, O. K. Mahabadi, G. Grasselli, P. Marschall, G. W. Lanyon, R. Vaissière, H. Shao, H. Leung, and C. Nussbaum (2015b), Hybrid finite-discrete element simulation of the EDZ formation and mechanical sealing process around a microtunnel in Opalinus Clay, Rock Mech. Rock Eng., doi:10.1007/s00603-015-0847-2.

Lockner, D. A., J. D. Byerlee, V. Kuksenko, A. Ponomarev, and A. Sidorin (1991), Quasi-static fault growth and shear fracture energy in granite, Nature, 350, 39-42.

Long, J. C. S., and D. M. Billaux (1987), From field data to fracture network modeling: An example incorporating spatial structure, Water Resour. Res., 23(7), 1201-1216.

Long, J. C. S., J. S. Remer, C. R. Wilson, and P. A. Witherspoon (1982), Porous media equivalents for networks of discontinuous fractures, Water Resour. Res., 18(3), 645-658.

Long, J. C. S., P. Gilmour, and P. A. Witherspoon (1985), A model for steady fluid flow in random

three-dimensional networks of disc-shaped fractures, Water Resour. Res., 21(8), 1105-1115.

Lu, P., and J.-P. Latham (1999), Developments in the assessment of in-situ block size distributions of rock masses, Rock Mech. Rock Eng., 32(1), 29-49.

Madden, T. R. (1983), Microcrack connectivity in rocks: A renormalization group approach to the critical phenomena of conduction and failure in crystalline rocks, J. Geophys. Res., 88(B1), 585-592.

Mahabadi, O. K. (2012), Investigating the Influence of Micro-scale Heterogeneity and Microstructure on the Failure and Mechanical Behaviour of Geomaterials [PhD Thesis], University of Toronto, Toronto.

Mahabadi, O. K., A. Lisjak, A. Munjiza, and G. Grasselli (2012), Y-Geo: new combined finite-discrete element numerical code for geomechanical applications, Int. J. Geomech., 12, 676-688.

Mahabadi, O. K., G. Grasselli, and A. Munjiza (2010), Y-GUI: A graphical user interface and pre-processor for the combined finite-discrete element code, Y2D, incorporating material heterogeneity, Comput. Geosci., 36, 241-252.

Mahabadi, O. K., P. Kaifosh, P. Marschall, and T. Vietor (2014a), Three-dimensional FDEM numerical simulation of failure processes observed in Opalinus Clay laboratory samples, J. Rock Mech. Geotech. Eng., 6, 591-606.

Mahabadi, O. K., B. S. A. Tatone, and G. Grasselli (2014b), Influence of microscale heterogeneity and microstructure on the tensile behavior of crystalline rocks, J. Geophys. Res. Solid Earth, 119, 5324-5341.

Mandelbrot, B. B. (1982), The Fractal Geometry of Nature, WH Freeman, New York.

Manzocchi, T. (2002), The connectivity of two-dimensional networks of spatially correlated fractures, Water Resour. Res., 38(9), 1162.

Marrett, R., O. J. Ortega, and C. M. Kelsey (1999), Extent of power-law scaling for natural fractures in rock, Geology, 27(9), 799-802.

Martin, C. D., and R. Christiansson (2009), Estimating the potential for spalling around a deep nuclear waste repository in crystalline rock, Int. J. Rock Mech. Min. Sci., 46, 219-228.

Mas Ivars, D., Pierce M. E., Darcel C., Reyes-Montes J., Potyondy D. O., Young R. P., and Cundall P. A. (2011), The synthetic rock mass approach for jointed rock mass modelling, Int. J. Rock Mech. Min. Sci., 48(2), 219-244.

Masihi, M., and P. R. King (2007), A correlated fracture network: Modeling and percolation properties, Water Resour. Res., 43, W07439.

Masihi, M., and P. R. King (2008), Connectivity prediction in fractured reservoirs with variable fracture size: analysis and validation, SPE J., 13(1), 88-98.

Matthäi, S. K., and M. Belayneh (2004), Fluid flow partitioning between fractures and a permeable rock matrix, Geophys. Res. Lett., 31, L07602.

Meyer, T., and H. H. Einstein (2002), Geologic stochastic modeling and connectivity assessment of fracture systems in the Boston area, Rock Mech. Rock Eng., 35(1), 23-44.

Min, K.-B., and L. Jing (2003), Numerical determination of the equivalent elastic compliance tensor for fractured rock masses using the distinct element method, Int. J. Rock Mech. Min. Sci., 40,

795-816.

Min, K.-B., and L. Jing (2004), Stress dependent mechanical properties and bounds of Poisson's ratio for fractured rock masses investigated by a DFN-DEM technique, Int. J. Rock Mech. Min. Sci., 41(3), Paper 2A 13.

Min, K.-B., L. Jing, and O. Stephansson (2004a), Determining the equivalent permeability tensor for fractured rock masses using a stochastic REV approach: Method and application to the field data from Sellafield, UK, Hydrogeol. J., 12, 497-510.

Min, K.-B., J. Rutqvist, C.-F. Tsang, and L. Jing (2004b), Stress dependent permeability of fractured rock masses: a numerical study, Int. J. Rock Mech. Min. Sci., 41, 1191-1210.

Moore, D. E., and D. A. Lockner (1995), The role of microcracking in shear-fracture propagation in granite, J. Struct. Geol., 17, 95-114.

Moreno, L., Y. W. Tsang, C. F. Tsang, F. V. Hale, and I. Neretnieks (1988), Flow and tracer transport in a single fracture: A stochastic model and its relation to some field observations, Water Resour. Res., 24(12), 2033-2048.

Munjiza, A. (2004), The Combined Finite-Discrete Element Method, John Wiley & Sons, London.

Munjiza, A., and K. R. F. Andrews (1998), NBS contact detection algorithm for bodies of similar size, Int. J. Numer. Meth. Eng., 43, 131-149.

Munjiza, A., and K. R. F. Andrews (2000), Penalty function method for combined finite-discrete element systems comprising large number of separate bodies, Int. J. Numer. Meth. Eng., 49, 1377-1396.

Munjiza, A., D. R. J. Owen, and N. Bicanic (1995), A combined finite-discrete element method in transient dynamics of fracturing solids, Eng. Comput., 12(2), 145-174.

Munjiza, A., K. R. F. Andrews, and J. K. White (1999), Combined single and smeared crack model in combined finite-discrete element analysis, Int. J. Numer. Meth. Eng., 44, 41-57.

Munjiza, A., J.-P. Latham, and K. R. F. Andrews (2000), Detonation gas model for combined finite-discrete element simulation of fracture and fragmentation, Int. J. Numer. Methods Eng., 49, 1495-1520.

Munjiza, A., J. Xiang, X. Garcia, J.-P. Latham, G. G. Schiava D'Albano, and N. W. M. John (2010), The virtual geosciences workbench, VGW: open source tools for discontinuous systems, Particuology, 8(2), 100-105.

Munjiza, A., E. E. Knight, and E. Rougier (2011), Computational Mechanics of Discontinua, John Wiley & Sons, Chichester.

Munjiza, A., E. E. Knight, and E. Rougier (2015), Large Strain Finite Element Method: A Practical Course, John Wiley & Sons, Chichester.

Neuman, S. P. (1994), Generalized scaling of permeabilities: validation and effect of support scale, Geophys. Res. Lett., 21(5), 349-352.

Neuman, S. P. (2008), Multiscale relationships between fracture length, aperture, density and permeability, Geophys. Res. Lett., 35, L22402.

Nick, H. M., A. Paluszny, M. J. Blunt, and S. K. Matthäi (2011), Role of geomechanically grown fractures on dispersive transport in heterogeneous geological formations, Phys. Rev. E, 84, 056301.

Nirex (1997a), Evaluation of heterogeneity and scaling of fractures in the Borrowdale Volcanic Group in the Sellafield Area, Nirex Report SA/97/028, Harwell, UK.

Nirex (1997b) Assessment of the in situ stress field at Sellafield, Nirex report S/97/003, Harwell, UK.

Noorian-Bidgoli, M., and L. Jing (2014), Anisotropy of strength and deformability of fractured rocks, J. Rock Mech. Geotech. Eng., 6, 156-164.

Noorian-Bidgoli, M., and L. Jing (2015a), Stochastic analysis of strength and deformability of fractured rocks using multi-fracture system realizations, Int. J. Rock Mech. Min. Sci., 78, 108-117.

Noorian-Bidgoli, M., and L. Jing (2015b), Water pressure effects on strength and deformability of fractured rocks under low confining pressures, Rock Mech. Rock Eng., 48, 971-985.

Noorian-Bidgoli, M., Z. Zhao, and L. Jing (2013), Numerical evaluation of strength and deformability of fractured rocks, J. Rock Mech. Geotech. Eng., 5, 419-430.

Oda, M. (1983), A method for evaluating the effect of crack geometry on the mechanical behavior of cracked rock masses, Mech. Mater., 2, 163-171.

Oda, M. (1984), Similarity rule of crack geometry in statistically homogeneous rock masses, Mech. Mater., 3, 119-129.

Oda, M. (1985), Permeability tensor for discontinuous rock masses, Géotechnique 35, 483-495.

Oda, M. (1986), An equivalent continuum model for coupled stress and fluid flow analysis in jointed rock masses, Water Resour. Res., 22(13), 1845-1856.

Oda, M., T. Yamabe, Y. Ishizuka, H. Kumasaka, H. Tada, and K. Kimura (1993), Elastic stress and strain in jointed rock masses by means of crack tensor analysis, Rock Mech. Rock Eng., 26(2), 89-112.

Odling, N. E. (1992), Network properties of a two-dimensional natural fracture pattern, Pure Appl. Geophys., 138(1), 95-114.

Odling, N. E. (1997), Scaling and connectivity of joint systems in sandstones from western Norway, J. Struct. Geol., 19(10), 1257-1271.

Odling, N. E., and I. Webman (1991), A "Conductance" mesh approach to the permeability of natural and simulated fracture patterns, Water Resour. Res., 27(10), 2633-2643.

Odling, N. E., P. Gillespie, B. Bourgine, C. Castaing, J. P. Chiles, N. P. Christensen, E. Fillion, A. Genter, C. Olsen, L. Thrane, R. Trice, E. Aarseth, J. J. Walsh, and J. Watterson (1999), Variations in fracture system geometry and their implications for fluid flow in fractures hydrocarbon reservoirs, Petro. Geosci., 5, 373-384.

Olson, J. E. (1993), Joint pattern development: Effects of subcritical crack growth and mechanical crack interaction, J. Geophys. Res., 98(B7), 12251-12265.

Olson, J. E. (2003), Sublinear scaling of fracture aperture versus length: An exception or the rule? J. Geophys. Res., 108, 2413.

Olson, J. E. (2004), Predicting fracture swarms - the influence of subcritical crack growth and the crack-tip process zone on joint spacing in rock, in The Initiation, Propagation, and Arrest of Joints and Other Fractures, Geol. Soc. London Spec. Publ., vol. 231, edited by J. W. Cosgrove and T. Engelder, pp. 73-87, Geological Society, London.

Olson, J. E. (2007), Fracture aperture, length and pattern geometry development under biaxial

loading: a numerical study with applications to natural, cross-jointed systems, in The Relationship between Damage and Localization, Geol. Soc. London Spec. Publ., vol. 289, edited by H. Lewis and G. D. Couples, pp. 123-142, Geological Society, London.

Olson, J. E., and D. D. Pollard (1989), Inferring paleostresses from natural fracture patterns: A new method, Geology, 17, 345-348.

Olson, J. E., and D. D. Pollard (1991), The initiation and growth of en échelon veins, J. Struct. Geol., 13(5), 595-608.

Olson, J. E., Y. Qiu, J. Holder, and P. Rijken (2001), Constraining the spatial distribution of fracture networks in naturally fractured reservoirs using fracture mechanics and core measurements, SPE J., 71342.

Olson, J. E., S. E. Laubach, and R. H. Lander (2007), Combining diagenesis and mechanics to quantify fracture aperture distributions and fracture pattern permeability, in Fractured Reservoirs, Geol. Soc. London Spec. Publ., vol. 270, edited by L. Lonergan et al., pp. 101-116, Geological Society, London.

Olsson, R, and N. Barton (2001), An improved model for hydromechanical coupling during shearing of rock joints, Int. J. Rock Mech. Min. Sci., 38, 317-329.

Oreskes, N., K. Shrader-Frechette, and K. Belitz (1994), Verification, validation, and confirmation of numerical models in the earth sciences, Science, 263, 641-646.

Oron, A. P., and B. Berkowitz (1998), Flow in rock fractures: The local cubic law assumption reexamined, Water Resour. Res., 34(11), 2811–2825.

Ouillon, G., C. Castaing, and D. Sornette (1996), Hierarchical geometry of faulting, J. Geophys. Res., 101(B3), 5477-5487.

Owen, D. R. J., and Y. T. Feng (2001), Parallelised finite/discrete element simulation of multi-fracturing solids and discrete systems, Eng. Comput., 18(3-4), 557-576.

Owen, D. R. J., Y. T. Feng, E. A. de Souza Neto, M. G. Cottrell, F. Wang, F. M. Andrade Pires, and J. Yu (2014), The modelling of multi-fracturing solids and particulate media, Int. J. Numeric. Methods Eng., 60, 317-339.

Paluszny, A., and S. K. Matthäi (2009), Numerical modeling of discrete multi-crack growth applied to pattern formation in geological brittle media, Int. J. Solid Struct., 46(18-19), 3383-3397.

Paluszny, A., and S. K. Matthäi (2010), Impact of fracture development on the effective permeability of porous rocks as determined by 2-D discrete fracture growth modelling, J. Geophys. Res., 115, B02203.

Paluszny, A., and R. W. Zimmerman (2011), Numerical simulation of multiple 3D fracture propagation using arbitrary meshes, Comput. Meth. Appl. Mech. Eng., 200(9-12), 953-966.

Paluszny, A., and R. W. Zimmerman (2013), Numerical fracture growth modeling using smooth surface geometric deformation, Eng. Frac. Mech., 108, 19-36.

Paluszny, A., S. K. Matthäi, and M. Hohmeyer (2007), Hybrid finite element finite volume discretization of complex geologic structures and a new simulation workflow demonstrated on fractured rocks, Geofluids, 7, 186-208.

Paluszny, A., X. H. Tang, and R. W. Zimmerman (2013), Fracture and impulse based finite-discrete element modeling of fragmentation, Comput. Mech. 52(5), 1071-1084.

Pan, P.-Z., X.-T. Feng, X.-H. Huang, Q. Cui, and H. Zhou (2009), Coupled THM processes in EDZ of crystalline rocks using an elasto-plastic cellular automaton, Environ. Geol., 57, 1299-1311.

Park, S.-I., Y.-S. Kim, C.-R. Ryoo, and D. J. Sanderson (2010), Fractal analysis of the evolution of a fracture network in a granite outcrop, SE Korea, Geosci. J., 14(2), 201-215.

Petit, J.-P., and M. Barquins (1988), Can natural faults propagate under mode II conditions? Tectonics, 7(6), 1243-1256.

Petit, J.-P., and M. Mattauer (1995), Palaeostress superimposition deduced from mesoscale structures in limestone: the Matelles exposure, Languedoc, France, J. Struct. Geol., 17(2), 245-256.

Petit, J.-P., C. A. J. Wibberley, and G. Ruiz (1999), 'Crack-seal', slip: a new fault valve mechanism? J. Struct. Geol., 21(8-9), 1199-1207.

Pickering, G., J. M. Bull, and D. J. Sanderson (1995), Sampling power-law distributions, Tectonophysics, 248, 1-20.

Pine, R. J., J. S. Coggan, Z. N. Flynn, and D. Elmo (2006), The development of a new numerical modelling approach for naturally fractured rock masses, Rock Mech. Rock Eng., 39(5), 395-419.

Pine, R. J., D. R. J. Owen, J. S. Coggan, and J. M. Rance (2007), A new discrete fracture modelling approach for rock masses, Géotechnique, 57(9), 757-766.

Pollard, D. D., and P. Segall (1987), Theoretical displacements and stresses near fractures in rock: With applications to faults, joints, veins, dikes, and solution surfaces, in Fracture Mechanics of Rock, edited by B. K. Atkinson, pp. 277-349, Academic Press, San Diego.

Pollard, D. D., and A. Aydin (1988), Progress in understanding jointing over the past century, Geol. Soc. Am. Bull., 100, 1181-1204.

Potyondy, D. O., and P. A. Cundall (2004), A bonded-particle model for rock, Int. J. Rock Mech. Min. Sci., 41(8), 1329-1364.

Poulsen, B. A., D. P. Adhikary, M. K. Elmouttie, and A. Wilkins (2015), Convergence of synthetic rock mass modelling and the Hoek–Brown strength criterion, Int. J. Rock Mech. Min. Sci., 80, 171-180.

Pouya, A., and O. Fouché (2009), Permeability of 3D discontinuity networks: New tensors from boundary-conditioned homogenisation, Adv. Water Resour. 32, 303-314.

Price, N. J., and J. W. Cosgrove (1990), Analysis of Geological Structures, Cambridge University Press, New York.

Priest, S. D. (1993), Discontinuity Analysis for Rock Engineering, Chapman and Hall, London.

Putz-Perrier, M. A. and D. J. Sanderson (2008), Spatial distribution of brittle strain in layered sequences, J. Struct. Geol., 30, 50-64.

Ramsey, J. M., and F. M. Chester (2004), Hybrid fracture and the transition from extension fracture to shear fracture, Nature, 428, 63-66.

Rawnsley, K. D., T. Rives, and J.-P. Petit (1992), Joint development in perturbed stress fields near faults, J. Struct. Geol., 14(8/9), 939-951.

Read, R. S. (2004), 20 years of excavation response studies at AECL's Underground Research Laboratory, Int. J. Rock Mech. Min. Sci., 41, 1251-1275.

Reches, Z., and D. A. Lockner (1994), Nucleation and growth of faults in brittle rocks, J. Geophys. Res., 99(B9), 18159-18173.

Renard, P., and G. de Marsily (1997), Calculating equivalent permeability: a review, Adv. Water Resour. 20, 253-578.

Renshaw, C. E. (1996), Influence of subcritical fracture growth on the connectivity of fracture networks, Water Resour. Res., 32(6), 1519-1530.

Renshaw, C. E. (1997), Mechanical controls on the spatial density of opening-mode fracture networks, Geology, 25(10), 923-926.

Renshaw, C. E. (1998), Sample bias and the scaling of hydraulic conductivity in fractured rock, Geophys. Res. Lett., 25(1), 121-124.

Renshaw, C. E. (1999), Connectivity of joint networks with power law length distributions, Water Resour. Res., 35(9), 2661-2670.

Renshaw, C. E., and D. D. Pollard (1994), Numerical simulation of fracture set formation: A fracture mechanics model consistent with experimental observations, J. Geophys. Res., 99(B5), 9359-9372.

Renshaw, C. E., and J. C. Park (1997), Effect of mechanical interactions on the scaling of fracture length and aperture, Nature, 386, 482- 484.

Rispoli, R. (1981), Stress fields about strike-slip faults inferred from stylolites and tension gashes, Tectonophysics, 75, T29-T36.

Rives, T., M. Razack, J. P. Petit, and K. D. Rawnsley (1992), Joint spacing: analogue and numerical simulations, J. Struct. Geol., 16 (3), 419-423.

Robinson, P. C. (1983), Connectivity of fractures systems-a percolation theory approach, J. Phys. A, 16, 605- 614.

Robinson, P. C. (1984), Numerical calculations of critical densities for lines and planes, J. Phys. A, 17, 2823-2830.

Rockfield (2011), ELFEN User's Manual, Version 4, Rockfield Software Ltd., Swansea, UK.

Ronayne, M. J., and S. M. Gorelick (2006), Effective permeability of porous media containing branching channel networks, Phys. Rev. E, 73, 026305.

Rougier, E., E. E. Knight, S. T. Broome, A. J. Sussman, and A. Munjiza (2014), Validation of a three-dimensional Finite-Discrete Element Method using experimental results of the Split Hopkinson Pressure Bar test, Int. J. Rock Mech. Min. Sci., 70, 101-108.

Roy, A., E. Perfect, W. M. Dunne, and L. D. McKay (2007), Fractal characterization of fracture networks: an improved box-counting technique, J. Geophys. Res., 112, B112201.

Rutqvist, J., A.Bäckström, M. Chijimatsu, X.-T. Feng, P.-Z. Pan, J. Hudson, L. Jing, A. Kobayashi, T. Koyama, H.-S. Lee, X.-H. Huang, M. Rinne, and B. Shen (2009), A multiple-code simulation study of the long-term EDZ evolution of geological nuclear waste repositories. Environ. Geol., 57, 1313-1324.

Rutqvist, J., and O. Stephansson (2003), The role of hydromechanical coupling in fractured rock engineering, Hydrogeol. J., 11(1), 7-40.

Rutqvist, J., C. Leung, A. Hoch, Y. Wang, and Z. Wang (2013), Linked multicontinuum and crack tensor approach for modeling of coupled geomechanics, fluid flow and transport in fractured rock, J. Rock Mech. Geotech. Eng., 5, 18-31.

Rutqvist, J., Y.-S. Wu, C.-F. Tsang, and G. Bodvarsson (2002), A modeling approach for analysis of

coupled multiphase fluid flow, heat transfer, and deformation in fractured porous rock, Int. J. Rock Mech. Min. Sci., 39, 429-442.

Saeb, S., and B. Amadei (1990), Modelling joint response under constant or variable normal stiffness boundary conditions, Int. J. Rock Mech. Min. Sci. Geomech. Abstr., 27(3), 217-217.

Saeb, S., and B. Amadei (1992), Modelling rock joints under shear and normal loading, Int. J. Rock Mech. Min. Sci. Geomech. Abstr., 29, 267-278.

Sanderson, D. J., and X. Zhang (1999), Critical stress localization of flow associated with deformation of well-fractured rock masses, with implications for mineral deposits, in Fractures, Fluid Flow and Mineralization, Geol. Soc. London Spec. Publ., vol. 155, edited by K. J. W. Mccavvrey et al., pp. 69-81, Geological Society, London.

Sanderson, D. J., and X. Zhang (2004), Stress controlled localization of deformation and fluid flow in fractured rocks, in The Initiation, Propagation, and Arrest of Joints and Other Fractures, Geol. Soc. London Spec. Publ., vol. 231, edited by J. W. Cosgrove and T. Engelder, pp. 299-314, Geological Society, London.

Sanderson, D. J., and C. W. Nixon (2015), The use of topology in fracture network characterization, J. Struct. Geol., 72, 55-66.

Sarda, S., L. Jeannin, R. Basquet, and B. Bourbiaux (2002), Hydraulic characterization of fractured reservoirs: Simulation on discrete fracture models, SPE Reserv. Eval. Eng., 5, 154-162.

Scholtès, L., and F.-V. Donzé (2012), Modelling progressive failure in fractured rock masses using a 3D discrete element method. Int. J. Rock Mech. Min. Sci., 52, 18-30.

Scholtès, L, and F.-V. Donzé (2013), A DEM model for soft and hard rocks: Role of grain interlocking on strength, J. Mech. Phys. Solids, 61(2), 352-369.

Scholz, C. H., N. H. Dawers, J.-Z. Yu, M. H. Anders, and P. A. Cowie (1993), Fault growth and fault scaling laws: preliminary results, J. Geophys. Res., 98, 21951-21961.

Scholtès, L, F.-V. Donzé, and M. Khanal (2011), Scale effects on strength of geomaterials, case study: coal, J. Mech. Phys. Solids, 59(5), 1131-1146.

Schultz, R. A. (2000), Growth of geologic fractures into large-strain populations: review of nomenclature, subcritical crack growth, and some implications for rock engineering, Int. J. Rock Mech. Min. Sci., 37, 403-411.

Schultz, R. A., R. Soliva, H. Fossen, C. H. Okubo, and D. M. Reeves (2008), Dependence of displacement-length scaling relations for fractures and deformation bands on the volumetric changes across them, J. Struct. Geol., 30, 1405-1411.

Segall, P. (1984a), Rate-dependent extensional deformation resulting from crack growth in rock, J. Geophys. Res., 89(B6), 4185-4195.

Segall, P. (1984b), Formation and growth of extensional fracture sets, Geol. Soc. Amer. Bull. 95(4), 454-462.

Segall, P., and D. D. Pollard (1983a), Joint formation in granitic rock of the Sierra Nevada, Geol. Soc. Amer. Bull., 94, 563-575.

Segall, P., and D. D. Pollard (1983b), Nucleation and growth of strike slip faults in granite, J. Geophys. Res., 88(B1), 555-568.

Séranne, M., A. Benedicto, P. Labaum, C. Truffert, and G. Pascal (1995), Structural style and

evolution of the Gulf of Lion Oligo-Miocene rifting: role of the Pyrenean orogeny, Mar. Petrol. Geol., 12(8), 809-820.

Shekhar, R., and R. L. G. Jr (2011), Generation of spatially correlated fracture models for seismic simulations, Geophys. J. Int., 185, 341-351.

Shen, B., and O. Stephansson (1993), Numerical analysis of mixed mode I and mode II fracture propagation, Int. J. Rock Mech. Min. Sci. Geomech. Abstr., 30(7), 861-867.

Shen, B., and N. Barton (1997), The disturbed zone around tunnels in jointed rock masses, Int. J. Rock Mech. Min. Sci., 34(1), 117-125.

Shi, G.-H. (1992), Discontinuous deformation analysis—a new numerical model for the statics, dynamics of block structures, Eng. Comput., 9, 157-168.

Shi, G.-H., and R. E. Goodman (1985), Two dimensional discontinuous deformation analysis, Int. J. Numer. Anal. Methods Geomech., 9, 541-556.

Shi, G.-H., and R. E. Goodman (1989), Generalization of two-dimensional discontinuous deformation analysis for forward modelling, Int. J. Numer. Anal. Methods Geomech., 13(4), 359-380.

Si, G., J.-Q. Shi, S. Durucan, A. Korre, J. Lazar, S. Jamnikar, and S. Zavšek (2015), Monitoring and modelling of gas dynamics in multi-level longwall top coal caving of ultra-thick coal seams, Part II: Numerical modelling, Int. J. Coal Geol., 144-145, 58-70.

Sibson, R. H. (1994), Crustal stress, faulting and fluid flow, in Geofluids: Origin, Migration and Evolution of Fluids in Sedimentary Basins, Geol. Soc. London Spec. Publ., vol. 78, edited by J. Parnell, pp. 69-84, Geological Society, London.

Sitharam, T. G., J. Sridevi, and N. Shimizu (2001), Practical equivalent continuum characterization of jointed rock masses, Int. J. Rock Mech. Min. Sci., 38, 437-448.

Snow, D. T. (1969), Anisotropic permeability of fractured media, Water Resour. Res., 5, 1273-1289.

Snow, D. T. (1970), The frequency and apertures of fractures in rock, Int. J. Rock Mech. Min. Sci. Geomech. Abstr., 7(1), 23-40.

Souley, M., F. Homand, and B. Amadei (1995), An extension to the saeb and amadei constitutive model for rock joints to include cyclic loading paths, Int. J. Rock Mech. Min. Sci. Geomech. Abstr., 32(2), 101-109.

Spence, G. H., and E. Finch (2014), Influences of nodular chert rhythmites on natural fracture networks in carbonates: an outcrop and two-dimensional discrete element modelling study, in Advances in the Study of Fractured Reservoirs, Geol. Soc. London Spec. Publ., vol. 374, edited by G. H. Spence et al., pp. 211-249, Geological Society, London.

Stead, D., E. Eberhardt, and J. S. Coggan (2006), Developments in the characterization of complex rock slope deformation and failure using numerical modelling techniques, Eng. Geol., 83(1-3), 217-235.

Stüben, K. (2001), A review of algebraic multigrid, J. Comput. Appl. Math., 128(1-2), 281-309.

Su, K., J.-P. Latham, D. Pavlidis, J. Xiang, F. Fang, P. Mostaghimi, J. R. Percival, C. C. Pain, and M. D. Jackson (2015), Multiphase flow simulation through porous media with explicitly resolved fractures, Geofluids, doi:10.1111/gfl.12129.

Tang, C. A. (1997), Numerical simulation of progressive rock failure and associated seismicity, Int. J.

Rock Mech. Min. Sci., 34(2), 249-261.

Tang, C. A., and J. A. Hudson (2010), Rock Failure Mechanisms: Illustrated and Explained, Taylor & Francis Group, London.

Tang C. A., Y. B. Zhang, Z. Z. Liang, T. Xu, L. G. Tham, P. A. Lindqvist, S. Q. Kou, and H. Y. Liu (2006), Fracture spacing in layered materials and pattern transition from parallel to polygonal fractures, Phys. Rev. E, 73, 056120.

Tang, C. A., S. B. Tang, B. Gong, and H. M. Bai (2015), Discontinuous deformation and displacement analysis: From continuous to discontinuous, Sci. China, 58(9), 1567-1574.

Tang, X. H., A. Paluszny, and R. W. Zimmerman (2013), Energy conservative property of impulse-based methods for collision resolution, Int. J. Numer. Meth. Eng., 95(6), 529-540.

Tang, X. H., A. Paluszny, and R. W. Zimmerman (2014), An impulse-based energy tracking method for collision resolution, Comput. Methods Appl. Mech. Eng. 278(15), 160-185.

Tatone, B. S. A., and G. Grasselli (2015), A calibration procedure for two-dimensional laboratory-scale hybrid finite–discrete element simulations, Int. J. Rock Mech. Min. Sci., 75, 56-72.

Taylor, W. L., D. D. Pollard, and A. Aydin (1999), Fluid flow in discrete joint sets: Field observations and numerical simulations, J. Geophys. Res., 104(B12), 28983–29006.

Tham, L. G., T. H. Yang, and C. A. Tang (2004), Progressive failure of jointed rocks, Int. J. Rock Mech. Min. Sci., 41, 182-187.

Thompson, M. E., and S. R. Brown (1991), The effect of anisotropic surface roughness on flow and transport in fractures, J. Geophys. Res., 96(B13), 21923–21932.

Tsang, C.-F. (1999), Linking thermal, hydrological, and mechanical processes in fractured rocks, Annu. Rev. Earth Planet. Sci., 27, 359-384.

Tsang, C.-F., and I. Neretnieks (1998), Flow channeling in heterogeneous fractured rocks, Rev. Geophys., 36(2), 275-298.

Tsang, C.-F., F. Bernier, and C. Davies (2005), Geohydromechanical processes in the Excavation Damaged Zone in crystalline rock, rock salt, and indurated and plastic clays—in the context of radioactive waste disposal, Int. J. Rock Mech. Min. Sci., 42, 109-125.

Tsang, C.-F., J. Rutqvist, and K.-B. Min (2007), Fractured rock hydromechanics: from borehole testing to solute transport and CO_2 storage, in Rock Physics and Geomechanics in the Study of Reservoirs and Repositories, Geol. Soc. London Spec. Publ., vol. 284, edited by C. David and M. Le Ravalec-Dupin, pp. 15-34, Geological Society, London.

Tsang, C.-F., I. Neretnieks, and Y. Tsang (2015), Hydrologic issues associated with nuclear waste repositories, 51, doi:10.1002/2015WR017641.

Tsang, Y. W., and P. A. Witherspoon (1981), Hydromechanical behavior of a deformable rock fracture subject to normal stress, J. Geophys. Res., 86, 9287-9298.

Vallejos, J. A., K. Suzuki, A. Brzovic, and D. Mar Ivars (2016), Application of Synthetic Rock Mass modeling to veined core-size samples, Int. J. Rock Mech. Min. Sci., 81, 47-61.

Vermilye, J. M., and C. H. Scholz (1995), Relation between vein length and aperture, J. Struct. Geol., 17(3), 423-434.

Viré, A., J. Xiang, and C. C. Pain (2015), An immersed-shell method for modelling fluid-structure

interactions, Phil. Trans. R. Soc. A, 373, 20140085.

Vyazmensky, A., D. Stead, D. Elmo, and A. Moss (2010a), Numerical analysis of block caving-induced instability in large open pit slopes: a finite element/discrete element approach, Rock Mech. Rock Eng., 43(1), 21-39.

Vyazmensky, A., D. Elmo, and D. Stead (2010b), Role of rock mass fabric and faulting in the development of block caving induced surface subsidence, Rock Mech. Rock Eng., 43(5), 533-556.

Walmann, T., A. Malthe-Sørenssen, J. Feder, T. Jøssang, P. Meakin, and H. H. Hardy (1996), Scaling relations for the lengths and widths of fractures, Phys. Rev. Lett., 77: 5393-5396.

Walsh, J. J., and J. Watterson (1988), Analysis of the relationship between displacements and dimensions of faults, J. Struct. Geol., 10, 239-247.

Walsh, J. J., and J. Watterson (1993), Fractal analysis of fracture patterns using the standard box-counting technique: valid and invalid methodologies, J. Struct. Geol., 15(12), 1509-1512.

Wang, Z., J. Rutqvist, Y. Wang, C. Leung, A. Hoch, and Y. Dai (2014), The effect of stress on flow and transport in fractured rock masses using an extended multiple interacting continua method with crack tensor theory, Nucl. Technol., 187, 158-168.

Willemse, E. J. M., and D. D. Pollard (1998), On the orientation and patterns of wing cracks and solution surfaces at the tips of a sliding flaw or fault, J. Geophys. Res., 103(B2), 2427-2438.

Willemse, E. J. M., D. C. P. Peacock, and A. Aydin (1997), Nucleation and growth of strike-slip faults in limestones from Somerset, U.K., J. Struct. Geol., 19(12), 1461-1477.

Wilson, C. E., A. Aydin, M. Karimi-Fard, L. J. Durlofsky, A. Sagy, E. E. Brodsky, O. Kreylos, and L. H. Kellogg (2008), From outcrop to flow simulation: Constructing discrete fracture models from a LIDAR survey, AAPG Bull., 95(11), 1883-1905.

Witherspoon, P. A., J. S. Y. Wang, K. Iwai, and J. E. Gale (1980), Validity of cubic law for fluid flow in a deformable rock fracture, Water Resour. Res. 16, 1016-1024.

Wu, H., and D. D. Pollard (2002), Imaging 3-D fracture networks around boreholes, AAPG Bull., 86(4), 593-604.

Wu, J.-H., Y. Ohnishi, and S. Nishiyama (2004), Simulation of the mechanical behavior of inclined jointed rock masses during tunnel construction using Discontinuous Deformation Analysis (DDA), Int. J. Rock Mech. Min. Sci., 41, 731-743.

Xiang, J., A. Munjiza, J.-P. Latham, and R. Guises (2009a), Finite strain, finite rotation quadratic tetrahedral element for the combined finite-discrete element method, Int. J. Numer. Meth. Eng., 79, 946-978.

Xiang J, A. Munjiza, J.-P. Latham, and R. Guises (2009b), On the validation of DEM and FEM/DEM models in 2D and 3D, Eng. Comput., 26, 673-687.

Xu, C., and P. A. Dowd (2010), A new computer code for discrete fracture network modelling, Comput. Geosci., 36, 292-301.

Yeo, L. W., M. H. de Freitas, and R. W. Zimmerman (1998), Effect of shear displacement on the aperture and permeability of a rock fracture, Int. J. Rock Mech. Min. Sci., 35(8), 1051-1070.

Zhang, X., and D. J. Sanderson (1995), Anisotropic features of geometry and permeability in fractured rock masses, Eng. Geol., 40, 65-75.

Zhang, X., and D. J. Sanderson (1996), Effects of stress on the two-dimensional permeability tensor

of natural fracture networks, Geophys. J. Int., 125, 912-924.

Zhang, X., and D. J. Sanderson (1998), Numerical study of critical behaviour of deformation and permeability of fractured rock masses, Mar. Petrol. Geol., 15(6), 535-548.

Zhang, X., and D. J. Sanderson (1999), Scale up of two-dimensional conductivity tensor for heterogeneous fracture networks, Eng. Geol., 53, 83-99.

Zhang, X., and D. J. Sanderson (2002), Numerical Modelling and Analysis of Fluid Flow and Deformation of Fractured Rock Masses, Pergamon, Oxford.

Zhang, X., D. J. Sanderson, R. M. Harkness, and N. C. Last (1996), Evaluation of the 2-D Permeability tensor for fractured rock masses, Int. J. Rock Mech. Min. Sci. Geomech. Abstr., 33(1), 17-37.

Zhang, Z., and Q. Lei (2013), Object-oriented modelling for three-dimensional multi-block systems, Comput. Geotech., 48, 208-227.

Zhang, Z., and Q. Lei (2014), A morphological visualization method for removability analysis of blocks in discontinuous rock masses, Rock Mech. Rock Eng., 47, 1237-1254.

Zhao, Z., J. Rutqvist, C. Leung, M. Hokr, Q. Liu, I. Neretnieks, A. Hoch, J. Havlicek, Y. Wang, Z. Wang, Y. Wu, and R. Zimmerman (2013), Impact of stress on solute transport in a fracture network: A comparison study, J. Rock Mech. Geotech. Eng., 5, 110-123.

Zhao, Z., L. Jing, and I. Neretnieks (2010), Evaluation of hydrodynamic dispersion parameters in fractured rocks, J. Rock Mech. Geotech. Eng., 2(3), 243-254.

Zhao, Z., L. Jing, I. Neretnieks, and L. Moreno (2011), Numerical modeling of stress effects on solute transport in fractured rocks, Comput. Geotech., 38, 113-126.

Zimmerman, R. W., and G. S. Bodvarsson (1996), Effective transmissivity of two-dimensional fracture networks, Int. J. Rock Mech. Min. Sci. Geomech. Abstr., 33(4), 433-438.

Zimmerman, R. W., and I. Main (2004), Hydromechanical behavior of fractured rocks, in Mechanics of Fluid-Saturated Rocks, edited by Y. Gueguen, and M. Bouteca, pp. 363-421, Elsevier, London.

Zoback, M. (2007), Reservoir Geomechanics, Cambridge University Press, New York.

Appendix A

This appendix gives a detailed compilation of a series of multiscale fracture patterns mapped from the Languedoc region of SE France (Table A.1 and Fig. A.1-A.2). A regional-scale (~100 km) fault pattern (Fig. A.3), denoted as RP, was generated from the geological map made by Bureau de Recherches Géologiques et Minières (BRGM) [2011] at a scale of 1:250,000. Three intermediate-scale (~10 km) fracture patterns containing both faults and joint corridors, denoted as IP1-3 (Fig. A.4-A.6), were digitised from assembled aerial photographs taken at an anticipated constant flight height (resolution may vary slightly due to the uneven terrain). Eleven local-scale (1-10 m) joint patterns, denoted as LP1-11 (Fig. A.7-A.17), were drawn based on outcrop mapping. Each outcrop map was constructed from a number of images taken at a fixed height of 1.5 m and rectified for perspective biases before assembly. When manually tracing fracture geometries from digital maps, the image pixel size was set as the connectivity threshold to determine the persistence of fracture traces. All fracture patterns may suffer from incomplete sampling due to lack of exposure caused by the vegetation and erosion effects.

The fractal dimension D (formally known as the correlation dimension) that describes the spatial organisation of fractures is calculated using the normalised two-point correlation function [Bonnet et al., 2001] as defined by $C_2(r/L) = N_d(r)/N_2$, where N is the total number of fracture barycentres, L is the domain size, and N_d is the number of pairs of barycentres whose normalised separation is smaller than r/L. The domain size L is calculated as the square root of the area of the irregular map bounded by the outermost nodes of each fracture network. The D value of each pattern is derived from a power law fitting to the data points of (r/L, $C_2(r/L)$). The local value of apparent logarithmic slope is also analyzed for uncertainty evaluations. A short plateau of local slope over less than one order of magnitude can be found in some patterns. Such phenomenon may be caused by the mechanical interaction of different fracture sets [Du Bernard et al., 2002] or incomplete mapping due to the vegetation and erosion effects. The power law length exponent a is derived from the density distribution of fracture lengths for each pattern. The truncation effect is eliminated by using a lower cut-off of 5% × L for each map when fitting the power law curve [Odling et al., 1999]. The censoring bias of the regional map is corrected by removing traces that intersect the window sampling boundaries [Bour et al., 2002], with the artificial

density perturbation amended using an effective system size estimated as the square root of the coverage area of the remaining fractures [Lei et al., 2015a]. Such a censoring effect is not considered for the intermediate-scale and local-scale patterns bounded by irregular sampling boundaries.

Table A.1 summarises the key statistical parameters of all sampled fracture networks. Fig. A.1 and A.2 illustrates the variation of the measured D and a values for different networks. Fig. A.3-A.17 present the individual fracture patterns and the derivation of their scaling exponents D and a.

Table A.1 The key statistical parameters of the fracture networks

Patterns	Domain size L (m)	Number of fractures	Fractal dimension D	Power law length exponent a	Percolation parameter p
RP	63,879	518	1.68	2.61	7.18
IP1	9,271	399	1.66	2.41	5.30
IP2	10,989	2,088	1.48	2.62	14.69
IP3	8,572	1,237	1.20	2.53	6.90
LP1	4.52	1,234	1.71	2.96	9.37
LP2	4.34	396	1.43	2.73	4.91
LP3	5.02	647	1.59	2.37	9.53
LP4	1.78	240	1.65	2.13	7.36
LP5	2.05	413	1.74	2.59	6.68
LP6	2.90	443	1.62	2.69	6.79
LP7	2.52	2,185	1.73	3.30	10.62
LP8	1.19	331	1.62	2.52	5.46
LP9	1.39	480	1.41	3.04	4.60
LP10	3.88	1,429	1.59	3.26	4.85
LP11	3.26	266	1.48	2.41	4.79
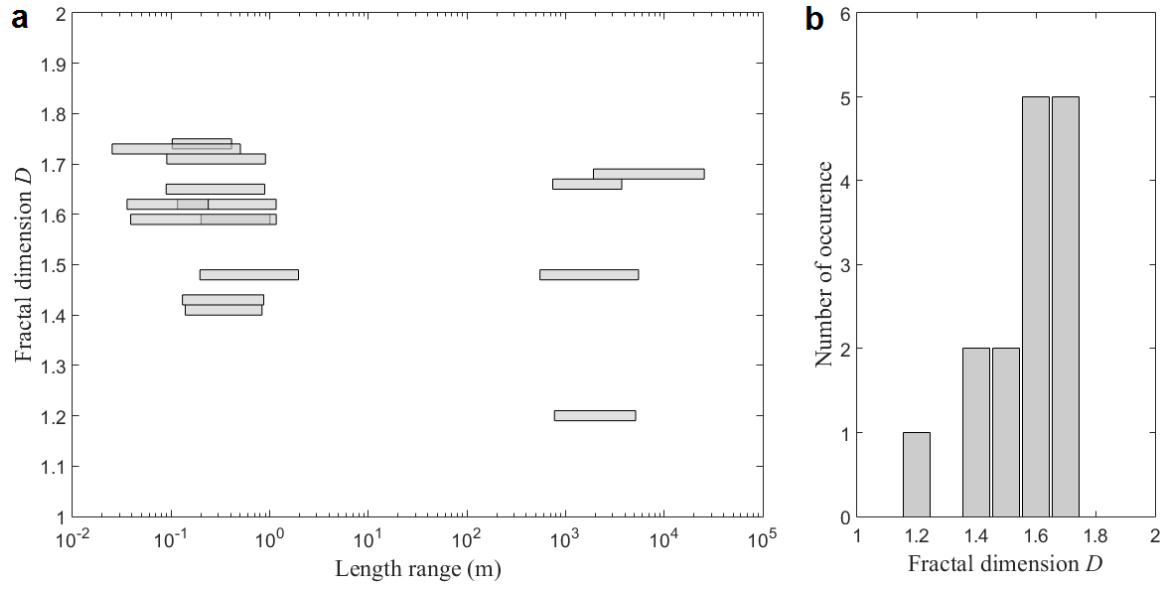
Fig. A.1 Synthesis of the measured fractal dimensions of different patterns. (a) Each fractal dimension is plotted with respect to the length range over which it has been determined. (b) A histogram of the measured fractal dimensions.
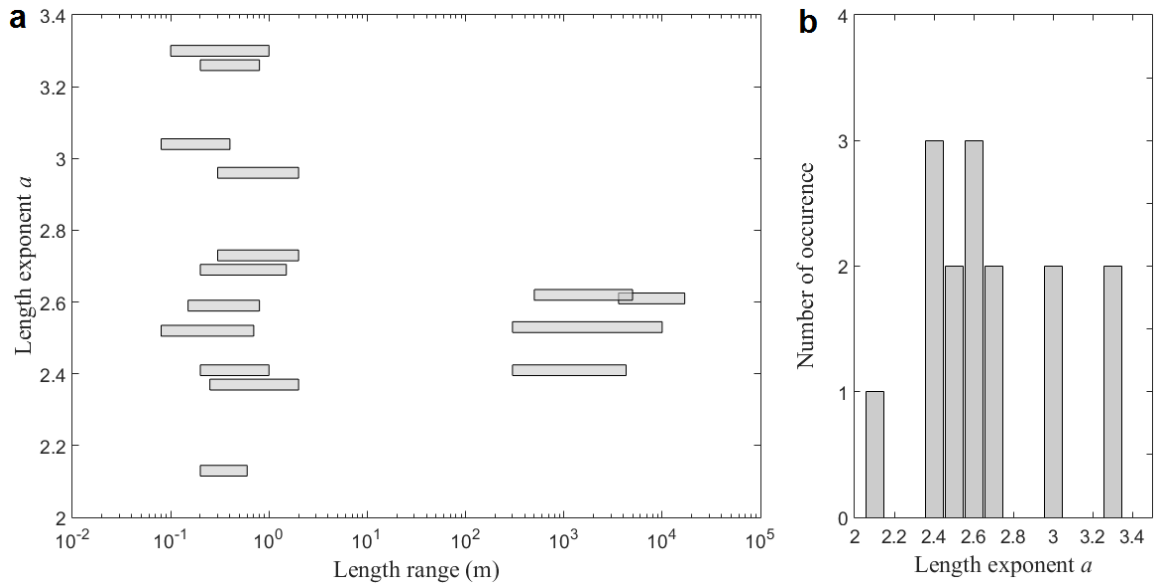
Fig. A.2 Synthesis of the measured power law length exponents of different patterns. (a) Each length exponent is plotted with respect to the length range over which it has been determined. (b) A histogram of the measured length exponents.
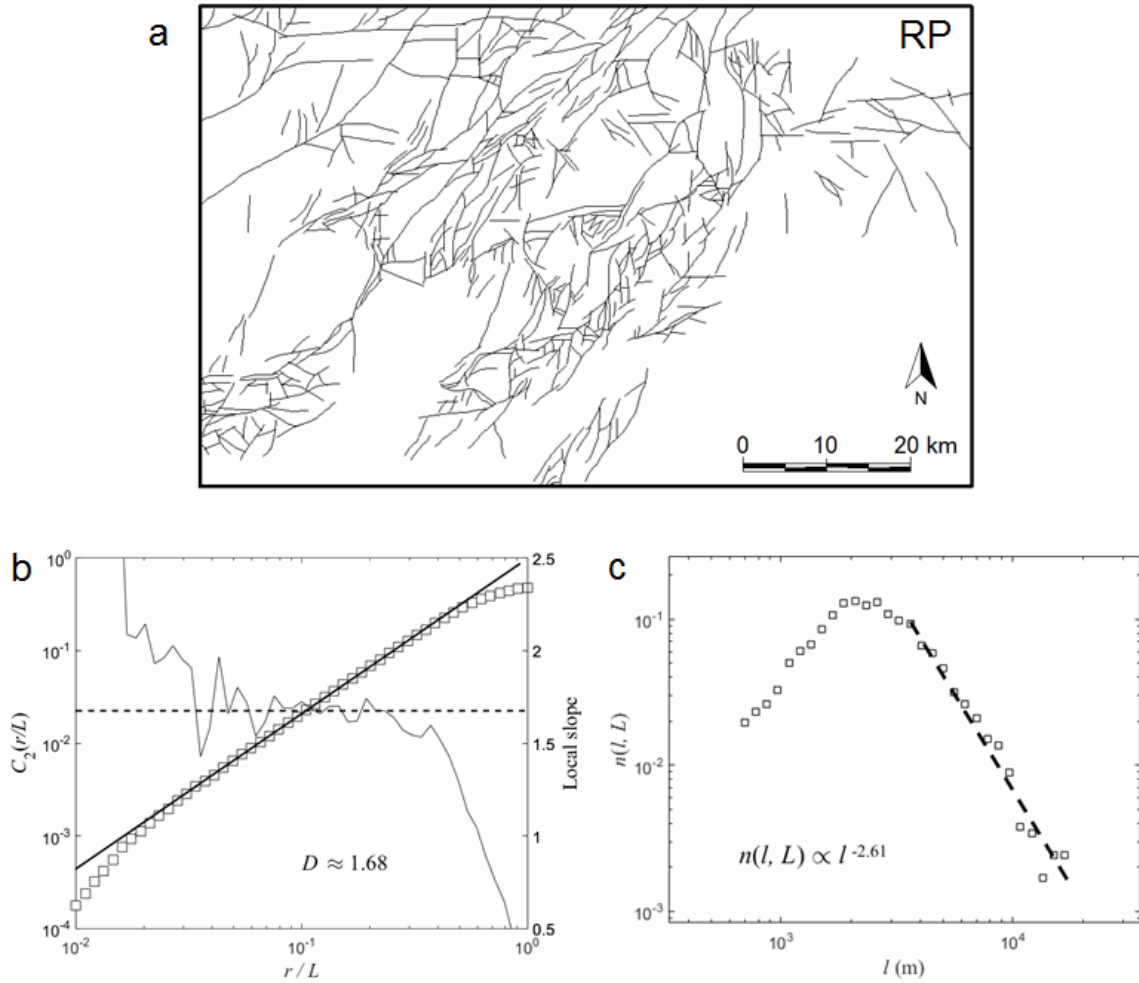
Fig. A.3 (a) A regional-scale (~100 km) lineament fault pattern, denoted as RP, was generated from the geological map made by Bureau de Recherches Géologiques et Minières (BRGM) [2011] at a scale of 1:250,000. (b) Calculation of the normalised two-point correlation function $C_2(r/L)$ as a function of r/L. Squares correspond to the correlation integral, and the bold solid line corresponds to a power law fitting line with a fractal dimension $D = 1.68$ derived from a scale range of $0.03<r/L<0.4$. The light solid line corresponds to the local value of logarithmic slope, and the dashed line represents the slope value $D = 1.68$. (c) The density distribution of fracture lengths (represented by squares). The dashed line corresponds to a power law fitting line with an exponent $a = 2.61$.
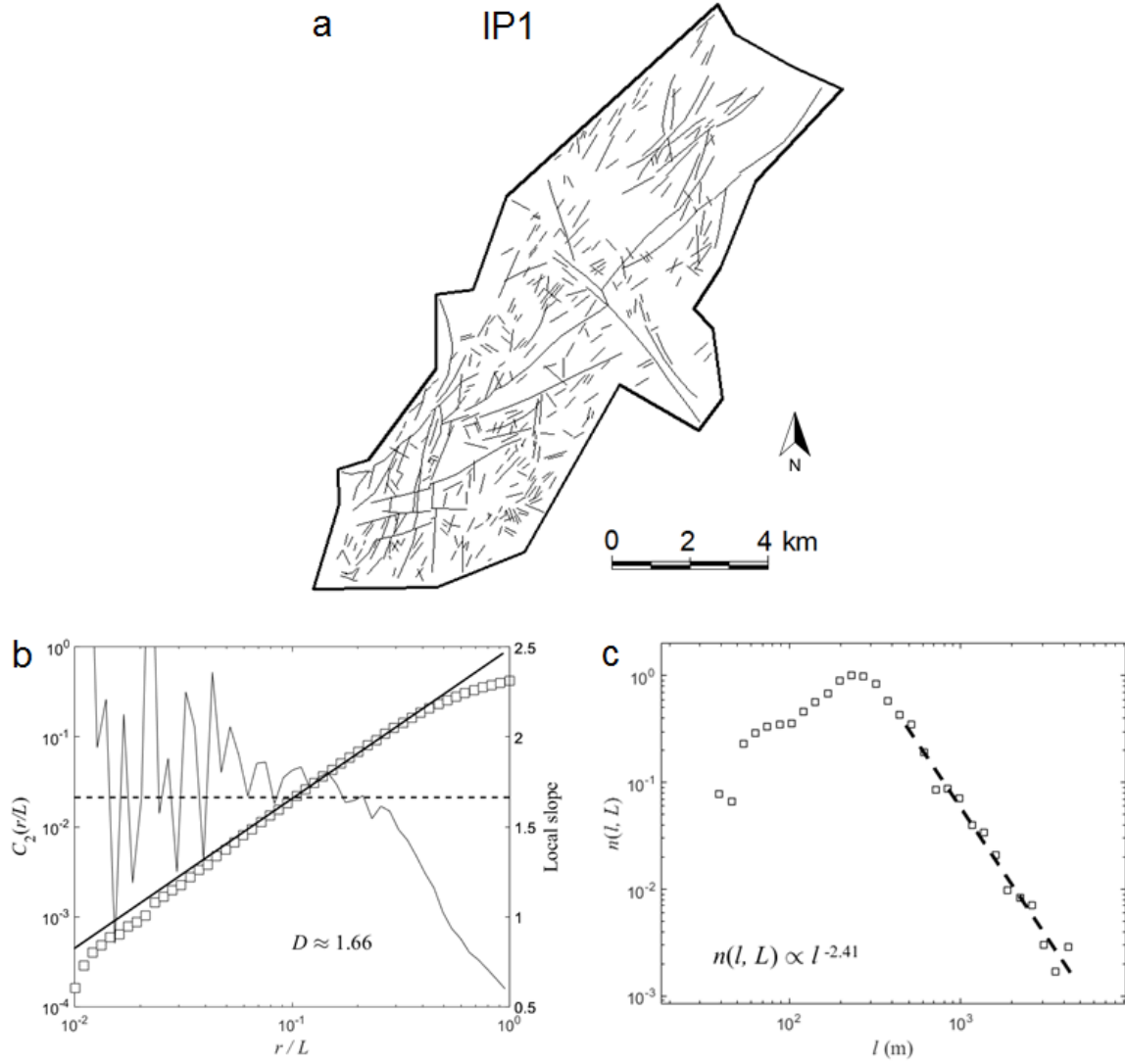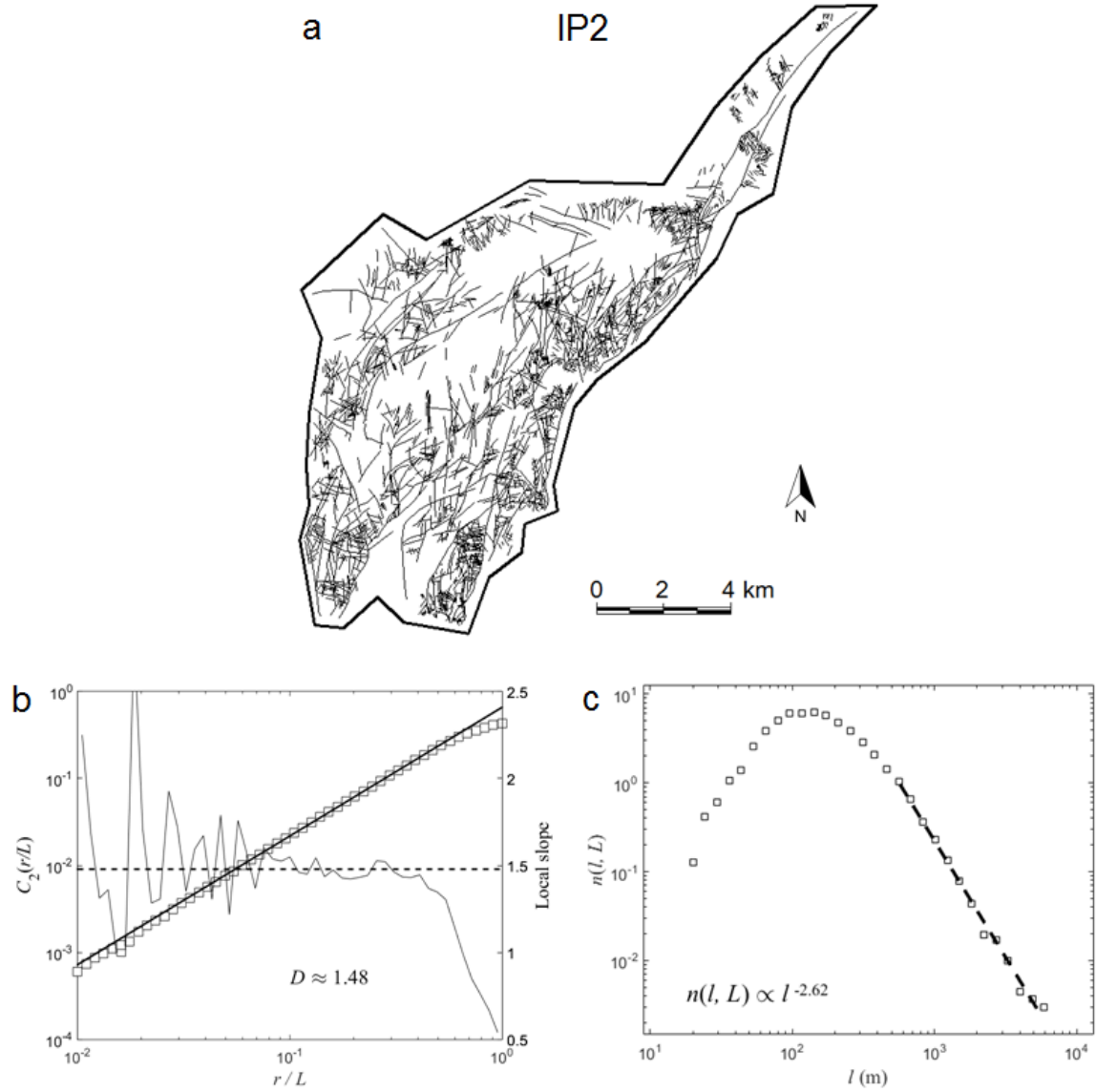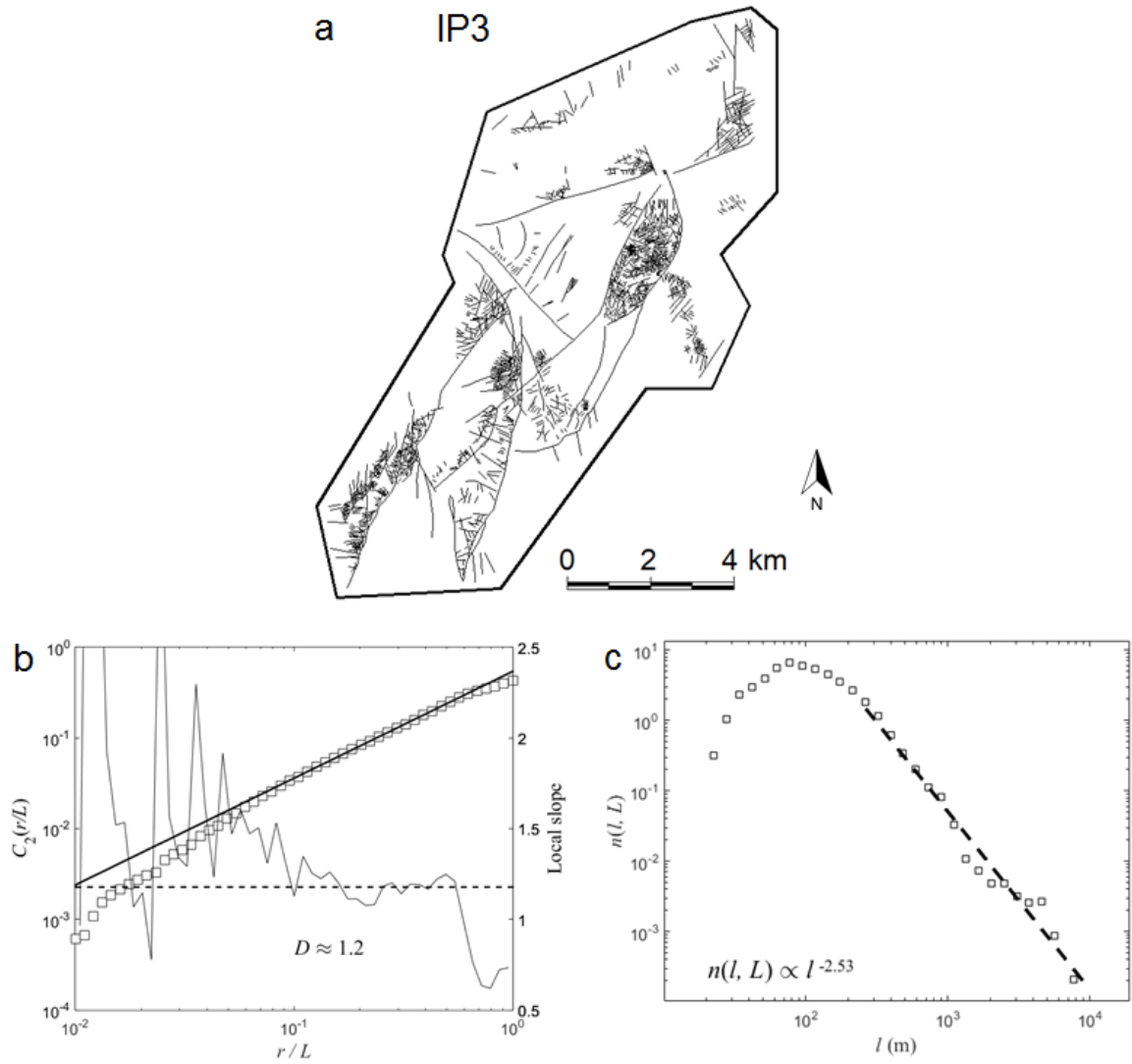
Fig. A.4 (a) An intermediate-scale (~10 km) fracture pattern including both faults and joint, denoted as IP1, was drawn from assembled aerial photographs. (b) Calculation of the normalised two-point correlation function $C_2(r/L)$ as a function of r/L. Squares correspond to the correlation integral, and the bold solid line corresponds to a power law fitting line with a fractal dimension $D = 1.66$ derived from a scale range of $0.08 < r/L < 0.4$. The light solid line corresponds to the local value of logarithmic slope, and the dashed line represents the slope value $D = 1.66$. (c) The density distribution of fracture lengths (represented by squares). The dashed line corresponds to a power law fitting line with an exponent $a = 2.41$.

Fig. A.5 (a) An intermediate-scale (~10 km) fracture pattern including both faults and joint, denoted as IP2, was drawn from assembled aerial photographs. (b) Calculation of the normalised two-point correlation function $C_2(r/L)$ as a function of r/L. Squares correspond to the correlation integral, and the bold solid line corresponds to a power law fitting line with a fractal dimension $D = 1.48$ derived from a scale range of $0.05 < r/L < 0.5$. The light solid line corresponds to the local value of logarithmic slope, and the dashed line represents the slope value $D = 1.48$. (c) The density distribution of fracture lengths (represented by squares). The dashed line corresponds to a power law fitting line with an exponent $a = 2.62$.

Fig. A.6 (a) An intermediate-scale (~10 km) fracture pattern including both faults and joint, denoted as IP3, was drawn from assembled aerial photographs. (b) Calculation of the normalised two-point correlation function $C_2(r/L)$ as a function of r/L. Squares correspond to the correlation integral, and the bold solid line corresponds to a power law fitting line with a fractal dimension $D = 1.20$ derived from a scale range of $0.09 < r/L < 0.6$. The light solid line corresponds to the local value of logarithmic slope, and the dashed line represents the slope value $D = 1.20$. (c) The density distribution of fracture lengths (represented by squares). The dashed line corresponds to a power law fitting line with an exponent $a = 2.53$.
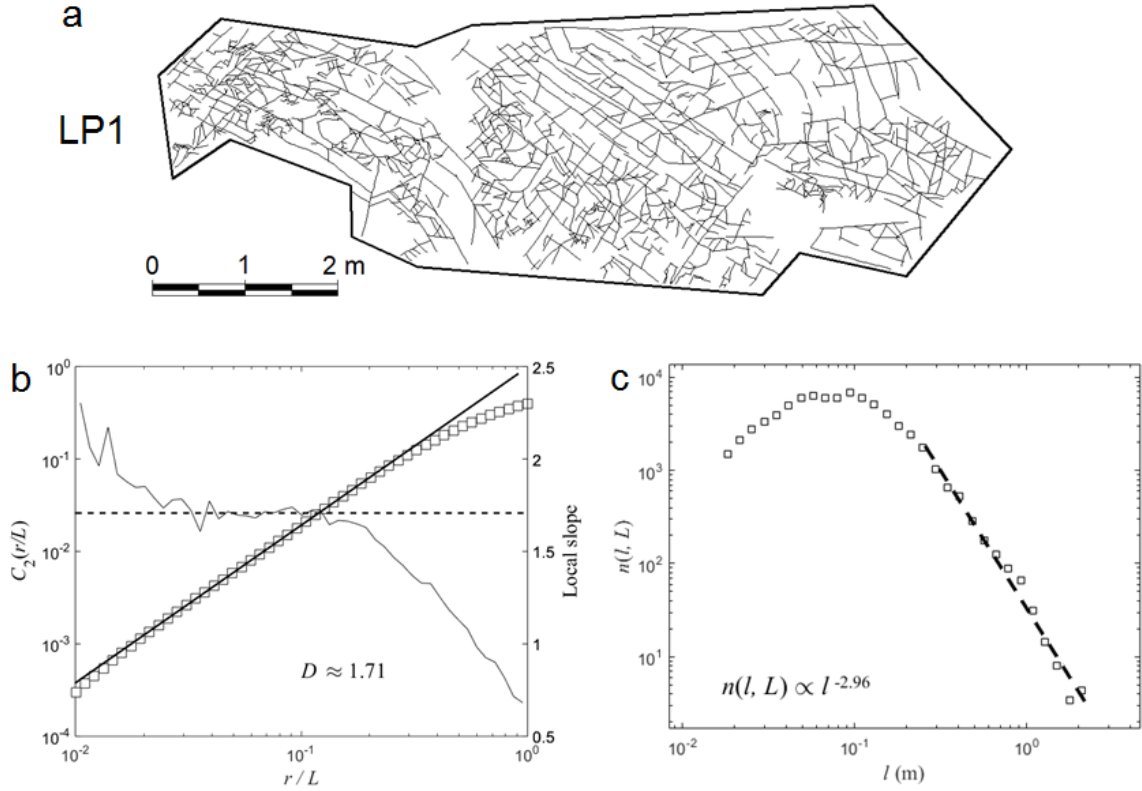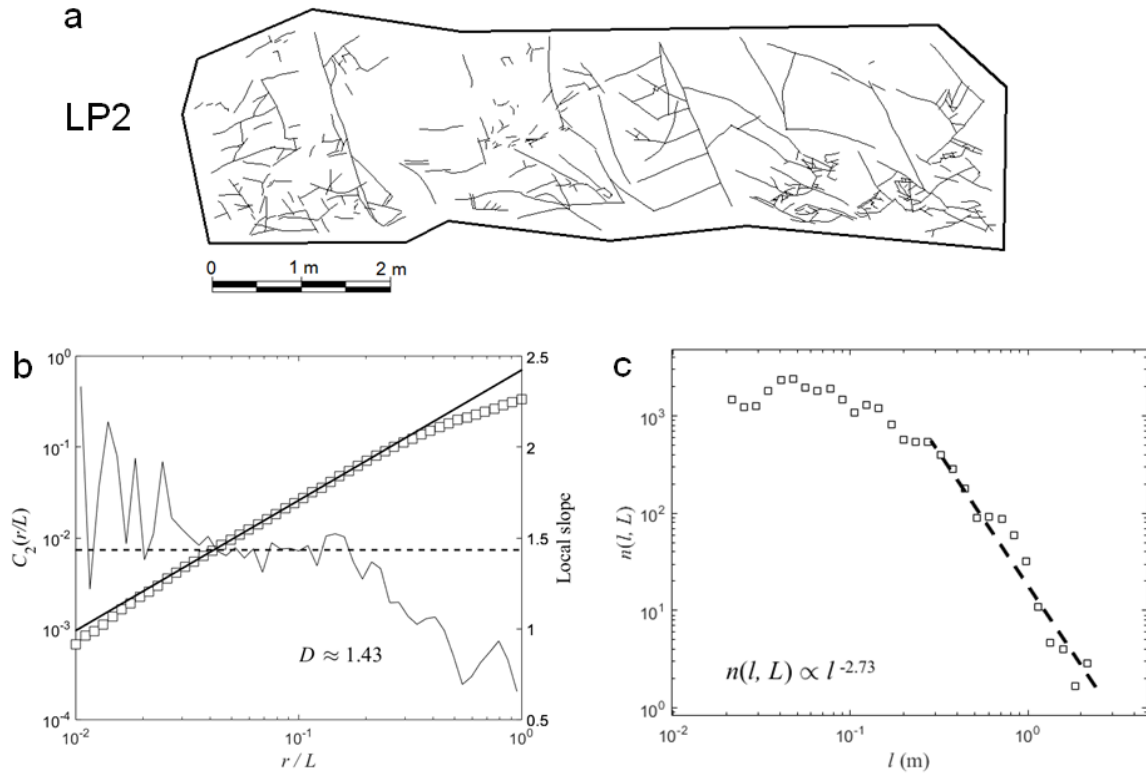
Fig. A.7 (a) A local-scale (~5 m) joint pattern, denoted as LP1, was mapped from an outcrop exposure. (b) Calculation of the normalised two-point correlation function $C_2(r/L)$ as a function of r/L. Squares correspond to the correlation integral, and the bold solid line corresponds to a power law fitting line with a fractal dimension $D = 1.71$ derived from a scale range of $0.02 < r/L < 0.2$. The light solid line corresponds to the local value of logarithmic slope, and the dashed line represents the slope value $D = 1.71$. (c) The density distribution of fracture lengths (represented by squares). The dashed line corresponds to a power law fitting line with an exponent $a = 2.96$.
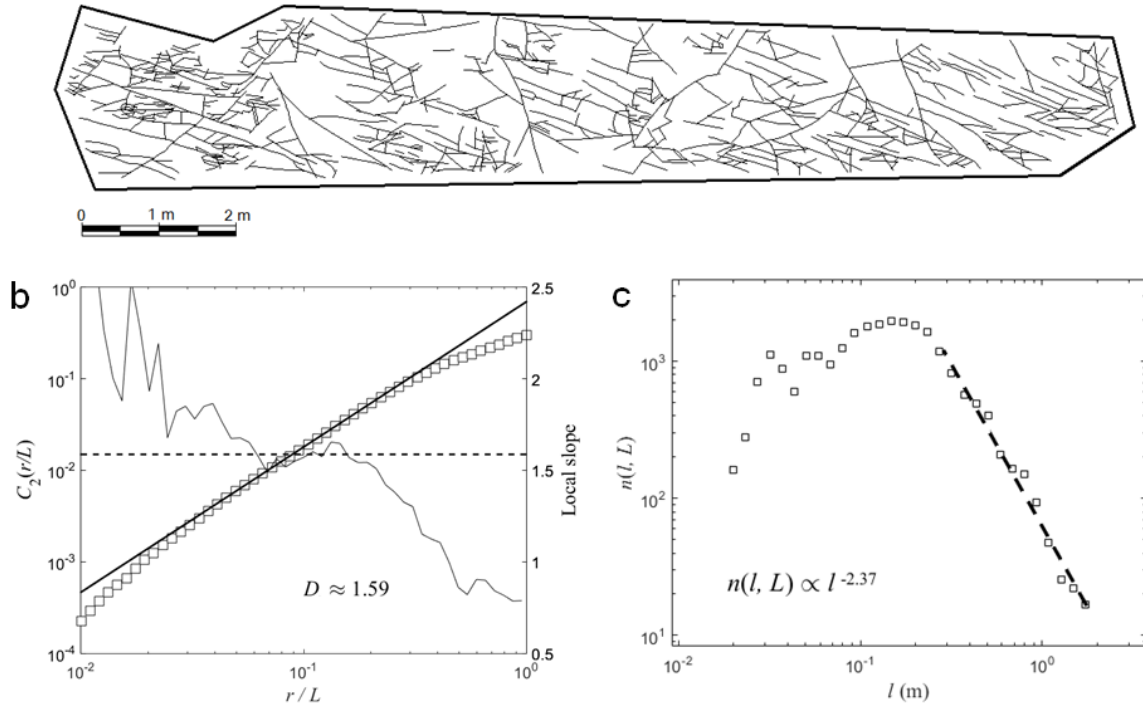
Fig. A.8 (a) A local-scale (~5 m) joint pattern, denoted as LP2, was mapped from an outcrop exposure. (b) Calculation of the normalised two-point correlation function $C_2(r/L)$ as a function of r/L. Squares correspond to the correlation integral, and the bold solid line corresponds to a power law fitting line with a fractal dimension $D = 1.43$ derived from a scale range of $0.03 < r/L < 0.2$. The light solid line corresponds to the local value of logarithmic slope, and the dashed line represents the slope value $D = 1.43$. (c) The density distribution of fracture lengths (represented by squares). The dashed line corresponds to a power law fitting line with an exponent $a = 2.73$.
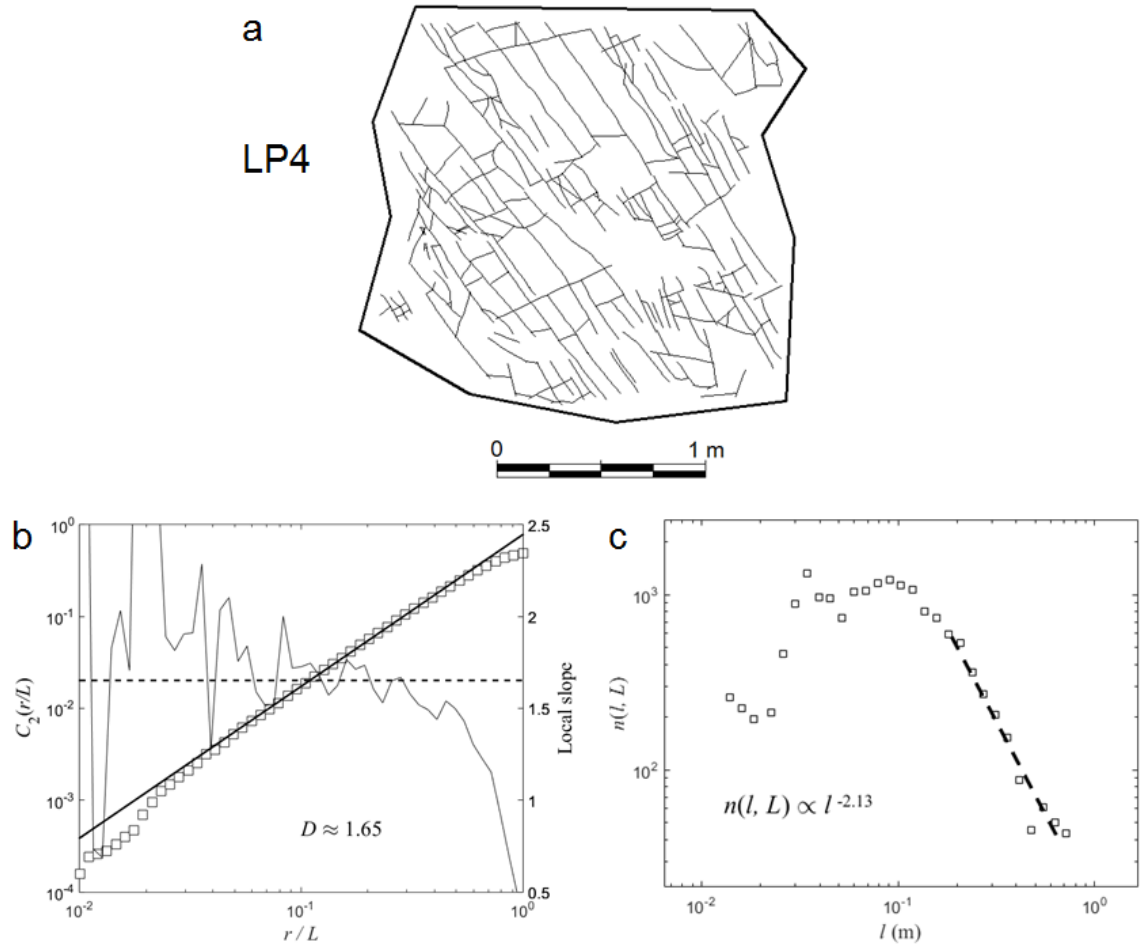
Fig. A.9 (a) A local-scale (~5 m) joint pattern, denoted as LP3, was mapped from an outcrop exposure. (b) Calculation of the normalised two-point correlation function $C_2(r/L)$ as a function of r/L. Squares correspond to the correlation integral, and the bold solid line corresponds to a power law fitting line with a fractal dimension $D = 1.59$ derived from a scale range of $0.04 < r/L < 0.2$. The light solid line corresponds to the local value of logarithmic slope, and the dashed line represents the slope value $D = 1.59$. (c) The density distribution of fracture lengths (represented by squares). The dashed line corresponds to a power law fitting line with an exponent $a = 2.37$.
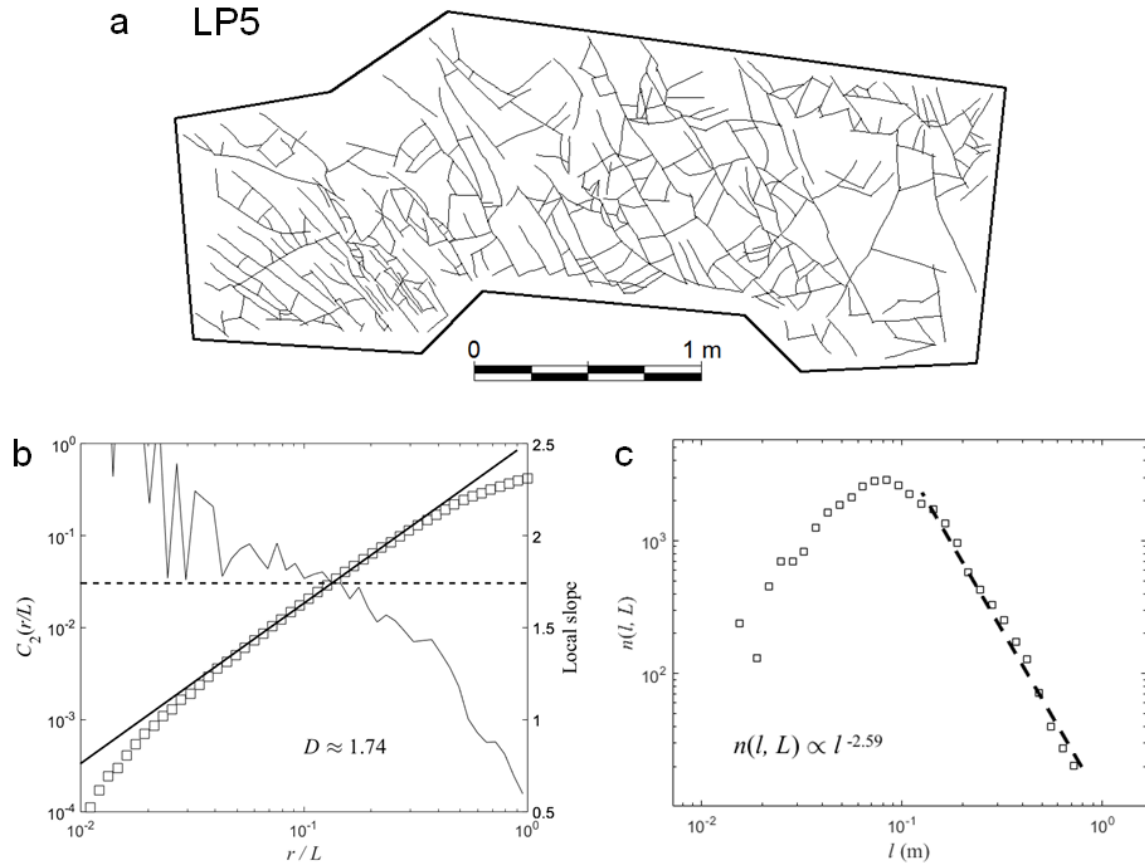
Fig. A.10 (a) A local-scale (~2 m) joint pattern, denoted as LP4, was mapped from an outcrop exposure. (b) Calculation of the normalised two-point correlation function $C_2(r/L)$ as a function of r/L. Squares correspond to the correlation integral, and the bold solid line corresponds to a power law fitting line with a fractal dimension $D = 1.65$ derived from a scale range of $0.05<r/L<0.5$. The light solid line corresponds to the local value of logarithmic slope, and the dashed line represents the slope value $D = 1.65$. (c) The density distribution of fracture lengths (represented by squares). The dashed line corresponds to a power law fitting line with an exponent $a = 2.13$.
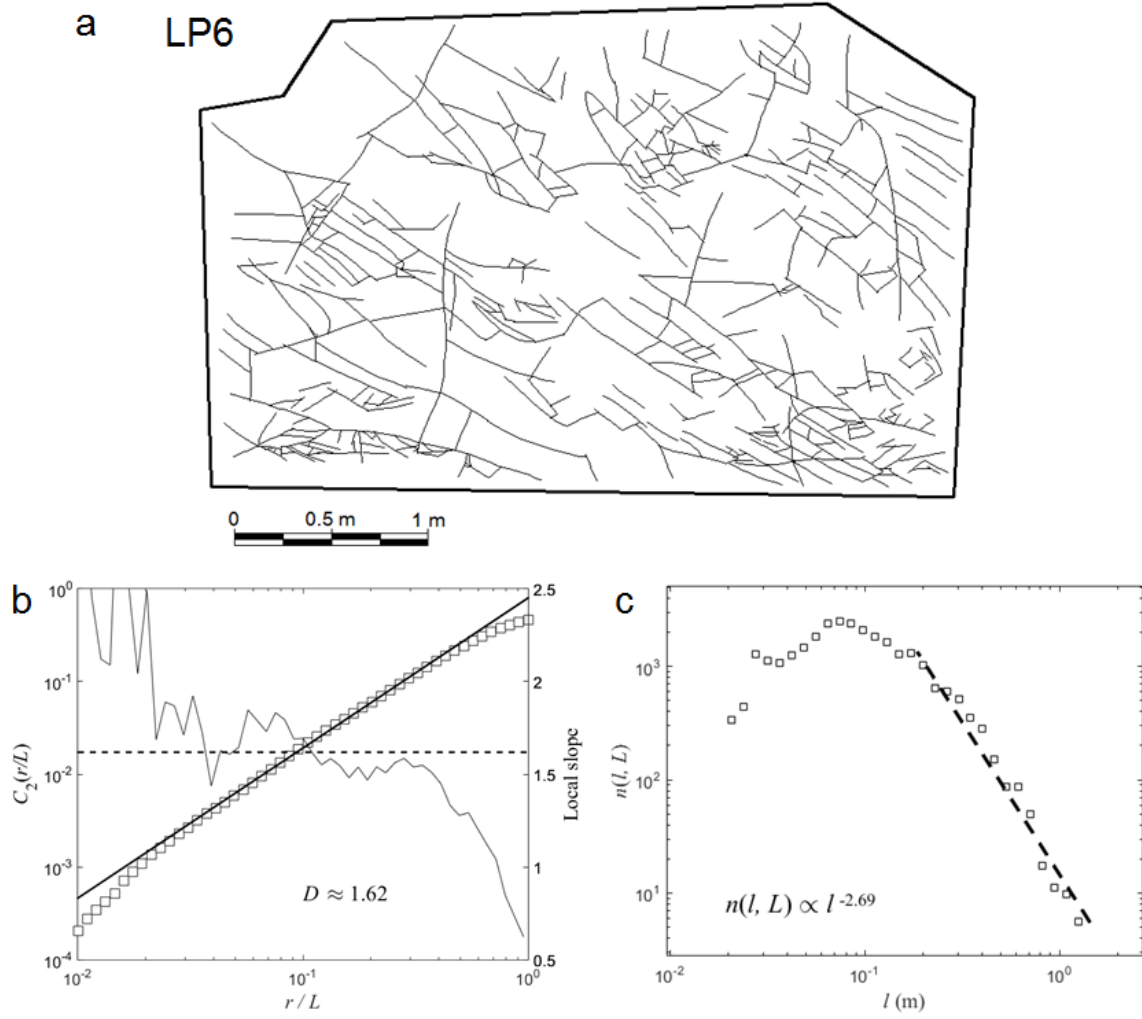
Fig. A.11 (a) A local-scale (~2 m) joint pattern, denoted as LP5, was mapped from an outcrop exposure. (b) Calculation of the normalised two-point correlation function $C_2(r/L)$ as a function of r/L. Squares correspond to the correlation integral, and the bold solid line corresponds to a power law fitting line with a fractal dimension $D = 1.74$ derived from a scale range of $0.05<r/L<0.2$. The light solid line corresponds to the local value of logarithmic slope, and the dashed line represents the slope value $D = 1.74$. (c) The density distribution of fracture lengths (represented by squares). The dashed line corresponds to a power law fitting line with an exponent $a = 2.59$.
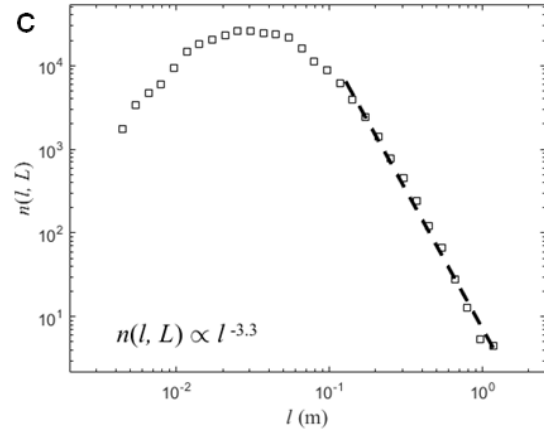
Fig. A.12 (a) A local-scale (~3 m) joint pattern, denoted as LP6, was mapped from an outcrop exposure. (b) Calculation of the normalised two-point correlation function $C_2(r/L)$ as a function of r/L. Squares correspond to the correlation integral, and the bold solid line corresponds to a power law fitting line with a fractal dimension $D = 1.62$ derived from a scale range of $0.04 < r/L < 0.4$. The light solid line corresponds to the local value of logarithmic slope, and the dashed line represents the slope value $D = 1.62$. (c) The density distribution of fracture lengths (represented by squares). The dashed line corresponds to a power law fitting line with an exponent $a = 2.69$.
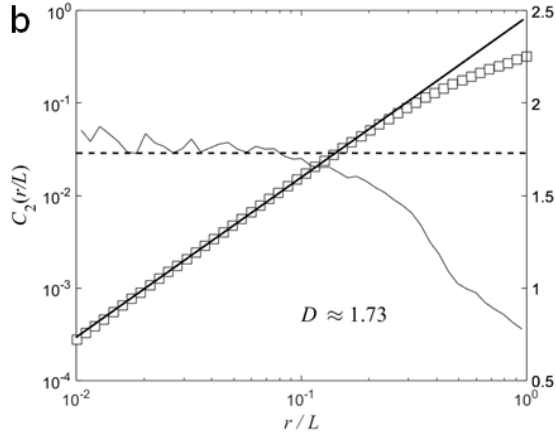
Fig. A.13 (a) A local-scale (~3 m) joint pattern, denoted as LP7, was mapped from an outcrop exposure. (b) Calculation of the normalised two-point correlation function $C_2(r/L)$ as a function of r/L. Squares correspond to the correlation integral, and the bold solid line corresponds to a power law fitting line with a fractal dimension $D = 1.73$ derived from a scale range of $0.01<r/L<0.2$. The light solid line corresponds to the local value of logarithmic slope, and the dashed line represents the slope value $D = 1.73$. (c) The density distribution of fracture lengths (represented by squares). The dashed line corresponds to a power law fitting line with an exponent $a = 3.3$.
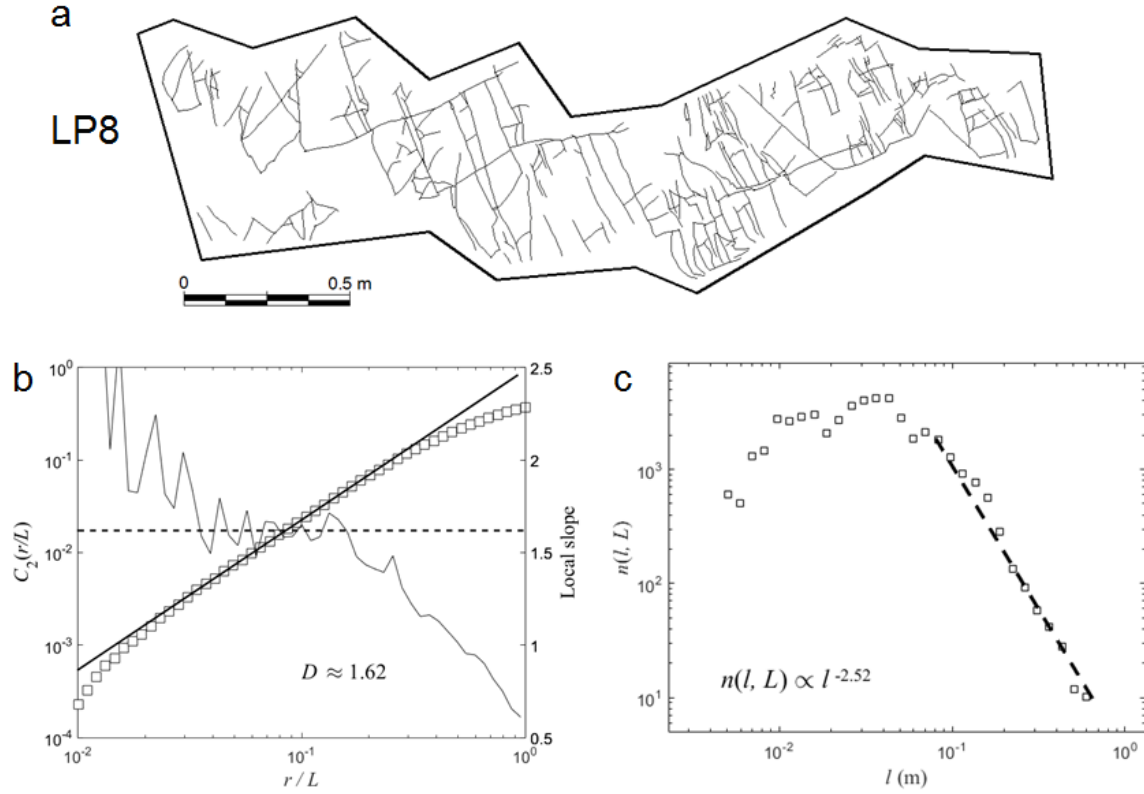
Fig. A.14 (a) A local-scale (~1 m) joint pattern, denoted as LP8, was mapped from an outcrop exposure. (b) Calculation of the normalised two-point correlation function $C_2(r/L)$ as a function of r/L. Squares correspond to the correlation integral, and the bold solid line corresponds to a power law fitting line with a fractal dimension $D = 1.62$ derived from a scale range of $0.03<r/L<0.2$. The light solid line corresponds to the local value of logarithmic slope, and the dashed line represents the slope value $D = 1.62$. (c) The density distribution of fracture lengths (represented by squares). The dashed line corresponds to a power law fitting line with an exponent $a = 2.52$.
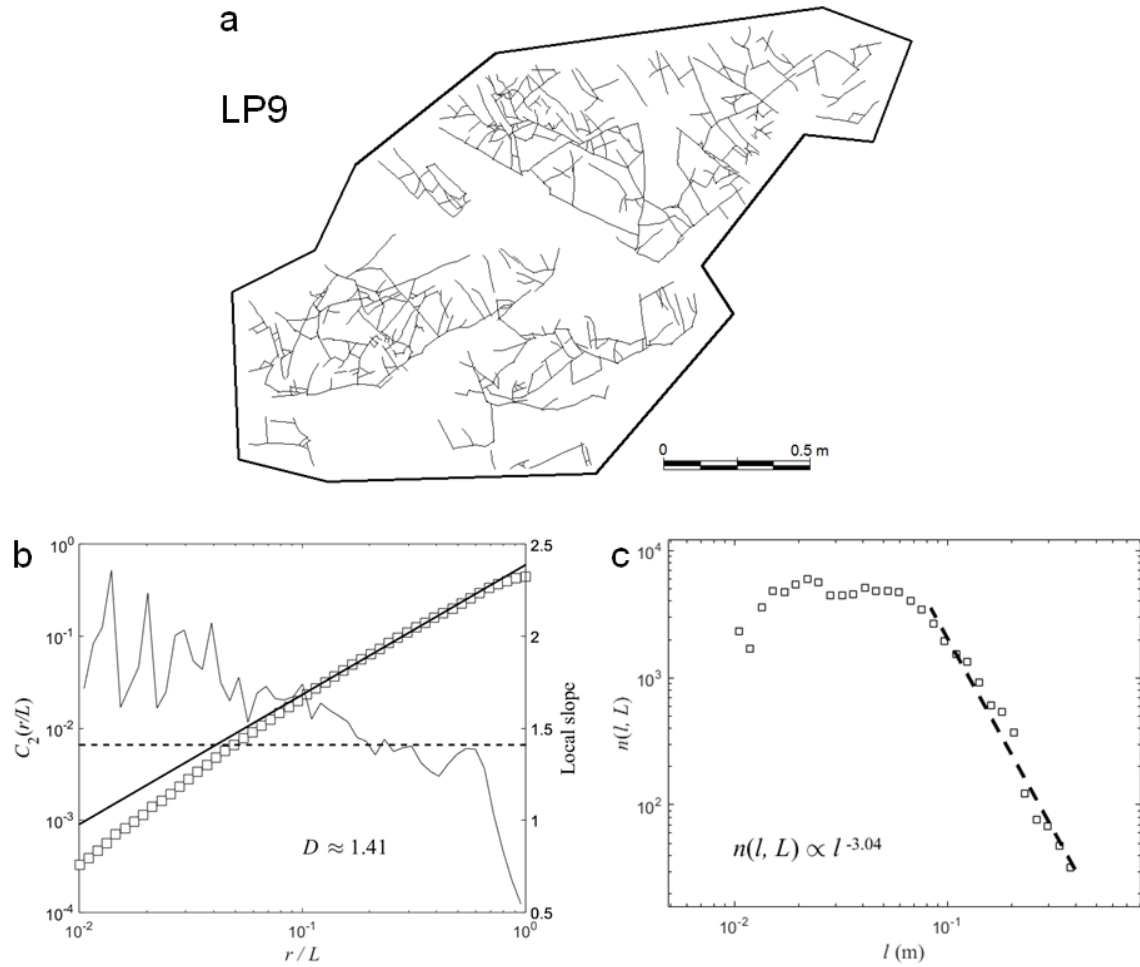
Fig. A.15 (a) A local-scale (~2 m) joint pattern, denoted as LP9, was mapped from an outcrop exposure. (b) Calculation of the normalised two-point correlation function $C_2(r/L)$ as a function of r/L. Squares correspond to the correlation integral, and the bold solid line corresponds to a power law fitting line with a fractal dimension $D = 1.41$ derived from a scale range of $0.1<r/L<0.6$. The light solid line corresponds to the local value of logarithmic slope, and the dashed line represents the slope value $D = 1.41$. (c) The density distribution of fracture lengths (represented by squares). The dashed line corresponds to a power law fitting line with an exponent $a = 3.04$.
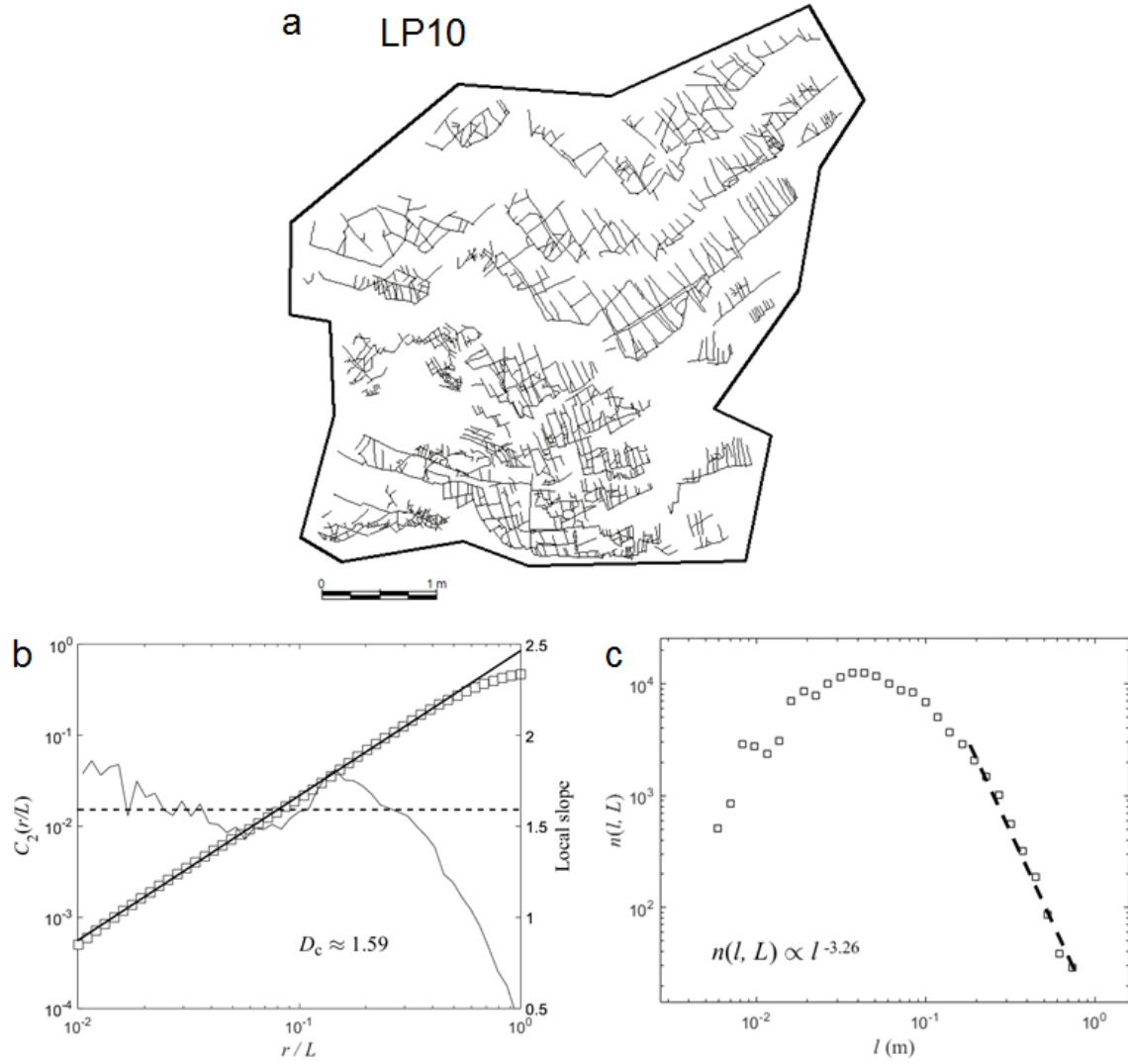
Fig. A.16 (a) A local-scale (~5 m) joint pattern, denoted as LP10, was mapped from an outcrop exposure.

(b) Calculation of the normalised two-point correlation function $C_2(r/L)$ as a function of r/L. Squares

correspond to the correlation integral, and the bold solid line corresponds to a power law fitting line with a

fractal dimension $D = 1.59$ derived from a scale range of $0.01 < r/L < 0.3$. The light solid line corresponds to

the local value of logarithmic slope, and the dashed line represents the slope value $D = 1.59$. (c) The

density distribution of fracture lengths (represented by squares). The dashed line corresponds to a power
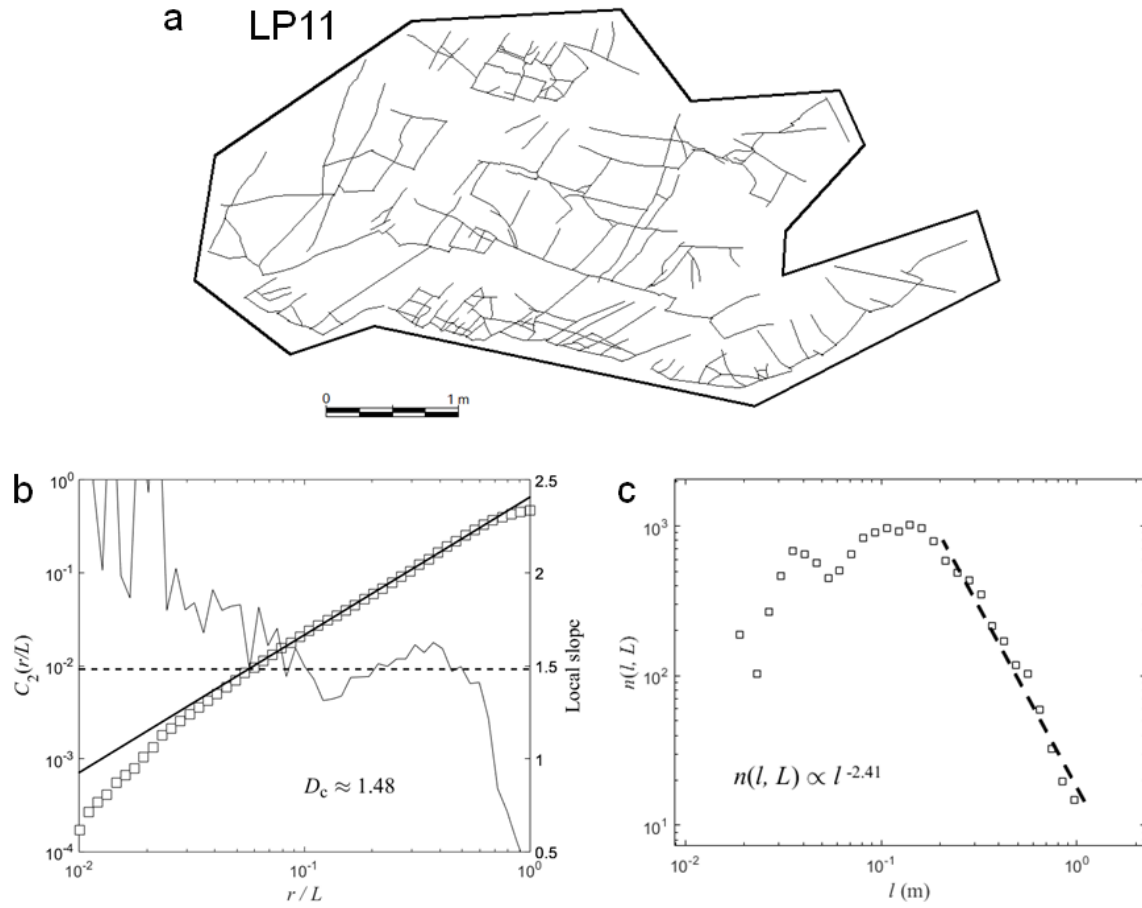
law fitting line with an exponent $a = 3.26$.

Fig. A.17 (a) A local-scale (~3 m) joint pattern, denoted as LP11, was mapped from an outcrop exposure.

(b) Calculation of the normalised two-point correlation function $C_2(r/L)$ as a function of r/L. Squares

correspond to the correlation integral, and the bold solid line corresponds to a power law fitting line with a

fractal dimension $D = 1.48$ derived from a scale range of $0.06 < r/L < 0.6$. The light solid line corresponds to

the local value of logarithmic slope, and the dashed line represents the slope value $D = 1.48$. (c) The

density distribution of fracture lengths (represented by squares). The dashed line corresponds to a power

law fitting line with an exponent $a = 2.41$.